

# OPTICAL FIBRE SENSORS AND DEEP LEARNING ALGORITHMS BASED STRUCTURAL HEALTH MONITORING FRAMEWORK FOR REINFORCED CONCRETE BEAMS

A Thesis submitted by

Minol Narajith Jayawickrema Udagedara B.Sc. Engineering (Hons)

For the award of

Doctor of Philosophy

2023

#### **ABSTRACT**

This thesis presents a novel framework for structural health monitoring (SHM) of reinforced concrete (RC) beams based on fibre optic sensor (FOS) technology, finite element analysis (FEA), and deep learning (DL). The proposed research addresses the limitations of existing SHM methods by constructing a tailored sensor network, a comprehensive strain dataset, and an efficient DL model for accurate predictions. The study began with a comprehensive analysis of current SHM practises, focusing on applying and incorporating FOS, FEA, and DL in monitoring structural health. Distributed optical fibre sensors were used to establish a sensor network and acquire strain data from RC beams subjected to different loading conditions. Concrete damaged plasticity-based FEA model was established and validated with experimental strain data. The validated model has been used to generate a strain dataset. This dataset was then used to train a DL model for predicting the structural health of RC beams based on artificial neural network architecture. The proposed SHM framework was exhaustively validated via a two-tiered experimental procedure involving short and long-span RC beams subjected to various loading scenarios. The predictive capabilities of the DL model were evaluated rigorously using the extensive strain data derived from these experiments. The model prediction has been classified into eight classes, and the prediction accuracy was impressive 81.25%. Sensitivity analysis revealed a robust prediction accuracy of 74% with only 20% of input data. This study is novel due to its integrated approach to SHM, which leverages the assets of FOS, FEA, and DL to provide precise, data-driven insights into the structural health of RC beams. This method not only improves the efficacy and precision of SHM, but it also has the potential to be applied to other types of structures, thereby creating new research opportunities and field advancements.

CERTIFICATION OF THESIS

I Minol Narajith Jayawickrema Udagedara declare that the PhD Thesis

entitled Optical Fibre Sensors and Deep Learning Algorithms Based

Structural Health Monitoring Framework for Reinforced Concrete Beams is

not more than 100,000 words in length including quotes and exclusive of

tables, figures, appendices, bibliography, references, and footnotes. The

thesis contains no material that has been submitted previously, in whole or

in part, for the award of any other academic degree or diploma. Except

where otherwise indicated, this thesis is my own work.

Date: 2023.07.19

Endorsed by:

Associate Professor Jayantha Ananda Epaarachchi

Principal Supervisor

Dr Nandita Hettiarachchi

Associate Supervisor

Dr Harsha Sooriyaarachchi

Associate Supervisor

Student and supervisors' signatures of endorsement are held at the

University.

ii

### **ACKNOWLEDGEMENTS**

This research voyage was made possible by the generous scholarship of the Australian Government Research Training Programme. I am eternally appreciative of this supportive assistance.

Associate Professor Jayantha Epaarachchi, my primary supervisor, has my sincerest gratitude. His unwavering commitment, invaluable feedback, profound subject knowledge, and unrelenting encouragement have been nothing short of invigorating.

Dr Nandita Hettiarachchi and Dr Harsha Sooriyaarachchi, associate supervisors, Faculty of Engineering, University of Ruhuna, deserve my sincere appreciation. Their timely insights, unwavering support, and consistent encouragement have been instrumental in my academic trajectory.

I sincerely thank the members of my confirmation of candidature (COC) committee, Associate Professor Mainul Islam, Dr Sourish Banerjee, and Dr Wijitha Senerdeera. Contributing to my COC report's rigorous academic standards, their invaluable input and thorough evaluations were instrumental in its refinement.

I would like to thank the extraordinary personnel at the University of Southern Queensland's higher education services, graduate research school, information and communication technology, library, and finance departments for their assistance. Their consistent assistance has fostered an environment conducive to my research.

My wife, Thakshila Dilupama, deserves special recognition. Her unwavering love, steadfast support, patience, and comprehension have been my anchor. I am incredibly grateful to her for accompanying me on this voyage.

My parents, Mahindika Manamendra and Ananda Jayawickrema, have been my guiding light due to their trust in me and the instillation of strong values. Your unwavering faith in my potential has inspired me to pursue excellence. Last but certainly not least, I extend my most profound appreciation to everyone who contributed to this research in any form. This accomplishment is a result of your inspiration, motivation, and unwavering support, in addition to my own. I appreciate your participation in this endeavour.

# **TABLE OF CONTENTS**

ABSTRACT	
CERTIFICATION OF THESIS	ii
ACKNOWLEDGEMENTS	iii
LIST OF TABLES	viii
LIST OF FIGURES	X
ABBREVIATIONS	xvi
CHAPTER 1: INTRODUCTION	1
1.1. Background	1
1.2. Research problems	4
1.3. Research objectives and signification	ance5
1.4. Structure of the thesis	7
1.5. List of publications	8
1.6. Summary	10
CHAPTER 2: LITERATURE REVIEW	11
2.1. Introduction	11
2.2. Fibre optic sensor-based SHM	12
2.2.1. FBG sensors	14
2.2.2. Distributed optical fibre senso	rs 25
2.3. Finite element analysis	36
2.3.1. Smeared crack model	37
2.3.2. CDP model	39
2.4. Deep learning	43
2.4.1. Supervised DL	45
2.4.2. Unsupervised DL	46
2.5. Critical components of RC beam	s 56
2.6. OFS and DL applications for SHN	1 56
2.6.1. Bridges	58
2.6.2. Buildings	65
2.7. Review outcome and research q	aps67

CHAPTER 3: TRAINING DATA GENERATION AND DEVELOPMENT	OF DEEP
LEARNING MODEL	71
3.1. Introduction	71
3.2. Overview of DL model for SHM predictions in RC beams	72
3.2.1. Artificial neuron	73
3.2.2. Artificial neural networks	75
3.2.3. Backpropagation algorithms	76
3.2.4. Proposed ANN architecture	78
3.3. How FEA enhances data collection in SHM	82
3.4. Material model for steel reinforcement	83
3.5. Material model for concrete	83
3.5.1. Elastic properties of concrete	83
3.5.2. CDP model	84
3.5.3. Finite element type and mesh	92
3.5.4. Constraints and contact interactions	93
3.5.5. Load application and analysis procedure	93
3.5.6. CDP model parameters	94
3.6. Strain data extraction from FEA models	95
3.6.1. Mesh convergence study	103
3.7. Summary	105
CHAPTER 4: IMPLEMENTATION OF DISTRIBUTED SENSOR NETW	ORKS
AND DATA ACQUISITION	107
4.1. Introduction	107
4.2. Sensor installation	108
4.2.1. Sensor installation on concrete	109
4.2.2. Sensor installation on rebar	110
4.3. Strain monitoring	113
4.4. The testing procedure of RC beams	115
4.4.1. Short-span RC beam	116
4.4.2. Long-span RC beams	120
4.5. Summary	131
CHAPTER 5: PERFORMANCE EVALUATION OF SHM FRAMEWORK	133

5.1. Introduction
5.2. Comparison of experimental and simulation results for short-span
RC beam 134
5.2.1. Rebar and surface strain
5.2.2. Exploring the relationship between steps, dilation angles, and
strain patterns for dataset construction
5.3. Experimental and simulation results for long-span RC beams . 142
5.3.1. Effect of SSQ on DOFS readings
5.3.2. Rebar and surface strain – R20C30
5.3.3. Rebar and surface strain – R16C30
5.3.4. Rebar and surface strain – R12C30
5.3.5. The behaviour of residual strain
5.3.6. Rebar and surface strain – R20C60
5.3.7. Rebar and surface strain – R16C60
5.3.8. Rebar and surface strain – R12C60
5.4. DL model training and testing with experimental data 169
5.4.1. Short-span RC beams
5.4.2. Long-span RC beams
5.4.3. DL model sensitivity analysis
5.5. Summary
CHAPTER 6: CONCLUSIONS AND FUTURE RESEARCH
6.1. Overview of the research work
6.2. Summary of the key findings190
6.3. Summary of the contributions
6.4. Generalisation of the SHM framework
6.5. Suggestions for future research
REFERENCES

# **LIST OF TABLES**

Table 2.1: FBG sensors used in SHM for civil structures	. 24
Table 2.2: DOFS used in SHM for civil structures	. 34
Table 2.3: Applications of CDP modelling in RC beams	. 41
Table 2.4: DL-based methods used in SHM for civil structures	. 50
Table 2.5: The combined applications of OFS and DL for SHM	. 57
Table 3.1: CDP properties for FEA model	. 95
Table 3.2: Material properties for the short-span RC beam	. 97
Table 3.3: CDP model parameters for strain data generation	. 99
Table 3.4: Material properties the long-span RC beam FEA model	100
Table 3.5: Beam nomenclature	103
Table 3.6: FEA model parameters for strain data generation	103
Table 3.7: CDP properties of short-span RC beam	104
Table 3.8: CDP properties for long-span R20C30 Beam	105
Table 4.1: The cure characteristics and cured properties of TECHNIG	LUE
R60	110
Table 4.2: The cure characteristics and cured properties of TECHNIG	
R15	
Table 4.3: Specifications of LUNA OBR 4600	114
Table 4.4: Beam description for R12C30, R16C30, and R20C30	121
Table 4.5: Beam description for R12C60, R16C60, and R20C60	130
Table 5.1: Load with respect to step	139
Table 5.2: Effect of SSQ on beams	147
Table 5.3: Comparison of experimental outcome vs predicted outcome	e of
the DL model	171
Table 5.4: Assigned classes	173
Table 5.5: Guide for predictions	173
Table 5.6: DL model predictions for R20C30, R16C30, and R12C30	173
Table 5.7: Sensitivity analysis of input parameters	177
Table 5.8: DL Model performance indicators – Training with stat parameters	
	178

Table	5.9:	The	DL	model	predictions	for	R20C30,	R16C30,	R12C30
R20C3	30, R1	6C30	, an	d R12C	30				179
Table	5.10:	Sens	itivit	y analy	sis for Phase	1			184

# **LIST OF FIGURES**

Figure 1.1: SHM framework for RC beams6
Figure 2.1: (a) Working principle of FBG; (b) Typical configuration of FBG
interrogation15
Figure 2.2: FBGs in shrinkage, creep, fatigue, and prestressed concrete (a)
Shrinkage strain readings from FBG sensors [85]; (b) Creep strain readings
from FBG sensors [85]; (c) Load vs wavelength curves of adhesive-bonded
FBGs in cyclic loading and unloading tests with steel wire sample [86]; (d)
The distribution of stress in a steel strand under load [87]; (e) Cylinder
with embedded FBG sensor [85]; (f) Steel wire attached FBGs sample
fatigue test [86]
Figure 2.3: FBGs in rebars, corrosion and crack length measurements (a)
Experimental distributions of reinforcing strains along steel bars at various
loading stages [88]; (b) Strain history as determined by the FBG strain
measurement [89]; (c) Strain throughout the grating direction as measured
by the FBG1 sensor at various crack lengths [90]; (d) Experimental setup
of FBG sensor test [88]; (e) Reinforced mortar specimen and sensor
installation [89]23
Figure 2.4: (a) Backscattered lights from different locations of the fibre and
scattering modes; (b) Typical configuration of OTDR setup; (c) Typical
configuration of BOTDA setup27
Figure 2.5: DOFS in crack detection in rebar and surface, and crack width
monitoring (a) Multiple strain profiles from the DOFS, with the red
triangular shape indicating the determined crack location based on the
strain profile at maximum load and the grey shaded region corresponding
to the DIC position [112]; (b) Detection and identification of cracks at the
commencement of load cycles [113]; (c) Information about the position
and width of cracks is included in the development of crack functions [39];
(d) Installation of OFSs [39]; (e) Sensors mounted to beams and adhesives
used [113]30
Figure 2.6: DOFS in corrosion and deformation monitoring (a) Strain

distributions with the optical fibre in detail [115]; (b) Hoop strain
distribution measured by one DOFS [48]; (c) Comparison of strain data
measured by DOFS and ESGs for the lower surface of pipeline [116]; (d)
Comparison of strain data measured by DOFS and ESGs for the upper
surface of pipeline [116]; (e) Steel bar with a helix optical fibre [115]; (f)
Corrosion test pipe [48]33
Figure 2.7: DL in crack detection and structural damage identification 49
Figure 2.8: FBG-based SHM system at steel bridge crossing the Beijing-
Hangzhou Grand Canal located in Hangzhou-China [98]59
Figure 2.9: Monitoring site at Cheong-ri Bridge [117] (a) Optical fibre
mounted on the outer surface of the rail; (b) mounted on the lower flange
of the girder; (c) DOFS system based on BOCDA method; (d) configuration
of the optical system61
Figure 2.10: Monitoring site of Jin-Hu Bridge [222]64
Figure 2.11: Bridge girder testing at a laboratory (a) Placement of sensors;
(b) loading setup [225] 65
Figure 2.12: DOFS mounted on the masonry vaults at Sant Pau hospital,
Barcelona [118] 66
Figure 3.1: Overview of technical contents of Chapter 3
Figure 3.2: Biological Neuron74
Figure 3.3: Mathematical model of the artificial neuron [235] 74
Figure 3.4: Typical ANN topology77
Figure 3.5: (a) ReLU transfer function; (b) Logistic sigmoid transfer function
81
Figure 3.6: Schematic representation of the stress-strain relation for
uniaxial compression (CEB FIP Model code 1990)87
Figure 3.7: Response of concrete to uniaxial loading in compression
(ABAQUS manual) 88
Figure 3.8: Stress-strain and stress-crack opening diagram for uniaxial
tension (CEB FIP Model code 1990)90
Figure 3.9: Reinforcement details and sectional view of the short-span RC
beam 97

Figure 3.10: FEA model of short-span RC beam (a) Boundary conditions
and loading configuration; (b) Mesh configuration98
Figure 3.11: Loading arrangement and data extraction paths of short-span
RC beam (a) Surface and rebar data extraction path; (b) FEA surface and
rebar strain data extraction path99
Figure 3.12: Beam definitions for R20C30 RC beam 100
Figure 3.13: (a) Loading and boundary condition; (b) Mesh configuration
Figure 3.14: (a) FEA Bottom surface data extraction path; (b) FEA side
surface data extraction path; (c) FEA rebar surface data extraction path
Figure 3.15: Proposed loading arrangements for strain data generation
Figure 3.16: Mesh convergence study for short-span RC beam 104
Figure 3.17: Mesh convergence study for long-span beam
Figure 4.1: Overview of the technical contents of Chapter 4 108
Figure 4.2: TECHNIGLUE R60 and H60
Figure 4.3: Concrete surface attached to FOS
Figure 4.4: TECHNIGLUE R15 and H15
Figure 4.5: (a) The groove cut on the rebar; (b) DOFS before attachment;
(c) Attached DOFS to the rebar by R15 Epoxy glue 111
Figure 4.6: (a) PE tubing; (b) Furcation tubes
Figure 4.7: OBR 4600 system for interrogation of DOFS
Figure 4.8: FC/APC connector
Figure 4.9: Short-span RC beam definition
Figure 4.10: (a) Reinforcement cage inside the mould; (b) Cast concrete
beam
Figure 4.11: Sensor layout for short-span RC beam
Figure 4.12: (a) Surface-mounted FOS; (b) Rebar-mounted FOS 118
Figure 4.13: Testing of the beam
Figure 4.14: Beam definitions of R12C30, R16C30, and R20C30 120
Figure 4.15: (a) Reinforcement cage; (b) Reinforcement cage inside the

mould; (c) Casted concrete beam
Figure 4.16: Sensor Layout
Figure 4.17: Configuration for rebar testing
Figure 4.18: Experimental setup of rebar testing
Figure 4.19: Strain variation along the rebar R12 124
Figure 4.20: Strain variation along the rebar R16 125
Figure 4.21: Strain variation along the rebar R20 125
Figure 4.22: Mounted surface sensors
Figure 4.23: Schematic diagram of loading arrangement
Figure 4.24: The experimental beam loading arrangement
Figure 4.25: The connected OBR 4600 with the beam
Figure 4.26: Beam definition of R12C60, R16C60, and R20C60 130
Figure 4.27: The proposed schematic diagrams for loading configurations
Figure 5.1: Overview of the technical contents of Chapter 5 133
Figure 5.2: Experimental strain vs simulation strain results of the bottom
rebar of the beam B1 at 16 kN load 135
Figure 5.3: Experimental surface strain vs simulation surface strain results
of the beam B2 at 16 kN load
Figure 5.4: Hairline crack locations appeared on the bottom surface of the
beams
Figure 5.5: FOS in a cracked concrete surface
Figure 5.6: Surface strain against sensor length obtained from simulation
under increasing load – Beam B1
Figure 5.7: Rebar strain against sensor length obtained from simulation
under increasing load – Beam B1140
Figure 5.8: Surface strain against sensor length obtained from simulation
for varying dilation angles – Beam B1 140
Figure 5.9: Rebar strain against sensor length obtained from simulation for
varying dilation angles – Beam B1141
Figure 5.10: Raw strain data, after removing raw strain data below 0.15
SSQ threshold, SSQ and 0.15 SSQ threshold for rebar DOFS at different

loadings 144
Figure 5.11: Raw strain data, after removing raw strain data below 0.15
SSQ threshold, SSQ and 0.15 SSQ threshold for bottom surface DOFS at
different loadings
Figure 5.12: Experimental vs simulation rebar strain for beam R20C30149
Figure 5.13: Strain variation of rebar and bottom surface sensor at 10 kN
load for beam R20C30 149
Figure 5.14: Experimental vs simulation bottom surface strain for beam
R20C30 at 40kN
Figure 5.15: Experimental vs simulation side surface strain for beam
R20C30 (a) at 40kN; (b) at 60kN
Figure 5.16: The experimental rebar strain variation for R16C30 153
Figure 5.17: The experimental bottom surface strain variation for R16C30
(a) 0-25kN; (b) 0-25kN; (c) 0-30kN
Figure 5.18: The experimental side surface strain variation for R16C30 (a)
0-25kN; (b) 0-25kN; (c) 0-40kN
Figure 5.19: The experimental rebar strain variation for R12C30 157
Figure 5.20: The experimental bottom surface strain variation for R12C30
(a) 0-15kN; (b) 0-15kN; (c) 0-20kN
Figure 5.21: The experimental side surface strain variation for R12C30159
Figure 5.22: Comparison of residual rebar strain after the first stage of
loading and second stage of loading for beam R12C30 161
Figure 5.23: Comparison of residual rebar strain after the first stage of
loading and second stage of loading for beam R16C30 161
Figure 5.24: Schematic diagram of rebar with attached DOFS 162
Figure 5.25: Experimental setup of rebar testing
Figure 5.26: Rebar strain variation at loading and unloading 163
Figure 5.27: The experimental rebar strain variation for beam R20C60 164
Figure 5.28: The experimental bottom surface strain variation for beam
R20C60
Figure 5.29: The experimental side surface strain variation for beam
R20C60

Figure 5.30: The experimental rebar strain variation for beam R16C60 166
Figure 5.31: The experimental bottom surface strain variation for beam
R16C60
Figure 5.32: The experimental side surface strain variation for beam
R16C60
Figure 5.33: The experimental rebar strain variation for beam R12C60 168
Figure 5.34: The experimental bottom surface strain variation for beam
R12C60
Figure 5.35: The experimental side surface strain variation for beam
R12C60
Figure 5.36: Proposed ANN for short-span RC beams
Figure 5.37: DL model accuracy vs number of epochs
Figure 5.38: Proposed ANN for long-span RC beams
Figure 5.39: Proposed ANN with new input parameters
Figure 5.40: Strain data extracting segments for phase 1
Figure 5.41: Strain data extracting segments for phase 2
Figure 5.42: Variation of prediction accuracy for phase 2
Figure 6.1: Flowchart for generalisation of the framework

## **ABBREVIATIONS**

AE Acoustic emission

ANN Artificial neural networks

ASPP Atrous spatial pyramid pooling

BOCDA Brillouin optical correlation domain analysis

BOTDA Brillouin optical time domain analysis

BOTDR Brillouin optical time domain reflectometer

CDP Concrete damaged plasticity

CFRP Carbon-fibre-reinforced plastic

CNN Convolutional neural network

CWT Continuous welded turnouts

DCNN Deep convolutional neural network

DL Deep learning

DOFS Distributed optical fibre sensor

ESG Electrical strain gauge

FBG Fibre bragg grating

FEA Finite element analysis

FFNN Feedforward neural network

FOS Fibre optic sensor

FRP Fibre reinforced plastic

GPR Ground-penetrating radar

HPC High-performance concrete

MFNN Multilayer feedforward neural network

ML Machine learning

MLPNN Multilayer perceptron neural network

MSE Mean squared error

NDT Non-destructive testing

OBR Optical backscattered reflectometer

OFDR Optical frequency domain reflectometry

OFS Optical fibre sensor

PGA Peak ground acceleration

PGD Peak ground velocity

PGV Peak ground displacement

PVC Polyvinyl chloride

RC Reinforced concrete

RNN Recurrent neural network

SCM Smeared crack model

SHM Structural health monitoring

UHPC Ultra-high performance concrete

UHPFRC ultra-high performance fibre reinforced concrete

### **CHAPTER 1: INTRODUCTION**

#### 1.1. Background

The significance of structural health monitoring (SHM) in civil engineering has increased in recent years, as it is essential for sustaining the safety, resilience, and durability of infrastructure assets such as bridges [1-3], buildings [4-6], and pipelines [7-9], which are the backbone of modern societies. Demand for dependable and efficient civil structures has increased as the global population and rate of urbanisation continue to rise. These structures are subject to a multitude of stressors, such as natural hazards such as earthquakes [10-12] and floods [13-15], material degradation due to ageing [16-18] and corrosion [19-21], and mechanical loads from traffic and wind forces [22, 23], which can lead to structural deterioration or even destructive failure.

Engineers can identify and monitor the health of these structures by using SHM techniques, allowing for the early detection of damage, defects, or other distress symptoms. This data enables asset managers to make informed decisions regarding maintenance, repair, and replacement, ensuring the infrastructure's structural integrity and functionality [24]. This proactive approach reduces the risk of structural failure and its associated consequences, including loss of life and property. It also optimises resource allocation, thereby reducing financial and environmental costs associated with infrastructure management.

SHM also contributes to the ecological development of our built environment by extending the service life of structures and decreasing the demand for new construction [25]. The environmental impact of civil engineering projects can be diminished by perpetually monitoring and addressing structural issues, as fewer raw materials and energy are consumed, and waste generation is minimised. In addition, SHM technologies can monitor infrastructure resilience to climate change and other environmental challenges [26] by providing data-driven insights into

structural behaviour under varying conditions and facilitating the development of adaptive strategies.

SHM systems can also provide valuable data for research and development, enabling engineers to better understand the structures' behaviour under various loading conditions [27]. This leads to more efficient, durable, and resilient infrastructure design and construction. In this way, SHM contributes to developing innovative materials, designs, and construction techniques that will influence the future of our built environment.

Reinforced concrete (RC) beams serve as a fundamental component in the construction of a broad range of civil structures, including buildings [28] and bridges [29]. They play a crucial role in the modern infrastructure. The inherent properties of RC, a composite material formed by embedding steel reinforcement bars within a concrete matrix, enable it to withstand both compressive and tensile loads effectively. This unique combination of strength and ductility enables RC beams to distribute structural loads efficiently and provide robust support for the diverse load-carrying needs of infrastructure assets.

Current methods of SHM for civil structures, including concrete beams, play a crucial role in preserving the integrity and safety of these vital infrastructure components. Several non-destructive techniques have been developed and implemented to evaluate and monitor the condition of civil structures, allowing engineers and asset managers to make informed decisions regarding maintenance and repair strategies [30].

Non-destructive testing (NDT) techniques are extensively employed in SHM because they permit structural health evaluation without damaging the beams. Despite the subjectivity of human judgement and accessibility restrictions, visual inspection [31, 32] continues to be a popular and cost-effective technique. Advanced NDT techniques like ground-penetrating radar (GPR) [33], which uses electromagnetic waves to detect internal defects, acoustic emission (AE) monitoring [34], which tracks the release of elastic energy due to micro-cracking within the concrete, and vibration-

based monitoring [35], which tracks changes in a structure's vibrational characteristics (such as natural frequency, mode shapes, or damping ratio) to track damage, have been developed to overcome these limitations.

Even though the mentioned SHM methodologies are effective and indispensable, they have limitations. For example, visual inspection heavily relies on the observer's subjective judgement and experience [36]. This technique may neglect internal irregularities or flaws that are not readily apparent on the surface. Moreover, conducting a thorough visual examination can be difficult when dealing with expansive or architecturally complex structures.

Although GPR is an effective method for detecting internal defects, The difficulty associated with interpreting and comprehending the resulting data is one of the most significant drawbacks of the GPR technique, which is the subject of substantial criticism regarding its potential application [37]. AE testing is similarly circumscribed; it is susceptible to interference from ambient noise, necessitating stringent control of the testing environment. Associating each AE signal with a particular damage mechanism is a significant concern when employing the AE technique [38]. In addition, AE can only detect active defects presently emitting sound, leaving dormant defects undetected. Furthermore, in vibration-based SHM, damage detection, localization, and quantification are complex tasks. Although numerous damage indicators and damage indices based on vibration parameters have been proposed, their sensitivities are insufficient for early damage detection [35].

The potential of distributed fibre optic sensor (DFOS) networks, finite element analysis (FEA), and deep learning (DL) in SHM are enormous, as these cutting-edge technologies can revolutionise how infrastructure is evaluated and maintained. Distributed optical fibre sensor (DOFS) allow for the continuous, real-time monitoring of structures, capturing vital data regarding their response to various loads and environmental conditions. These sensor networks can be configured to monitor specific parameters, such as strain [39], temperature [40], or vibration [41], providing valuable

insights into the behaviour and performance of the structure. These sensor networks can be deployed to monitor a parameter in a distributed fashion [42], allowing comprehensive structural health evaluation.

When coupled with DL algorithms, FEA and DOFS-based large datasets can be efficiently processed and analysed, enabling the detection of subtle structural changes that may indicate damage or deterioration. DL models can learn complex patterns and relationships from data, enhancing the precision and dependability of health predictions. Moreover, integrating distributed sensor networks and DL models in SHM systems can result in the development of proactive maintenance strategies, optimising resource allocation, and extending the service life of structures. Combining these technologies can revolutionise the field of SHM by enhancing the safety and resiliency of our civil infrastructure while simultaneously reducing maintenance costs and environmental impact. Therefore, the researchers are investigating the viability of DOFS networks, FEA, and the use of DL technologies to surmount the limitations of current SHM methods for RC beams.

#### 1.2. Research problems

- 1. Lack of research work on proper integration of recent advancements in sensing, large data analysis, and health predictions into a framework is a major remaining problem in SHM of civil infrastructures.
- 2. Unavailability of a comprehensive and representative dataset of strains for DL model training, i.e., analytical which can be correlated from operational data of a RC structure/component.
- 3. Scarcity of procedures for designing and implementing sensor networks for RC structures/components.
- 4. Inadequate research work on creating, training and evaluating an Effective DL Model for a SHM framework

#### 1.3. Research objectives and significance

This research intends to develop an SHM framework for RC beams, concentrating on creating a detailed FEA model for training data generation, developing a DL model for structural health prediction, and implementation of distributed sensor networks for data acquisition. The research objectives are:

- Review current methods and applications of fibre optic sensor (FOS), FEA, and DL-based SHM models for civil infrastructures; identify the critical points within RC beams for developing a distributed sensor network integral to the proposed SHM framework based on this understanding.
- Create a comprehensive strain dataset from a validated FEA model for training a DL model. Within the SHM framework, this procedure will serve as the foundation for developing a robust structural health prediction algorithm.
- 3. Develop a distributed sensor network for RC beams. The sensor network will function as the SHM framework's primary mechanism for data acquisition.
- 4. Train a DL model for structural health prediction using FEA model data and test this model using sensor network data. This procedure will evaluate the performance of the DL model in predicting the structural health of RC beams under various conditions. This objective is the last part of the proposed framework.

This study's significance is broad, as it addresses critical aspects of SHM for RC beams through a comprehensive approach that includes sensor network installation, FEA modelling, and DL model development for structural health prediction. This research contributes to the SHM field by developing a systematic method for selecting critical items in RC beams for sensor network installation, thereby improving the efficiency and precision of monitoring structural health. In addition, the design and development of distributed sensor attachments and installation procedures will enhance the

quality of data collected for real-world applications. The detailed FEA model, validated by experimental data from the sensor network, will improve the accuracy and dependability of SHM techniques. The proposed SHM framework for RC beams is illustrated in Figure 1.1.

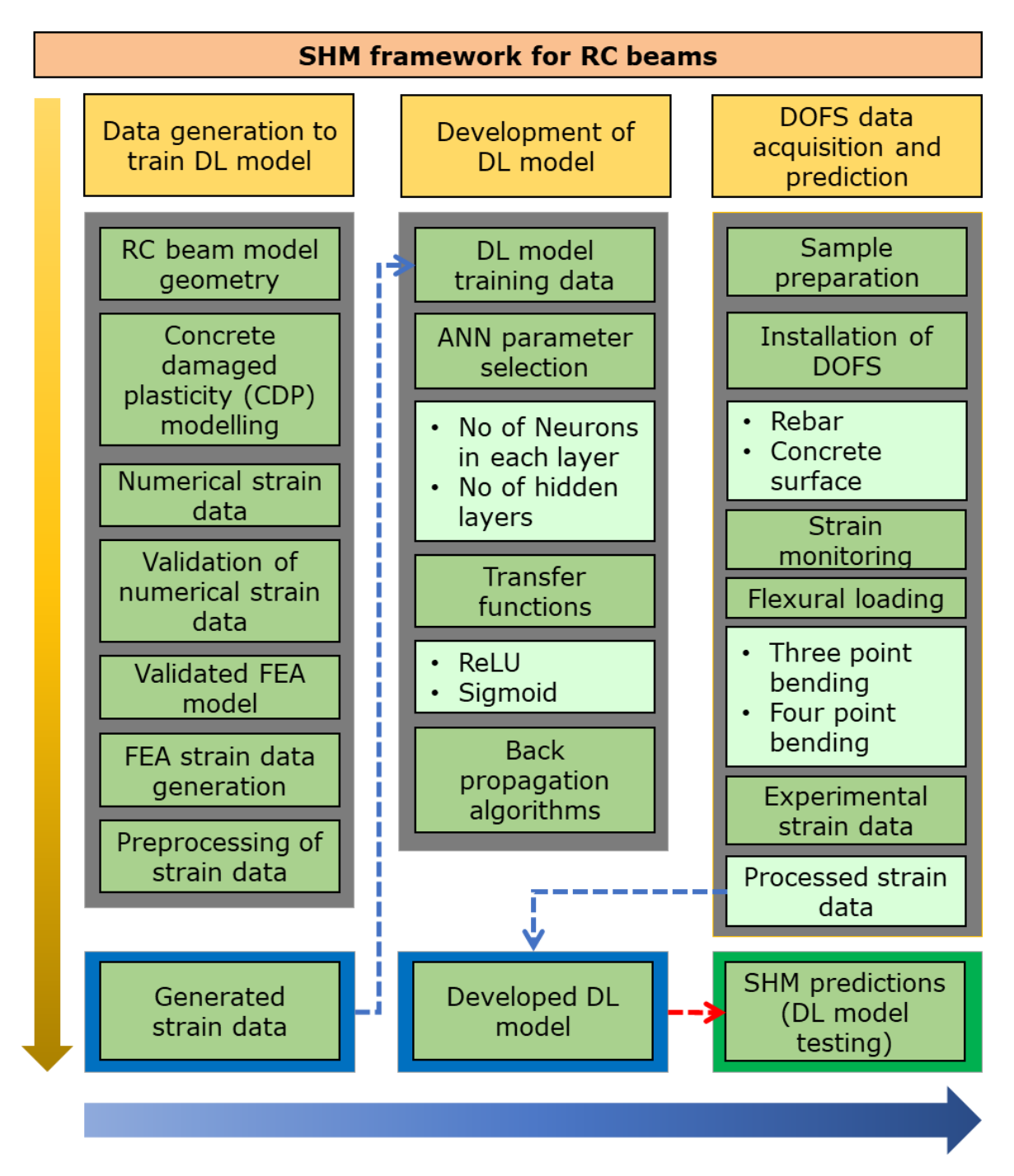


Figure 1.1: SHM framework for RC beams

Effective SHM techniques will enable early detection of structural damage. Hence it will enhance overall safety and minimise the risk of catastrophic failure. This study also offers significant advantages for infrastructure management and maintenance. The proposed framework for structural health prediction will facilitate more informed decision-making, resulting in cost reductions, improved resource allocation, and possibly an extension of RC beams' service life.

The framework devised in this study can applies to other types of structures, such as bridges, buildings, and tunnels, thereby expanding the research scope and applicability. SHM's efficacy and precision can be enhanced by incorporating additional data sources and advances in sensor technology. In addition, the multidisciplinary nature of this study, which combines civil engineering, computer science, and fibre optic sensing, can inspire new research collaborations, and advance the field of SHM.

#### 1.4. Structure of the thesis

The structure of the thesis is as follows:

- 1. Introduction: This chapter provides the background, research problems, research objectives and significance, and a thesis outline.
- Literature review: This chapter reviews the existing literature on SHM in reinforced civil structures, DFOS networks, FEA modelling methods for RC beams, and DL models for structural health prediction. The first objective of the study is addressed here.
- 3. Training data generation and development of deep learning model: This chapter discusses the FEA model, creating the strain dataset, and developing DL models. This chapter covers the development of the proposed framework's DL model as well as data generation for DL model training. The second objective of the research is covered in this chapter.
- 4. Implementation of distributed sensor networks and data acquisition: This chapter covers developing sensor attachments and installation procedures, and the experimental setup and data acquisition from the sensor network. In addition to describing the DOFS data acquisition

- component of the framework, this chapter in-depth addresses the third objective of the study.
- 5. Performance evaluation of SHM framework: This chapter presents the correlation of FEA models with experimental data, evaluation of the performance of the DL model, and sensitivity analysis. The SHM prediction, the last element of the suggested SHM framework, is covered in this chapter along with the fourth objective.
- 6. Conclusions and future research: This final chapter summarises the overview of the research work, key findings, contributions, generalisation of the SHM framework, and recommendations for future research and development in the field of SHM.

This structure provides a coherent and logical research organisation, guiding the reader through various study stages.

#### 1.5. List of publications

- > Journal articles
- J1 UMN Jayawickrema, HMCM Herath, NK Hettiarachchi, HP Sooriyaarachchi, JA Epaarachchi (2022). Fibre-optic Sensor and Deep Learning-based Structural Health Monitoring Systems for Civil Structures: A Review. *Measurement*.
  - https://doi.org/10.1016/j.measurement.2022.111543
- J2 UMN Jayawickrema, A Kumar, HMCM Herath, NK Hettiarachchi, HP Sooriyaarachchi, JA Epaarachchi (2022). Strain patterns of short span reinforced concrete beams under flexural loading: A comparison between distributed sensing and concrete damaged plasticity modelling. Journal of Intelligent Material Systems and Structures.
  - https://doi.org/10.1177/1045389X221128764
- J3 UMN Jayawickrema, HMCM Herath, NK Hettiarachchi, HP Sooriyaarachchi, S Banerjee, JA Epaarachchi, & G Prusty (2023). A

- Distributed Sensing and Supervised Deep Learning-Based Novel Approach for Long-Term Structural Health Assessment of Reinforced Concrete Beams. *Engineering Applications of Artificial Intelligence*. (Submitted for review)
- J4 Hua-Ping Wang, Cong Chen, Yi-Qing Ni, UMN Jayawickrema, & JA Epaarachchi (2023). Computer-aided feature recognition of CFRP plates based on real-time strain fields reflected from FBG-measured signals. Composite part B.

https://doi.org/10.1016/j.compositesb.2023.110866

## Conference proceedings

- C1 UMN Jayawickrema, JA Epaarachchi, NK Hettiarachchi, LH Janitha Jeewantha, & HMCM Herath (2019). Monitoring structural performance of concrete beams using embedded Fibre Bragg Grating (FBG) sensors, The 10th International Conference on Structural Engineering and Construction Management, Kandy, Sri Lanka, 2019, pp. 264-271.
- C2 UMN Jayawickrema, AS Kumar, HMCM Herath, NK Hettiarachchi, HP Sooriyaarachchi, & JA Epaarachchi (2021). Surface-Mounted Distributed Fibre Optic Sensor Measurements, and Concrete Damaged Plasticity Modelling for Damage Analysis of Reinforced Concrete Beams. ASME 2021 Conference on Smart Materials, Adaptive Structures, and Intelligent Systems, Virtual Online, September 14–15, 2021.
- C3 **UMN Jayawickrema**, HMCM Herath, NK Hettiarachchi, HP Sooriyaarachchi, S Banerjee, & JA Epaarachchi (2023). Impact of Spectral Shift Quality (SSQ) on FOS Readings in Reinforced Concrete Beams, IWSHM 2023, Conference on Designing SHM for Sustainability, Maintainability and Reliability, Hybrid Conference, Stanford University, CA, September 12–14, 2023.

#### 1.6. Summary

This introductory chapter lays the groundwork for thoroughly examining the development of an SHM framework for RC beams. The proposed research will evaluate and enhance current methods and applications of FOS technology, FEA, and DL in SHM models.

Evaluation of extant methodologies and their incorporation into a cohesive SHM framework constitutes the research problem. This comprehensively analyses how FOS, FEA, and DL complement one another and their compatibility with current practices. A secondary problem entails implementation of optimal sensor network for RC beams that can react to the changing conditions of the beam it monitors. Creating an exhaustive and representative strain dataset from a validated FEA model for training DL models is an additional challenge. The accuracy of the FEA model is essential for producing a high-quality strain dataset, which directly impacts the DL model's ability to predict structural health. Developing, training, and evaluating an effective DL model within the proposed SHM framework is challenging. The model must be able to process vast volumes of data, extract meaningful features, and make accurate predictions.

The significance of this study resides in its potential contributions to SHM, infrastructure management, and maintenance for RC beams. The proposed framework will enhance the quality of collected data, improve the efficacy and precision of monitoring structural health, and facilitate making informed decisions. This study also bears promise for future research because its methodologies and tools could be applied to other structure types, fostering new research collaborations and advancements in the SHM field.

#### **CHAPTER 2: LITERATURE REVIEW**

#### 2.1. Introduction

SHM plays a pivotal role in safeguarding the integrity of civil infrastructures, especially RC beams, which are a fundamental element of such structures. Early detection of possible problems allows for preventative maintenance, thus saving time, resources, and, potentially, lives. This literature review will delve into the existing body of knowledge around three key areas:

- (1) the use and application of FOS networks in SHM,
- (2) the application of FEA in modelling RC beams, and
- (3) the potential of DL models in predicting structural health.

Despite significant advances in these areas, there are noticeable gaps in integrating and optimizing these technologies for the specific context of RC beams. While FOS technologies have been employed successfully for SHM in various contexts, their systematic application, particularly concerning optimal distribution and data interpretation, needs further exploration. Similarly, the correlation of FEA models with experimental data from FOS sensor networks is another relatively less researched area. Additionally, creating accurate and reliable strain datasets from FEA models for training DL models requires further investigation.

The use of DL models has been ground-breaking in numerous fields; however, its application for SHM in predicting the health of RC beams is not exploited fully. Current models may need refinement or exploration of different types of neural networks that could yield better results. Combining SHM with FOS, FEA, and DL models opens up a promising new area of research.

This literature review aims to provide a comprehensive understanding of these themes, critically assess the current methodologies and technologies, and identify potential gaps in the literature that could serve as focal points for future research.

#### 2.2. Fibre optic sensor-based SHM

SHM systems rely heavily on the sensors' precision, the quantity of data collected, and the data analysis algorithms' efficacy. Due to its lightweight reliability, stability, small size, immunity to external electromagnetic perturbations, low power, high sensitivity, multiplexing capability, and wide bandwidth, fibre optic sensing is among the most exciting and rapidly expanding research fields for enhancing inspection accuracy and performance. In addition, substantial drawbacks include high costs and end-user unfamiliarity [42-47]. Due to the numerous advantages of fibre optic sensing, FOSs are preferred over conventional sensors [48-53].

FOSs have replaced conventional sensors in various applications, i.e., strain, vibration, electric, acoustic, magnetic fields, acceleration, rotation, pressure, temperature, linear and angular position, humidity, viscosity, and chemical measurements. Due to their dielectric property, fibre-optic sensors can be used in harsh environments such as relatively high temperatures, high voltage, or corrosive materials; they can also conduct remote sensing [54]. Different types of embedded or surface-mounted sensors are available for SHM systems. However, only fibre-based systems quasi-distributed, perform integrated, and fully distributed can measurements on or even within the structure over long distances [55]. Due to their distinct capabilities, research on various optical fibre sensors (OFSs) has risen to the top of engineers' and scientists' research agendas. Consequently, more research has been performed on OFSs for SHM systems, such as civil infrastructure [56-59], mechanical apparatus [60], robotics [61], and aerospace applications [62-65].

Fibre optic monitoring systems have been devised and successfully implemented recently. When properly engineered and manufactured, OFS can be highly resilient and long-lasting in the most demanding environment. Owing to the long-term dependability and low maintenance requirements of OFS, optical sensing will be less expensive than its electrical counterpart. The sensor in optical sensing is contained within an

optical fibre. Changes to a monitored parameter, such as strain and temperature, alter the directed light's intensity, phase, spectral content, polarization state, or a combination thereof. These modifications could be interpreted as parameter modifications. The optical fibre connects the sensor to the data acquisition system. A single optical fibre can be used for transmission and sensing, and multiple sensors can operate simultaneously. Consequently, installation in the environment can be made more accessible.

OFSs are classified according to their sensors, which include discrete or point sensors and distributed sensors. A point sensor provides a single measurement parameter pertinent to the sensor's location, whereas distributed sensors measure multiple measurements continuously and not at a specific location [66]. The cost of distributed sensing of multiple measurement sites can be significantly lower than that of a conventional single-point sensor due to the absence of expensive and difficult deployment and complex data acquisition methods. Point or distributed FOSs capture only the positional strains in the fibre. A crack alters the strain field only close to the crack's tip, leaving the global strain field unaffected; therefore, it can be detected only when damages occur close to the optical fibre path. This will be the most significant limitation of the technique. Many inherent benefits are associated with modern OFS, such as it is inherently safe and explosion-proof and is particularly suited for health monitoring applications [67]. The smaller size of OFS allows it to operate in environments with limited space [68]. However, the OFS is highly fragile and susceptible to failure or damage in harsh field conditions [39, 69].

The FOSs can measure over long distances without electrically active components and are crucial for monitoring large and distant structures such as pipelines, bridges, and dams [68]. The only devices that require the power supply are the laser light source and the analyser. Power supplies for commercially available FBG interrogators range from 15 W to 25 W (2 to 16 channels); Optical Distributed Sensor Interrogators are 240W to 300W (Luna ODiSI 6100/ ODiSI-B 5.0), and optical backscatter

reflectometers are 100W (Luna OBR 4600). FBG and DOFS sensors will be further discussed since they are used extensively in SHM-based applications in civil engineering structures.

#### 2.2.1. FBG sensors

FBG sensors are the most widely used grating-based sensors, extensively used for SHM in civil structures, aerospace, automotive, biomechanics, and maritime areas [70, 71] due to their high sensitivity to multiple physical, chemical, and biomedical environmental parameters [57]. An FBG reflects a portion of incoming light with a specific wavelength, known as the *Bragg wavelength* while allowing the preponderance of incoming light to pass through unaffected. The index of fibre refraction and the grating pitch determine the Bragg wavelength, which is affected by external environment variations [72, 73]. The grating's period and reflected wavelength change correspondingly when a local deformation is present, allowing the detection of the local strain [74]. Figures 2.1a, b illustrate the FBG operating principle and a typical configuration for FBG interrogation.

Changes in the transmitted and reflected optical spectra can help investigate physical and chemical parameters [75-77]. Numerous physical parameter changes can be monitored when an FBG is embedded or bonded to the necessary host material. Any strain in the fibre at the Bragg grating can alter the Bragg wavelength reflected, which can be precisely detected. FBG sensors can measure temperature, humidity, strain, vibration, deformation, and displacement [78-84]. FBG sensors offer the same advantages as optical fibre sensors (OFS). Because wavelength-division multiplexing, spatial-division-multiplexing, and time-division-multiplexing can be implemented directly in the fibre without altering the fibre diameter, FBG sensors can be multiplexed using the same techniques as FOS. This property makes FBG sensors ideal for a wide range of applications. Designing and packaging these devices using sensitive packaging techniques is necessary to guarantee the safety of FBG sensors. FBG sensors have been used over the past five years to measure concrete-

related parameters, fatigue responses of steel wires, the use of FBGs in prestressed concrete, reinforcement strain corrosion, and leakage monitoring. The subsequent section will elaborate on the use of FBG sensors.

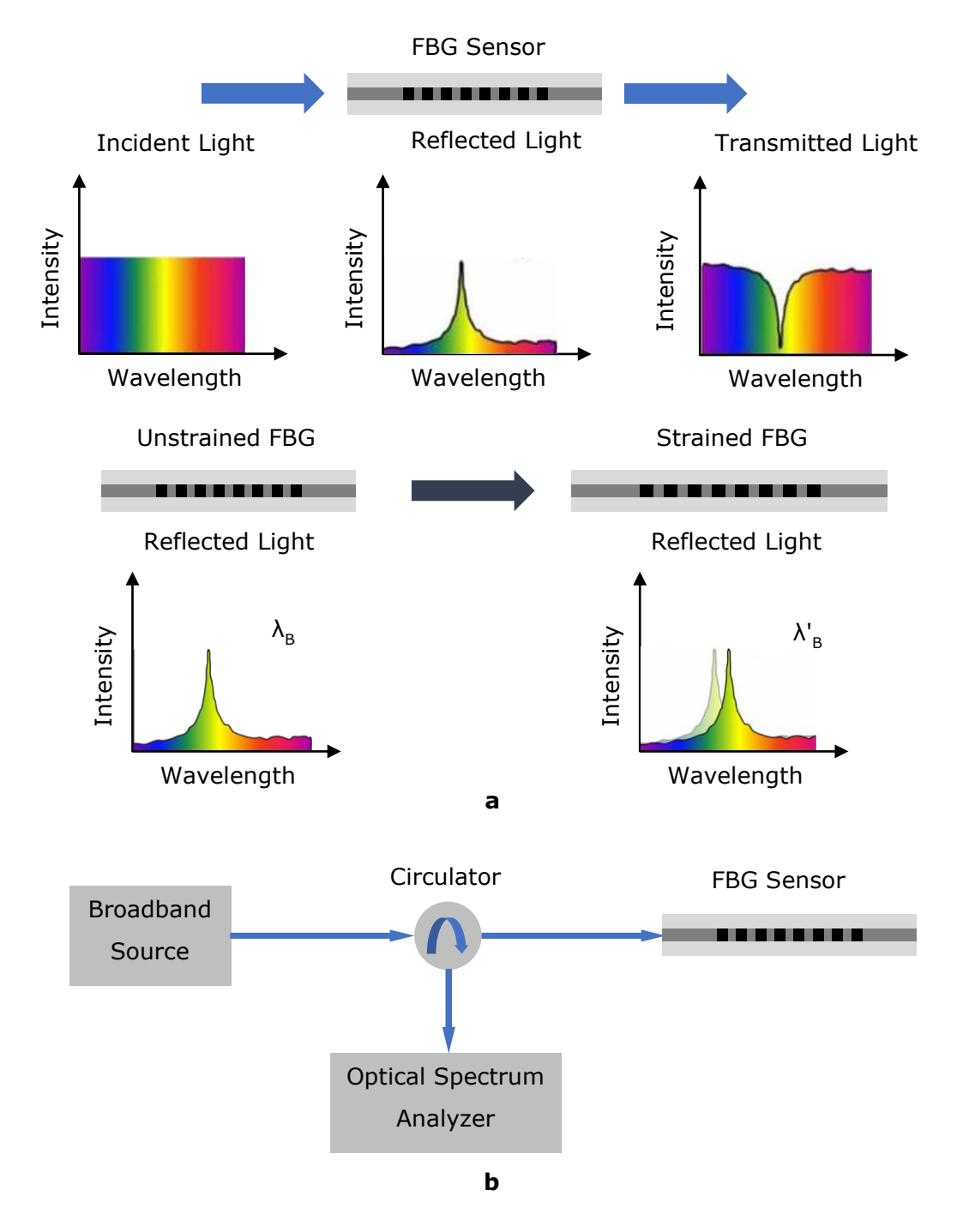


Figure 2.1: (a) Working principle of FBG; (b) Typical configuration of FBG interrogation

Applications of FBG sensors are dispersed across a vast region. Yazdizadeh et al. (2017) employed electrical strain gauges (ESG) and embedded FBG sensors to investigate shrinkage and creep in three distinct concrete grades: Normal strength concrete, high-performance concrete (HPC), and ultra-high-performance concrete (UHPC).

Figure 2.2(a) displays the shrinkage strain variation measured by FBG sensors over 56 days for three different concrete types. The maximum shrinkage is observed within the first week after casting, and the shrinkage strains have remained stable after 35 days. The overall shrinkage strain of concrete is nearly equivalent to the shrinkage strain measured after 35 days, so long-term shrinkage is not required to be measured. This graph demonstrates that high-strength concrete diminishes less than ordinary concrete, and shrinkage decreases with increased concrete strength.

Figure 2.2(b) illustrates the creep strain variation over 28 days (after loading). As can be seen, the creep strain increased rapidly in all three varieties of concrete during the first week after loading and stabilised after three weeks. Alternatively, it becomes less eerie as concrete matures. The graphs demonstrate that as the strength of the concrete increases, creep decreases and that the creep characteristics of UHPC and HPC follow the same pattern as those of standard concrete. The fibre-optic method is preferable to using an ESG for analysing the time-dependent properties of concrete [85].

Cable is the predominant load-bearing component on cable-supported bridges. Zheng et al. (2018) conducted experiments using FBGs to monitor the force of bridge cable tension. The FBGs were bonded with steel wire using structural adhesive, and the relevant measurability and dependability of the adhesive-bonded FBGs with steel wire were evaluated using cyclic loading and unloading tests and fatigue tests. As depicted in Figure 2.2(c), the load-wavelength lines for the fatigued sample fell slightly, indicating that the 200 million fatigue cycles reduced the wavelength of FBGs operating at the same load on steel wire. Load and wavelength had a linear relationship for both the loading and unloading processes, and the

data line from the loading process was parallel to the data line from the unloading process [86].

The value and distribution law of prestress and the bond stress of the steel strand determine the structural integrity of a prestressed concrete structure. Zhu et al. (2021) studied the stress distribution in a prestressed steel strand and the bond stress development between the steel strand and concrete. It was proposed to embed a quasi-distributed FBG sensor in a longitudinal groove of the centre wire of a steel strand. The test results indicate that the quasi-distributed FBG sensor embedded in the centre wire of the steel strand can effectively monitor the steel strand's stress distribution and beam damage, with a maximum tensile monitoring error of 3.42%.

Figure 2.2(d) illustrates the stress distribution in T-beam FBG sensors at different load levels. Notably, the stress in the steel strands increases with the load's progressive increase. The diagrams demonstrate that the stress distribution in the steel strands of the beam changes from dense to sparse. Under load, the reactive powder concrete beam's steel fibres and bottom tensile steel bars carry the tensile tension. As a result, the tension in the steel strand is barely increased.

Nonetheless, once the tensile steel bars have yielded, the steel strand's stress increases swiftly. On the self-sensing steel strand, tensile tests are conducted to ascertain the distribution of prestress and bond stress along the anchorage length. During the tensile process, the quasi-distributed FBG sensor can accurately measure fluctuations in steel strand stress and bond stress along its anchorage length, according to the results [87].

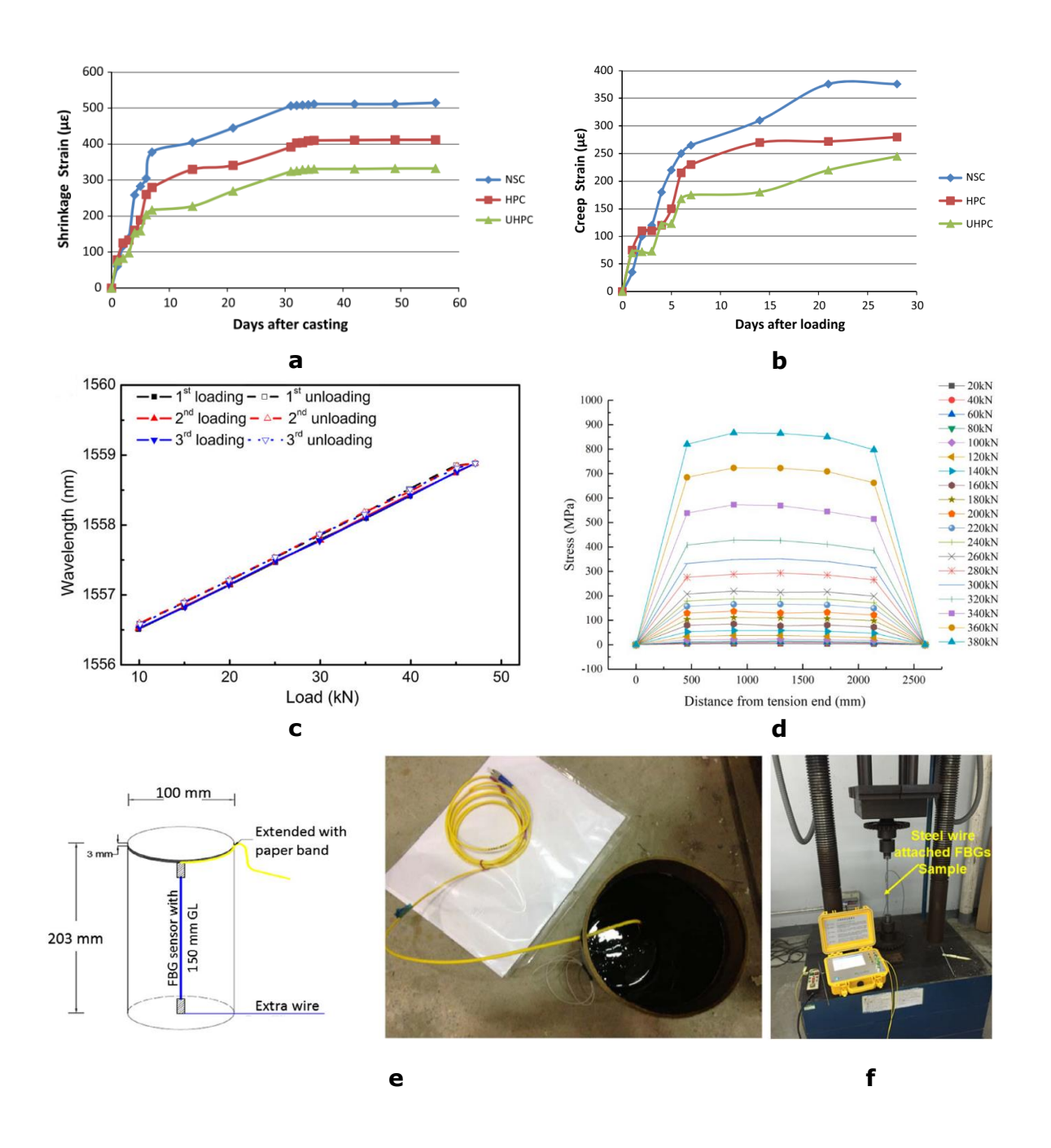


Figure 2.2: FBGs in shrinkage, creep, fatigue, and prestressed concrete (a) Shrinkage strain readings from FBG sensors [85]; (b) Creep strain readings from FBG sensors [85]; (c) Load vs wavelength curves of adhesive-bonded FBGs in cyclic loading and unloading tests with steel wire sample [86]; (d) The distribution of stress in a steel strand under load [87]; (e) Cylinder with embedded FBG sensor [85]; (f) Steel wire attached FBGs sample fatigue test [86]

Since RC is a highly nonlinear material, its distinguishing characteristics are more complicated than other structural substances. Kaklauskas et al. (2019) evaluated a variety of experimental configurations to acquire more precise and reliable information on reinforcing strain distribution. Accurate information regarding the relationship between the concrete and embedded reinforcement is necessary to make less dispersed and more reliable predictions for cracking in RC elements. This experiment's most significant outcomes were the reinforcement strain measurements at various loading values for each strain gauge location (FBGs and ESGs). The acquired data allowed for plotting spatial variations in the strain distribution along the reinforcement length. Figure 2.3(a) displays the results of both experimental experiments at four different loading intervals. As loading increases, the strain profile gradient becomes more precipitous. Greater loading, i.e. the strain rate, increases bond stress—bond properties directly influence this result. While the experimental methods yielded reasonably accurate and uniform strain variations throughout the steel bar, the specimen strain results from the FBG optical gauge test revealed anomalies, particularly near the specimen's end [88].

Corrosion of RC components has been identified as the primary mechanism of structural deterioration for reinforced steel structures. By combining AE and FBG strain measurement, Li et al. (2017) presented the results of an experimental investigation into corrosion monitoring of a steel-reinforced mortar block. The initiation and propagation of cracks, and the onset of concrete cover cracking, were identified using continuous tensile strain monitoring with FBG strain sensors.

The circumferential strain fluctuation of the reinforced mortar was determined using an FBG strain sensor. The specimen was measured from the moment the electrical current was introduced until the moment it cracked. Figure 2.3(b) depicts the strain data over 36 days. As observed, the strain increased as corrosion products accumulated and imposed internal pressure on the mortar. Initially, the strain grew at a rate of

approximately 1,000 µs per five days but later reduced to around 500 µs per five days. Cracks caused the increase in strain rate, which made more space for corrosion by-products. When cracks form, corrosion products fill the crevices before applying stress to the mortar. The jagged variation in the strain curve after twenty-four days results from redistributing corrosion products into the expanding fractures as the crack front propagates deeper into the cover. This phase is called the *crack propagation phase*. The AE events characterise the corrosion development in terms of corrosion-induced AE events. In contrast, the FBG strain measurement describes the corrosion in terms of concrete expansion due to rebar corrosion. The results suggest that combining these two non-destructive techniques has tremendous potential to monitor and characterise RC degradation [89].

Failure due to fatigue occurs when cyclic (or variable) stress causes cracks in materials and structural components. By analysing the deformation mechanism of FBG reflection spectra, Zhao et al. (2020) introduced a novel damage feature, *spectral area*, which was effectively retrieved for detecting crack sites.

First, strain data were obtained using the extended finite element method (XFEM) and fatigue crack propagation. Secondly, a fatigue crack growth monitoring test was performed using FBG sensors, and the strain values at the FBG sensor locations associated with crack propagation were determined using the digital image correlation (DIC) technique. The full-field strain measurement technique surmounted the standard strain gauge limitation, which measured only the mean strain along the grating. Figure 2.3(c) illustrates the strain distribution across the FBG1 grating for varying crack lengths. While the spectral region was immune to temperature change and experimental noise, it was extremely sensitive to the complex, non-uniform strain field induced by crack damage. In addition, the 10 mm FBG sensor demonstrated a wider detection range for fracture damage than the 5 mm FBG sensor [90].

FBG sensors have been used to study shrinkage and creep, monitor bridge cable force, investigate stress distribution in a prestressed steel

strand, and determine the development of bond stress between a prestressed steel strand and concrete. It also examines the reinforcing strain distribution, monitors corrosion, and detects crack sites. Due to installation difficulties, harsh conditions on construction sites, and cost considerations resulting from the increased number of sensors, the methodologies described in many published works are inapplicable to a broader range of engineering applications. Table 2.1 illustrates the use of FBG sensors for SHM on civil structures. Overall, the strain was the most frequently measured parameter; most applications have utilised a maximum of 64 FBGs.

FBG sensors have historically held a prestigious position in the field of SHM, due to their pioneering innovations and inherent robustness. In numerous SHM applications, these sensors have solidified their position over time. One cannot ignore their unrivalled sensitivity and versatility, which enables the precise measurement of a variety of environmental parameters. Given their numerous applications, FBGs have become an integral part of everything from aerospace structures to biomechanical systems. As with all technological landscapes, the only constant is change. Recent data and prevalent trends have shed light on a discernible preference shift in certain industries, notably civil constructions. Here, the previously uncontested domain of FBGs appears to be diminishing [30]. This preference shift merits investigation into its fundamental causes.

Investigating this transition reveals a wide range of variables. First off, while FBGs are praised for their flawless sensitivity and precision, their cost implications are significant from an economic perspective [91]. They are frequently compared to newly developed distributed sensing technologies, which promise comparable precision while offering extensive coverage and possibly smaller environmental impacts. Moreover, in an era characterised by accelerated technological advancements, the emergence of DOFS technology is an important sign. DOFS, with its truly distributed sensing capabilities and enticing cost structures [92], may be overshadowing the benefits that were once exclusive to FBGs.

For detecting AEs and ultrasonic waves, FBGs have long been extensively used [93-95]. However, DOFS appear to offer a more practical answer when one considers large-scale civil engineering projects necessitating thorough coverage and complex strain profiling. This may be tipping the scales in favour of DOFS, along with the perception that it is simple to integrate and use DOFS in monitoring and data collecting procedures, particularly in expansive structures.

However, it is necessary to urge caution against premature generalisations. FBGs have etched out a niche in specific applications where their capabilities remain unmatched. Their indispensable role in detecting acoustic emissions, ultrasonic waves, and niche functions in civil engineering is not only maintained, but is also expanding. This demonstrates their dynamic significance within the overall SHM paradigm.

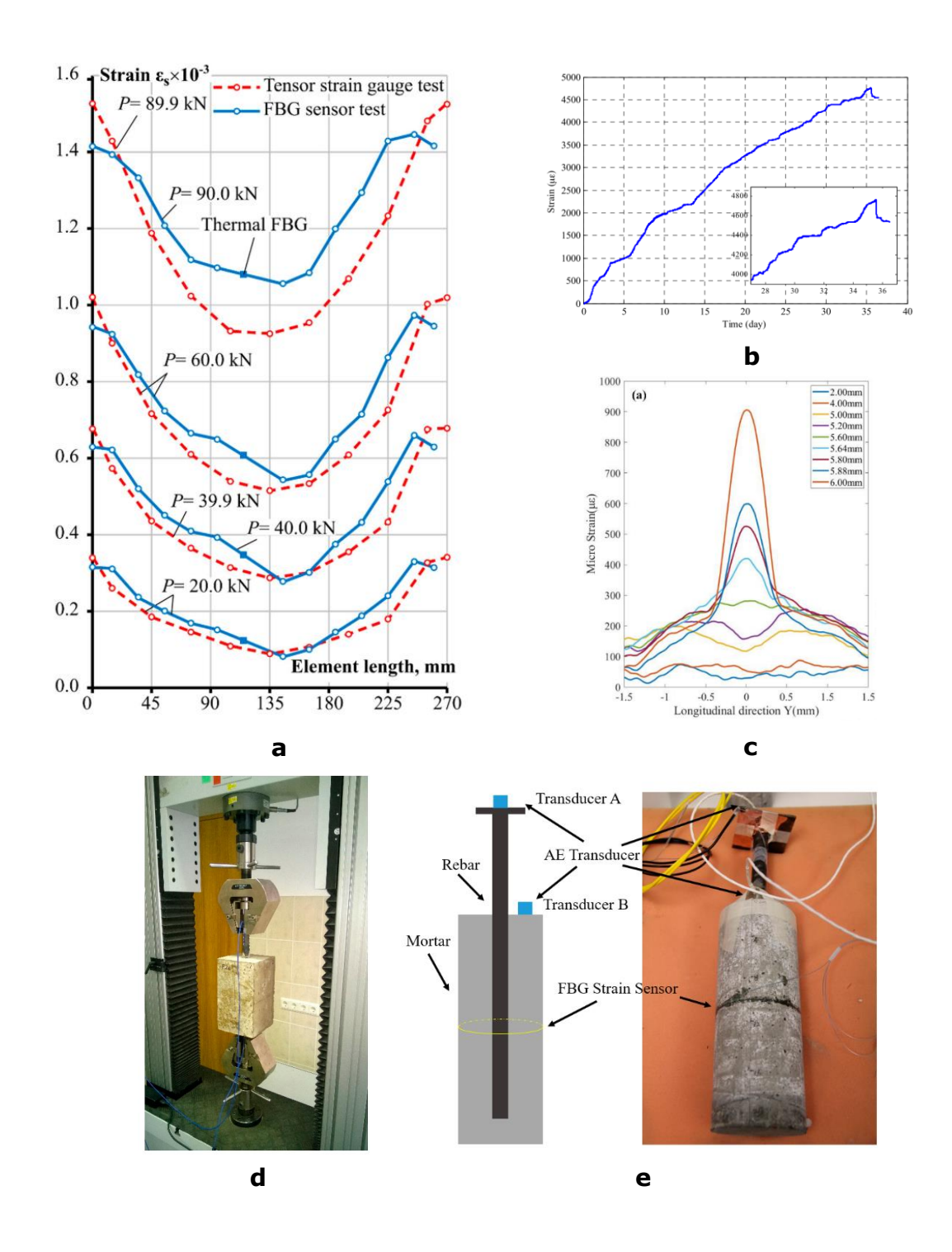


Figure 2.3: FBGs in rebars, corrosion and crack length measurements (a) Experimental distributions of reinforcing strains along steel bars at various loading stages [88]; (b) Strain history as determined by the FBG strain measurement [89]; (c) Strain throughout the grating direction as measured by the FBG1 sensor at various crack lengths [90]; (d) Experimental setup of FBG sensor test [88]; (e) Reinforced mortar specimen and sensor installation [89]

Table 2.1: FBG sensors used in SHM for civil structures

Reference	Structure	No. of FBG	Sensitivity	Measured parameters	Wavelengths (nm)	Integration technique	Remarks
[96]	Proposed for concrete structures	2	-	Strain with temperature compensation	-	Micron optics SM 130	-
[97]	Proposed for bridges	1	3.357 pm/με	Strain	-	Homemade FBG interrogator	Range: ±600με Reflectivity: 90%
[98]	Steel bridge crossing the Beijing-Hangzhou grand canal located in Hangzhou, China	64	-	Strain	1526 to 1561	Si425 optical sensing interrogator from micron optics	Reflectivity: more than 85%
[99]	No. 14301 longwall working face of the Shaqu coal Mine, Lvliang city, Shanxi province, China	2	1.21 pm/με	Strain	1530.859 and 1537.568	SM125 FBG interrogator produced by micron optics	-
[100]	Bridge No. 24 of highway No. 86 in Taiwan	7	-	Strain	1,526.96	Sm130 micron optics	Reflectivity: 93.87%
[101]	The cantilever bridge of Shaba An'ning river bridge on line 2 of the Chengdu-Kunming railway	2	-	Strain	1531.885 and 1534.184	OSA	Resolution: 0.1 pm
[102]	Dongsheng garden A5 building, located in Fushan Bay area (Qingdao, China)	8	0.5013 pm/με	Strain and temperature	1529, 1564, 1557, 1525, 1519, 1548, 1534, 1562	SI425 (Micron optics incorporated)	-
[103]	Proposed for buildings	2	FBG1: 0.132 nm/° FBG2: 0.128 nm/°	Inclination angle	1548.877 and 1551.84	OSA	-

## 2.2.2. Distributed optical fibre sensors

DOFS is one of the potential SHM solutions among the numerous new sensing technologies [104]. As a function of the spatial distribution of the monitoring probe, DOFS has the potential to become a key technology for dynamic *in situ* data acquisition (strain and temperature) on a wide variety of structures. Consequently, these sensing systems can be combined with novel instrumentation technologies to evaluate the entire structure. This can also establish a real-time connection between the local monitoring probe and decision-makers via internet-based telecommunication apparatus [105]. DOFS provides the same advantages as OFS.

Nevertheless, they can monitor the physical variations of the entire fibre in a genuinely distributed manner. In distributed sensing, a single connection cable is sufficient for communication, whereas traditional sensors require multiple cables for the same purpose. This unique benefit makes DOFS more cost-effective and appropriate for civil structures [106].

Typically, a specific and limited number of data points are extracted to evaluate structural behaviour [107]. The number of strain sensors required to generate the complete strain profile may increase swiftly for large-scale structures. Sensors that are quasi-distributed may provide valuable information about local behaviour. However, these sensors cannot measure an object's behaviour along a predefined path. DOFS typically provides thousands of sensing sites and can measure two- or three-dimensional strain distributions.

Raman, Brillouin, and Rayleigh scattering processes can occur in a DOFS [108]. Figure 2.4 illustrates backscattered light from various fibre locations, three scattering modes, and a typical OTDR and Brillouin optical time domain analysis (BOTDA) configuration. Raman-based sensors measure only temperature, whereas Brillouin- and Rayleigh-based sensors measure strain, temperature, and vibration [109]. Brillouin optical time domain reflectometer (BOTDR) relies on spontaneous Brillouin scattering, whereas BOTDA relies on stimulated Brillouin scattering. The BOTDR-based system has the advantage of being able to be monitored from one end of

the sensing fibre [110]. Optical frequency domain reflectometry (OFDR) is based on Rayleigh scattering with spatial resolution on a millimetre scale [111]; Optical backscattered reflectometer (OBR) utilises the same technology. In the past five years, DOFS have been employed to measure concrete parameters, fatigue responses, corrosion, and leakage monitoring.

Sensing devices are crucial components of SHM systems. Berrocal et al. (2021) investigated the use of DOFS based on the OFDR of Rayleigh backscattering for SHM in civil engineering structures. The DOFS system acquired strain measurements of rebar with the same precision as standard electrical foil gauges. Figure 2.5(a) depicts the evolution of DOFS-measured strain profiles throughout the cyclic loading test of the beam via a series of curves. Cracks can be linked to local maximums in the reinforcement's strain profile using the same reasoning as in the preceding section. Away from the crack, as the load is partially transferred to the concrete through bond action, the strain at the reinforcement decreases until the stresses are compatible, or the concrete reaches its tensile strength—a new crack will form at this point. In addition, examining DOFS strain profiles with high spatial resolution enabled the early detection of crack initiation [112].

All civil engineering infrastructures are susceptible to the effects of time and deterioration and external factors that imperil their structural integrity, cause significant economic losses, pollute the environment, and endanger the safety of their users. Barrias et al. (2019) reported laboratory test results in which two RC beams were outfitted with DOFS to monitor strain in four longitudinal segments affixed to their bottom surface. The test aimed to validate the DOFS's capability and efficacy in monitoring bridge structures over time, and two specimens were subjected to a 2 million load cycle fatigue test for this purpose. The amplitude of the fatigue test's stress range was comparable to that of a typical highway bridge subjected to automobile traffic. In addition, each of the four DOFS components was bonded with a specific adhesive to evaluate the fatigue resistance of common adhesive agents.

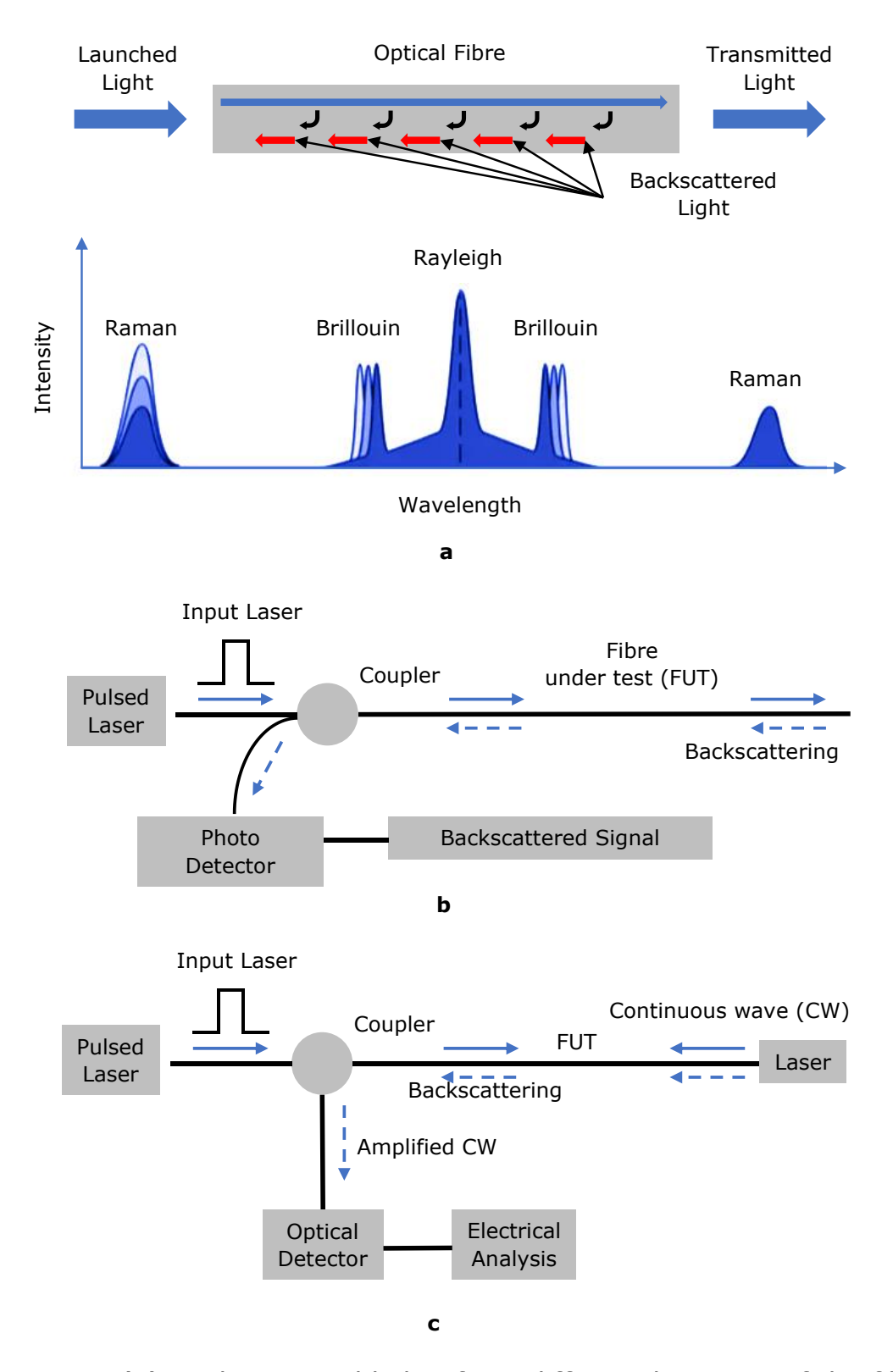
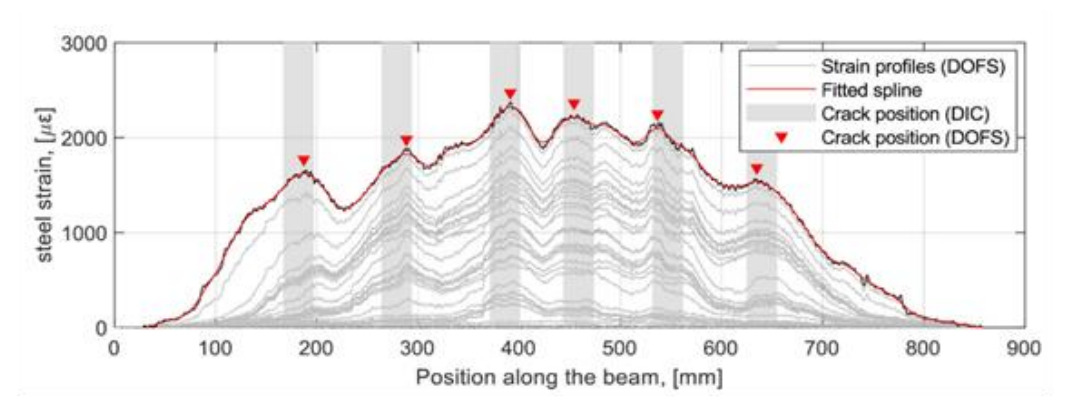


Figure 2.4: (a) Backscattered lights from different locations of the fibre and scattering modes; (b) Typical configuration of OTDR setup; (c)

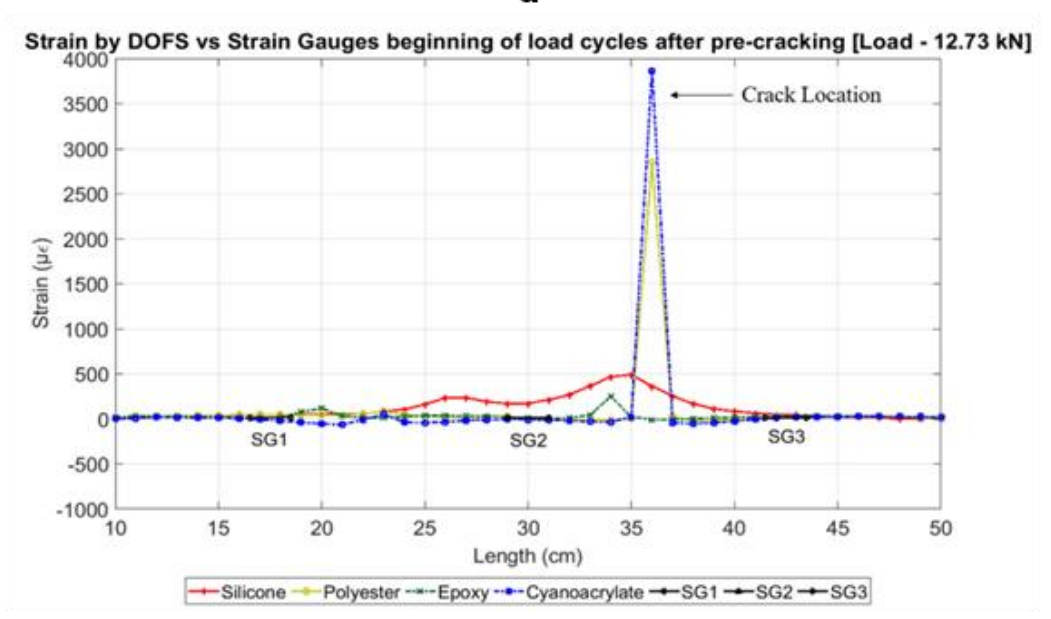
Typical configuration of BOTDA setup

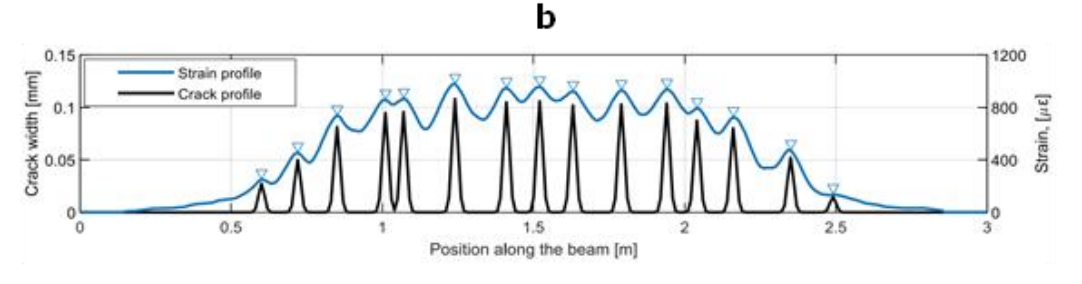
Figure 2.5(b) depicts a pre-cracked beam subjected to two million load cycles with the same load range during the test. As observed from the various DOFS bonded segments, the location of the cracks is between SG2 and SG3. The strain values across the numerous DOFS segments and strain gauges differ slightly after crack detection. This may result from strain redistribution in the component following cracking around the discontinuity that creates the crack, influenced by the stiffness of the bonding materials used. Compared to findings derived with strain gauges, the strains measured throughout the experiments were accurate and consistent, as demonstrated by the results. Therefore, fatigue loading did not affect the DOFS's ability to acquire longitudinal strain profiles [113].

Monitoring systems for structural health could make structures already under construction safer and more durable. In terms of vertical deflection and crack width, Berrocal et al. (2021) assessed the suitability of embedding robust DOFS within a protective sheath in order to accurately measure the performance indicators of three RC beams subjected to four-point bending. Results revealed that robust embedded DOFS are susceptible to strain attenuation compared to commonly used thin polyimide-coated DOFS bonded to steel reinforcement rods. In contrast, the protective coating prevents the formation of strain reading abnormalities, a frequent complaint. Performance-wise, the robust DOFS provided a reasonable approximation of the beam deflections with errors ranging from 12.3% to 6.5%.

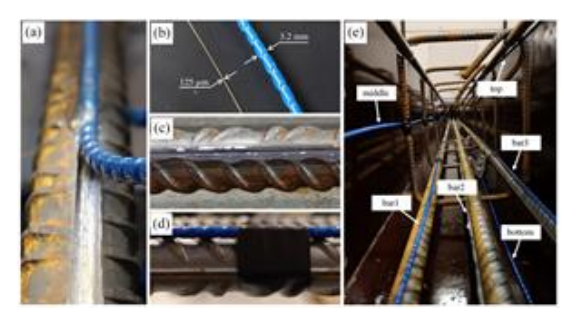


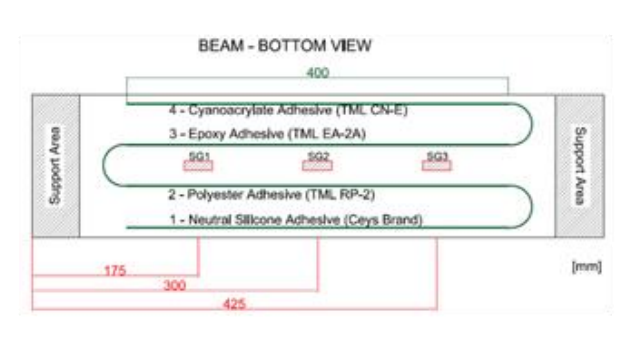
а





C





d e

Figure 2.5: DOFS in crack detection in rebar and surface, and crack width monitoring (a) Multiple strain profiles from the DOFS, with the red triangular shape indicating the determined crack location based on the strain profile at maximum load and the grey shaded region corresponding to the DIC position [112]; (b) Detection and identification of cracks at the commencement of load cycles [113]; (c) Information about the position and width of cracks is included in the development of crack functions [39]; (d) Installation of OFSs [39]; (e) Sensors mounted to beams and adhesives used [113]

Figure 2.5(c) demonstrates generating a crack profile by adding the individual crack functions of all cracks observed in a strain profile. Since the method for determining crack widths assumes that the DOFS provides a measurement of the reinforcement strains, it is not strictly accurate to apply it to strain profiles that do not correspond to a reinforcement bar. Because the magnitude of the various strain profiles is virtually proportional to the distance from the neutral axis, the resulting crack widths will also be proportionate. This method yields wedge-shaped cracks, a plausible approximation for elements with dominant bending behaviour. Crack widths calculated from DOFS strain measurements differed by no more than ±20 με from digital image correlation values, assuming individual fissures could be identified in the strain profiles [39]. Figure 2.5(d) and (c) shows the installation of OFS on rebars and OFS mounted on the surface of the RC beam. Although these applications [39, 113, 114] discuss the installation procedures of DOFS, a step-by-step guide is necessary for better understanding.

Monitoring the corrosion status of steel bars in RC is essential for maintaining safety and effective asset management. Experiments led Fan et al. (2020) to devise a DOFS-based *in situ* corrosion monitoring technique for RC. Beams immersed in a NaCl solution were impressed with a continuous current to accelerate corrosion. The DOFS was mounted in a helix pattern on the steel bar to monitor strains caused by corrosion. Figure

2.6(a) depicts data from the optical fibre length in contact with the monitored bar. The installed optical fibre's typical strain is recorded along the vertical axis, and the strain measurement is positive in tension. Until t = 15 h, the strain change detected by the OFS is comparatively small, indicating that the volume change caused by corrosion products is minimal in the early stages. After t = 15 hours, tensile strains manifest in the dispersed sensor, increasing their magnitudes with time.

The uneven distribution of expanding strain along with the OFS suggests that corrosion is irregularly distributed along the steel bar. Every strain distribution curve displays peaks and declines. A half-turn of the optical fibre on the steel bar corresponds to a distance of three centimetres between the adjacent peak and valley. The proposed solution based on a DOFS is feasible for *in situ* real-time monitoring of steel corrosion and concrete deterioration in RC [115].

Due to its high precision in distributed strain measurement, the optical frequency domain reflectometry (OFDR) method is more appropriate for pipeline monitoring. Ren et al. (2018) proposed a novel corrosion monitoring application of the OFDR method. Corrosion simulations were conducted to validate this technology. Multiple OFSs were affixed to the pipe surface at the same corrosion test interval, establishing a sensor array. Figure 2.6b) depicts the distributed strain profile recorded at various times and under the same internal pressure. When the pipe model was not subjected to corrosion, the circumferential distribution of hoop strain fluctuated around 30 µε. However, after 50 hours, tension was concentrated on a length between 0.2 and 0.40 m, indicating that this area's interior wall had already started to corrode. Comparing the test results for 0 h, 50 h, 100 h, 150 h, and 200 h reveals that the hoop strain increases when the internal wall corrodes. The tests demonstrate that corrosion can be identified using the hoop strain distribution measurement of the DOFS. The test results suggest pipeline corrosion can be measured using the hoop strain theory and the DOFS [48].

Long-distance pipelines deform more rapidly when subjected to severe conditions such as freezing-thawing and earthquakes. Oil and gas frequently leak from damaged pipelines once the deformation exceeds a predetermined threshold. Zhang et al. (2019) proposed a method for pipeline deformation monitoring that combines DOFS and conjugated beam techniques. A finite element (FE) model of a 50 m long pipeline and a 4 m long Polyvinyl Chloride (PVC) pipeline were created to validate the deformation method.

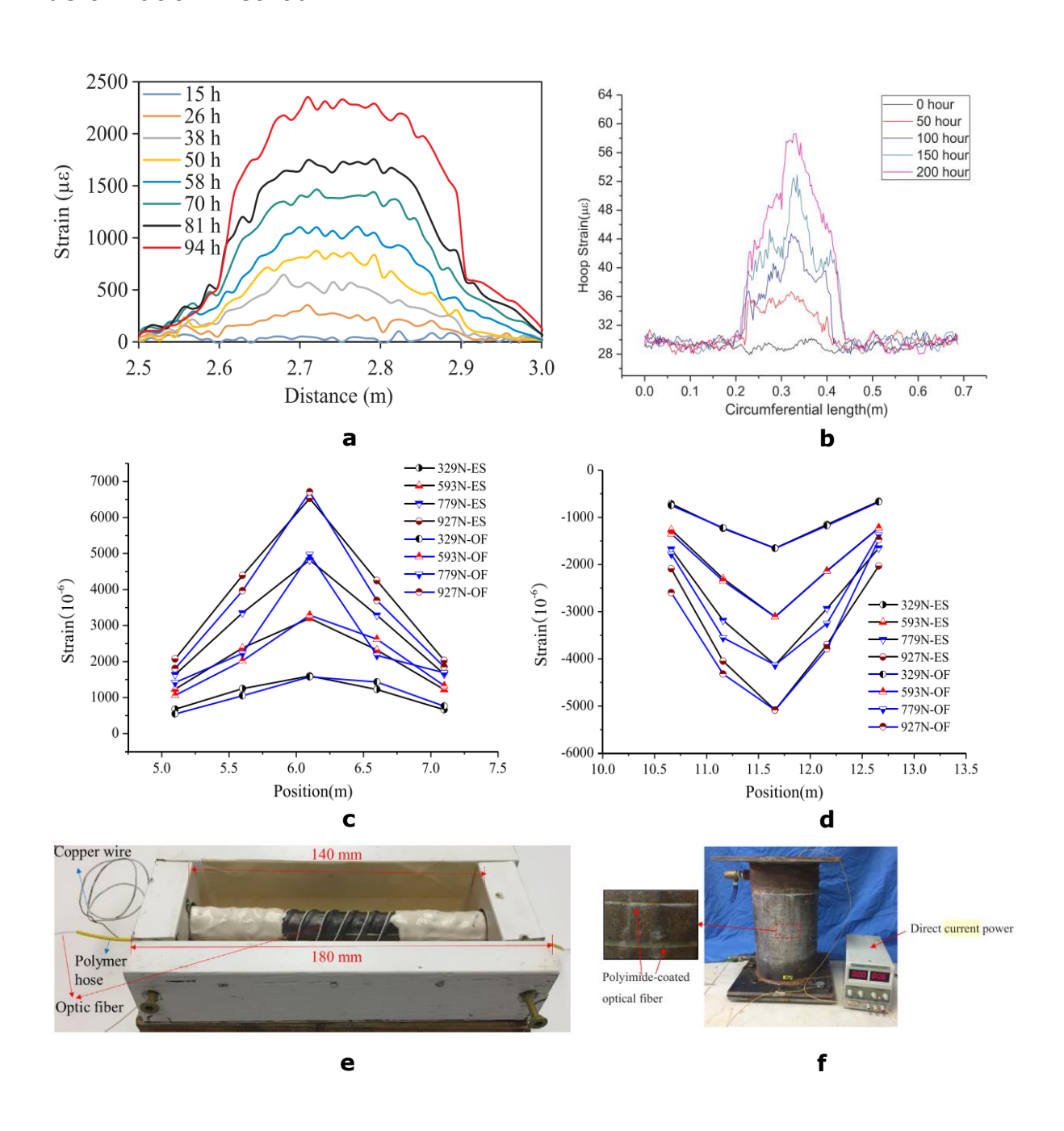


Figure 2.6: DOFS in corrosion and deformation monitoring (a) Strain distributions with the optical fibre in detail [115]; (b) Hoop strain distribution measured by one DOFS [48]; (c) Comparison of strain data measured by DOFS and ESGs for the lower surface of pipeline [116]; (d) Comparison of strain data measured by DOFS and ESGs for the upper surface of pipeline [116]; (e) Steel bar with a helix optical fibre [115]; (f) Corrosion test pipe [48]

The PVC pipeline was progressively subjected to varying loads at the midspan, while the FEA pipeline model simultaneously loaded vertical displacement at multiple points. In the two investigations, the conjugate beam method was used to calculate the pipeline's deformation based on continuous or distributed strain data and discrete strain data. As shown in Figures 2.6(c) and (d), the distributed strain recorded by the DOFS, and the local strain measured by the ESGs is in good agreement. A comparison between the displacement curve generated using distributed strain data and the displacement curve calculated using discrete strain data was performed to validate the deformation monitoring approach. The results of the two experiments demonstrate that accurate monitoring of pipeline deformation is possible and that the technology can be applied in the field [116].

Table 2.2 demonstrates the application of DOFS sensors for SHM on civil structures. As shown in Table 2.2, the increased spatial resolution provided by OBR attracted more researchers to OFDR technology.

Table 2.2: DOFS used in SHM for civil structures

Reference	Structure	System	Spatial resolution	Sensor length (m)	No. of sensors	Measurement	Integration technique	Measured frequency	Remarks
[117]	Cheong-ri bridge, Korea	Brillouin optical correlati on domain analysis (BOCDA)	31.1 cm	40.26	1	Strain	DOFS system based on the BOCDA method	9	Measurement interval: 4.2 sec  Strain resolution: ±15 με
[118]	Sant Pau hospital, Barcelona	OFDR	1 cm	50	1	Strain	OBR system	-	Measurement interval: 1 min, 10 min, 1 hour
	Sarajevo bridge, Barcelona	OFDR	1 cm	50	2	Strain	OBR system	-	Measurement interval: 5 min
[119]	Fibre- reinforced polymer composite, bridge, Rzeszow, Poland	OFDR	1 cm	9.6	10	Strain and temperature	OBR 4600	-	-
[120]	Proposed for concrete, I	OFDR	1 cm	10	1	Strain	OBR system	-	Measurement interval: 5 sec
	beam	OFDR	1 cm	5	1	Strain	OBR system	-	Measurement interval: 5 sec
[113]	Concrete beam	OFDR	1 cm	5.2	1	Strain	OBR system	0.2	Measurement interval: 5 sec

Reference	Structure	System	Spatial resolution	Sensor length (m)	No. of sensors	Measurement	Integration technique	Measured frequency	Remarks
	(Laborator y scale)								
[114]	Concrete cylinder (Laborator y scale)	OFDR	5 mm	7.6	1	Strain	OBR 4600	-	Measurement interval: Few Seconds
	Concrete bar (Laborator y scale)	OFDR	5 mm	12	1	Strain	OBR 4600	-	Measurement interval: Few Seconds
[121]	Timber concrete composite slab (Laborator y scale)	BOTDA	0.1 m	25	1	Temperature and strain	OZ Optics foresight <sup>tm</sup> DSTS	-	Measurement interval: 20 min
[122]	Concrete specimen	OFDR	1.3 mm	-	10	Strain	OBR system	20	-
[123]	RC tensile members	OFDR	5 mm and 7.5 mm	1.2	5	Strain	OBR Odisi-A manufactured by LUNA technologies	-	Measurement interval: 3 – 5 sec

DOFS sensors have been successfully used to study strain measurements of rebar, confirm the capability and performance of DOFS in monitoring bridge structures, evaluate the adequacy of embedding robust DOFS in a protective sheath, and monitor corrosion. Due to greater measurement distances and high spatial resolution, the procedures specified in numerous publications apply to a broader spectrum of civil engineering applications, despite installation difficulties and harsh conditions on construction sites. Therefore, DOFS were selected for this study to construct the sensor networks over FBG sensors.

# 2.3. Finite element analysis

FEA is a computer-based numerical method for calculating the behaviour of engineering structures. It predicts how a product will react to real-world forces [124], vibration [125], heat [126], and fluid flow [127]. FEA can be used to simulate the structural behaviour of RC when subjected to various loads and stresses. RC is a composite material in which the concrete resists compression and steel reinforcement bars (rebar) resist tension. FEA divides the entire structure into smaller, more specific components called *finite elements*. The material properties (e.g., elasticity, plasticity) and governing equations (e.g., equilibrium, compatibility) are applied to these elements connected at nodes. Unknowns, such as displacements, strains, and stresses, are obtained by solving the assembled equations.

FEA can predict the RC behaviour under different loads, identify weak points in the structure, simulate the effects of varying reinforcement configurations, and aid in the design of more efficient and resilient structures. This is especially important when designing structures, such as bridges, buildings, and dams, that must withstand significant stress. However, modelling RC in FEA can be pretty complicated due to the nonlinear behaviour of the materials, the interaction between concrete and rebar, and other factors such as concrete cracking and crushing. Consequently, complex material models and numerical techniques are

frequently required. Material models define how the material functions under various conditions, and selecting the proper model is crucial for accurately predicting the behaviour of structures using FEA.

The following are the material models that can be used for RC:

The *smeared crack model* (SCM) represents cracking in concrete by 'smearing' the cracks over the volume of an element, effectively reducing the element's stiffness in the cracked direction. The *concrete damaged plasticity (CDP) model* is a more complex model that can simulate concrete's complex behaviour. It can represent plastic deformation and damage (cracking and crushing). The linear elastic model, the elastic-plastic model, and the nonlinear elastic model each have flaws. Hence, the researcher will further discuss the SCM and the damaged plasticity model.

#### 2.3.1. Smeared crack model

The SCM is a numerical method utilised in FEA to represent the stress-induced behaviour of materials such as concrete. This model is used explicitly for monitoring the development and spread of cracks in such materials. The central premise of the SCM is the distribution or 'smearing' of individual cracks over an area, as opposed to representing them as discrete entities.

This method simplifies the complexity of cracking by transforming individual cracks into a continuous damage measure within the finite element; hence the term "smeared". Thus, the model modifies the stiffness of the finite elements to reflect the averaged or "smeared" effect of multiple cracks.

The SCM can help analyse the mechanical behaviour and loading conditions listed below. Tensile cracking [128], shear cracking [129], compressive cracking [130], cyclic loading [131], thermal loading [132], and impact loading [133] are material failure types.

The literature emphasises how well a finite element model simulates concrete cracking using the smeared crack method, as confirmed by experimental data from RC beams. The model successfully considers

variables like bond, fracture energy, and mesh size, and it effectively predicts the maximum crack width, which is crucial in engineering applications [134, 135]. The study emphasises the importance of fracture energy and bond modelling and the influence of mesh size on crack prediction. However, when attempting to predict the maximum to mean crack width ratio, the model's shortcomings became apparent, most likely due to the inherent heterogeneity of concrete [136].

Dias-da-Costa et al. (2018) highlighted the importance of understanding model uncertainties in SCM finite element simulations for concrete structures. Their research revealed differences in mesh sensitivity between models and emphasised the potential advantages of incorporating random material properties [137]. Barros et al. (2021) studied RC beams using a multi-directional smeared crack model, emphasising the significance of particular parameters. Specific finite elements and bonding conditions yielded improved results; further research is suggested [138]. For concrete and RC structures, Edalat-Behbahani et al. (2017) proposed a multidirectional fixed-smeared crack approach and a plastic-damage model, effectively predicting behaviour up to failure. Additionally, crucial model parameters influencing load-bearing capability were determined by the study [130].

Regarding concrete, the SCM provides a practical method for simulating the material's non-linear response to external loads, specifically the formation and development of cracks [128]. The smeared method accurately depicts the impact of numerous small cracks and their contribution to the overall deformation and failure of the concrete structure. Even though the SCM improves computational efficiency, it has limitations. It may have convergence problems probably created by cracking and strain localisation [139]. It may have mesh-dependency issues, in which the analysis results depend on the discrete elements' size and orientation [140]. Despite these limitations, the SCM continues to be a valuable instrument for simulating the behaviour of concrete and other materials in numerous structural engineering applications.

#### 2.3.2. CDP model

The Damage Plasticity Model is a complex material model used in FEA. It is intended to effectively represent concrete's complex, nonlinear behaviour under load [141]. This model is founded on combined continuum damage mechanics and plasticity theory, which collectively account for the two most important aspects of a material's response to stress: plasticity and damage [142].

In the Damage Plasticity Model, the total strain in the material is determined by adding the elastic strain and plastic strain [143]. By formulating and solving equations for these strains, the model can predict the behaviour of concrete under different stress conditions, such as cracking and crushing [142, 144]. The CDP model can be utilised to analyse the subsequent mechanical behaviour and load conditions, Fatigue [145], cyclic loading [143], thermal loading [146], seismic loading [143], creep and shrinkage [147].

Singh et al. (2017) investigated the use of ultra-high performance fibre reinforced concrete (UHPFRC) in structural components and the challenges in its design. They incorporated limited tests with the validation of the CDP finite element model. Their findings demonstrated that the CDP model can precisely predict the behaviour of UHPFRC beams, potentially reducing the need for physical testing [148]. Swoo-Heon (2020) analysed post-tensioned concrete beams utilising ABAQUS and the CDP model under the assumption of a perfect steel-concrete bond. Simulations closely matched real-world tensile deformations and crack patterns, validating the CDP model's accuracy when appropriately parameterized [149]. Kadhim et al. (2020) created a 3D CDP model to evaluate the impact behaviour of RC beams, particularly when reinforced with carbon-fibre-reinforced plastic (CFRP) sheets. The study discovered that CFRP reinforcement can prevent concrete failure and reduce displacement. It also highlighted the importance of transverse sheets and corner treatments in optimising the impact resistance of CFRP [150]. Zhu et al. (2021) performed a FEA investigation on pre-damaged RC beams reinforced with UHPC. Their precise model included both novel tracking technology and the CDP model. They provided insights for improving the design of these beams by analysing various parameters [151].

Both the CDP model and the SCM can simulate the behaviour of RC in FEA; still, the CDP model frequently provides more comprehensive and reliable results, making it the model of choice in several situations [152]. The CDP model's ability to precisely represent both damage and plasticity in concrete is one of its key advantages. It incorporates elements of continuum damage mechanics and plasticity theory, thereby capturing the entire nonlinear behaviour of concrete, including both cracking and plastic deformation [152]. Therefore, the CDP model was selected for this study.

Table 2.3 lists the applications of CDP modelling in RC beams from the year 2015 onwards. CPE4R, C3D8R, and C3D8 element types were used for concrete, while T2D2, T3D2, and B31 were used for reinforcement. However, C3D8R and T3D2 element types were mostly used for concrete and reinforcement, respectively. Therefore, the same element types were selected for this study.

Table 2.3: Applications of CDP modelling in RC beams

Reference	Elen	nent types	Mesh sizes	Dilation	Viscosity	Remarks		
	Concrete	Reinforcement	(mm)	angle/s (°)	parameter			
[144]	CPE4R	T2D2	25, 50, and 75	35, 37, 40, and	-	The FEA modelling was conducted		
				45		under three test cases.		
			40, 50, and 70	30, 40, and 50				
			10, 25, and 50	20, 30, and 40	=			
[149]	CPS4R	T2D2	20	38	0.1, 0.5,	The FEA modelling was conducted		
					0.5, and	under four series.		
					0.005			
[153]	-	-	25 and 10	35	0.01	Static, modal dynamic and dynamic		
						implicit analysis was conducted.		
[148]	C3D8R	T3D2	50, 25, and 15	30	0.005	Four beam specimens were tested in		
						the investigation.		
[154]	C3D8	B31	-	35	-	The elasto-plastic numerical modelling		
						was investigated under monotonic		
						loading.		
[155]	C3D8R	T3D2	-	53.2	0.0005	The study was conducted on shear		
						behaviour.		
[156]	C3D8R	C3D8R	15	50	0.001	The structural response of gravity		
						beams was assessed.		
[157]	C3D8R	T3D2	-	39	0.0001	Modelling response of ultra-high-		
						performance fibre RC beams were		
						analysed.		

Reference	Elen	nent types	Mesh sizes	Dilation	Viscosity	Remarks
	Concrete	Reinforcement	(mm)	angle/s (°)	parameter	
[158]	C3D8R	C3D8R	50, 35, 17, 10,	40	-	The study aimed to analyse the
			5, 4, and 3			behaviour of foamed concrete beams
						containing partial cement replacement.
[159]	C3D8R	B31	35, 30, 25, and	30	-	The structural behaviours of steel-
			20			reinforced geopolymer concrete beams
						were analysed.
[160]	C3D8R	T3D2	20	36	-	FEA model was used to study the
						behaviour of RC deep beam with web
						openings strengthened with CFRP
						sheet.
[161]	C3D8R	T3D2	40	20 for concrete	0	The shear behaviour of RC beams
				and 36 UHPFRC		strengthened by various ultrahigh-
						performance fibre-reinforced concrete
						systems was studied.
[162]	C3D8R	T3D2	5	23	-	The behaviour of RC beams under low
						temperatures was studied.
[163]	C3D8R	T3D2	-	50	0.0001	Retrofitting of RC members was
						studied.
[164]	C3D8R	T3D2	20 to 100	30, 25 15	0	The size effect in shear strength of fibre
						reinforced plastic (FRP) RC beams was
						studied.

## 2.4. Deep learning

DL is an AI subfield of machine learning (ML). Traditional ML is limited in its ability to process natural data in its unprocessed form, necessitating feature extraction specialists to identify patterns in the input. When unprocessed data are fed to a DL system, the system autonomously learns the representation required for detection or classification. DL thrives at discovering relationships in complex, high-dimensional data, making it applicable to numerous scientific disciplines [165]. Due to the development of algorithms and computing hardware, DL has become a topic of much discussion. DL has been implemented in numerous fields (including mail filtering, computer vision, speech recognition, audio recognition, machine translation, bioinformatics, drug design, content design, and game design) and has demonstrated learning and inference capabilities comparable to or superior to those of humans [166].

Current applications of DL include fraud detection in financial services [167, 168], forecasting of financial time series [169, 170], prognostics and health monitoring [171, 172], medical image processing [173, 174], power systems [175, 176], and recommender systems [177, 178]. In addition, there are optimisation algorithms with superior performance in damage detection and SHM [179-182].

However, in conventional ML techniques, a domain expert must identify the most applied features to reduce data's complexity and make patterns more evident to learning algorithms. DL algorithms endeavour to learn high-level characteristics from data incrementally, which is their most significant advantage. This eliminates the need for domain-specific knowledge and extraction of fundamental features. In addition, DL powered by large amounts of data is a significant factor in comprehending the reasons for its popularity.

One of the key reasons for the surge in interest in DL-based SHM is the remarkable decline in the price of sensors, which has made it possible to install enormous numbers of sensors in host structures and send the resulting data wirelessly to supercomputers in the cloud. Second, multicore processors have advanced dramatically over the past decade. As a result, researchers have been focusing on training deep neural networks in record time by making use of the capabilities of graphics processing units (GPUs) with the help of newly developed software libraries for programming languages like Python and MATLAB and cloud computing services provided by companies like Amazon and Google. As a third point, data is the lifeblood of every SHM application, and data science and data engineering are now indispensable for data-driven programs like SHM.

Artificial neural networks (ANN) are computer systems designed to mimic the biological learning mechanism found in human brains. ANN consists of processing components known as neurons, which resemble biological neurons in that they are highly interconnected [183]. These networks are extensively employed in developing intelligent systems for pattern recognition, function approximation, optimisation, and forecasting. The input, hidden, and output layers are the three major layers in a typical ANN structure. The input layer neurons are utilised to input values from the environment, the output layer neurons help to obtain the output, and the hidden layer neurons are positioned between the input and output layers [184].

In an ANN, the number of concealed layers, connections, and neurons is proportional to the data complexity. If the data are more complex, the neural network will require more concealed layers and neurons [185]. The three primary stages of ANN implementation are the selection of network parameters, training, and testing. In the first phase of modelling a neural network, the number of neurons in the input and output layers, the number of hidden layers, the number of neurons in hidden layers, and the activation functions must be determined [184]. An ANN with more than one concealed layer is considered a deep model. Deep models are capable of simulating complex real-world data. This style of architecture is trained using DL [186]. A DL model attempts to predict the future using existing measured or simulated response data.

## 2.4.1. Supervised DL

This is the most prevalent approach to DL. A large data set is required for training purposes, and the output should be appropriately labelled. During the training period, the error between the predicted output and the desired output is calculated using an objective function, and the weights are updated using backpropagation to reduce the error value. Methods based on gradients are used to optimise the objective function [187]. The system's performance is evaluated using a test set following the training procedure. The testing procedure evaluates the ability to generate applicable responses to novel inputs or generalisation ability [165]. If the model's outputs are discrete or categorical variables, it is a classifier; otherwise, it is a regression model. Due to its simplicity and training, it continues to be a popular design among academics and scientists in virtually all engineering fields. The use of supervised DL in civil engineering structure applications over the past five years will be investigated in greater detail.

Vision-based technology, which employs imaging devices as sensors, is rapidly becoming the most efficient method for structural inspection and monitoring. Kim et al. (2018) developed a technique using CNN for the automated detection of fractures on concrete surfaces *in situ*. AlexNet, a well-known CNN, has been trained to identify flaws in Internet photographs. Figures 2.7 (a) and (b) illustrate that the proposed method effectively identified cracks, even though the experimental environment affects the difficulty of crack detection. The proposed method's applicability is evaluated using field photographs and real-time video frames captured by an unmanned aerial vehicle. The evaluation results indicate that the proposed method for fracture detection is highly applicable in the real world [188].

Atha and Jahanshahi (2018) evaluated CNNs for corrosion detection. Two pre-trained state of the art CNN architectures and two proposed CNN architectures are assessed for their efficacy. CNN outperforms vision-based corrosion detection techniques devised using a simple multi-layered

perceptron network based on texture and colour analysis. Compared to the state-of-the-art pre-trained CNN, one of the proposed CNNs significantly reduces computation time while maintaining corrosion detection performance equivalent to the state of the art CNN [189].

The increasing number of automobiles, trucks, and other vehicles has raised the issue of traffic monitoring and management. Frniak et al. (2020) constructed an experimental platform with horizontally and vertically placed FBG sensor arrays in the upper pavement strata. Interrogators were affixed to sensor arrays to monitor pavement deformation caused by automobiles passing over the pavement. An ANN for visual classification was utilised to divide automobiles into distinct classes via a closed-circuit television camera. The output of sensor arrays was confirmed using this classification. The developed ANN could distinguish trucks from other automobiles with a 94.9% accuracy rate and classify automobiles into three distinct categories with a 70.8% accuracy rate [190].

Analysis of seismic hazards is an essential component of construction engineering. Derakhshani and Foruzan (2019) developed novel models to estimate the three most critical time-domain parameters of seismic ground motion. A novel combination of DL and an ANN is employed for forecasting strong ground motion characteristics such as peak ground acceleration (PGA), peak ground velocity (PGV), and peak ground displacement (PGD). The models precisely estimate the site's PGA, PGV, and PGD [191].

### 2.4.2. Unsupervised DL

Creating resilient features that preserve the essential data is a method for more accurately modelling complex real-world data. Developing domain-specific characteristics for each activity is expensive, time-consuming, and requires data expertise. Unsupervised learning is the process of acquiring knowledge from unlabelled data, such as datasets with undefined outputs that conform to a general rule and (maybe) are classified in a predictable pattern. This has the benefit of utilising unlabelled data, which is abundant and simple to acquire, and learning features from data

instead of manually creating them. In addition, these feature representation layers can be stacked to construct deep neural networks, which more accurately model complex data structures. The following section will elaborate on using Unsupervised DL for civil engineering structure applications over the past five years.

Autoencoders are unsupervised learning models aiming to find a representation for a data set, typically involving dimensionality reduction. Pathirage et al. (2018) presented an autoencoder-based framework for structural damage detection compatible with deep neural networks that can identify optimal solutions for highly nonlinear pattern recognition tasks. The input vector denotes vibration characteristics, mode shapes, and natural frequencies, while the output vector denotes structural damage.

Figure 2.7(c) depicts the detected structural defects for a particular case. It has been demonstrated that the identified stiffness reductions using the proposed methodology are highly close to the actual values, with fewer false identifications and lower false values compared to the actually introduced damages and results from ANN approaches. This suggests that the proposed method may effectively detect predetermined structural flaws in a laboratory model using experimental testing data containing ambient noise and uncertainty. The proposed framework has been numerically and experimentally validated on steel frame structures, and the results demonstrate that it is more precise and efficient than existing ANN approaches [192].

Rafiei et al. (2018) proposed a method for evaluating structural systems' global and local health based on ambient vibration responses recorded by sensors. Unsupervised DL was utilised during model creation. The proposed model has the benefit of not requiring costly experimental results from a scaled-down version of the structure to simulate various phases of damage. Only the ambient vibrations of a robust structure are required. A novel structural health index is proposed in this investigation. It can monitor the health of structures in real time, both locally and globally, so that maintenance decisions can be made with better knowledge [193].

The ANN is trained more efficiently in supervised learning mode when data from undamaged and damaged structures are available. Real-world structures, such as bridges, cannot be destroyed to generate damaged data; consequently, only data from the pristine structure is accessible, and unsupervised learning mode techniques are necessary. Finite element modelling can be used as a remedy to generate data during damage and combined with supervised DL algorithms to produce effective models. DL-based techniques have been used to detect structural damage and fractures on concrete surfaces, monitor traffic, and estimate the three most important time-domain parameters of seismic ground motion. Because AI-based decision-making strategies are superior, the methodologies outlined in numerous published papers apply to a broader spectrum of engineering applications.

Table 2.4 provides DL-based approaches for SHM in civil structures. The neural network type was selected based on the prediction requirements and the provided data type. Feedforward neural network (FFNN), Backpropagation neural network, multilayer feedforward neural network (MFNN), and multilayer perceptron neural network (MLPNN) are all types of ANNs, while CNN is a specific type of neural network architecture, particularly well-suited for image and visual data processing tasks. Most applications listed in Table 2.4 were based on ANN and CNN applications. ANN was selected over CNN because this study will not involve visual data processing.

According to the references, the input datasets for training a model can group into two main categories: experimental data and numerical data from finite element methods. It was noted that limited literature had used ANN and FEA combined applications for SHM predictions [194-196]. The most frequent data division for training and testing consisted of 80% training and 20% testing. According to peer-reviewed studies published over the past five years, there is a growing interest among academicians in using DL algorithms in SHM. The reasons could be the high level of prediction accuracy of these systems and their ability to manage highly

complex data.

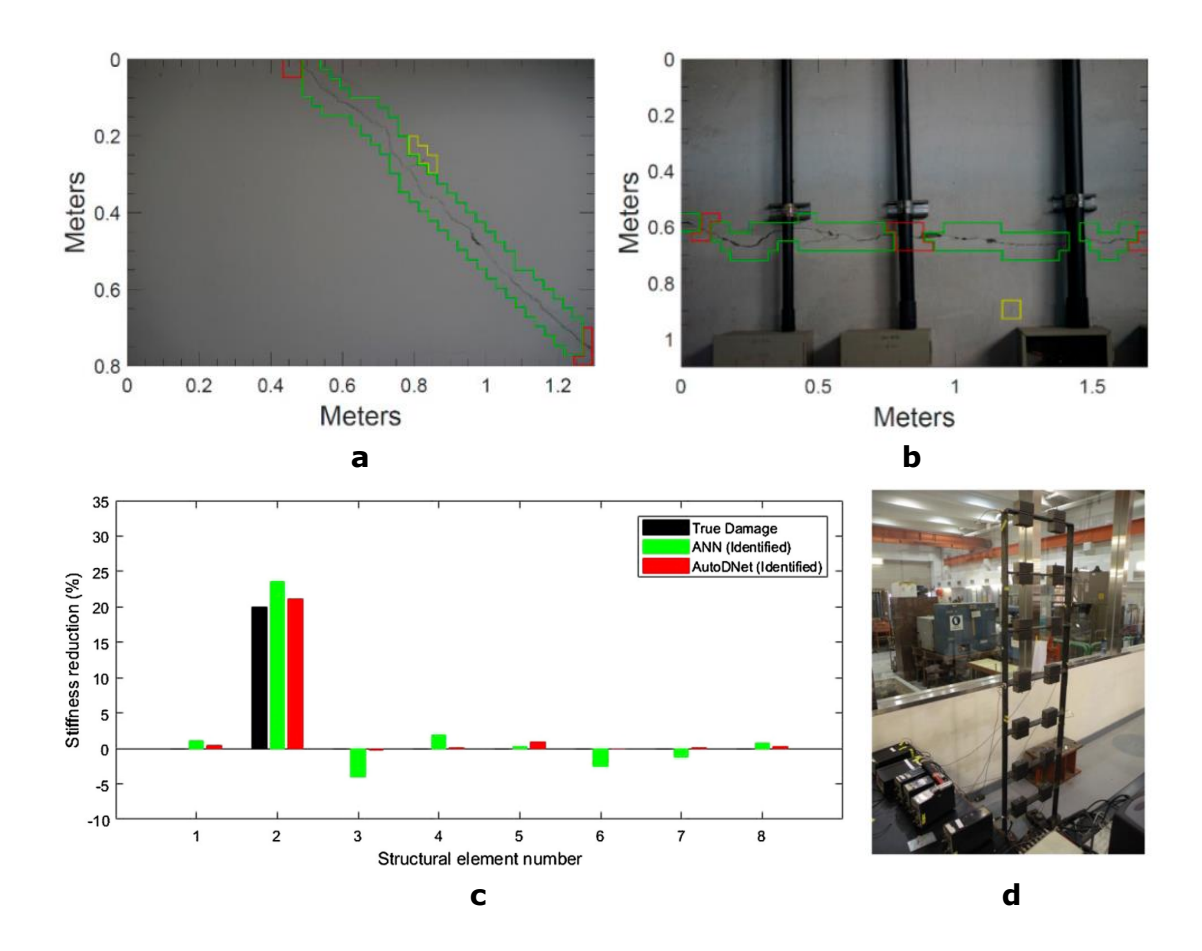


Figure 2.7: DL in crack detection and structural damage identification (a) Dark concrete surface [188]; (b) Concrete surface with pipes and electric distribution boxes [188]; (c) Damage identification results from ANN and the proposed approach [192]; (d) Laboratory model [192]

Table 2.4: DL-based methods used in SHM for civil structures

Reference	Neural			M	odel training				Remarks
	network type	Input	Output	Dataset	Activation function at the output layer	Training and testing data percentages/ sizes	Learning algorithm	Evaluation of model performance	
[197]	ANN	The number of columns per bent, backfill type, the number of spans, the number of columns, span length, concrete compressive strength (One million samples)	Seismic demand for bridge components	The dataset generated on the probabilistic distribution	Sigmoid	Training set (70%), a validation set (15%), and a test set (15%)	-	The mean squared error (MSE), coefficient of correlation (R), and coefficient of determination (R²)	ANN offers a high level of predictability even when all features are blended to estimate demand models
[198]	FFNN	Temperature and precipitation of the 30 weather stations around the basin	Daily streamflow	Historical temperature and precipitation profiles were collected for 15 years from 2000 for 30 different stations around the basin	-	80% Training, 20% Test	-	Coefficient of determination (R <sup>2</sup> )	Six hidden layers were occupied with 2048, 1024, 512, 256,128, and 64 neurons
	FFNN	Scour depth, lateral loads, angle of friction, and axial loads	Bending moment	FEA created the training dataset	-	80% Training, 20% Test	-	-	Four hidden layers were occupied by 1024, 512, 256, and 128 neurons
[199]	CNN	4058 crack images and 2011 background images	Crack detection	The bridge crack dataset in [170] is artificially augmented to generate the dataset	Softmax	80% Training, 20% Test	A mathematic ally reduced learning rate	Accuracy, precision, Specificity and F1 score	Atrous spatial pyramid pooling (ASPP) was used
[200]	CNN	The author manually labelled 1,154 images for three models	Three models (The existence of major failure, the component detection,	The images were gathered from two primary sources: related research studies on RC bridges and search	Softmax	80% Training, 20% Test	Bayesian optimisatio n	Accuracy, precision	Because of data scarcity, the pre- trained model VGG-16 was used.

Reference	Neural			M	odel training				Remarks
	network type	Input	Output	Dataset	Activation function at the output layer	Training and testing data percentages/ sizes	Learning algorithm	Evaluation of model performance	
			and the damage localisation)	engines (Ex: Google Image)					
[201]	FCNN	Crack, background, and handwriting images contain 67200 sub- images (each class has 22400 images)	Crack, handwriting, and background	Original images (steel box girders of bridges) are obtained by a consumer-grade camera (Nikon D7000); Raw images were divided into subimages.	Softmax	Training set (80%), a validation set (10%), and a test set (10%)	Momentum algorithm	Accuracy, precision, Specificity and F1 score	The recall for the crack class and the F1 scores for all three classes show that the super-resolution method reduces identification accuracy.
[194]	MFNN	Strains from verified FEM model; 60000 data points	Displacement from verified FEM model	The FEA model was used to generate strain data, and strains and displacement readings were taken at 11 different locations.	Purelin	96% Training, 4% Test	The scaled conjugate gradient backpropag ation algorithm	MSE	The commercial software ABAQUS was used for FEA modelling purposes.
[202]	CNN	6820 total samples. Each of the four data sets had 1,705 samples, including intact state and three forms of simulated damage.	Intact state and three forms of simulated damage.	The original data set consisted of 390 samples and was artificially augmented to generate the dataset.	Softmax	Only 10% of the whole data set was used for testing, while the remaining 90% was split into training (80%) and validation (20%).	Adam	Accuracy	The CNN model consists of 11 trainable hidden layers
[203]	Region- based convoluti onal neural	Crack images	Crack detection and Boundary boxes have been generated to	The crack dataset is created by labelling crack locations on	-	-	-	Accuracy	NVIDIA Titan V Volta hardware was used to train the network in an acceptable amount of time

Reference	Neural			M	odel training				Remarks
	network type	Input	Output	Dataset	Activation function at the output layer	Training and testing data percentages/ sizes	Learning algorithm	Evaluation of model performance	
	Networks (R-CNN)		approximate the cracks' size.	cropped bridge surface pictures.					and handle the UAV data.
[204]	CNN	3000 damaged images	Damage location (51 classes were created). The intact girder damage class is 0.	FEA model was used to create the dataset of images to identify 50 locations of damage using the damage index based on the gapped smoothing method	Softmax	-	-	Accuracy	The bridge girder was modelled using SI bridge 20 (SAP2000)
[195]	ANN	The normalised modal strain energy-based damage index (Z)	Stiffness reduction at the respective nodes.	The FEA model generated a total number of 114 samples.	-	-	The Levenberg- Marquardt backpropag ation	MSE and R- value	The commercial software ABAQUS was used for FEA modelling purposes.
[205]	ANN Strain data CRFV samples - 570 Non-CRFV	Strain data CRFV samples – 570	Close-range following vehicles (CRFV) and non-CRFV	Data extracted by 7-day field application. Strain signal	Sigmoid	Training set (60%), a	Adam	Accuracy	This is a combined application of ANN and CNN.
	CNN	Vehicle class datasheet	11 possible vehicle types (Based on axle clustering)	samples of 7295 vehicles were used to train the models.	-	validation set (20%), and a test set (20%)	Adam	was ANI	NMS algorithm was used with ANN for CRFV separation.
[206]	ANN	The deck chord, the deck weight, the structural damping ratio, and the air density (90000 data points)	Critical flutter velocities	Data are generated directly from the experiment results.	-	Training set (70%), a validation set (15%), and a test set (15%)	The Levenberg- Marquardt backpropag ation	The coefficient of determination (R)	Five almost similar ANN topologies were studied during the study. ANN topology No. 1 is presented here.

Reference	Neural			M	odel training				Remarks
	network type	Input	Output	Dataset	Activation function at the output layer	Training and testing data percentages/ sizes	Learning algorithm	Evaluation of model performance	
[207]	CNN	By using 100 panorama images, 19200 images were created. Categories: Disease and background	Disease and background	The image acquisition step generated 17,755 photos of the steel box girder's bottom. Every 100 photos were merged, and 138 panoramas were obtained.	-	Training set (90%), a validation set (5%), and a test set (5%)	Adam	Accuracy, precision, and recall	Image stitching and fusion methods were used.
[208]	Deep convoluti onal denoising autoenco der (DCDAE)	One million data points for acceleration data.	Reconstructin g same data	Only healthy data is used for training. Ten thousand data points were produced to test the damaged conditions. The FEA model was used to create the dataset.	Linear	Training set (85%), a validation set (7.5%), and a test set (7.5%)	Adam	Reconstruction error	DCDAE does not require damage labels
[209] Cr	CNN	800 images	-	Used the DIV2K dataset, which contains 1000 high-quality pictures with a resolution of 2K and high-frequency multiplex features.	-	Training – 800 images Validation - 100 images	-	-	The study was conducted in 2 phases and separately trained.
		2000 images with different crack types	Crack detection	Five hundred raw crack photos were augmented to 2K using web scraping and mobile and DSLR cameras to photograph	Softmax	Validation – 55 crack images	Adam	Accuracy, categorical cross-entropy loss	

Reference	Neural	Model training									
	network type	Input	Output	<b>Dataset</b> concrete	Activation function at the output layer	Training and testing data percentages/ sizes	Learning algorithm	Evaluation of model performance			
				structures.							
[210]	Deep convoluti onal neural network (DCNN)	Vibration responses from smart building	Health condition	The proposed DCNN-based approach is trained and validated using 19 numerical scenarios.	Softmax	-	Stochastic gradient decent	K-fold cross- validation (k=10)	The suggested system operates directly on vibration signals acquired from detected structures, eliminating the need for time-consuming denoising and feature-selection step.		
[211]	CNN	1890 Images were used (Normal and with defects)	Four classes: mould, stain, deterioration, and normal	VGG-16 was used to pre-train the model.  The total dataset contains 2622 images.	Softmax	80% Training, 20% Validation Seven hundred thirty-two images were used for testing purposes.	-	Accuracy, recall, precision, F1 Score	VGG-16 is based on the imagenet dataset, which comprises 14 million annotated photos and over 20,000 categories for classifying photos with mould, stain, or paint deterioration.		
[212]	CNN	A balanced mix of undamaged and damaged samples (6571 – intact, 6560 damaged)	Damage or intact	Images can be divided into three categories based on their spatial resolution: satellite, airborne, and unmanned aerial vehicle (UAV) images.	-	80% Training, 20% Testing	-	Accuracy, recall, precision, F1 Score	Three pre-trained networks tailored for satellite, airborne, and UAV image spatial resolutions and viewing angles have been made publicly available to the research community.		

Reference	Neural	Model training						Remarks	
	network type	Input	Output	Dataset	Activation function at the output layer	Training and testing data percentages/sizes	Learning algorithm	Evaluation of model performance	
[213]	MLPNN	Building height, building length, building length, building width, building stiffness ratio, inflexion point, maximum settlement, eccentricity, horizontal strain, axial stiffness ratio, and bending stiffness ratio (Total of 44 datasets)	Crack width and number of cracks	The data set was acquired from the KUR Project, each consisting of ten inputs and two outputs.	-	With varied combinations of training and testing data sets, the models were trained and tested four times.	Particle swarm optimisatio n (PSO)	K-fold cross-validation technique (k=4), The coefficient of determination (R²), rmse <sub>ave</sub>	Ground and building movements were closely monitored during the station's construction, utilising ground, and building settlement indicators. Data from 44 buildings near the station were collected and analysed.
[214]	Recurren t neural network (RNN)	Time variant grouting pressure – GP, Face support pressure - SP	Time variant settlements of 18 monitoring points	The FEA model generated the dataset	Linear	Training set (70%), a validation set (15%), and a test set (15%)	The Levenberg- Marquardt algorithm	Coefficient of determination R <sup>2</sup>	60 Finite element simulations were used to generate the dataset.
	FFNN	Eight settlements at the facade foundation	Maximum strain ε <sub>max</sub> anywhere in the facade						
[215]	CNN	10000 google street view images of buildings	Eight building typologies	The dataset was manually annotated.	-	Training set (60%), a validation set (20%), and a test set (20%)	-	Recall, precision, accuracy	Building typology predictions should be cautiously utilised, as the CNN performance for some building classes is insufficient for a straightforward building classification.

## 2.5. Critical components of RC beams

An RC beam, or RC beam, is a common structural element in construction. Typically utilised in buildings, bridges, and other structures, it is designed to resist loads that induce bending and shear stresses. The essential components include Concrete, Steel Reinforcing Bars (Rebars), Stirrups or Shear Reinforcing, and Concrete Cover. The design of these components must consider several factors, including the anticipated beam loads, environmental conditions, and safety considerations. They must adhere to the applicable building codes and standards to ensure safety and longevity [216].

The most prevalent loading condition for RC beams is flexure (or bending). Under flexural loading, the steel reinforcement bars (rebars) are the most critical component of an RC beam. Flexural loading causes beam bending, which generates tensile stresses at the bottom and compressive stresses at the top. Concrete is strong in compression but brittle in tension. Therefore, high-tensile-strength steel rebars are located at the bottom of the beam, where tensile stresses occur. Under tensile stress, the beam might crack and fail without adequate reinforcement [217].

The steel reinforcement's design, positioning, and quantity are critical under flexural loads. The anticipated tensile forces should determine the reinforcing rod's size and placement to ensure the beam can safely support the anticipated loads. In addition, proper anchorage and bonding between the rebar and the concrete are essential for efficiently transmitting stresses between the two materials [218].

## 2.6. OFS and DL applications for SHM

Widespread OFS and DL-based real-world applications can be observed in SHM systems designed for civil structures such as bridges and buildings. Over time, the OFS sensor networks installed in key civil structures generate enormous volumes of raw data (Big data) [219, 220]. The Sant Pau hospital in Barcelona utilised a 50 m long OFS with a 1 cm spatial resolution and a 1-minute measurement interval [118]. This sensor

network can generate 43,200 readings along with the fibre per month if data recording is continuous. The foundation of Big Data Analytics is mining and extracting meaningful patterns from large input data for decision-making, prediction, and other inferences.

DL's capacity to extract high-level, sophisticated abstractions and data representations from massive amounts of data, especially unsupervised data, makes it an intriguing instrument for Big Data Analytics. Conventional ML and feature engineering algorithms are inadequate for deriving the complex and nonlinear patterns frequently observed in Big Data. By identifying these features, DL enables the use of relatively simpler linear models for Big Data analytical tasks such as classification and prediction, which is essential when building models to accommodate the scope of Big Data [221]. The subsequent section provided concise information on how the technologies above were utilised for SHM purposes in the recent past.

Table 2.5 presents the combined applications of OFS and DL for SHM in civil structures. The researchers preferred supervised to unsupervised ML. Supervised DL algorithms can attain greater prediction accuracy with less complex algorithms than unsupervised DL algorithms. Based on the author's review of the relevant literature, currently, there is no integration or combined application of OFS, FEA, and DL techniques for SHM purposes.

Table 2.5: The combined applications of OFS and DL for SHM

Reference	Sensor	Measurement	DL Training	DL			
	Туре	(Strain/Temperature)	Туре	Framework			
	(FBG/DOFS)						
Bridge							
[222]	FBG	Temperature, Stress,	Supervised	-			
		and displacement data					
[223]	FBG	Strain and temperature	Supervised	TensorFlow			
[224]	FOSs were	Strain and temperature	Unsupervised	TensorFlow			
	used; the						

	sensor type is						
	not specified.						
[225]	FBG	Temperature,	Supervised	-			
		deflection, and strain					
[226]	FBG	Dynamic strain	Supervised	-			
Buildings							
[227]	FBG	Strain	Supervised	-			

# 2.6.1. Bridges

The erosion of soils and gravels encircling bridge piers and abutments is called *bridge scour*. Due to its catastrophic impact on bridge safety, bridge scour garnered considerable attention. Kong et al. (2017) conducted field tests on an innovative bridge scour monitoring system using FBG sensors in East Baton Rouge Parish, Louisiana. The functionality of the proposed system has been validated by sensor responses measured [228]. Ye et al. (2018) installed an SHM system based on FBGs on a steel bridge spanning the Beijing-Hangzhou Grand Canal in Hangzhou, China. A total of 64 FBG sensors are affixed in the midspan and quarter span of the orthotropic steel bridge.

Figure 2.8 depicts the FBG-based SHM system installed on the steel bridge that crosses the Beijing-Hangzhou Grand Canal in Hangzhou, China. A wavelet multi-resolution analysis approach presented the local stress behaviours induced by highway loading and temperature impact during construction and service [98].

Monitoring the deflection of a long-span cantilever bridge during construction is hampered by multiple construction methods, complex wiring, and the incapacity to capture real-time data, among other flaws. Zhang et al. (2019) designed an inclination sensor-based on FBG to monitor the deflection of cantilever bridges to address these deficiencies. The prototype deflection monitoring structure is manufactured, and testing reveals a sensitivity of 10.566 pm/mm and a fitting error of 0.9997.

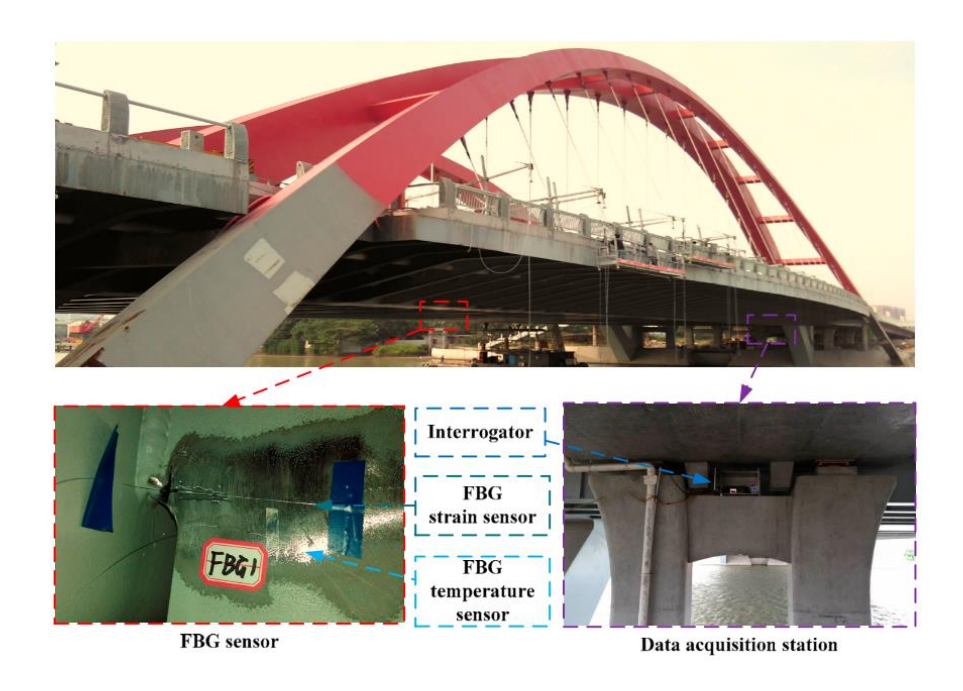


Figure 2.8: FBG-based SHM system at steel bridge crossing the Beijing-Hangzhou Grand Canal located in Hangzhou-China [98]

The designed deflection monitoring device was installed in the cantilever bridge of the Shaba An'ning River Bridge on Chengdu-Kunming Railway Line 2, and the feasibility of the deflection sensing structure in monitoring the construction of cantilever bridges was confirmed [101]. The Chulitna River Bridge is a five-span steel-girder composite bridge that spans 790 feet (241 m) and connects Fairbanks and Anchorage in Alaska. Xiao et al. (2020) installed FBG strain gauges on the lower chord members of the bridge, and dynamic features such as natural frequencies and mode shapes were effectively detected using strain gauge readings as vehicles crossed the bridge. Additionally, a FE model validated the results. The presented method applies to various bridge vibration sensing applications [229].

Cheong-ri Bridge connects Cheong-ri Station and Oksan Station on a commercial railroad line administered by Korea Railroad Corporation; Figure 2.9 depicts the Cheong-ri Bridge monitoring site. Yoon et al. (2016) devised a DOFS based on BOCDA to monitor the distributed strain of a railway bridge's rail and girder. The distributed strain of a 40.26 m long

girder and rail was recorded in real-time at 9Hz. The analysis pinpointed the region of excessive strain on the bridge's girder induced by the effects of unsupported sleepers [117]. Rzeszow, the capital of the Podkarpackie voivodeship, is home to the country's first road bridge made solely of FRP composites. This bridge spans a small local stream on an urban route. The FRP bridge was equipped with distributed optical fibre sensing technology by Siwowski et al. (2018). The applicability of DOFS based on Rayleigh scattering for SHM objectives was demonstrated by analysing field data [119].

Derivation of fragility curves is a standard method for evaluating seismic vulnerability. Mangalathu et al. (2018) proposed a multi-parameter fragility methodology that develops bridge-specific fragility curves using an ANN without clustering bridge classes. The proposed methodology aids in determining the relative significance of fragility curves for every uncertain parameter [197]. The widespread opinion holds that hydraulic-related hazards (e.g., flooding and scour) pose the greatest threat to the safety of bridges throughout their service lifetimes.

Khandel and Soliman (2019) designed a multi-hazard probabilistic method to provide bridge administrators and decision-makers with flood fragility curves based on service life and predicted flood variability. Next, DL networks and FE modelling quantify the structural performance of the investigated bridge. The proposed structure is demonstrated on an existing Oklahoma bridge [198]. Typically, a specialised crew is dispatched to conduct post-disaster status screenings manually. This method is time-consuming and susceptible to bias because it significantly relies on the qualitative opinion of an inspector. Xiao Liang (2019) proposed a three-level image-based solution for post-disaster monitoring of RC bridges using DL and novel training methods. CNN was utilised as the neural network. Bayesian optimisation yielded promising results with >90% accuracy and robustness across all three-level DL models [200].

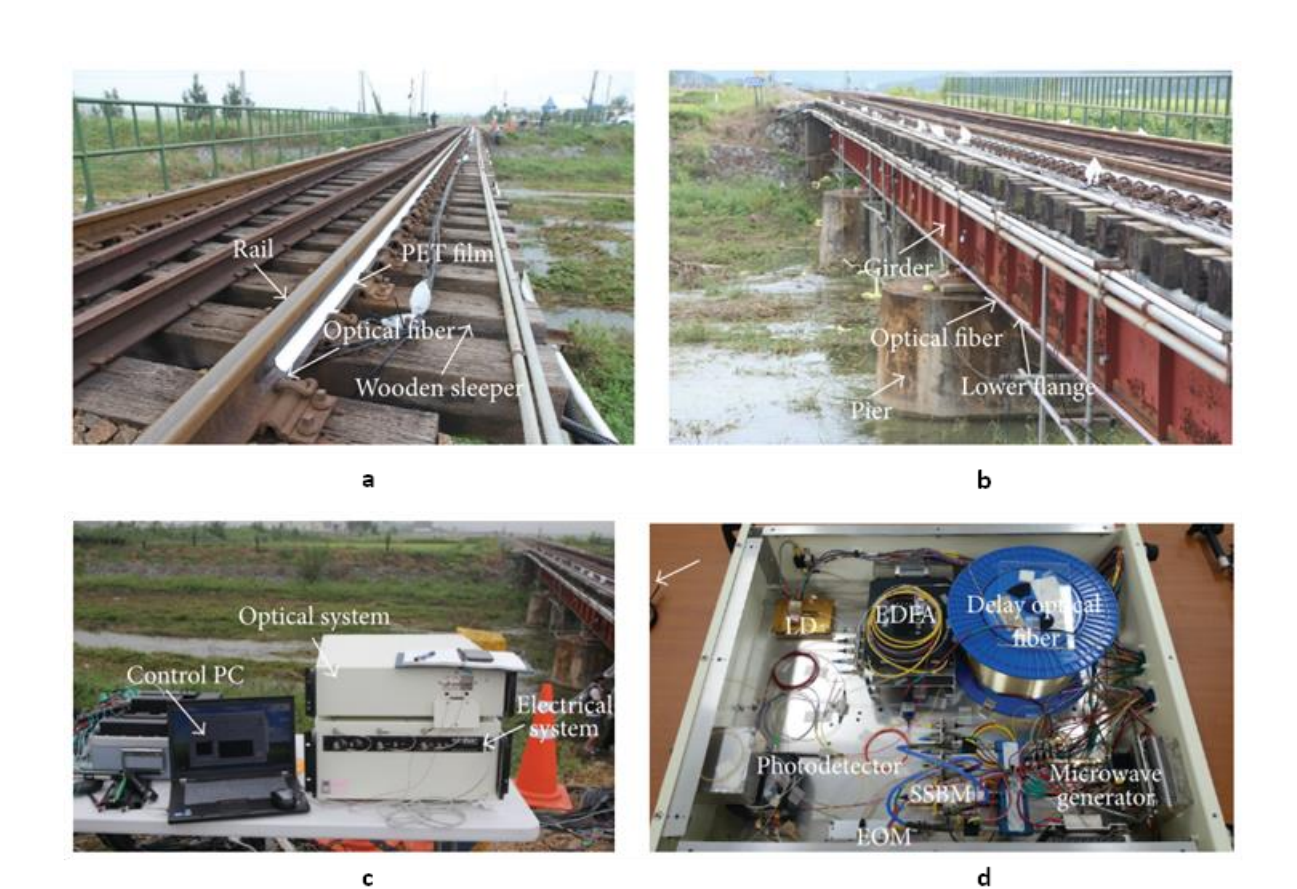


Figure 2.9: Monitoring site at Cheong-ri Bridge [117] (a) Optical fibre mounted on the outer surface of the rail; (b) mounted on the lower flange of the girder; (c) DOFS system based on BOCDA method; (d) configuration of the optical system

Detecting concrete bridge cracks is essential to ensure transportation safety. The adoption of DL technology enables the automatic and precise detection of bridge cracks. Xu et al. (2019) suggested a CNN-based end-to-end bridge crack detection model that takes advantage of atrous convolution, the ASPP module, and depth-wise separable convolution. The suggested model attained a 96.37% detection accuracy without prior training. Experiments revealed that the proposed classification model outperforms traditional classification models [199].

The construction of long-span bridges widely uses steel box girders. Xu et al. (2019) identified the fatigue cracks using real-world photos, including complex disturbance information contained within steel box girders. A customised fusion CNN architecture is developed that considers

the multilevel and multiscale characteristics of the input images. The fusion CNN's recognition errors are less than that of a standard CNN during the training and validation stages [201]. A real-time prediction approach based on a multilayer ANN for determining a bridge's vertical dynamic displacements from longitudinal strains was presented by Moon et al. (2019) when automobiles pass across it. The proposed method was tested using a computational model for a real five-girder bridge with a span of 36 m backed up by actual experimental results. The findings show that the model can accurately forecast overall bridge displacements in real time based on strain in the field [194].

The increasing use of sophisticated SHM systems in civil infrastructures generates voluminous data. However, the hostile environment in which civil structures are constructed contaminates the data collected by SHM systems, substantially affecting data analysis results. Bao et al. (2019) proposed a computer vision and DL-based data anomaly detection system. The model was developed utilising stacked autoencoders. Acceleration data from the SHM system of a real long-span bridge in China are utilised to demonstrate the training technique and validate its efficacy [230].

Data storage has become a significant concern, leading to the emergence of data compression and reconstruction in SHM as the new domain for vast infrastructure systems. Frequently, SHM data contaminate with anomalies that impede structural investigation and evaluation. The underlying causes of data irregularities are extraordinarily complex. As a result, reconstructing abnormal data is inherently challenging and obtaining high accuracy after data compression presents significant obstacles.

Ni et al. (2020) presented a novel data compression and reconstruction system enabled by DL. The framework comprises a Convolutional Neural Network (CNN) and an Autoencoder, which can recover data with high precision at such a low compression ratio. The proposed technique was validated using China's long-span bridge acceleration data [224]. Human eye evaluation, which is inherently

subjective and time-consuming, is the most prevalent method for bridge maintenance and monitoring currently available. Wang et al. (2020) presented a novel computer vision-based automated inspection method for degrading a steel box girder's underside. CNN utilised a technique for image synthesis. Experiments indicate that this method is a viable alternative to manual inspection and can provide a more standardised and accurate evaluation [207].

Bae et al. (2020) proposed a novel end-to-end deep super-resolution crack network (SrcNet) to enhance computer vision-based automatic crack detection. The proposed SrcNet can significantly improve its ability to detect cracks through DL by augmenting the pixel resolution of the unprocessed digital image. According to validation test results, the proposed SrcNet has a 24% higher detectability of cracks than the fracture identification results obtained using raw digital images [209]. The "Las Navas" viaduct is located close to Cabezón de La Sal on the A8 at kilometre 250 (Cantabria, Spain). The bridge is one of the first in Spain to employ embedded FBG microstrain sensors, making it one of a kind. Using this realworld example constructed in 2000, Urquijo et al. (2019) investigated the hazards and benefits of fibre optic technologies. Using ML techniques such as RNN, the originally designed structural sensors help detect, quantify, and classify operational traffic utilising the infrastructure. This is an additional advantage of using these measurement sensors in the infrastructure world [223].

A turnout is a crucial piece of equipment; that is one of the weakest connections in the railway infrastructure. Due to topographical and environmental constraints, Continuous Welded Turnouts (CWTs) have been implemented frequently on high-speed railway bridges, where extra care is required to ensure high-speed railway safety. The operational status of the CWT on the bridge was evaluated using FBG sensors and a real-time monitoring system. Cai et al. (2019) created and implemented this for the first time in China. Figure 2.10 depicts the Jin-Hu Bridge Monitoring Site. Using the regression model and the BP neural network model, Multiple

indicators, such as rail stress and switch rail displacement, were predicted [222]. Due to their greater precision and durability than conventional strain gauges, FOSs are ideal for obtaining accurate strain and temperature measurements of structural members in real time.

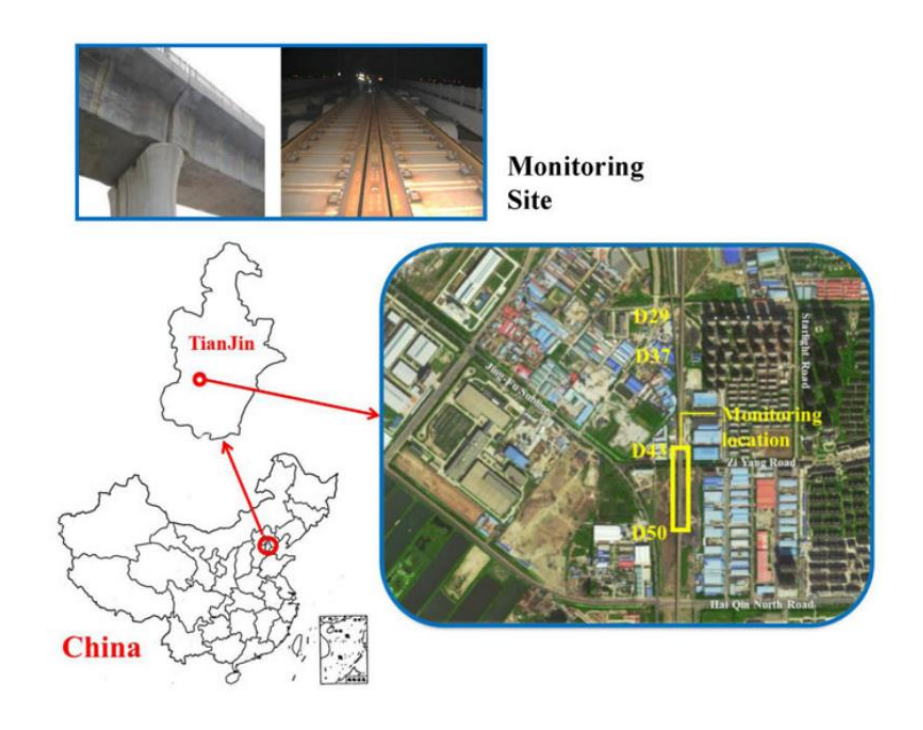


Figure 2.10: Monitoring site of Jin-Hu Bridge [222]

Khandel et al. (2020) employed FBGs to provide a statistical damage identification and localisation method for assessing the performance of prestressed concrete bridge girders. Figure 2.11 depicts the laboratory testing of the ridge girder. The present methodology uses ANNs to establish a connection between the strain profiles obtained at various sensor locations across the studied girder. The method detects and localises the presence of harm at the sensor position [225] without requiring comprehensive loading information.

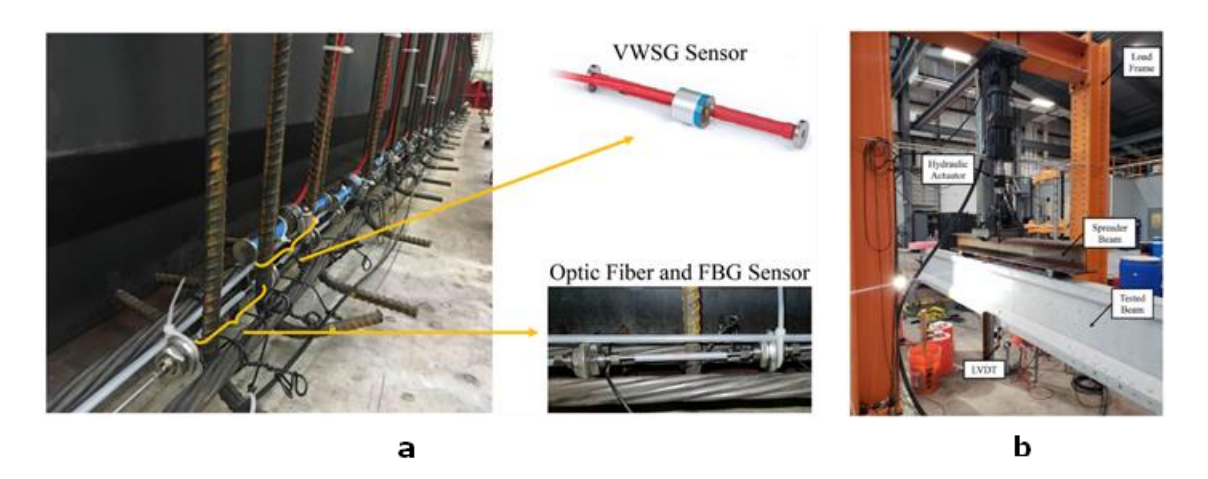


Figure 2.11: Bridge girder testing at a laboratory (a) Placement of sensors; (b) loading setup [225]

## 2.6.2. Buildings

Maintaining and preserving historical and cultural heritage buildings and ensuring their safe operation is becoming increasingly imperative to monitor their daily condition for early indications of damage or failure. Li et al. (2018) suggested FBG sensing-based deformation monitoring systems that can monitor beam deflection, column inclination angle, and mortise-and-tenon joint dislocation for Chinese traditional wooden constructions. The results indicate that the proposed deformation monitoring techniques are suitable and beneficial for monitoring the health of traditional Chinese wooden structures [231].

Measuring the tilt angle is essential for numerous applications, such as aviation and civil engineering. Chao et al. (2018) designed and evaluated a novel FBG-based optical fibre tilt sensor for detecting the tilt angle of a dual-axis in two dimensions. The proposed sensor can measure building inclination due to its superior sensing linearity [231]. Barrias et al. (2018) presented the main SHM findings from restoring a historically significant hospital building. Using a new DOFS based on the OBR technique, continuous strain data with a high spatial resolution was conveyed along with the optical fibre. Figure 2.12 depicts the DOFSs affixed on the masonry vaults of Barcelona's Sant Pau hospital. The DOFS-related OBR theory has demonstrated its viability in SHM applications for civil engineering and

continues to emphasise the promising future of such technological monitoring systems [118].

Current building condition assessment procedures are excessively time-consuming, laborious, and costly. They pose significant health and safety risks to surveyors, especially at height and on difficult-to-access roof levels. Perez et al. (2019) investigated using CNN for the automated detection and localisation of significant structural defects, such as mould, deterioration, and stain, in images. The proposed model employs a pretrained VGG-16 CNN classifier with class activation mapping for object localisation. The proposed method detects and localises building defects with reliability [211]. The ground surface movement caused by tunnelling in urban areas causes structural damage to adjacent buildings by distorting and rotating them.



Figure 2.12: DOFS mounted on the masonry vaults at Sant Pau hospital,

Barcelona [118]

Moosazadeh et al. (2019) developed a method to predict building damage utilising an ANN model and a particle swarm optimisation technique. Compared to the measured data, the model's results were deemed satisfactory [213]. Important structural components' long-term strain monitoring is problematic due to unanticipated issues such as sensor

and data logger failure, communication collapse, and data loss. Oh et al. (2017) proposed a long-term strain-sensing model using an ANN to predict column strain responses based on wind-induced behaviour of high-rise buildings. The ANN model is founded on evolutionary learning and consists of Radial basis function neural network training and genetic algorithm evolution. The proposed model is trained and validated using wind data, such as wind velocities and directions, and associated strains collected by FBGs [227].

## 2.7. Review outcome and research gaps

Decades of research have demonstrated the necessity of SHM and the specifics of SHM measures implemented for numerous critical infrastructures. This review analysed the current state of optical sensor technology, FEA for RC beams, and the implementation of DL for SHM of civil infrastructures. Over the past five years, OFS has been applied to measure concrete properties, fatigue responses, corrosion, and leakage monitoring.

Despite their high sensitivity, the use of FBGs in civil structures for strain and temperature-based applications is declining. According to the literature, the maximum number of sensors employed was 64, and the maximum sensitivity achieved was  $1.2 \text{ pm/\mu\epsilon}$ . FBGS have an advantage for detecting AE and ultrasonic waves. In civil engineering, both applications are expanding at a steady rate. DOFS is gaining popularity within the scientific community. Most researchers preferred OFDR technology for strain measurements, and some applications have used spatial resolutions as low as 5 mm. According to the reviewed applications, the OBR technique was implemented with a maximal sensor length of 50 m and a measurement interval of 1 minute. Due to greater measurement distances and high spatial resolution, DOFS were selected over FBGs and other traditional sensors for this study.

Although both the CDP model and the SCM can simulate the behaviour of RC in FEA, the CDP model frequently provides more detailed

and accurate results, making it the model of choice in many instances. A crucial advantage of the CDP model is its ability to represent damage and plasticity in concrete accurately. Incorporating elements of continuum damage mechanics and plasticity theory, it captures the entire nonlinear behaviour of concrete, including fracture and plastic deformation. Therefore, the CDP model was chosen for this investigation. CPE4R, C3D8R, and C3D8 element types were used for concrete, while T2D2, T3D2, and B31 element types were used for reinforcement. However, the most commonly used element types for concrete and reinforcement were C3D8R (Standard 8-node linear brick element) and T3D2 (standard 2-node linear 3-D truss element), respectively. Therefore, the researcher used the same element types for this research.

Academics are intrigued by the application of DL algorithms to SHM. DL models can be trained utilising experimental and numerical data (finite element methods). The typical data split during model training consists of 80% training and 20% assessment. However, the literature on ANN and FEA combined applications for SHM predictions were limited. The vast majority of SHM applications were based on ANN, and the accuracy of each application was acceptable. Therefore, ANN was chosen for this study. The CNNs were disregarded because visual data processing is not involved in this study.

The highest number of training samples used was one million. The maximum presented prediction accuracy was over 97%. According to the combined applications of OFS and DL for SHM in civil constructions, the researchers preferred supervised over unsupervised DL. Strain, temperature, and vibration measurements were considered during the studies. According to peer-reviewed studies published over the past five years, there is a growing interest among academicians in using DL algorithms in SHM. This may be because these systems have a high prediction accuracy and can manage highly complex data.

The scalability and adaptability of the system is crucial when contemplating the integration of FEA, OFS, and DL for SHM in RC beams.

In the actual world, these beams could be components of smaller structures or large infrastructures such as bridges. The integrated method should be adaptable, adjusting to different dimensions without sacrificing precision. The dynamic nature of real-world conditions, which includes environmental variables and inherent structural shifts, emphasises the need for resilient and adaptable methodologies. Understanding the holistic performance of this integration amidst the complexities of diverse real-world situations involving RC beams is a significant gap in the current literature.

The literature review revealed the following research gaps: While some studies have investigated using FEA, OFS, and DL separately for SHM of concrete structures [194, 195, 222-227], no research is available on integrating these methods for an effective framework for SHM of RC beams. Since there are limited studies available on creating a strain dataset from FEA models for training DL models more research is needed following validation of the FEA models. Moreover, although many studies have investigated the use of sensor networks for SHM of concrete structures, a step-by-step guide on the efficient design and installation procedures of distributed sensor networks for RC beams is still necessary. Understanding this disparity can aid in developing more effective and efficient sensor networks. The efficacy of DL models for SHM of RC beams still requires further investigation.

After identifying the gaps in the literature and the potential for a synthesis, it is essential to identify and discuss the challenges that may accompany the integration of FEA, OFS, and DL for SHM. Data compatibility and integration constitute one of the most pressing obstacles. Each of the distinct systems, including FEA, OFS, and DL, generates data with its own distinct characteristics. Compiling these datasets into a unified entity for analysis necessitates precision, given the disparities in format and scope that each may present.

In addition to data harmonisation, the challenge of computational demand looms large. Combining the resource-intensive processes of deep learning with the intricate simulations of FEA may exceed the current computational limits in terms of processing speed and storage space. The inclusion of data from these systems also raises the issue of model validation. When using FEA model outputs as training data for DL models, the dependability and validity of FEA models become crucial. A lapse in this phase could perpetuate errors, resulting in overfitting or incorrect interpretations in the DL phase. While the OFS offers unmatched sensitivity, it occasionally captures data that is excessively complex or contaminated with noise. Integrating this with FEA and DL will necessitate a comprehensive preprocessing regimen, highlighting the significance of stringent data filtration techniques.

Not to be overlooked is the fact that this project requires interdisciplinary expertise. The intersection of FEA, OFS, and DL necessitates a cross-disciplinary dialogue — a domain where domain-specific jargons and paradigms may impede effective communication. This integration, while promising, necessitates a culture of collaboration that is uncommon in highly specialised fields.

# CHAPTER 3: TRAINING DATA GENERATION AND DEVELOPMENT OF DEEP LEARNING MODEL

#### 3.1. Introduction

This chapter explores the process of devising and implementing a DL model based on ANN architecture for analysing strain data to predict the structural health of RC beams. The highlight of this novel method is the incorporation of a strain dataset derived from a CDP-based FEA model. This data set provides a sophisticated representation of nonlinear and damage-induced plasticity of concrete behaviour.

Initially, the chapter sets the groundwork by explicating the conceptual SHM framework. Then it delves into the specific stages of the ANN architecture's design and construction, illuminating the rigorous process required to ensure its reliability and efficacy. The chapter then investigates strain dataset creation, an essential aspect of this endeavour. This dataset, derived from a validated RC beam FEA model, is used to train DL models. The discussion incorporates the nuances of creating this unique dataset and clarifies its contribution to the model training process.

The training phase of the DL model, covered in Chapter 5, is an essential element of this research. The concentration here remains on creating and preparing the necessary components for successful model training, particularly the ANN architecture and the strain dataset. This chapter concludes by highlighting the enormous potential of incorporating DL techniques into the structural health prediction of RC beams. It paves the way for a novel method of predicting and assessing the health of RC structures by utilising a strain dataset from a CDP-based FEA model. Figure 3.1 illustrates the overview of Chapter 3's technical contents.

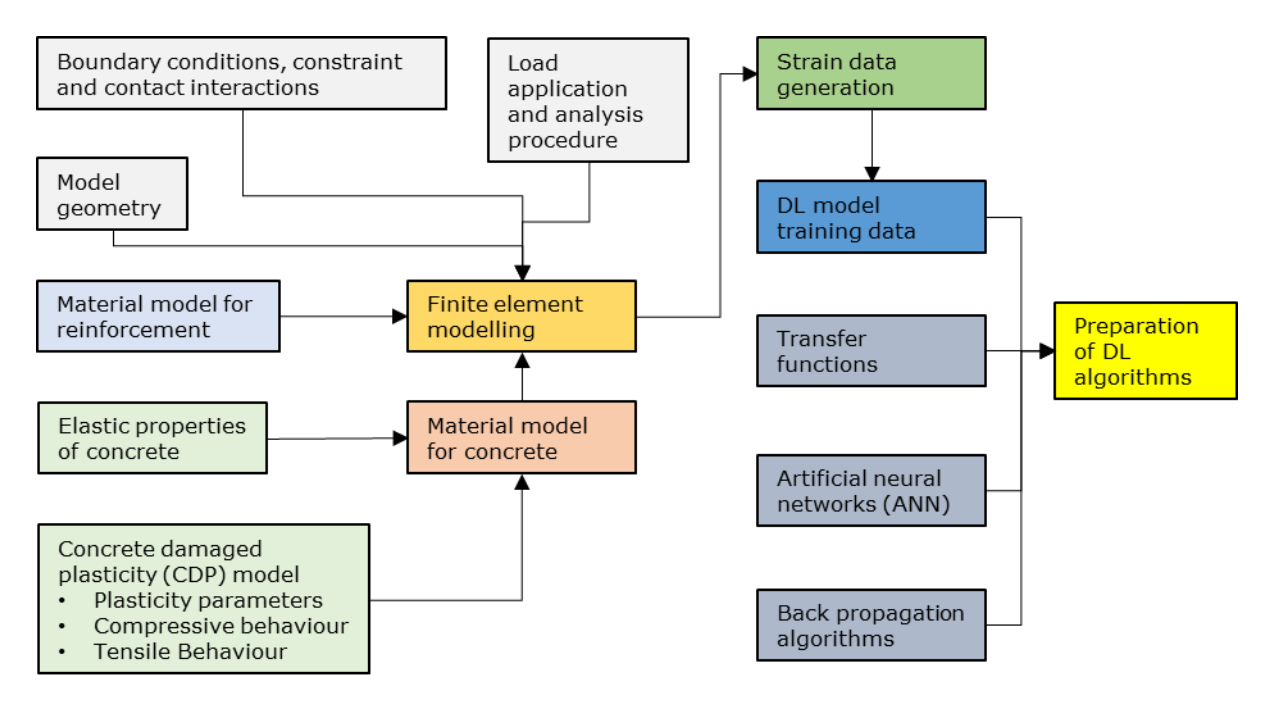


Figure 3.1: Overview of technical contents of Chapter 3

#### 3.2. Overview of DL model for SHM predictions in RC beams

DL is a branch of ML; however, when raw data is given to a system, it automatically learns the representation needed for classification or identification. To be employed in various scientific domains, DL must be adept at identifying relationships in complicated, high-dimensional data. The main benefit of using DL techniques is that they seek to extract high-level features from the data gradually. This eliminates the requirement for fundamental feature extraction and domain-specific knowledge. DL is important because it recognises these properties and enables the implementation of comparatively straightforward linear models for Big Data analysis tasks like classification and prediction. [Please note Chapter 4 discusses the sample preparation, installation of FOSs, and the experimental procedure].

Supervised DL is the most typical DL method. A sizable data set is necessary for training, and the output must be labelled appropriately [30]. During the training phase, an objective function is utilised to modify the weights via backpropagation. The aim is to minimise the error between the predicted and intended outputs. Gradient-based techniques are used in this

context to optimise the objective function [187]. The model's performance is assessed using a test set, and the testing process assesses how well the model generalises to new inputs. This study focused on supervised learning, where the network is trained with inputs and their associated outputs.

#### 3.2.1. Artificial neuron

McCulloch and Pitts (1943) were the forerunners in studying the artificial neural network concept [232]. They investigated the fundamental operational features of basic artificial neurones that corresponded to the function of biological neurones. The biological neurone and the artificial neurone can be approximately compared. The term "neurones" refers to the billions of tightly coupled cells that make up the human brain. According to Figure 3.2, a neurone consists of a body, an axon, dendrites, and synapses. The signals (inputs) first received by neighbouring neurones' dendrites are subsequently transmitted to the cell body, where they are processed before being transferred to the axon, which then sends the signal through the synapse to the neighbouring neurones' dendrites (outputs). The following neurone receivers (dendrites) across the synaptic junction receive chemical neurotransmitters when an impulse reaches a synapse. The neurone can receive and transmit numerous signals simultaneously because each synapse is connected to numerous dendrites. The volume of signals that flow through a receiving neurone is influenced by its threshold, the strength of Synoptics, and the strength of the signal coming from the feeding neurones. Additionally, each synaptic strength (comparable to the weights in neural networks) determines the strength of the postsynaptic neuron's impulse [233].

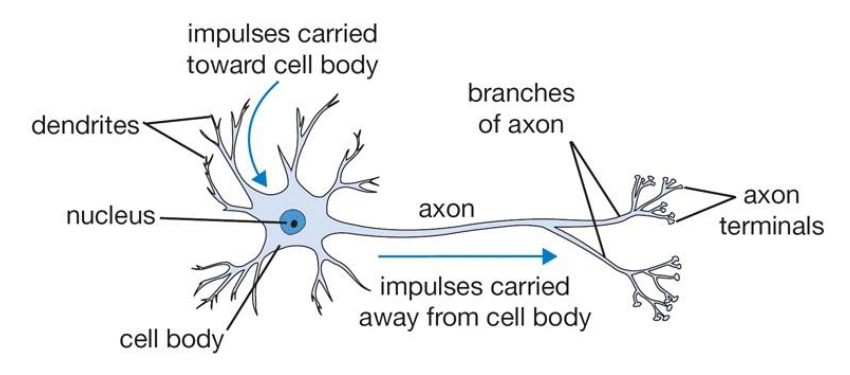


Figure 3.2: Biological Neuron

The connection weights and threshold roughly correspond to the activity in a soma, while the wires and interconnections represent the axons and dendrites, respectively. Both biological networks and ANNs learn by adjusting the magnitudes of the synapses' strengths or ANN weights [234].

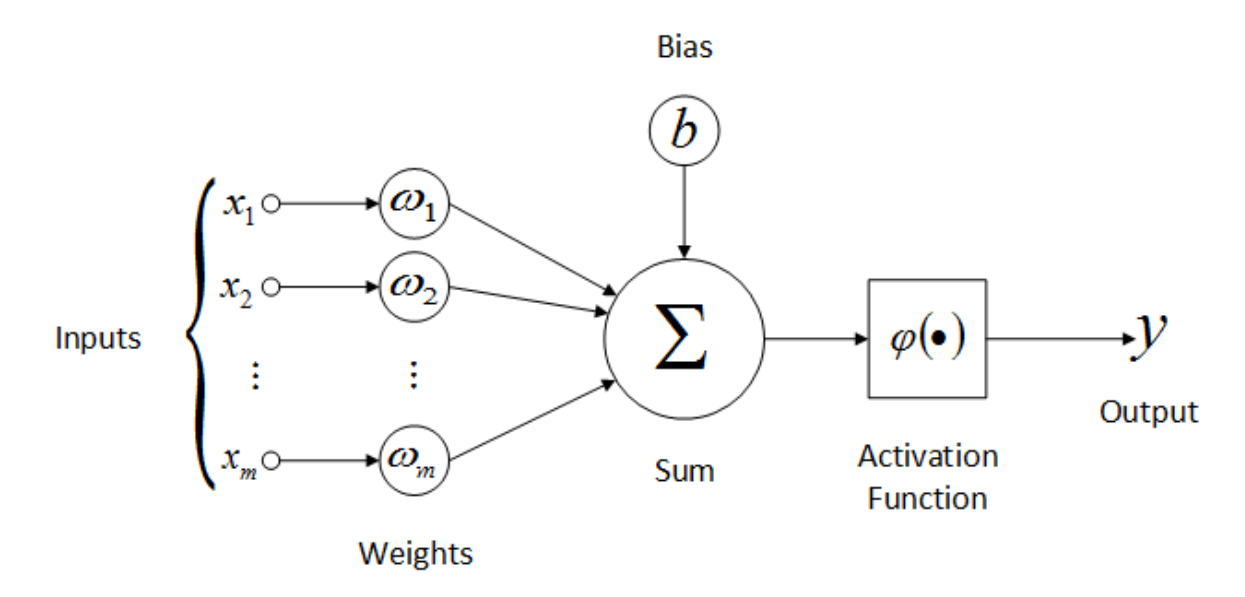


Figure 3.3: Mathematical model of the artificial neuron [235]

The artificial neurone, seen in Figure 3.3, is the fundamental processing component of an ANN. To determine the output y, the neurone performs the following mathematical operations on the inputs  $x_i$ .

$$y = \varphi\left(\sum_{i} (\omega_{i} x_{i}) + b\right) \tag{3.1}$$

## Where,

y = Output

 $\varphi$  = Activation function

 $\omega_i$  = Synaptic weights

 $x_i$  = Input variable

b = Bias

#### 3.2.2. Artificial neural networks

The building block of larger neural networks is the perceptron or a single neuron. Effective and potent multi-neuron networks were created to address non-linear challenges because the capabilities of single-neuron systems were restricted to linearly separable classes [236]. When designing multi-neuron networks, numerous single neurons are connected parallelly to form neurone layers. The total multi-layered ANN system is created by connecting these neuron layers in sequential order. Modifying the weights and the bias parameter in accordance with the learning rules produces the pre-defined outputs (targets) during neural network "learning", sometimes referred to as "training". Therefore, these input-output sets are also called "training sets" because the neurones are meant to learn from a set of user-defined experiences (a set of inputs and outputs).

The input layer, hidden layer, and output layer are the components of an ANN network. Each layer is built up of several groupings of neurones with the use of training parameters. The degree to which a network is generalisable depends significantly on the number of neurones in each hidden layer and the overall number of hidden layers in the network. One of the most important aspects of network training is the network's ability to generalise, which can be defined as the 'ability to reproduce outputs that are similar to training samples and to produce outputs that are plausible for inputs that were not utilised in training'.

Overtraining may result in the network becoming "overfitted", a problem in network training that a trained network should avoid. Overfitting

occurs when the learning algorithm fits the trained outputs very closely to the training set, minimising the training error. This has the negative effect of preventing generalisation and producing unrealistic outputs for the new set of inputs. In the past few decades, several strategies have been proposed to prevent overfitting and improve the generalisation capacity of the network. Pruning, the regularisation approach, and the early stopping method have reduced the overfitting effect. This study avoided network overfitting by adopting the early stopping strategy, which is the simplest method to manage while the network is being trained. This is accomplished by manually halting the training process when the validation set error increases while the training set error decreases.

## 3.2.3. Backpropagation algorithms

An ANN can be used to make predictions only after training with an existing input-output data set. The backpropagation supervised learning technique is often used to train ANNs. The training technique of an ANN employing backpropagation consists of two phases: forwards propagation followed by backward propagation. During forwards propagation, data are transferred to the output layer via random-weighted hidden layers. At the completion of the forwards pass, the predicted output of the model may not correspond to the desired output. Modifications are made to the network's weights such that the projected output is as close as possible to the desired result by adjusting the weight during the step of backward propagation. Backward propagation requires calculating and propagating the error's derivative (the difference between the desired output and the projected output). Backpropagation by gradient descent is the technical term for this process. The error derivative is employed to modify the weights to reduce output error [237]. Figure 3.4 displays a typical ANN topology.

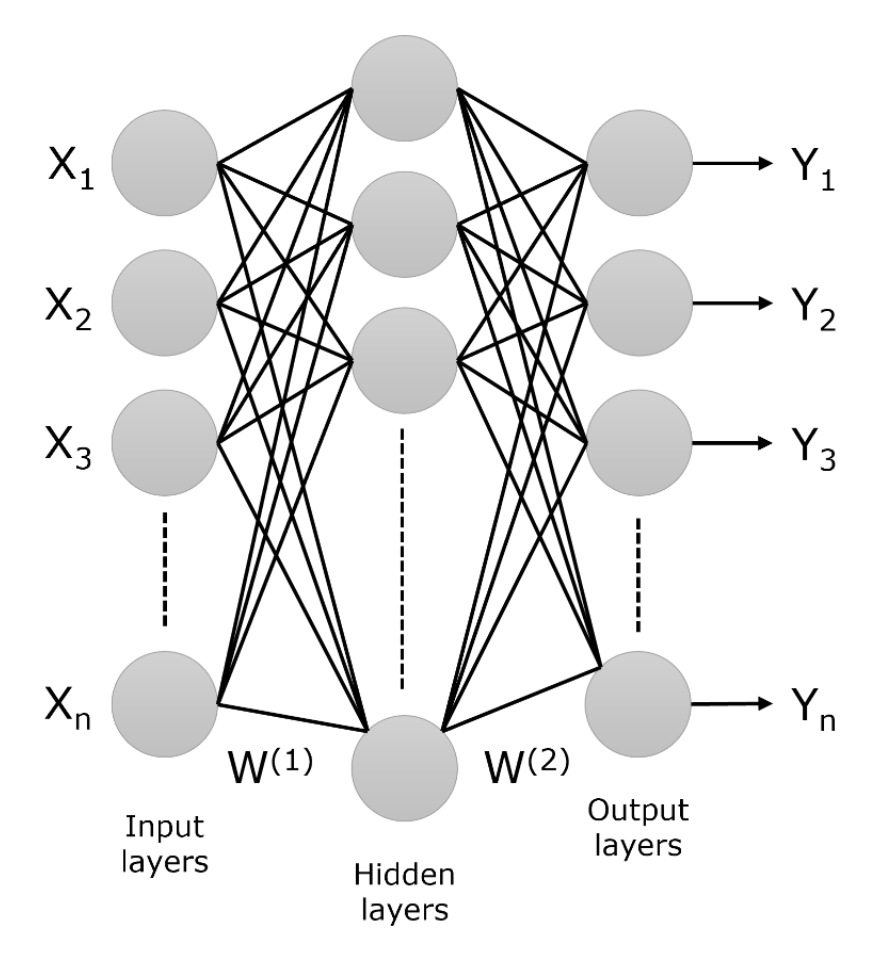


Figure 3.4: Typical ANN topology

At the end of the forwards pass, the error function corresponding to the weight W is computed as represented by the equation (3.2)

$$E(W) = \frac{1}{2} \sum_{k=1}^{k=n} |Y_k - \widehat{Y}_k|^2$$
 (3.2)

Where,

 $X = [X_1, X_2, ... X_n]$  = Input Vector

 $Y = [Y_1, Y_2, \dots Y_n]$  = Output Vector  $\hat{Y} = [\hat{Y_1}, \hat{Y_2}, \dots \hat{Y_n}]$  = ANN's estimated output vector

 $W = [W^{(1)}, W^{(2)}]$  = Weight matrices vector for layers 1 and 2

In the backwards pass, the derivative of the error function is computed and update the weights according to the following equation (3.3):

$$W_{ij} = W_{ij} - \alpha \frac{\delta E(W)}{\delta W_{ij}} \tag{3.3}$$

Where,

 $\alpha$  = Learning rate

 $W_{ij}$  = Specific weight connecting the units I and j

The general algorithm for backpropagation can be summarised as follows:

- 1. Initialise the network weights with modest random weights.
- 2. Present the training dataset's input vector to the network.
- 3. The propagation of the input to produce the output is known as the feedforward phase of the input.
- 4. Compute the error by comparing the predicted network output and the desired network output.
- 5. Backpropagate the error through the network, also known as the backpropagation of error.
- 6. Adjust the weight to reduce the error as much as possible.
- 7. Repeat steps 2–6 until there is no improvement in the error.

#### 3.2.4. Proposed ANN architecture

The main objective of the ANN is to predict the structural health of the tension rebar of an RC beam using the concrete surface strain data as an input. For this purpose, the optimal number of hidden layers was determined on the problem's complexity. When training data (obtained via FEA) and testing data (obtained experimentally) are in two dimensions, the ANN cannot help predict the outcomes. One potential solution to this issue

is to apply principal component analysis (PCA), which can simplify highdimensional data and preserve underlying trends and patterns.

PCA was used to set an equal number of input nodes for FEA-extracted data and experimental data by decreasing their dimensions. Each network's number of input and output nodes corresponds to the number of variables in the input and output data sets. The number of hidden layers and the number of neurones within a hidden layer were determined via trial and error to achieve optimal training and validation accuracy. This is because the trial-and-error method is more straightforward and intuitive, encourages the investigation of various hyperparameter combinations, and fosters a deeper understanding of the issue and how hyperparameters impact model performance.

The training data set is randomly split into training, validation, and testing subsets. Generally, data sets can be separated into 60% to 90% training data, 5% to 20% validation data, and 5% to 20% test data [197, 201, 205-207]. This study allocated 64% of the data to training, 16% to validation, and 20% to testing. In this work, the input data consisted of the strain retrieved along the surface sensor path from the FEA model, and the output was the rebar status showing whether a present rebar strain was exceeded (or not).

In the suggested ANN, the output node is adopted in the output layer, where "1" denotes that the limit was exceeded and "0" denotes that the limit was not exceeded. Therefore, this model has two output classes. The model was trained to predict the rebar tension status using the rebar yield limit (considered 2500  $\mu\epsilon$ ). Engineers can significantly benefit from using concrete surface strain data as input to DL models because embedded rebar is typically unavailable for visual inspection. This method allows early detection of deterioration indicators, including cracking and overloading.

Activation functions are of great significance in artificial neural networks since they are responsible for determining the output of a neuron based on a particular set of input(s). The inclusion of non-linearity in the model is crucial as it enables the network to effectively learn from errors

and adapt, hence facilitating the acquisition of intricate patterns. Given the nature of this investigation, which pertains to binary classification, it is expected that the outcome will yield the probability associated with the selection of the positive class. As a result, it is necessary for the output to be within the numerical range of 0 to 1. The selection of the "sigmoid" function appears to be an appropriate choice for this particular purpose. The sigmoid function is considered to be one of the earliest employed activation functions. The activation function, known for its distinctive Sshaped curve, has consistently been utilised in neural networks specifically developed for binary classification tasks. Due to its mathematical design, the sigmoid function effectively and seamlessly transfers its inputs to values within the range of 0 and 1. It is worth mentioning that greater negative inputs tend to approach 0, whilst larger positive inputs tend to approach 1. A crucial aspect of this mapping is the numerical value of 0.5. This assumption holds significance as it serves as a decisive factor in defining the inclination of an input towards one of the two classes.

When shifting focus to the concealed levels of architecture, a distinct paradigm emerges. The rectified linear unit (ReLU) function is given priority in this context. The ReLU has emerged as a widely adopted activation function in many neural network architectures. Upon initial observation, it may appear that ReLU consists of two linear segments combined. However, within the wider context of brain computations, ReLU is unequivocally classified as a nonlinear function. The hallmark of this system lies in its operational simplicity. Inputs that possess a positive value or are equal to zero remain unaltered and are transmitted in their original form. Nevertheless, any negative input experiences a process of transformation, resulting in its value being reduced to zero. This behaviour confers certain advantageous qualities upon the ReLU. Firstly, it demonstrates computational efficiency, frequently leading to expedited training epochs. Moreover, it has been observed that the use of the ReLU activation function might help alleviate the issue of the vanishing gradient problem, which is a well-known challenge often encountered when employing activation functions like as the sigmoid, particularly in networks with multiple layers. In order to provide a more concrete viewpoint, Figure 3.5 illustrates the distinctions between the ReLU and sigmoid functions in a visual manner. This depiction highlights their respective operational ranges and significant transition points.

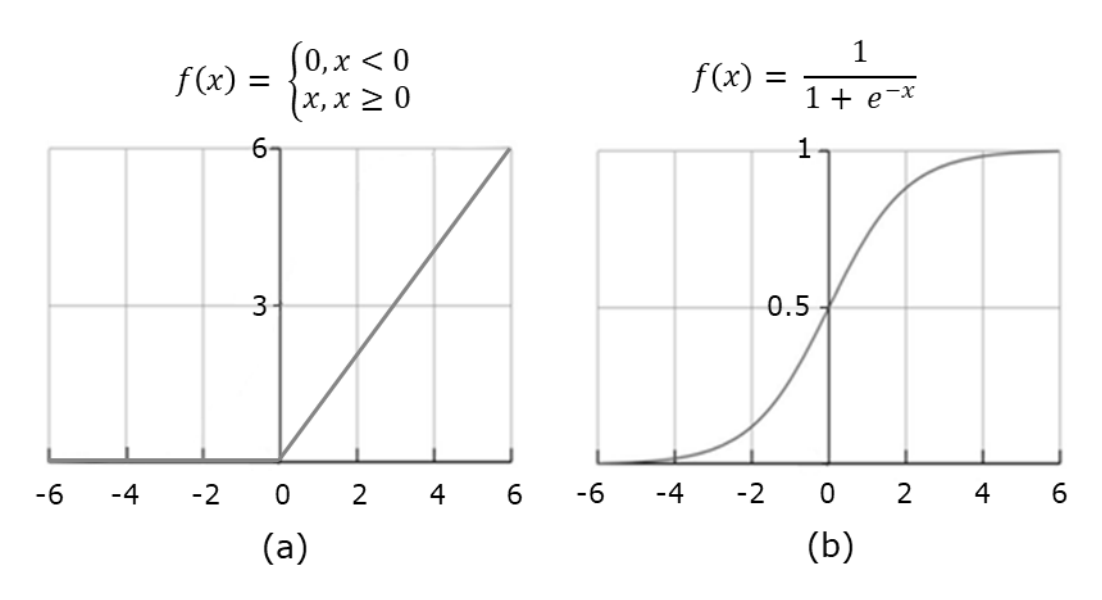


Figure 3.5: (a) ReLU transfer function; (b) Logistic sigmoid transfer function

The ANN proposed in this study comprises one input layer, two hidden layers, and one output layer. The ReLU function acts as the transfer function between the initial three contiguous layers, whereas the sigmoid function is implemented between the last two layers. One class have considerably more instances than the other. This imbalance can result in biased model performance, as the algorithm may become more sensitive to the majority class and fail to classify instances from the minority class accurately. The synthetic minority oversampling technique (SMOTE) was used to avoid the problem of class imbalance. Multiple performance indicators may be employed in classification tasks, but no single metric is thoroughly instructive. Therefore, this analysis employed accuracy (the of classified proportion correctly data), precision, and recall demonstrating the model's performance for each case.

Precision is calculated by dividing the proportion of accurately predicted positive outcomes (true positives) by the total number of positive outcomes predicted. The *Recall* is a measure of completeness calculated by dividing the proportion of positives accurately classified as positives (true positives) by the total number of positives. The upcoming sections will cover the technique for producing strain data, while Chapter 5 explores the outcomes of training the DL model and making predictions.

#### 3.3. How FEA enhances data collection in SHM

Data gathering or data accumulation is the most crucial phase of an SHM process, as it affects the success of future operations. FEA plays a crucial role in this procedure, especially in extracting strain data, a fundamental aspect of SHM. Several factors contribute to the importance of strain data extraction utilising FEA models in SHM.

First, FEA can accurately simulate the physical behaviour of a structure under various conditions, yielding accurate strain data for the SHM framework. It considers the complexities of material properties, loading conditions, and geometric details, which makes FEA strain data extraction a reliable starting point. Second, FEA models offer efficiency by reducing the need for expensive and time-consuming physical prototypes and tests. These models can simulate extreme conditions that may be difficult or dangerous to recreate in real life, thus saving additional time and resources. In addition, the FEA-generated strain data enables a comprehensive structural analysis. It facilitates the identification of strain peaks, potential sites of failure, and a comprehensive evaluation of the structure's safety.

The extracted strain data are crucial for training DL models within an SHM framework. The accurate, dependable, and exhaustive data generated by FEA enhances the prediction capabilities of these algorithms, allowing for the early detection of structural issues and boosting the overall performance of the SHM system. In conclusion, the retrieval of strain data from FEA models is not only significant but also the optimal method for

initiating and training an SHM framework. It lays the groundwork for dependable, efficient, and effective SHM, saving time, money, and possibly even lives.

#### 3.4. Material model for steel reinforcement

Rebars and stirrups (steel reinforcement) exhibit equivalent stress-strain characteristics. They exhibit linear elastic behaviour until they yield, after which they exhibit plasticity. For the steel reinforcement, it was assumed that the modulus of elasticity is 200 GPa and the yield stress is 450 MPa. The material parameters for the steel components were obtained from the datasheets of the material suppliers, and a stress-strain curve was generated using the model supplied by Ramberg and Osgood (1943) [238]. A density of 7800 kg/m³ was assumed for all steel components.

#### 3.5. Material model for concrete

The concrete material model is the most critical model for simulating a flexural test, as the member's failure is highly dependent on the behaviour of the concrete. Choosing an appropriate material model for concrete is crucial for FEA accuracy. Elastic properties and a damaged plasticity model for concrete are provided and analysed along with material parameters. It is noteworthy to acknowledge that the equations presented are widely accepted formulas utilised in the industry to forecast the performance of concrete under diverse load circumstances. The majority of these equations are from CEB-FIP Model Code 90 [239] which possess an empirical quality, as they have been obtained after comprehensive experimental testing conducted on concrete examples.

#### 3.5.1. Elastic properties of concrete

Concrete's elastic characteristics are primarily influenced by its constituent ingredients, particularly the aggregates. The concrete's elasticity modulus,  $E_{ci}$ , is an essential parameter in understanding its mechanical behaviour under load. The CEB-FIP Model Code 90 provides

methodologies and empirical relations, such as the one presented, which are based on extensive experimental data and collaborative research across different countries and institutions [239]. In this study  $E_{ci}$  was calculated using the CEB-FIP model code 90 specifications given in Equation (3.4).

$$E_{ci} = E_{co} \left[ \frac{f_{cm}}{f_{cmo}} \right]^{1/3}$$
 (f<sub>cm</sub> in MPa) (3.4)

$$f_{cm} = f_{ck} + 8$$
 (MPa)

Where,

 $f_{cm}$  = Mean value of concrete compressive strength

 $f_{cmo} = 10 \text{ MPa}$ 

 $E_{co} = 2.15 \times 10^4 \text{ MPa}$ 

 $f_{ck}$  = The characteristic compressive strength

Experimentally determining  $f_{cm}$  typically entails subjecting concrete samples to a compressive load until failure and measuring the maximal compressive load sustained by the sample. The compressive strength is then calculated by dividing this value by the sample's cross-sectional area. For the purposes the analyses, all concrete grades were deemed to have a Poisson's ratio of 0.2 and a normal-weight concrete density of 2400 kg/m<sup>3</sup>. The elastic properties outlined above were applied uniformly to all concrete material models utilised in this study. In cases which perform only an elastic analysis of a concrete structure, the initial plastic strain must be accounted for by adopting a reduced modulus of elasticity,  $E_c$ , as per equation (3.6).

$$E_c = 0.85E_{ci} (3.6)$$

#### 3.5.2. CDP model

The CDP model available in both ABAQUS/Standard and ABAQUS/Explicit can be utilised to simulate concrete and other quasi-brittle

materials in different structures. The CDP model relies on two primary failure modes: *tensile cracking* and *compressive crushing*. The evolution of the yield surface is determined by two hardening factors that lead to failure under tensile and compressive loads. A softening stress-strain response characterises the post-failure behaviour under compression. When dealing with cracked concrete in tension, the strain softening behaviour is defined by either a tension stiffening model that considers post-failure stress-strain behaviour or a fracture energy-based cracking criterion. The CDP model is intended for situations where concrete is exposed to arbitrary loading conditions, including cyclic loading.

# Plasticity parameters

A non-associated plasticity flow rule is followed in the CDP model, which means that the plastic potential function and yield surface are not coincident. Under extremely high levels of inelastic stress, concrete can undergo a considerable volume change, often known as *dilatation*. The dilatation is capable of being represented by a suitable plastic potential function. In contrast, the hardening rule could specify the yield surface. The plastic parameters considered by the CDP model are as follows:

Dilation angle,  $\Psi$  is defined in the p-q plane, and value is inserted in degrees.

Eccentricity,  $\epsilon$  is a small positive value that determines the rate at

which the hyperbolic flow potential approaches its

asymptotic limit.

 $f_{b0}/f_{c0}$   $\sigma_{b0}/\sigma_{c0}$  is the ratio of initial equi-biaxial compressive

yield stress to initial uniaxial compressive yield stress.

 $K_c$  is the ratio of the second stress invariant on the

tensile meridian, q(TM), to that on the compressive

meridian, q(CM), at initial yield for any given value of

the pressure invariant p such that the maximum

principal stress is negative. It must comply with the

condition  $0.5 < K_c < 1.0$ .

Viscosity In Abaqus/Standard analyses, the viscosity parameter

is utilised to introduce visco-plastic regularisation into

the concrete constitutive equations. This parameter is

disregarded in the Abaqus/Explicit.

The plastic characteristics discussed earlier, including dilation angle and eccentricity, are determined through the utilisation of empirical relationships and experimental observations of concrete subjected to different loading circumstances. The assessment of these parameters necessitates the use of specialised testing equipment and setups, as they play a crucial role in mimicking the behaviour of concrete under various stress conditions. To obtain comprehensive approaches about the derivation of these parameters, readers are kindly directed to references [144, 240].

# Compressive behaviour

parameter

The stress-strain relationship of plain concrete under uniaxial compression was obtained by applying Equation (3.7) from the CEB-FIP Model Code 90. Figure 3.6 presents the schematic representation of the stress-strain relationship for the nonlinear structural analysis of concrete.

$$\sigma_{c} = -\frac{\frac{E_{ci}}{E_{c1}} \cdot \frac{\varepsilon_{c}}{\varepsilon_{c1}} - \left(\frac{\varepsilon_{c}}{\varepsilon_{c1}}\right)^{2}}{1 + \left(\frac{E_{ci}}{E_{c1}} - 2\right) \cdot \frac{\varepsilon_{c}}{\varepsilon_{c1}}} \cdot f_{cm} \qquad \text{for } |\varepsilon_{c}| < |\varepsilon_{c,lim}| \qquad (3.7)$$

Where,

 $E_{ci}$  = The tangent modulus according to eq. 3.4

 $\sigma_c$  = The compression stress (MPa)

 $\varepsilon_c$  = The compression strain

 $E_{c1} = f_{cm}/0.0022 =$  Secant modulus from the origin to the peak compressive stress  $f_{cm}$ 

As seen in Figure 3.7, the compressive uniaxial response of concrete is linear up to the initial yield stress,  $\sigma_{c0}$ . After reaching the peak compressive stress, the material's response shifts towards plastic deformation characterised by stress hardening; subsequently, strain softening occurs  $\sigma_{cu}$ . When the concrete specimen is unloaded at any position on the softening branch of the stress-strain curve, the compressive damage variable,  $d_c$ , characterises the degradation of the material's elastic stiffness. The compressive damage variable has a value of zero (0) for undamaged material and a value of one (1) for complete loss of compressive strength.

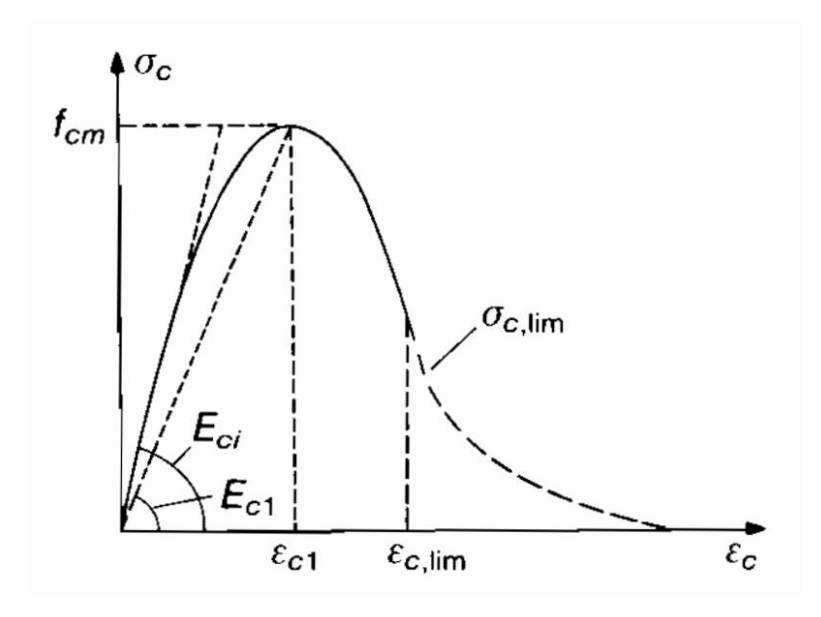


Figure 3.6: Schematic representation of the stress-strain relation for uniaxial compression (CEB FIP Model code 1990)

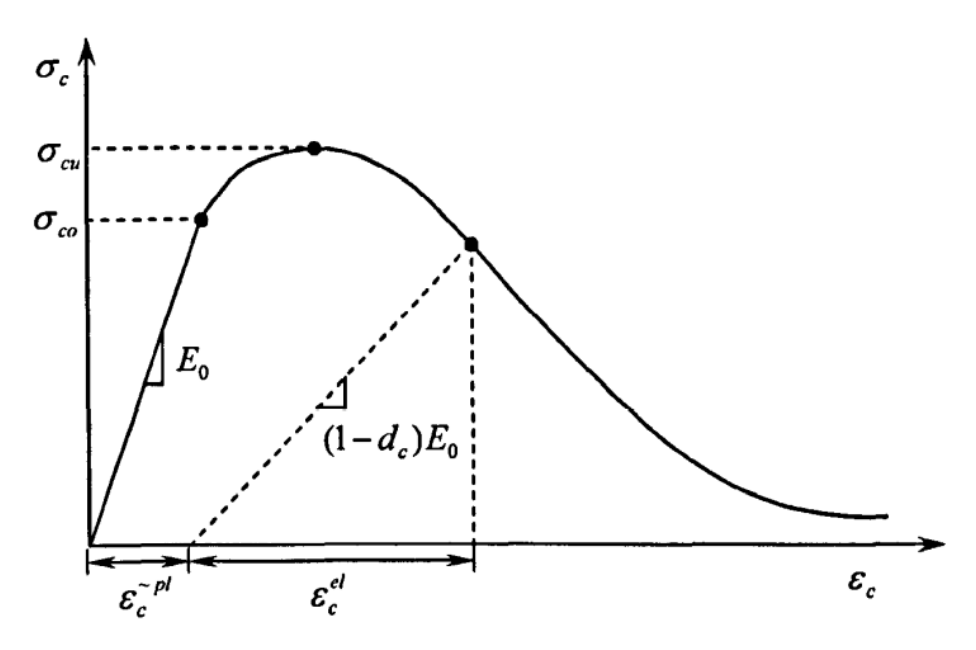


Figure 3.7: Response of concrete to uniaxial loading in compression (ABAQUS manual)

The compressive damage variable,  $d_c$ , was derived from Equation (3.8) as supplied in the ABAQUS manual if  $E_0$  is the elastic stiffness of the undamaged material and  $\varepsilon_c$  is the total compressive strain.

$$\sigma_c = (1 - d_c) E_0 (\varepsilon_c - \varepsilon_c^{pl}) \tag{3.8}$$

Where,

 $\varepsilon_c^{-pl}$  = Compressive equivalent plastic strain

To determine the compressive behaviour and concrete compression damage, the ABAQUS CDP model utilises the yield stress versus inelastic strain curve and the damage parameter versus inelastic strain curve. According to the ABAQUS manual, the compressive inelastic (or crushing) strain,  $\varepsilon_c^{-in}$ , is determined using Equation (3.9).

$$\varepsilon_c^{\sim in} = \varepsilon_c^{\sim pl} + \frac{d_c}{1 - d_c} \frac{\sigma_c}{E_0}$$
 (3.9)

The parameters utilised in equation (3.7) and the subsequent equations until equation (3.9) are derived from the stress-strain characteristics of concrete when subjected to compressive forces. The equations presented here are from the CEB-FIP Model Code 90 [239] and ABAQUS manual [241].

#### Tensile behaviour

Concrete tensile failure is usually a discrete phenomenon. Therefore, a stress-strain diagram for uncracked concrete and a stress-crack opening diagram, as shown in Figure 3.8, should describe the tensile behaviour. The bilinear stress-strain relationship given by equations (3.10) and (3.11) applies to uncracked concrete subjected to tension.

For 
$$\sigma_{ct} \leq 0.9 \, f_{ctm}$$

$$\sigma_{ct} = E_{ci} \cdot \varepsilon_{ct} \tag{3.10}$$

For 
$$0.9 f_{ctm} \le \sigma_{ct} \le f_{ctm}$$

$$\sigma_{ct} = f_{ctm} - \frac{0.1 f_{ctm}}{0.00015 - \frac{0.9 f_{ctm}}{E_{ci}}} \cdot (0.00015 - \varepsilon_{ct})$$
(3.11)

Where,

 $E_{ci}$  = The tangent modulus according to eq. 3.4

 $f_{ctm}$  = The tensile strength in (MPa)

 $\sigma_{ct}$  = The tensile stress in (MPa)

 $\varepsilon_{ct}$  = The tensile strain

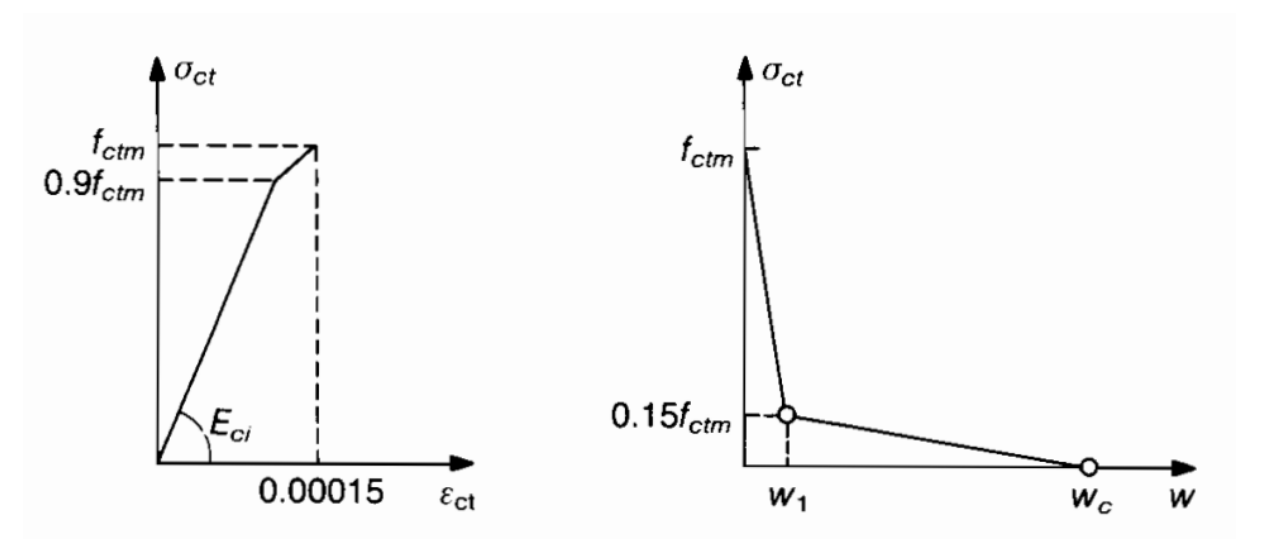


Figure 3.8: Stress-strain and stress-crack opening diagram for uniaxial tension (CEB FIP Model code 1990)

The ABAQUS manual recommends employing a tension stiffening technique for situations with no or minimal reinforcement in key model regions. When dealing with problems related to unreinforced or minimal RC, it is preferable to describe the brittle behaviour of concrete by specifying the fracture energy instead of defining a stress-strain relationship in tension. According to Hillerborg et al. (1976), fracture energy  $G_f$  can be defined as the amount of energy necessary to produce a stress-free crack with a unit area [242]. In a specific grade of concrete, the fracture energy can be represented by the area below the unloading section of the stress-crack opening curve.

The softening response of concrete can be defined in multiple ways using the fracture energy concept. Defining tensile cracking through a linear approximation that accounts for the loss of strength after cracking is a suitable approach. Although the linear softening method can produce reasonably accurate results, it tends to overestimate the stiffness of the material response. Hillerborg (1985) [243] proposed that using a bilinear function can provide a more precise definition of the softening behaviour of concrete under tension.

The variable  $d_t$  for tensile damage is derived from equation (3.12). Abaqus automatically converts cracking strain values to plastic strain values using the relationship (3.13). The fracture energy  $G_f$  computed from the expression (3.14) according to CEB-FIP model code 90, where  $f_{cmo}$  is the base value of mean compressive cylinder strength with a constant value of 10 MPa and  $G_{fo}$  is the base value of the fracture energy, which is dependent on the aggregate's maximum size. For a cracked section, the bilinear stress-crack opening relation given by equation (3.15) is used to determine the crack opening (3.18).

$$d_t = 1 - \frac{\sigma_{ct}}{f_{ctm}} \tag{3.12}$$

$$\varepsilon_t^{\sim ck} = \varepsilon_t^{\sim pl} + \frac{d_t}{1 - d_t} \frac{\sigma_t}{E_0}$$
 (3.13)

$$G_f = G_{fo} \left(\frac{f_{cm}}{f_{cmo}}\right)^{0.7} \tag{3.14}$$

$$\sigma_{ct} = f_{ctm} - \left(1 - 0.85 \frac{w}{w_1}\right)$$
 For  $0.15 f_{ctm} \le \sigma_{ct} \le f_{ctm}$  (3.15)

$$\sigma_{ct} = \frac{0.15 f_{ctm}}{(w_c - w_1)} \cdot (w_c - w) \qquad \text{For } 0 \le \sigma_{ct} \le 0.15 f_{ctm}$$
 (3.16)

$$w_1 = 2\frac{G_f}{f_{ctm}} - 0.15w_c ag{3.17}$$

$$w_c = \alpha_f \frac{G_f}{f_{ctm}} \tag{3.18}$$

## Where,

 $\varepsilon_t^{\sim ck}$  = cracking strain

 $\varepsilon_t^{\sim pl}$  = equivalent plastic strain in tension

w =The crack opening (mm)

 $w_1$  = The crack opening (mm) for  $\sigma_{ck} = 0.15 f_{ctm}$ 

 $w_c$  = The crack opening (mm) for  $\sigma_{ct} = 0$ 

 $G_f$  = The fracture energy (Nmm/mm<sup>2</sup>)

 $f_{ctm}$  = The tensile strength (MPa)

 $\alpha_f$  = The coefficient depends on the maximum aggregate size (d<sub>max</sub>)

# 3.5.3. Finite element type and mesh

In conventional numerical simulations of RC structures, it is commonly presumed that concrete is a homogeneous material [244]. Numerous studies [152, 245] have utilised a solid, homogeneous material to represent concrete. The literature review reveals that C3D8R and T2D2 are, respectively, the most common modelling elements for concrete and reinforcement. In this investigation, the concrete beams were modelled using C3D8R with reduced integration and hourglass control. Brick elements are favoured in many model sections because they provide an equally accurate solution while requiring less computational time. In the context of the current model, which was constructed using Abaqus/Explicit, it is important to note that there was no convergence issue associated with the brick elements.

Tetrahedral elements are known to exhibit a variety of geometric characteristics. To prevent shear locking in solid elements, the reduced integration method has to be utilised. Without this, the elements could become inappropriate for bending applications due to their extreme rigidity. This method is also advantageous because it reduces the required computational time for the analysis.

Separately, truss elements were used to depict rebars in the model. These truss components, specifically T3D2, were selected due to their efficiency in representing elements that can only support compressive or tensile stresses. Using these components for reinforcing bars and stirrups is a method for optimising the model for reduced computation time.

#### 3.5.4. Constraints and contact interactions

After assembling the model components, the appropriate constraints and contact interactions are applied to ensure that the simulation produces accurate and reliable results. The constraint between the reinforcement and the concrete beam was modelled using ABAQUS' embedded region feature to make modelling as simple as possible. This constraint links the nodes of a truss element with those of a solid element in a kinematic manner. As a result, the truss element node displacement is calculated as the average displacement of its nearby solid element nodes. The analysis, in this case, was conducted under the assumption that the reinforcement and concrete had a perfect bond. For the usual behaviour, the friction coefficient was selected to be 0.3, and a hard contact was selected as the contact interaction property between the loading arrangement and the concrete beam.

# 3.5.5. Load application and analysis procedure

FEA analyses of RC have been performed using a variety of approximation approaches and commercial software packages. ABAQUS / Explicit Version 2019 performed FE analysis in this work. The dynamic explicit procedure is an effective method for addressing a wide range of nonlinear issues, specifically in structural engineering. Explicit methods are not influenced by the characteristics or duration of the loading, and they necessitate a smaller increment size compared to implicit methods. In contrast, the increment size of implicit methods is typically determined by convergence and accuracy concerns. Hence, explicit methods have a lower computing cost per increment than implicit methods.

ABAQUS/Explicit was selected for this project due to its ability to handle problems involving complex contact interactions, extremely nonlinear quasi-static scenarios, and degrading or failing materials [246-249]. Complex contact interactions are frequently simpler to specify when explicit methods are used as opposed to implicit ones. Methodologies developed by ABAQUS/Explicit can be advantageous for structures

subjected to complex contact interactions during loading. While it is acknowledged that ABAQUS/Standard may provide verifiable results for non-stress wave dominated cases, ABAQUS/Explicit offers a more practical ABAQUS/Standard faces convergence approach, especially when challenges. Although recent developments such as XFEM have enhanced ABAQUS/Standard's failure simulation capabilities, in this study XFEM have not been provided results closer to experimental results. Therefore, ABAQUS/Explicit was chosen for this project due to its resource efficiency and prowess in addressing complex contact scenarios. Materials that exhibit stiffness degradation and failure, such as the brittle materials studied for this project, can cause significant convergence issues in implicit processes, which justifies the use of ABAQUS/Explicit. Such materials, comparable to concrete, may experience a sharp decrease in load-bearing capacity, resulting in a significant increase in kinetic energy, which ABAQUS/Explicit can simulate accurately.

The top surface of the beam is displaced in the dynamic explicit analysis by providing a uniform load to the "loading arrangement" using the amplitude function to ensure a quasi-static solution. Throughout the analysis, the quasi-static solution primarily restricts the kinetic energy of the flexural test to a modest value. After testing various loading rates, the optimal loading rate has been determined to be 2.5 mm/sec. The computing efficiency of a quasi-static analysis employing the dynamic explicit technique is ensured by raising the time increment or introducing mass scaling into the model. The ratio of kinetic energy to internal energy and external energy (ALLKE/ALLWK) must always be evaluated and should be less than 5 per cent. For all simulations, the ratio of kinetic energy to internal energy and external energy is less than 1%, which is within the permitted range of 5%.

## 3.5.6. CDP model parameters

The CDP model includes concrete's plastic, compressive, and tensile behaviours. The CDP model considers concrete homogeneous, isotropic, and continuous [240]. The primary parameters considered in this study were dilation angle ( $\psi$ ), flow potential eccentricity ( $\epsilon$ ), the ratio of compressive strength under biaxial loading to uniaxial compressive strength (fb0/fc0), shape factor (K), viscosity parameter ( $\mu$ ), elasticity modulus of concrete (Ec), concrete compressive behaviour, concrete tensile behaviour, and density. A viscosity parameter was not used because ABAQUS/Explicit was employed for the simulation; hence, its value was presumed to be 0 [249]. Table 3.1 lists the recommended CDP properties.

Table 3.1: CDP properties for FEA model

Dilation Angle	Eccentricity	f <sub>b0</sub> /f <sub>c0</sub>	К	Viscosity parameter
31° - 45°	0.1	1.16	0.667	0

#### 3.6. Strain data extraction from FEA models

SHM algorithms can make conclusions concerning the structural integrity of a structure. Modern AI approaches, such as DL, can serve the same function. Nevertheless, having thousands of data points may be necessary to effectively train DL models, as a higher amount of training data often leads to a more accurate model. However, executing thousands of experiments to extract data is not realistic in terms of time or cost. Hence, by adjusting various model parameters such as loads, boundary conditions, loading rates, and loading conditions, FEA models can generate hundreds of distributed data points. The study involved developing a Finite Element model specifically designed to extract distributed strain data by considering variations in load as a key factor.

The accuracy of a DL model is determined by the amount of training data used to train the model. In the CDP model, the dilation angle holds great significance as it is one of the most crucial features for smaller values, the material is brittle; for larger ones, it is stiff. Typically, the angle of dilatation of concrete ranges between 13° and 56° [250]. In this study, strain data were generated using a series of simulations in which the angle

of dilation was adjusted from 31° to 45° (with an increment of 1°). The field output request interval for each simulation was modified by considering the frequency of evenly spaced time intervals, and the CDP model was loaded until the rebar yields. Therefore, the surface and rebar data can be retrieved until reaching the elastic limit.

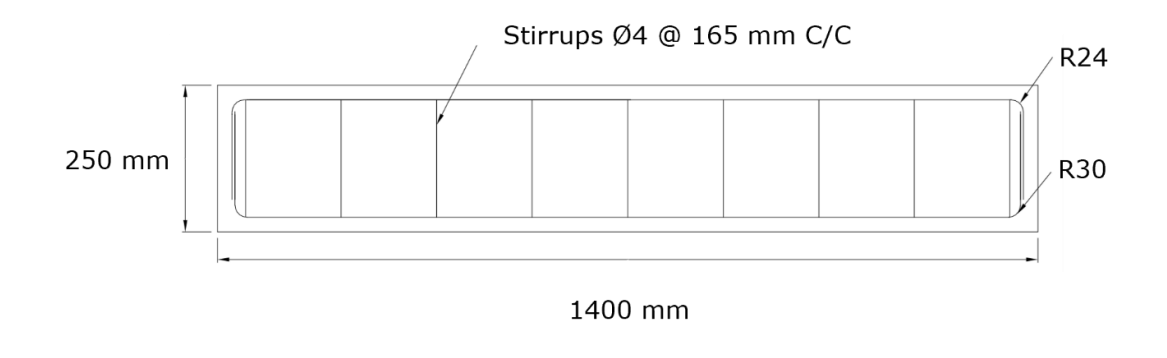
As described earlier, a notable adjustment was made to the angle of dilation parameter in the CDP model. This was done to obtain a comprehensive understanding of the DL model's sensitivity to changes in the angle of dilatation and its effect on the accuracy and reliability of the generated strain data. The choice of this particular parameter adjustment was motivated by the fundamental significance of the angle of dilatation in characterizing concrete behaviour, where moving leftwards represent brittle material responses and moving rightwards values represent stiffer behaviour. By exploring this parameter within the typical range observed in concrete structures [141, 142, 246, 251, 252] and conducting a series of simulations under varying conditions, this study aimed to generate strain data from the CDP model's ability to capture a broad spectrum of material behaviours. The simulations incorporated both elastic and plastic behaviour of concrete until the rebar yielded, allowing for a comprehensive analysis of strain patterns and structural responses. This investigation's findings provide valuable insights into the model's robustness and applicability in real-world engineering scenarios, thereby augmenting the understanding of concrete's behaviour under varying conditions.

Two types of RC beam geometries, namely *short-span* and *long-span* were modelled using CDP-based FEA. The FEA modelling process involved creating separate models for each type of beam geometry and specifying relevant material properties, dimensions, and loading conditions. The first FEA was performed with a short-span RC beam, followed by the long-span beams, and data extraction was used to analyse the beams' behaviour under different loading conditions. Figure 3.9 displays the Reinforcement details and sectional view of the short-span RC beam. The loading, boundary conditions, and mesh arrangement are displayed in Figure 3.10.

Table 3.2 lists the proposed concrete and steel properties for the shortspan RC beam FEA model.

Table 3.2: Material properties for the short-span RC beam

Material	Туре	Young's modulus (MPa)	Poisson's ratio
Concrete	Isotropic	26370	0.2
Steel	Isotropic	200000	0.3



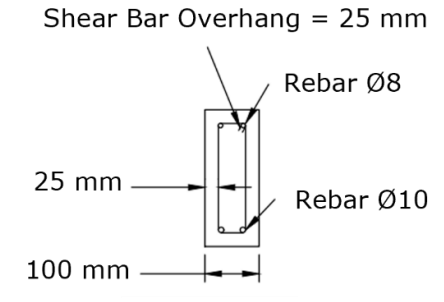


Figure 3.9: Reinforcement details and sectional view of the short-span RC beam

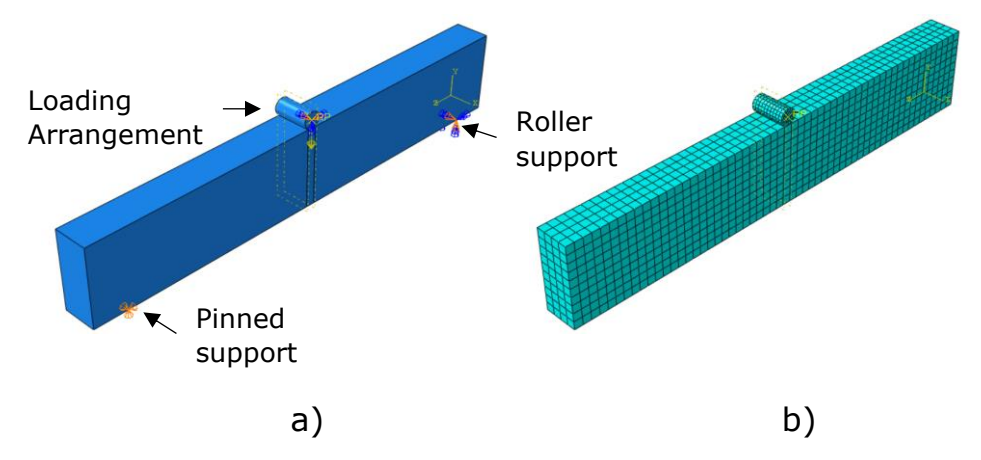


Figure 3.10: FEA model of short-span RC beam (a) Boundary conditions and loading configuration; (b) Mesh configuration

The FEA model was created using four different types of elements. There are 292 elements of the T3D2 type, 2712 elements of the C3D8R type, 218 elements of the R3D4 type, and only four elements of the R3D3 type. Figure 3.11 illustrates establishing two paths for data extraction, one for surface strain data and the other for rebar strain data. Strain data for each node was retrieved using ABAQUS's XY data option. Path points, including intersections, were selected, and the option "Remove duplicate XY pairs" was chosen. A long-span beam model of 4000 mm long with a 200 mm by 400 mm cross section was proposed for the simulation to generate strain data for the subsequent stage.

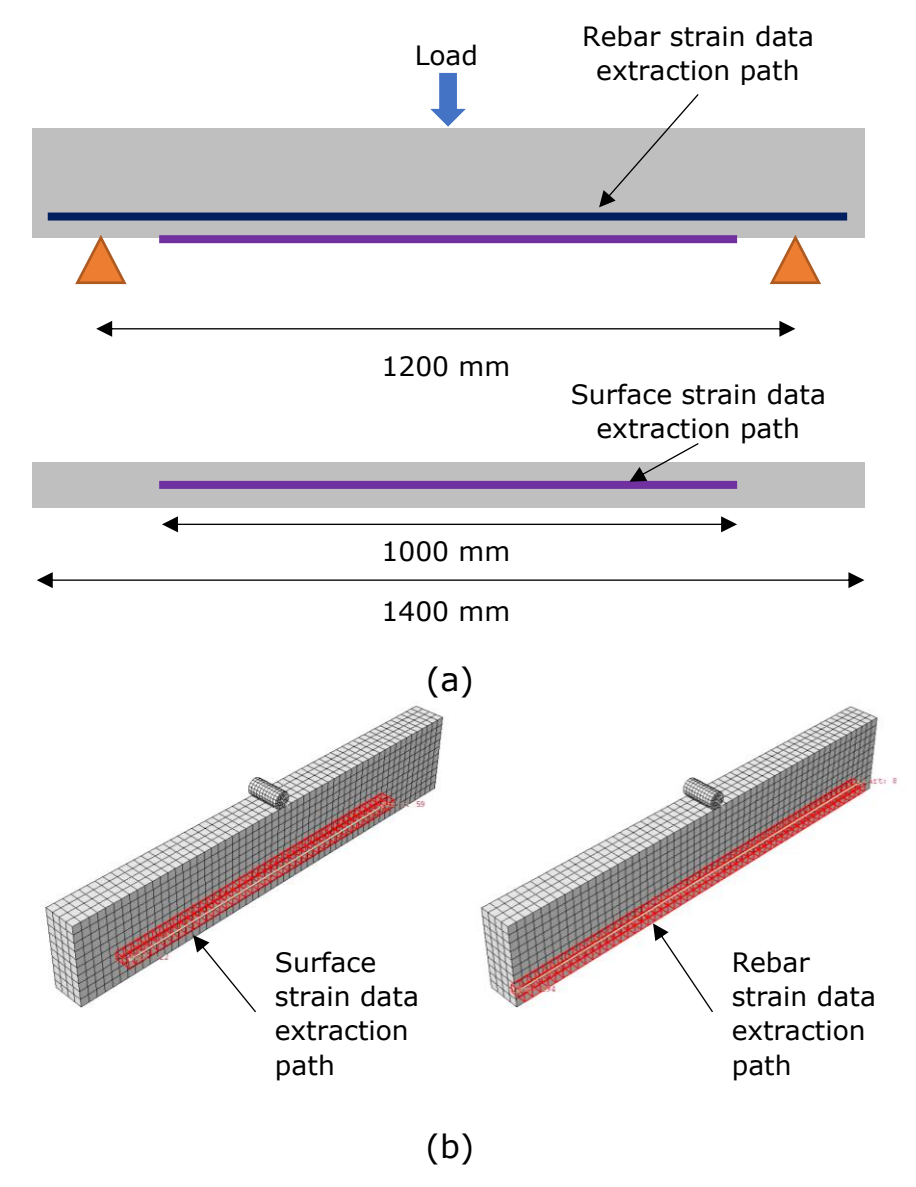


Figure 3.11: Loading arrangement and data extraction paths of shortspan RC beam (a) Surface and rebar data extraction path; (b) FEA surface and rebar strain data extraction path

Table 3.3: CDP model parameters for strain data generation

Dilation angle (°)	Steps	Number of data points per sensor	
		path	
		(No. of dilation angles * Steps)	
31° to 45°	2000	30,000	
(15 angles)			

Table 3.3 presents the CDP model parameters for strain data generation. Figure 3.12 displays beam definitions of the long-span RC beam, and Table 3.4 lists the proposed concrete and steel properties for the long-span RC beam FEA model.

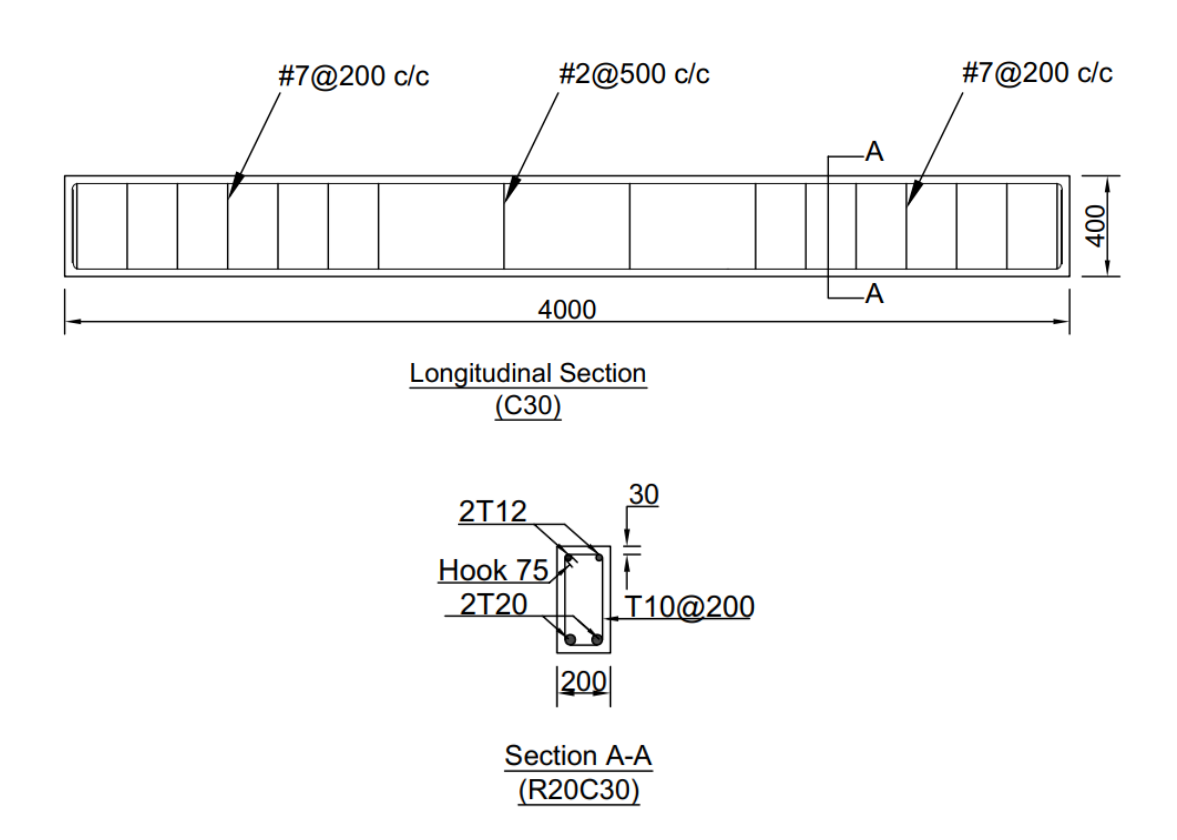


Figure 3.12: Beam definitions for R20C30 RC beam

Table 3.4: Material properties the long-span RC beam FEA model

Material	Туре	Young's modulus (MPa)	Poisson's ratio
Concrete	Isotropic	27106	0.2
Steel	Isotropic	200000	0.3

Figure 3.13 illustrates the load, boundary conditions, and mesh configuration of long-span beam. The Beam supports were modelled per Figure 3.13 (a), and the material was selected as steel. Figure 3.13 (b) displays the mesh configuration. The supports were subjected to encastre boundary condition, which means the supports have been rigidly fixed to

prevent any movement or rotation at their endpoints. The number and type of elements used in the model are 22156 – C3D8R and 1512 – T3D2.

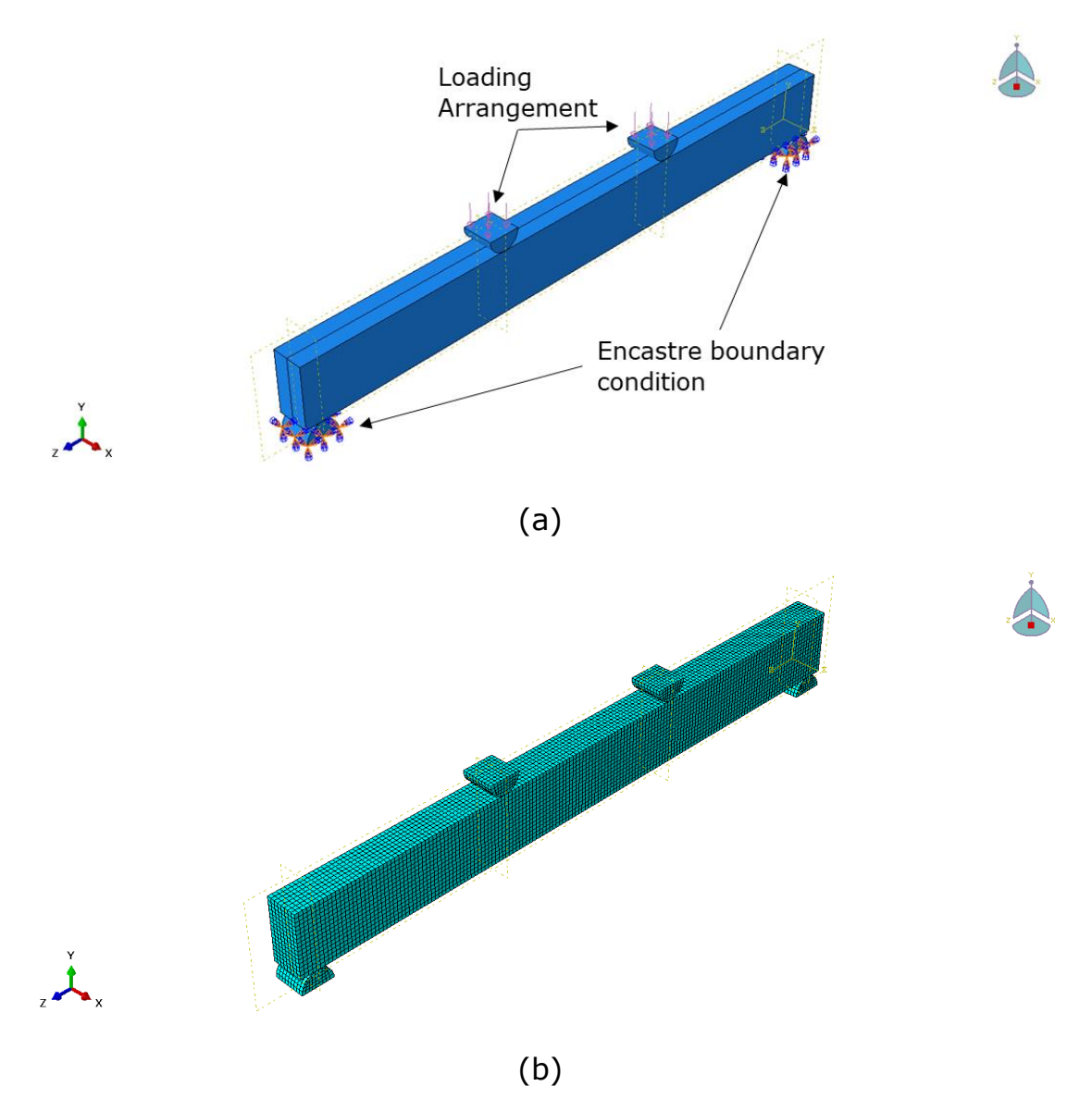


Figure 3.13: (a) Loading and boundary condition; (b) Mesh configuration

Three strain data generation paths were proposed as per Figure 3.14: the bottom surface path, the side surface path, and along the tension rebar. Table 3.5 presents the beam nomenclature. Strain data were generated through a series of simulations for 15 different dilation angles. Table 3.6 lists the CDP model parameters used to generate strain data, and Figure 3.15 shows the proposed loading arrangements for strain data generation.

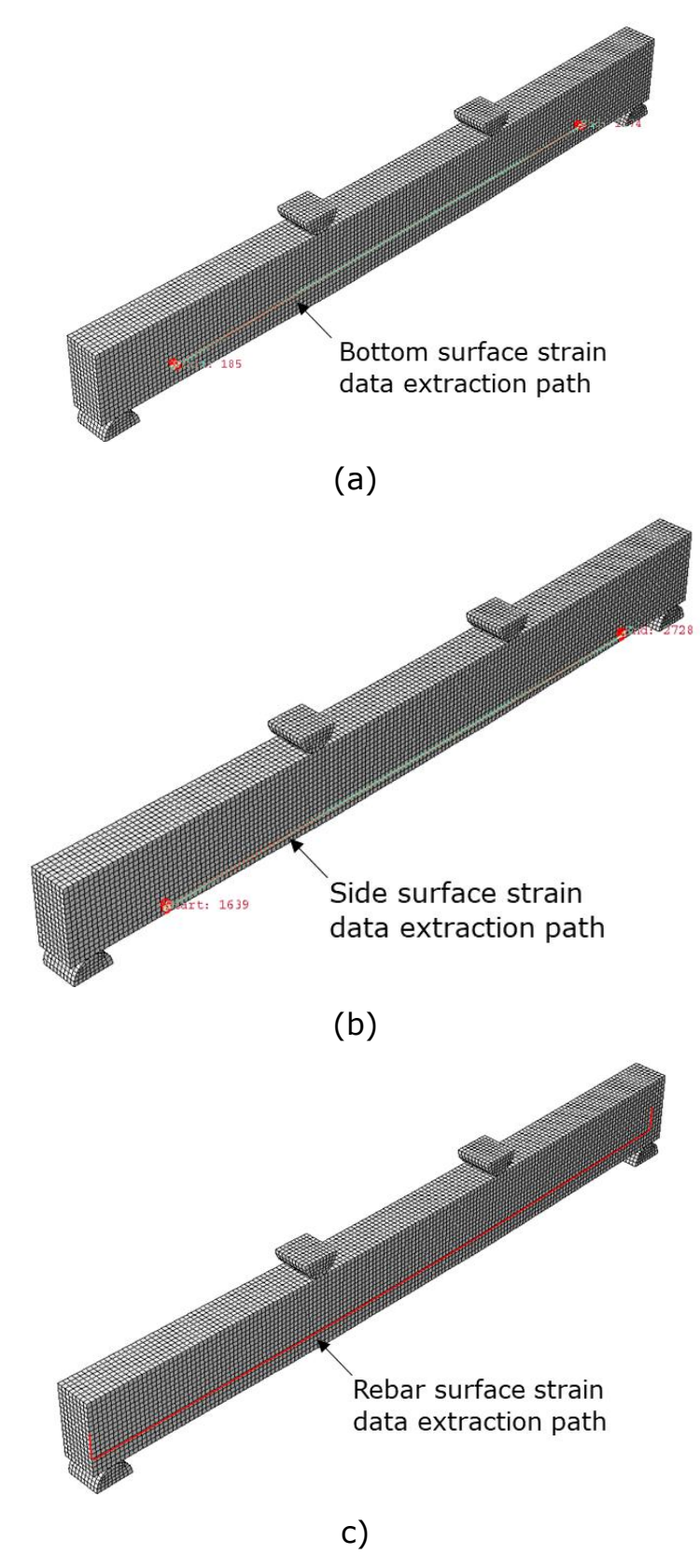


Figure 3.14: (a) FEA Bottom surface data extraction path; (b) FEA side surface data extraction path; (c) FEA rebar surface data extraction path

Table 3.5: Beam nomenclature

R20C30	
R20	- Rebar size is 20 mm
C30	- Concrete cover thickness is 30 mm

Table 3.6: FEA model parameters for strain data generation

Dilation angle (°)	Steps	Number of data points per each	
		sensor	
		(No. of dilation angles * Steps)	
31° to 45° (15 angles)	2500	37,500	
Total number of data use	ed to	75,000	
train the model			
(Bottom sensor + Side sensor)			

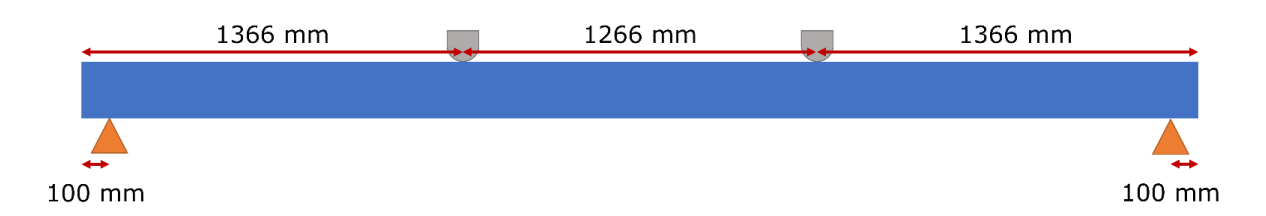


Figure 3.15: Proposed loading arrangements for strain data generation

The strain data were extracted, and the developed DL model was trained using two proposed FEA models. Initially, the DL model was trained using the dataset of short-span RC beams. After verifying the accuracy of the DL model's predictions against experimental measurements from DOFS, the next round of training began using the dataset of a long-span beam size. The results were presented in Chapter 5 for better understanding.

# 3.6.1. Mesh convergence study

The maximum mesh size studied was 50 mm since the beam width is limited to 100 mm. Mesh sizes smaller than 25 mm were not considered

because the aggregate size was 20 mm. A convergence study was done with 50 mm, 35 mm, 30 mm, and 25 mm mesh sizes. The mesh convergence study demonstrated that after reducing the mesh size to 25 mm, the results stabilised and closely mirrored the experimental behaviour. Therefore, a 25 mm mesh size was chosen for the FEA. Mesh convergence study for short-span RC beam was presented in Figure 3.16 at 16 kN load. The experimental deflection and simulation deflection were recoded as 1.325 mm and 1.281 mm, respectively. The percentage of difference was calculated as 3.32%. Table 3.7 presents the most appropriate dilation angle and other respective CDP properties for short-span RC beam.

Table 3.7: CDP properties of short-span RC beam

Beam No.	Dilation Angle	Eccentricity	f <sub>b0</sub> /f <sub>c0</sub>	К	Viscosity parameter
В1	43°	0.1	1.16	0.667	0

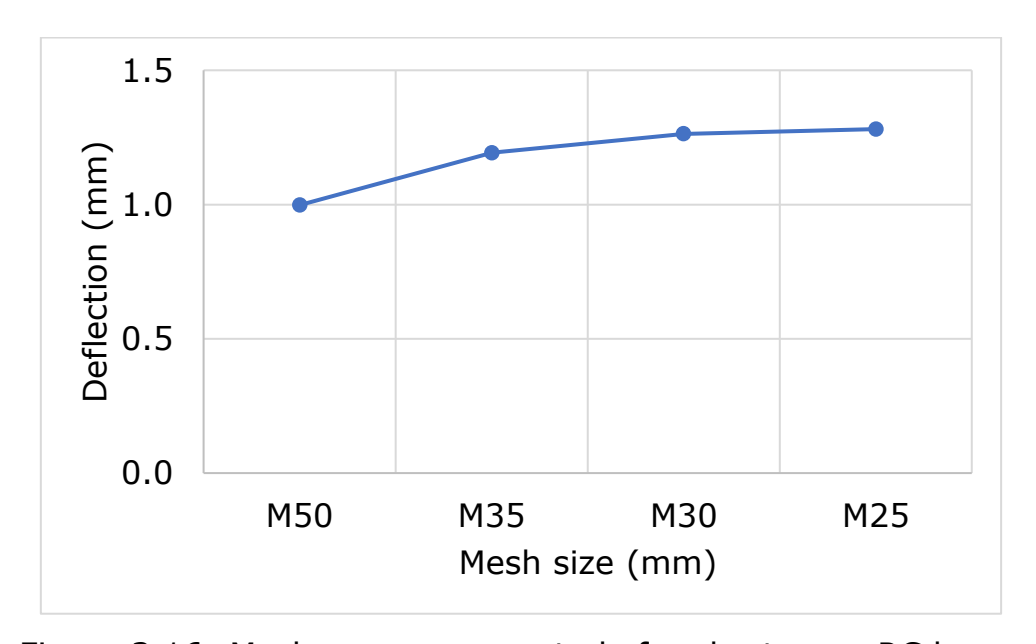


Figure 3.16: Mesh convergence study for short-span RC beam

For the long-span RC beam, the experimental deflection and simulation deflection were recorded as 21.42 mm and 22.32 mm,

respectively. The percentage difference between the two was calculated as 4.2%. Figure 3.17 presents the study results. The optimal dilation angle and corresponding properties of the CDP model are presented in Table 3.8. Chapter 5 of this study clearly presents the FEA model validation and simulation results.

Table 3.8: CDP properties for long-span R20C30 Beam

Beam No.	Dilation Angle	Eccentricity	f <sub>b0</sub> /f <sub>c0</sub>	К	Viscosity parameter
R20C30	43°	0.1	1.16	0.667	0

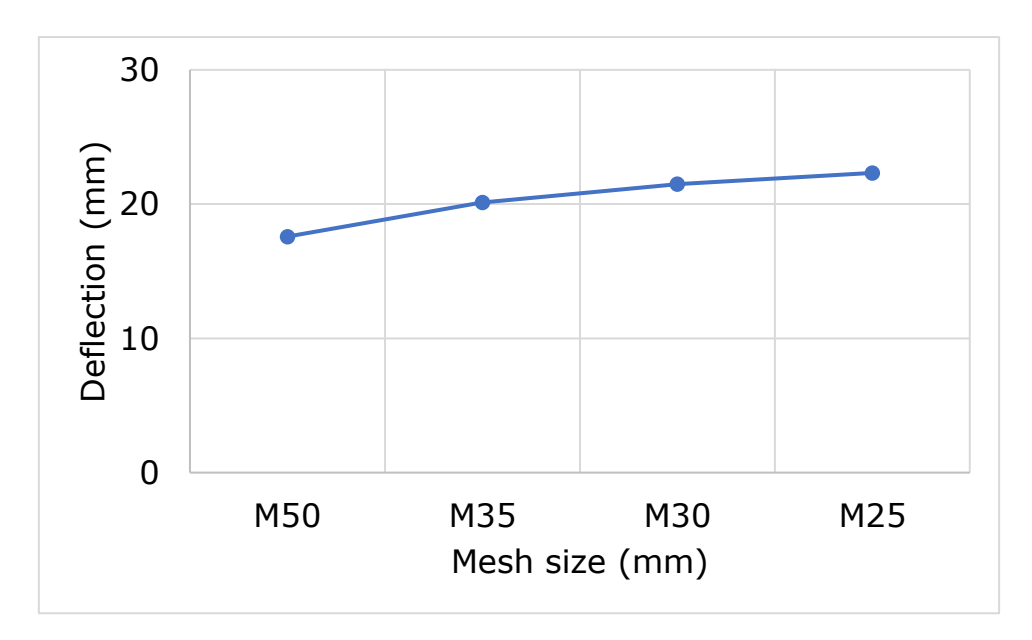


Figure 3.17: Mesh convergence study for long-span beam

# 3.7. Summary

The chapter begins with an explanation of the conceptual SHM framework, followed by a thorough examination of a DL model based on ANN architecture designed to interpret strain data for predicting the structural health of RC beams using a supervised learning approach. The DL model was developed using FEA based concrete surface strain data as input to predict the structural health of tension rebars in an RC beam. Adjusting the weights and biases of the neurons using the backpropagation

algorithm, which entails forward and backward propagation of data through the network, is to train an ANN.

This research proposes an ANN architecture with one input layer, two hidden layers, and one output layer. Between the input and hidden layers, the ReLU activation function is used, while the sigmoid activation function is used between the hidden and output layers. A classification-based DL model was developed using only strain data to predict the structural health of RC beams. The training phase of the DL model will be discussed in Chapter 5. The current emphasis is on assembling and preparing the necessary elements for successful model training, particularly the ANN architecture and the strain dataset.

Integrating the strain dataset generated by a CDP-based FEA model, which captures the nonlinearity and damage-induced plasticity of concrete, is novel to this method. Using CDP modelling, ABAQUS 2019 finite element software was used to develop two FEA models for short-span and long-span beam sizes. A method was proposed to extract strain data from FEA models, which was then used to train a DL model for the novel framework presented herein. These strain measurements were collected from two surfaces: the *surface of concrete* and the *surface of rebar*. In the proposed strain data generation method, the angle of dilation for the CDP model parameter was increased from 31 to 45 degrees. This data will be used to train a DL model, while experimental strain data will be used to evaluate the DL model.

# CHAPTER 4: IMPLEMENTATION OF DISTRIBUTED SENSOR NETWORKS AND DATA ACQUISITION

#### 4.1. Introduction

This chapter is an integral part of the research project. It investigates the installation and operation of the sensor network on RC beams, which inputs directly into the proposed SHM framework. This investigation is divided into three major sections, each addressing a topic essential to the successful implementation of DOFS networks, the primary data acquisition mechanism for the SHM framework.

Installation of sensors on concrete surfaces and rebars within RC beams requires meticulous attention to several factors, including sensor placement, orientation, and attachment methods. These factors are crucial for the sensor network's success and the SHM framework's overall efficacy, as improper sensor positioning, or attachment could result in inaccurate representations of the structural health.

Strain is an important structural health indicator for RC beams. This chapter explains the methods and procedures for strain monitoring using the installed sensors, including calibration and data collection. This chapter's ultimate goal is to provide a practical guide for designing and implementing distributed sensor networks for SHM of RC beams, thereby contributing directly to the efficacy of the proposed SHM framework. In addition to aiding in the practical implementation of the SHM system, this investigation endeavours to contribute to the larger objective of improving the safety, performance, and durability of RC infrastructures.

Figure 4.1 presents the overview of the technical contents of Chapter 4. Experimental results and their behaviour will be detailed for clarity in Chapter 5.

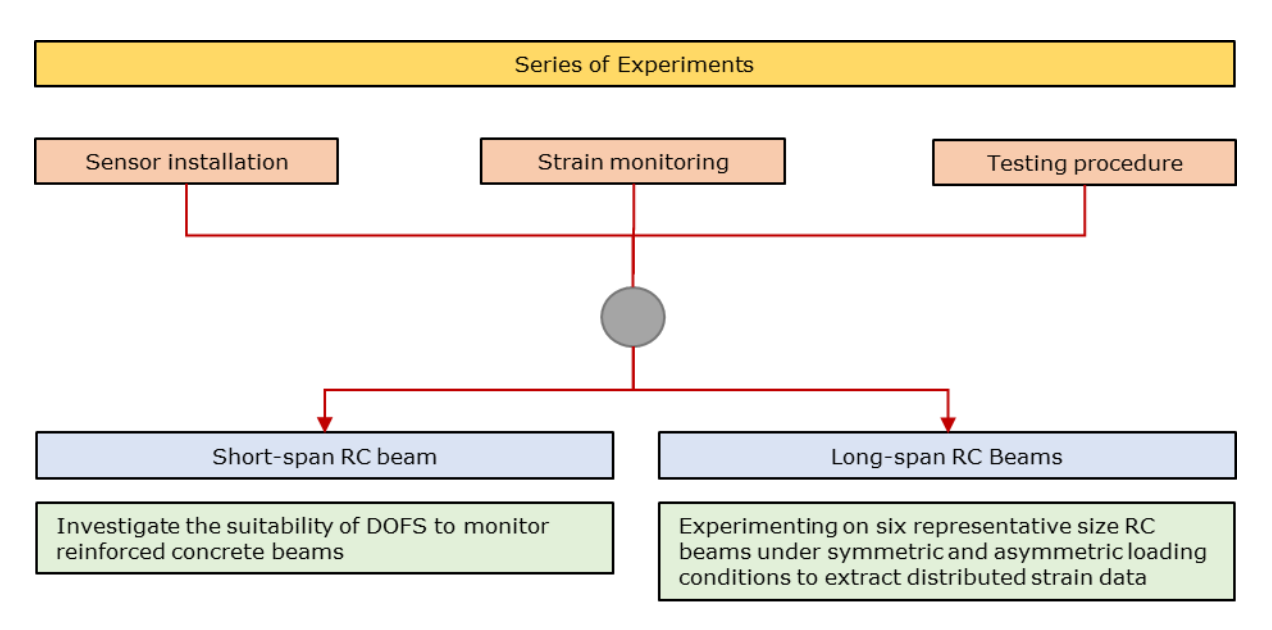


Figure 4.1: Overview of the technical contents of Chapter 4

#### 4.2. Sensor installation

The installation of sensors is a crucial factor in SHM applications as it directly impacts the overall system performance. This particular study used a single-mode optical fibre, SMF-28, with a cladding diameter of 125 micrometres, as the DOFS. The sensor was installed on two surfaces to ensure accurate measurements: the concrete surface and the rebar.

When choosing adhesives for the investigation, special consideration was paid to their innate qualities to make sure they complied with project requirements. Employing TECHNIGLUE R15 and R60 was based on a number of important considerations. Particularly important for long-term structural monitoring in concrete infrastructures that may be subject to moisture and environmental changes, their demonstrated endurance under various environmental circumstances is what made them stand out. The thixotropic properties of these adhesives, which guaranteed a continuous bond layer and, as a result, dependable and accurate data transfer from the sensors, were equally significant. Additionally, it was determined that their cost-performance balance was economically favourable for the investigation. Their simple mixing and room-temperature drying eliminated the need for specialist equipment, providing additional financial advantages.

#### 4.2.1. Sensor installation on concrete

The adhesive used to attach the DOFS to the concrete surface was TECHNIGLUE R60. This particular glue is an epoxy resin formulated to be solvent-free and can cure at room temperature when used with TECHNIGLUE hardeners. This results in a strong, waterproof bond. Additionally, the adhesive is thixotropic, allowing it to fill gaps and hold up well on vertical surfaces. The concrete surface should be wire brushed to remove dirt/debris before applying the adhesive. As per the datasheet, the resin and hardener should be mixed in a 2:1 ratio. Figure 4.2 displays TECHNIGLUE R60, and Figure 4.3 depicts a FOS attached to a concrete surface using this adhesive. Table 4.1 provides detailed information regarding the adhesive's curing and cured properties.



Figure 4.2: TECHNIGLUE R60 and H60

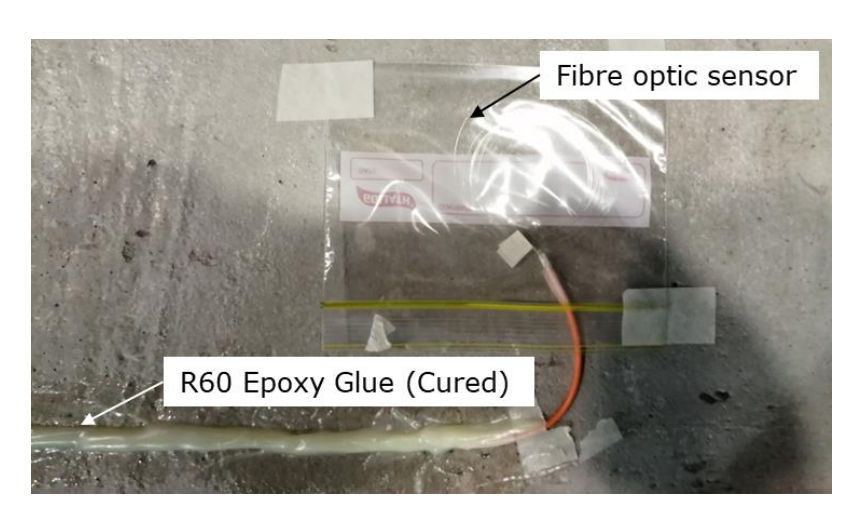


Figure 4.3: Concrete surface attached to FOS

Table 4.1: The cure characteristics and cured properties of TECHNIGLUE R60

Cure characteristics	
Pot life -100g @ 25°C (in air)	40 minutes
Cured to a solid state @ 25°C	12 hours
Cured properties	
Tensile strength (ASTM D638-97)	55 MPa
Tensile elongation at break (ASTM D638-97)	7%
Flexural strength (ASTM 790-03)	80 MPa
Flexural strain (ASTM 790-03)	5%

#### 4.2.2. Sensor installation on rebar

TECHNIGLUE R15 was used to attach the sensor to the rebar. The glue is a soft, thixotropic, solvent-free epoxy paste specifically formulated for use with H15 hardeners to cure at room temperature and produce a high-strength structural adhesive for bonding metals, particularly aluminium and steel. A grove is needed to position the sensor along the rebar. When the rebar length is low, this grove can be milled using a milling machine (the cutting length depends on the milling machine specification), while at higher lengths, the grove can be cut by an angle grinder. The surfaces should be clean and free from grease and/or loose particles before the application. The resin and hardener should be mixed in a 1:1 ratio per the datasheet.

Table 4.2 lists the cure characteristics and cured properties. Figure 4.4 shows the two-component epoxy glues used for the sensor mounting, and Figure 4.5 illustrates the groove on rebar, positioned DOFS and rebar attached sensor.



Figure 4.4: TECHNIGLUE R15 and H15

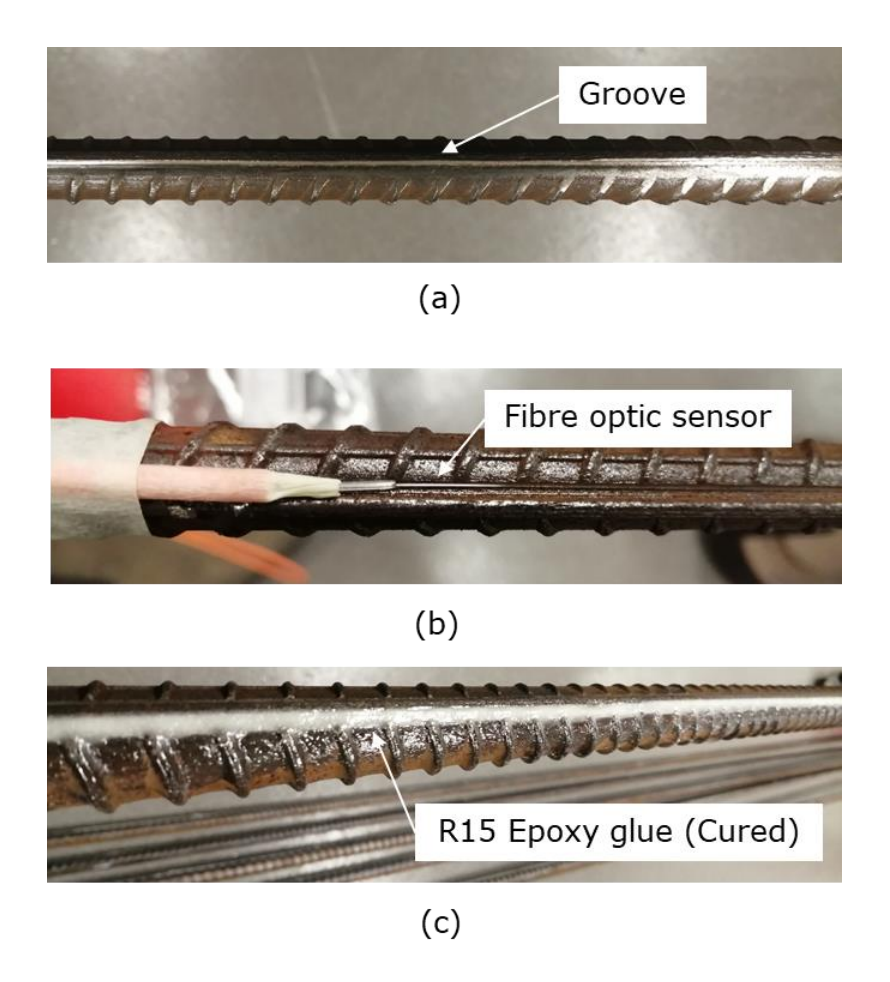


Figure 4.5: (a) The groove cut on the rebar; (b) DOFS before attachment; (c) Attached DOFS to the rebar by R15 Epoxy glue

Table 4.2: The cure characteristics and cured properties of TECHNIGLUE R15

Cure characteristics	
Pot life -100g @ 25°C (in air)	83 minutes
Cured to a solid state @ 25°C	8 hours
Mechanical properties	-
Ultimate tensile strength	22.4 MPa

The emerging sensors from the attachments should be carefully handled after attaching the sensor to a concrete surface or rebar. These sensors must be protected and ensure their reliable performance using proper safeguards. Polyethylene (PE) tubing  $(0.92 \text{ mm } \times 0.42 \text{ mm})$  and furcation tubes (3 mm) were used for this purpose. The PE tubing was inserted into the furcation tube before inserting the sensor. Figure 4.6 presents the PE tubing and furcation tubes.

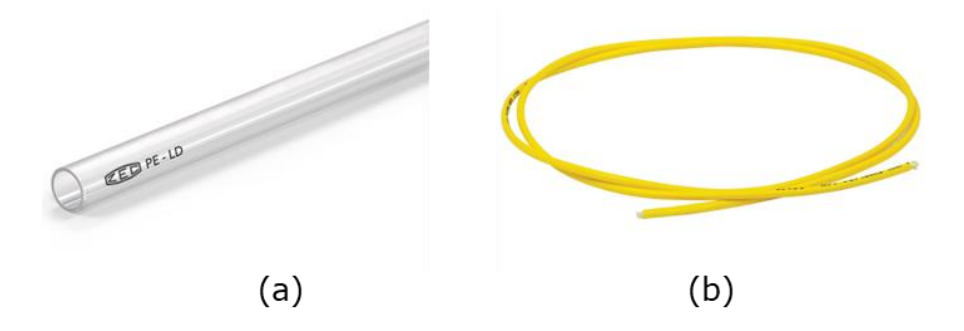


Figure 4.6: (a) PE tubing; (b) Furcation tubes

On reflection and analysis of the sensor installation performed on both the concrete surface and the reinforcing bars, the procedure appears to be effective and accurate based on the knowledge gained during this project. The careful selection of the appropriate adhesive for each surface, the proper preparation of the surfaces, the careful placement and attachment of sensors, and the subsequent implementation of protection measures for the installed sensors facilitated the installation of a robust sensor network. The meticulous execution of the procedure, the

performance history of the embedded sensors, and the data collected validated the approach. Therefore, it is proposed that this approach can serve as a trustworthy guideline for future sensor installations in similar SHM applications.

# 4.3. Strain monitoring

The strain monitoring was performed by using LUNA OBR 4600, which uses optical backscattered reflectometry (OBR) technology. Figure 4.7 shows the OBR 4600 system for interrogation of DOFS. OBR is an essential tool for shorter fibre spans due to its distinctive combination of ultra-high spatial resolution and sensitivity. OBR 4600 can detect and measure continuous strain and temperature by analysing the Rayleigh scatter inherent for commercially available optical fibres, with a user-specified spatial resolution as low as 0.32 mm. The apparatus features three scan measuring ranges: 30 m mode, 70 m mode, and 2000 m extended range. The whole experimental session used the 70 m mode.

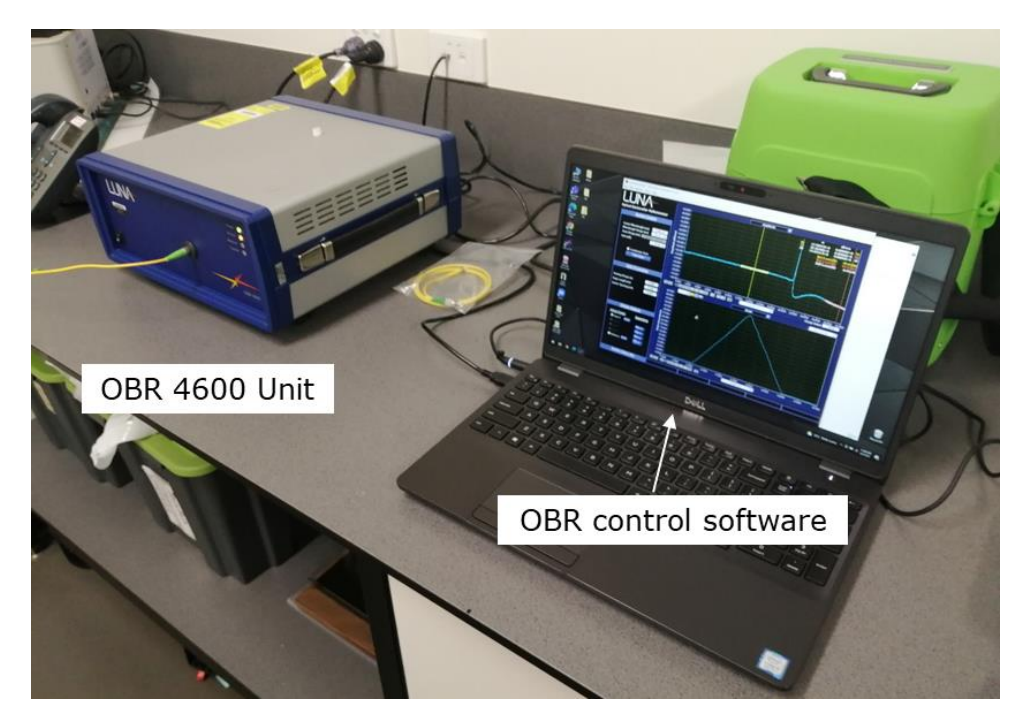


Figure 4.7: OBR 4600 system for interrogation of DOFS

Calibrating the OBR equipment is necessary before making measurements. The OBR calibration eliminates the impacts of the measurement network to ensure that the measured data only represent the device being tested. Calibration should be performed at least once every 24 hours in a typical laboratory or industrial environment. The area's ambient conditions mainly govern the necessity for recalibration. If the temperature fluctuates significantly, calibration may be required more frequently than once per 24 hours. A longer time may be sufficient if the ambient temperature is extremely stable.

The calibration process can be done using the supplied reference fibre and reflector to the instrument. The calibration should be checked after the calibration process by examining the return loss curve under the frequency domain. The resulting curve should be quite flat within the instrument's precision range, with a mean value of around 0.0 to -1.0 dB. The second calibration is necessary if the return loss curve is not flat. Table 4.3 provides the specifications of LUNA OBR 4600 according to the manufacturer's datasheet.

Table 4.3: Specifications of LUNA OBR 4600

Parameter	Specification	Units		
Wavelength range (nominal)	,	-		
OBR 4600	1525 - 1610	nm		
Maximum device length				
Standard mode	30 or 70	m		
Extended range mode	2000	m		
Sampling resolution				
30 m mode	10	μm		
70 m mode	20	μm		
Extended range mode (2000 m)	1	mm		
Distributed sensing				
Spatial resolution	±1.0	cm		

Temperature resolution	±0.1	°C
Strain resolution	±1.0	με

A spatial resolution of 1 cm [253] was used for the entire experimental session. The sensor length was considered 2.5 cm, and the sensor spacing was 1 cm. The OBR 4600 was used to store and monitor the strain measurements during the experiments. The attached DOFS to the beams should be connected to OBR 4600 via FC/APC connectors before taking any measurements. Since bare fibre does not come up with these connectors, splicing is necessary to connect the sensor to FC/APC connector. Figure 4.8 shows FC/APC connector.



Figure 4.8: FC/APC connector

# 4.4. The testing procedure of RC beams

Testing allows for evaluating the structural performance and behaviour of the RC beams under loading conditions. This study proposed two beam types to investigate flexural loading: *short-span RC beams* and *long-span RC beams*.

The three-point bending test is more appropriate for short-span RC beams because the highest moment occurs at the midpoint of the beam, where the load is applied. This maximises the bending moment, simplifying predicting and analysing the failure mode. In addition, this preliminary test is straightforward and economical. A four-point bending test is recommended for long-span beam dimensions since it generates a larger region of constant moment between the two applied loads, thereby providing a more accurate representation of the beam's behaviour under typical loading conditions. This provides more precise information on the

flexural capacity and response of the beam.

In addition, using this test to represent the beam size diminished shear effects and made the results more representative of real-world conditions. During flexural testing of beams, OBR 4600 recorded strain measurements from DOFS about the applied load.

It is essential to note that all flexural tests on the RC beams were conducted in a laboratory setting under standard conditions. Although specific data on temperature and humidity during testing periods were not recorded, the laboratory is typically kept at a constant temperature and relative humidity with minimal fluctuations. To maintain consistent conditions throughout the experiment, direct exposure to external elements such as sunlight, wind, and rain was avoided. It is essential to observe that the controlled environment was intended to mitigate any external influences that could affect the structural behaviour of the beams. The equipment used to record strain measurements from DOFS, the OBR 4600, was also operated under these standard laboratory conditions.

# 4.4.1. Short-span RC beam

As the first experimental session, a short-span RC beam was cast and instrumented with distributed FOSs to extract strain data along the concrete surface and rebars. These experimental data will help to correlate the FEA.

The beam cast used in this study had 1400 mm x 100 mm x 250 mm dimensions and was reinforced with 8 mm diameter rebars for the top reinforcement and 10 mm diameter rebars for the bottom reinforcement. For the stirrups, 6 mm diameter bars were used, with a stirrup spacing of 165 mm maintained for all beams. The stirrups' purpose was to minimise shear failure. Geometrical, mechanical, and reinforcing features were selected to accommodate the beam's dimensions for testing on the MTS sans testing machine and to facilitate its handling. Grade 25 concrete premix was used to cast the beam, then stored for seven days in wet conditions and 21 days in room conditions. After 28 days of casting, the

concrete's mean cylinder compressive strength was experimentally determined to be 28 MPa. The design was as per the British standards BS 8110 – Part 1:1985. Figure 4.9 shows the beam definition.

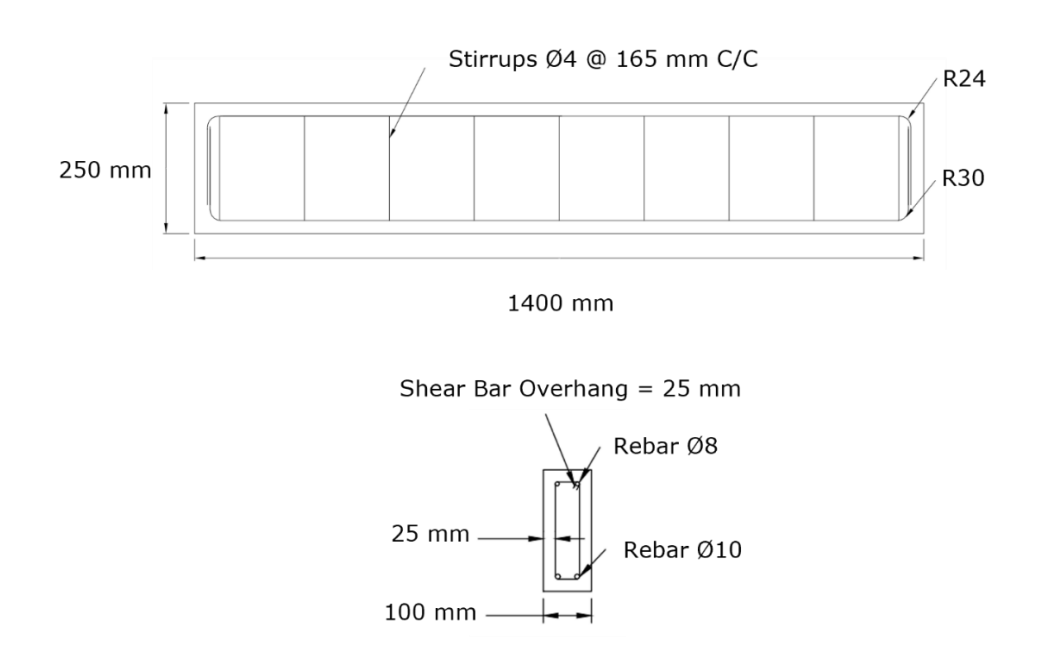


Figure 4.9: Short-span RC beam definition

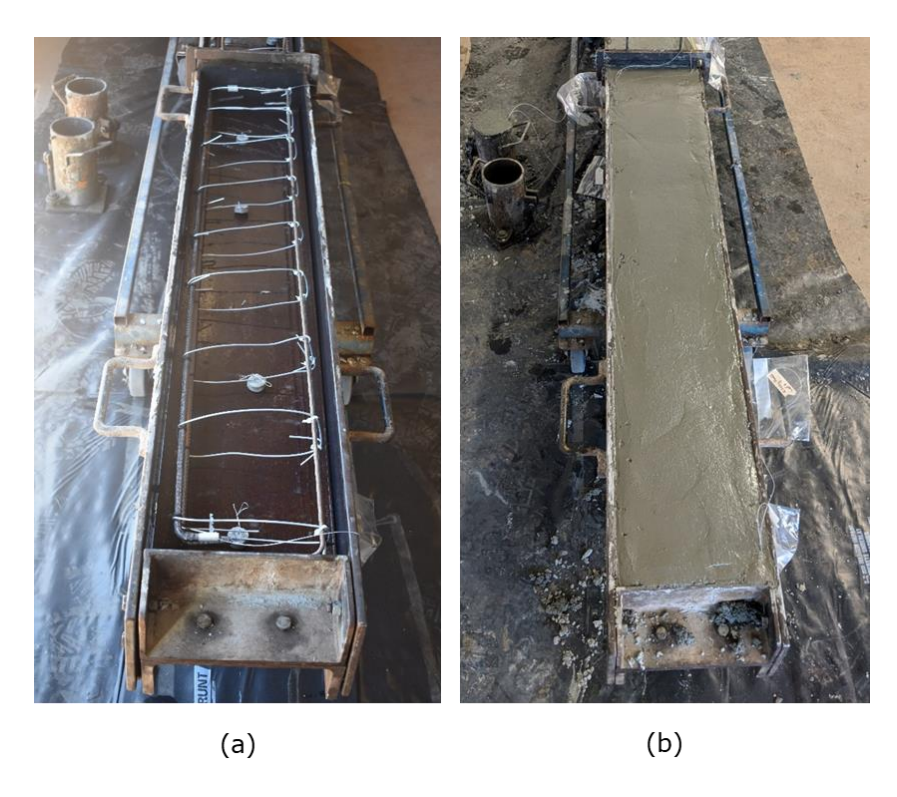


Figure 4.10: (a) Reinforcement cage inside the mould; (b) Cast concrete beam

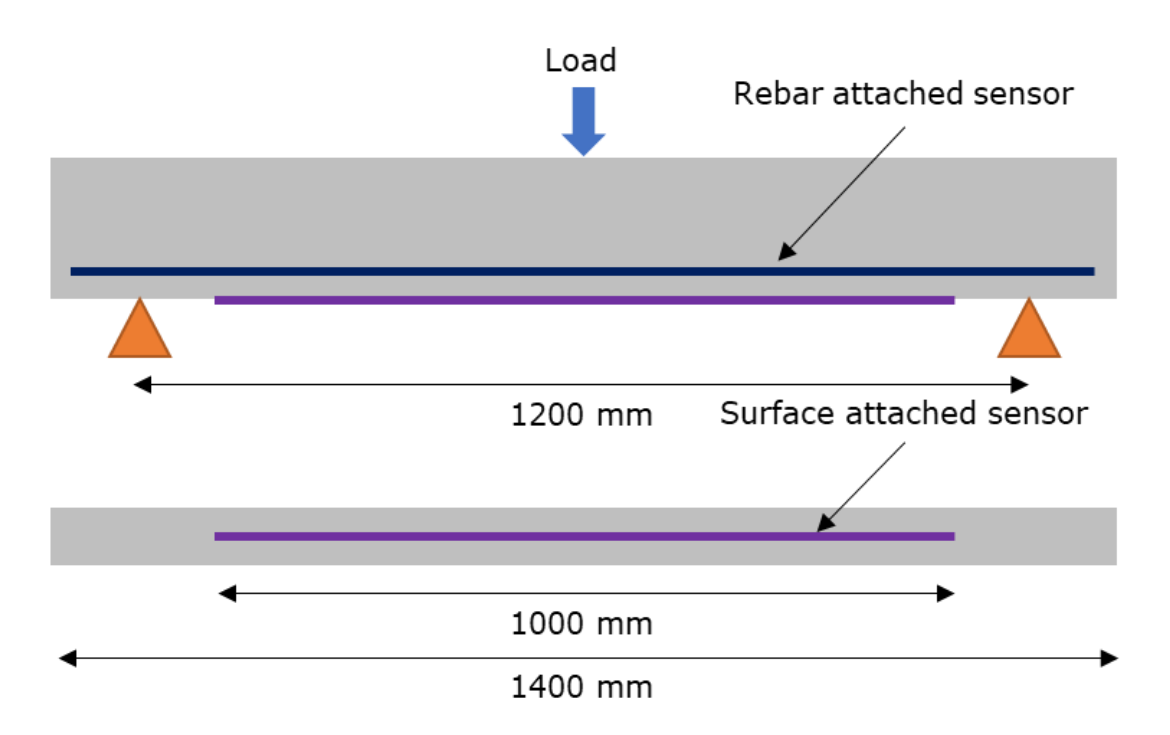


Figure 4.11: Sensor layout for short-span RC beam

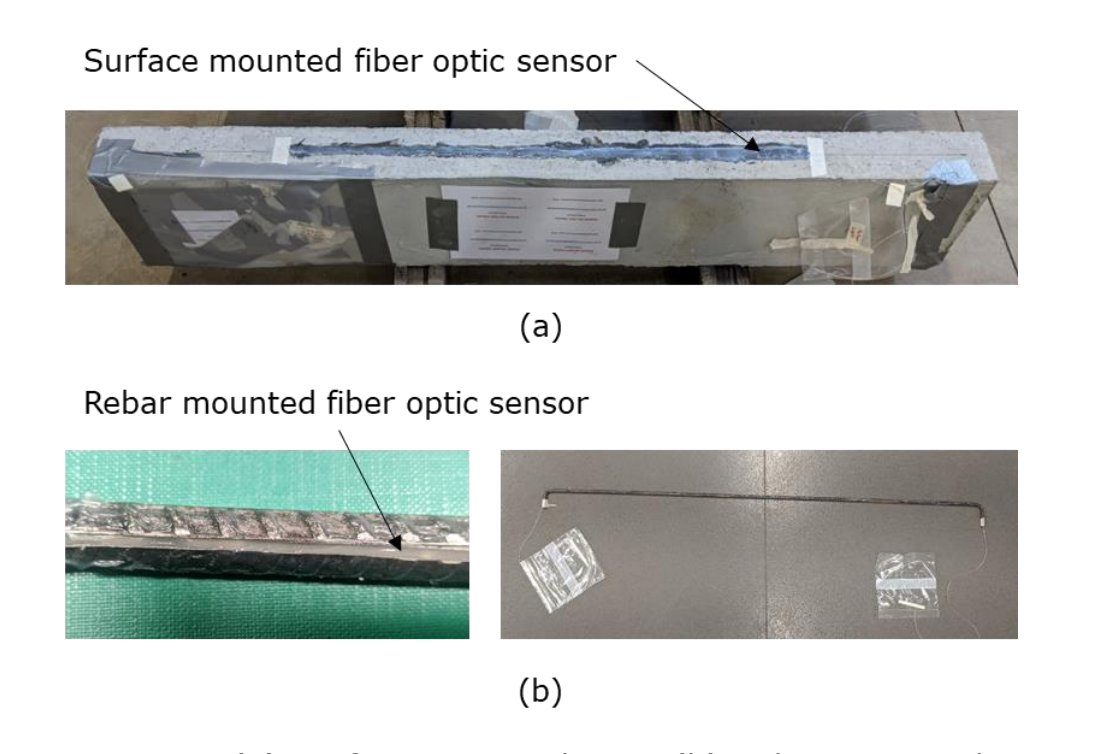


Figure 4.12: (a) Surface-mounted FOS; (b) Rebar-mounted FOS

Casting beam with DOFS sensor in short-span RC beam is illustrated in Figure 4.10, while Figure 4.11 displays the layout of sensors used for monitoring the beam. Figure 4.12 depicts both surface-mounted and rebar-

mounted FOSs installed on short-span RC beam. The mounted sensor length of the bottom sensor was limited to 1000 mm due to the ease of handling. The beams were tested using an MTS Sans Testing Machine with a 2000 kN capacity. The beam was subjected to a three-point bending arrangement and was simply supported. The loading span of the beams was 1200 mm, and they were loaded midway along the middle centreline. The beam was designated as B1 and loaded up to 16.0 kN.

The experiment aimed not to strain the rebar plastically but to examine the strain patterns below the beam's design load. As a result, applied load levels below the design load limit were selected. The crosshead movement rate on the testing apparatus was adjusted at 1 mm per minute, and 15-second intervals helped to space the measurements evenly. The test was stopped at 75 seconds (at 16 kN load). Figure 4.13 illustrates the testing procedure for the beam, conducted using the MTS sans testing machine.

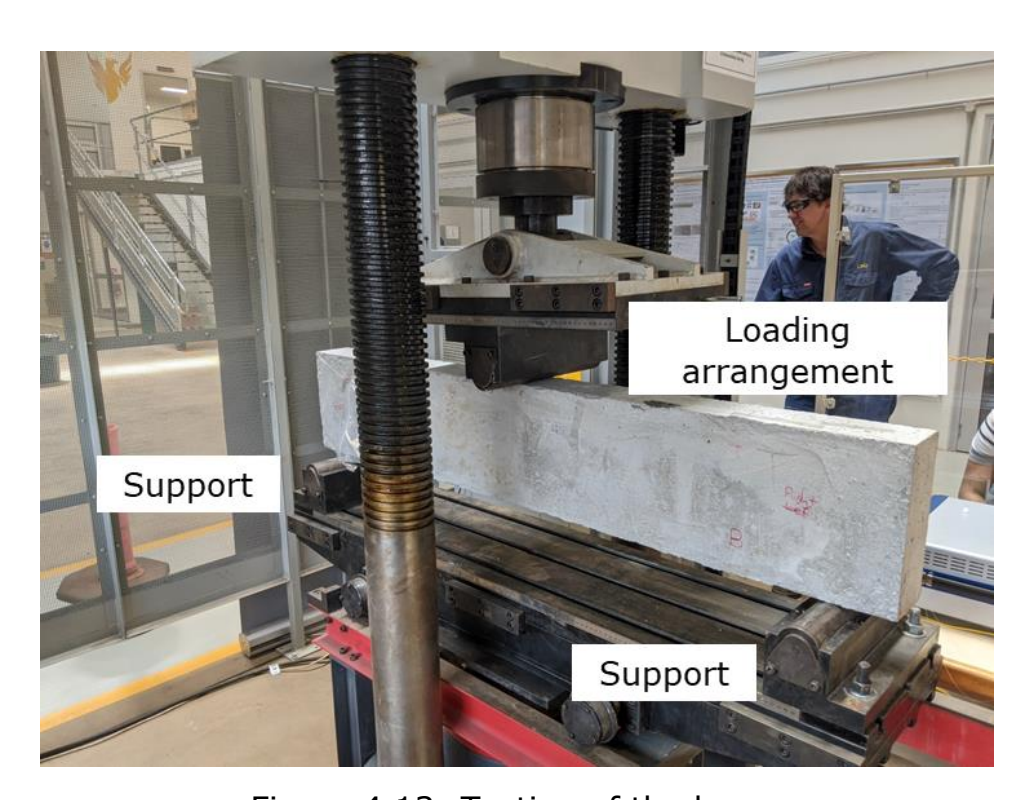


Figure 4.13: Testing of the beam

# 4.4.2. Long-span RC beams

After successfully completing the testing of short-span RC beams and FEA validation, it was concluded that DOFS measurements provide acceptable results and are suitable for monitoring concrete beams under flexural loading (Chapter 5 provides details). Moreover, the recorded experimental data were inserted into the developed DL model, and the model could predict the tension rebar status correctly. Therefore, the second series of experimental sessions commenced studying long-span beam sizes to represent real world structures.

Three RC beams were cast and instrumented with distributed FOSs to extract strain data along the concrete bottom surface, side surface, and rebars under symmetric flexural loading.

The beams were cast according to the beam definition shown in Figure 4.14. Each beam was 4000 mm long, 200 mm wide, and 400 mm high. A 12 mm rebar was selected for every beam for the compression side, and rebars of 12 mm, 16 mm, and 20 mm reinforced the tension side. Table 4.4 provides the beam description.

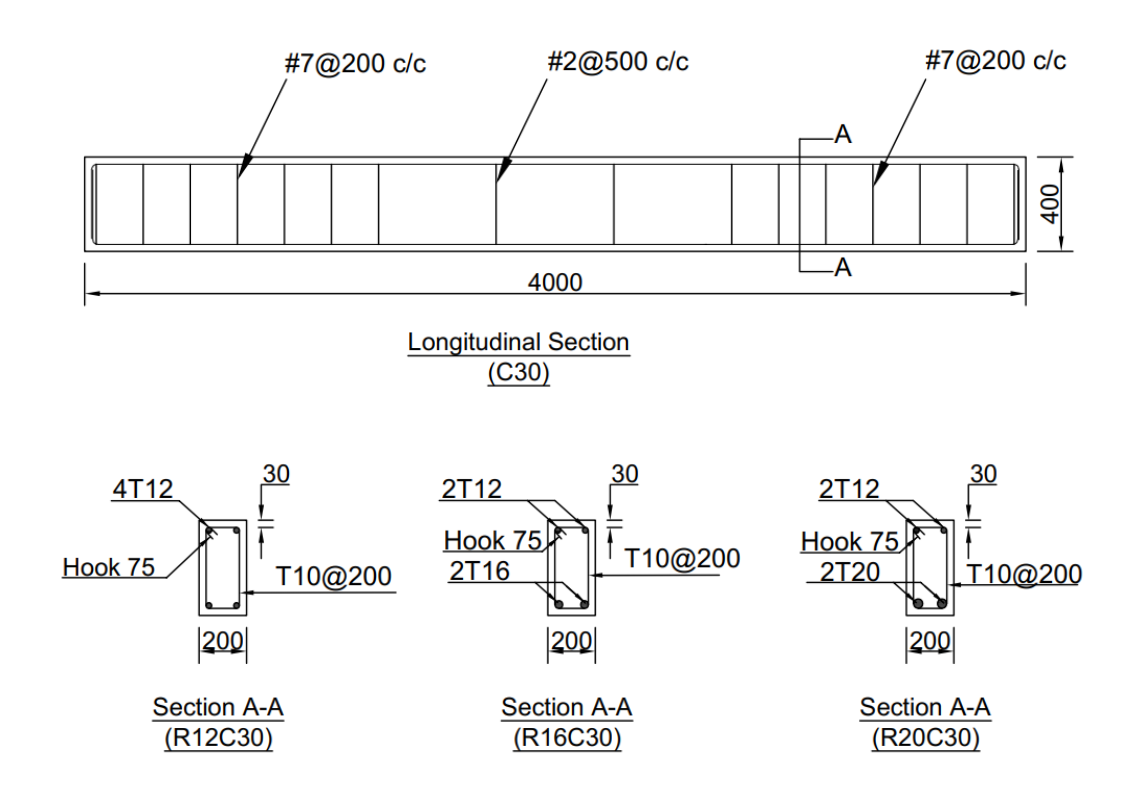


Figure 4.14: Beam definitions of R12C30, R16C30, and R20C30

Table 4.4: Beam description for R12C30, R16C30, and R20C30

Beam	Concrete	Tension	Compression	<b>Bottom cover</b>
	grade	rebar size	rebar size	thickness
		(mm)	(mm)	(mm)
R12C30		12		
R16C30	25	16	12	30
R20C30		20		

All beams were maintained with a 30 mm concrete cover. The beams were cast using a grade 25 concrete mix and kept wet for seven days. The experimental value of the concrete's mean cylinder compressive strength was 29.9 MPa. The RC beams were designated according to the tension rebar sizes used as R12C30, R16C30, and R20C30. The beam design followed the European Community standard EN 1992-1-1: Eurocode 2: Design of concrete structures. Figure 4.15 shows the casting process of the beams.





(5)

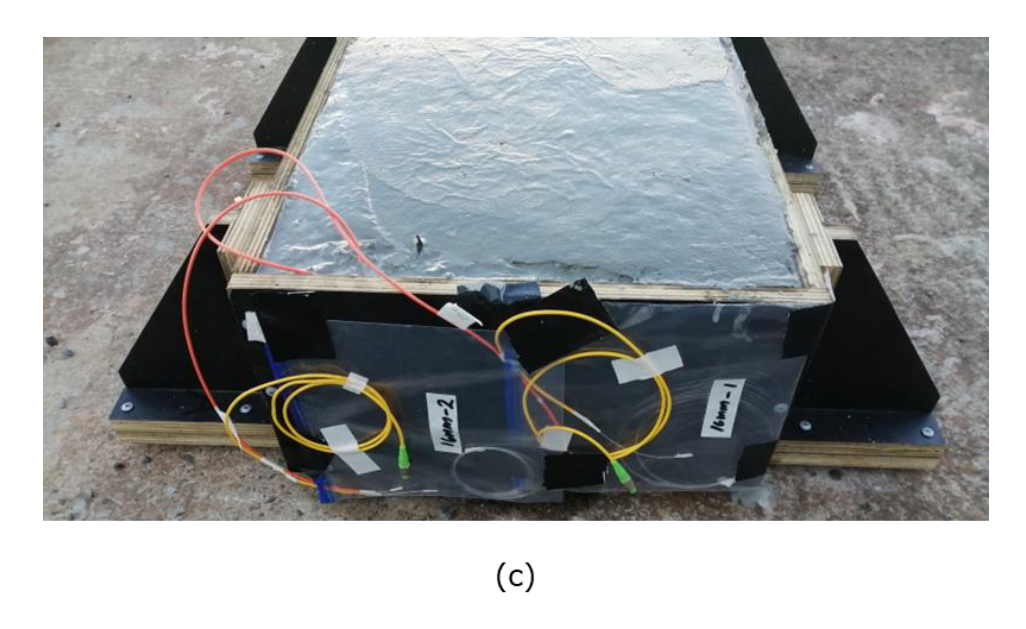


Figure 4.15: (a) Reinforcement cage; (b) Reinforcement cage inside the mould; (c) Casted concrete beam

Two concrete surface sensors, a side sensor, and a bottom sensor, were selected to analyse the sensor behaviour according to different paths. Due to the need for room for handling and transporting the beams, the length of both surface sensors was capped at 3000 mm. Figure 4.16 displays the sensor arrangement.

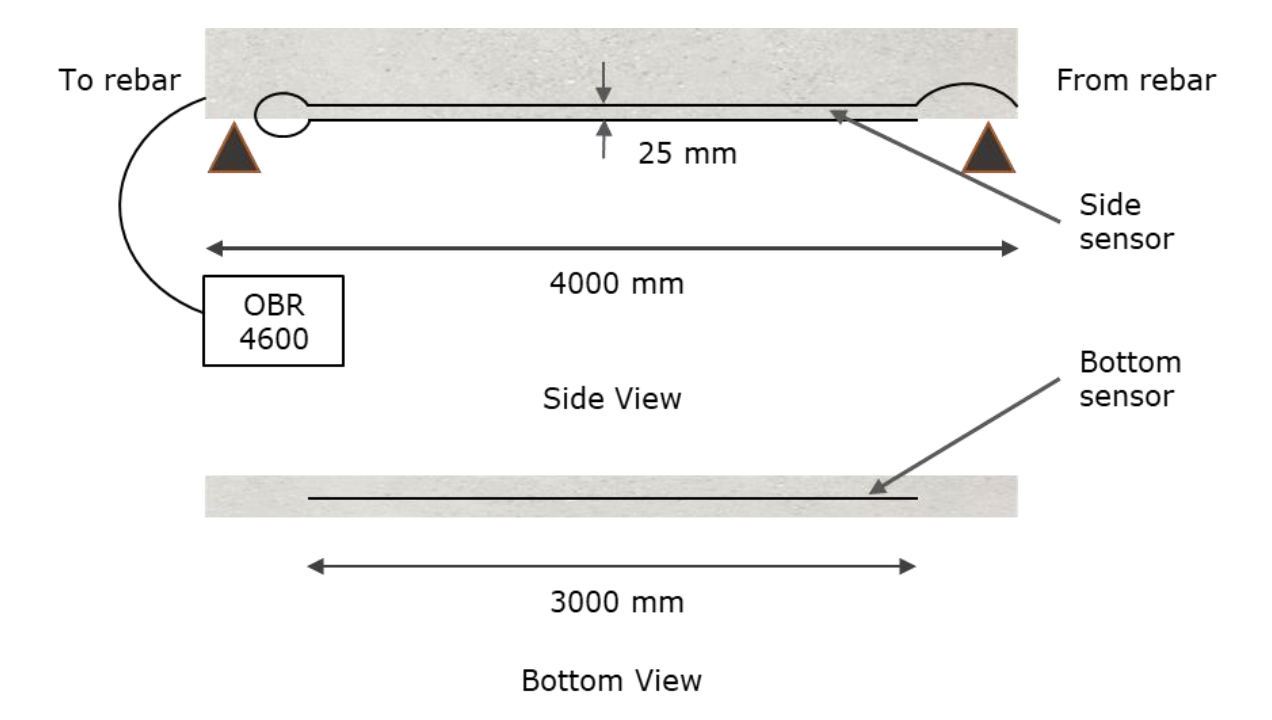


Figure 4.16: Sensor Layout

Before embedding sensors into the concrete beam, all DOFS-attached rebars (R12, R16, and R20) were tested under three-point loads to ensure their functionality and repeatability. Figure 4.17 presents the schematic configuration of rebar testing, while Figure 4.18 demonstrates the experimental setup for rebar testing. It was decided to use three weights to distribute the load across the rebar at the centre position. The weights were specified as 1.1 pounds, 2.5 pounds, and 5 pounds, respectively. Each weight was loaded and unloaded three consecutive times to each rebar.

Figure 4.19, Figure 4.20, and Figure 4.21 show the strain variation along the rebars R12, R16 and R20, respectively, for the loadings. The figures show no significant variation in strain for a particular load. The results indicated that all rebars had excellent functionality and repeatability. Therefore, these DOFS-attached rebars were good to embed inside the concrete.

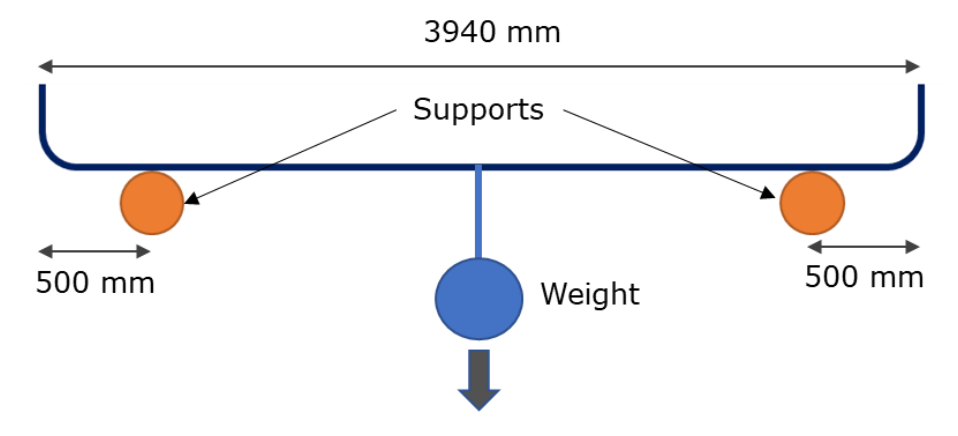


Figure 4.17: Configuration for rebar testing

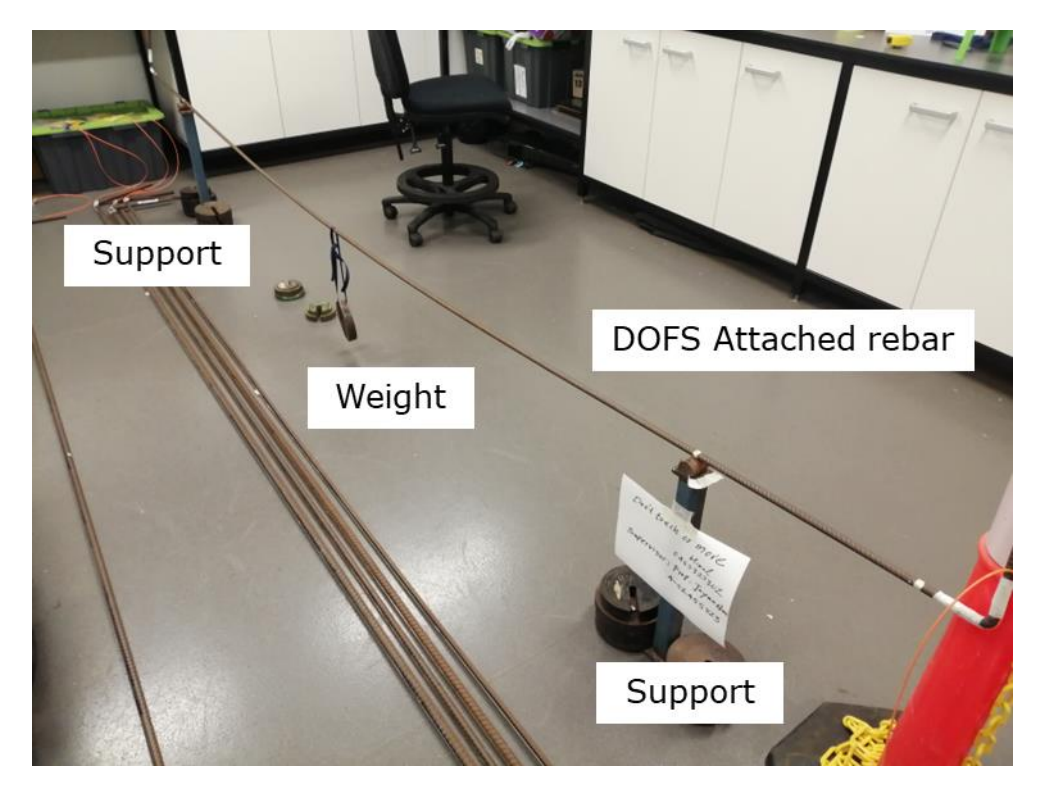


Figure 4.18: Experimental setup of rebar testing

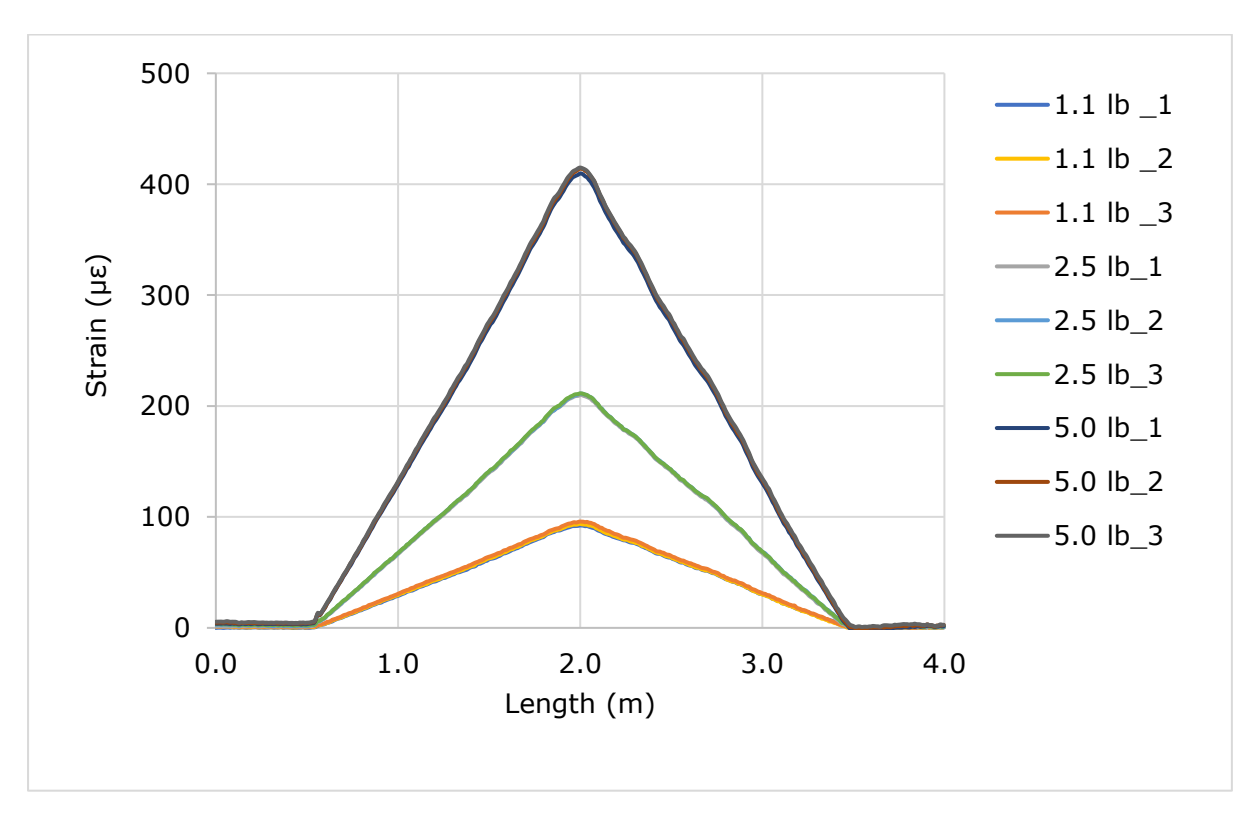


Figure 4.19: Strain variation along the rebar R12

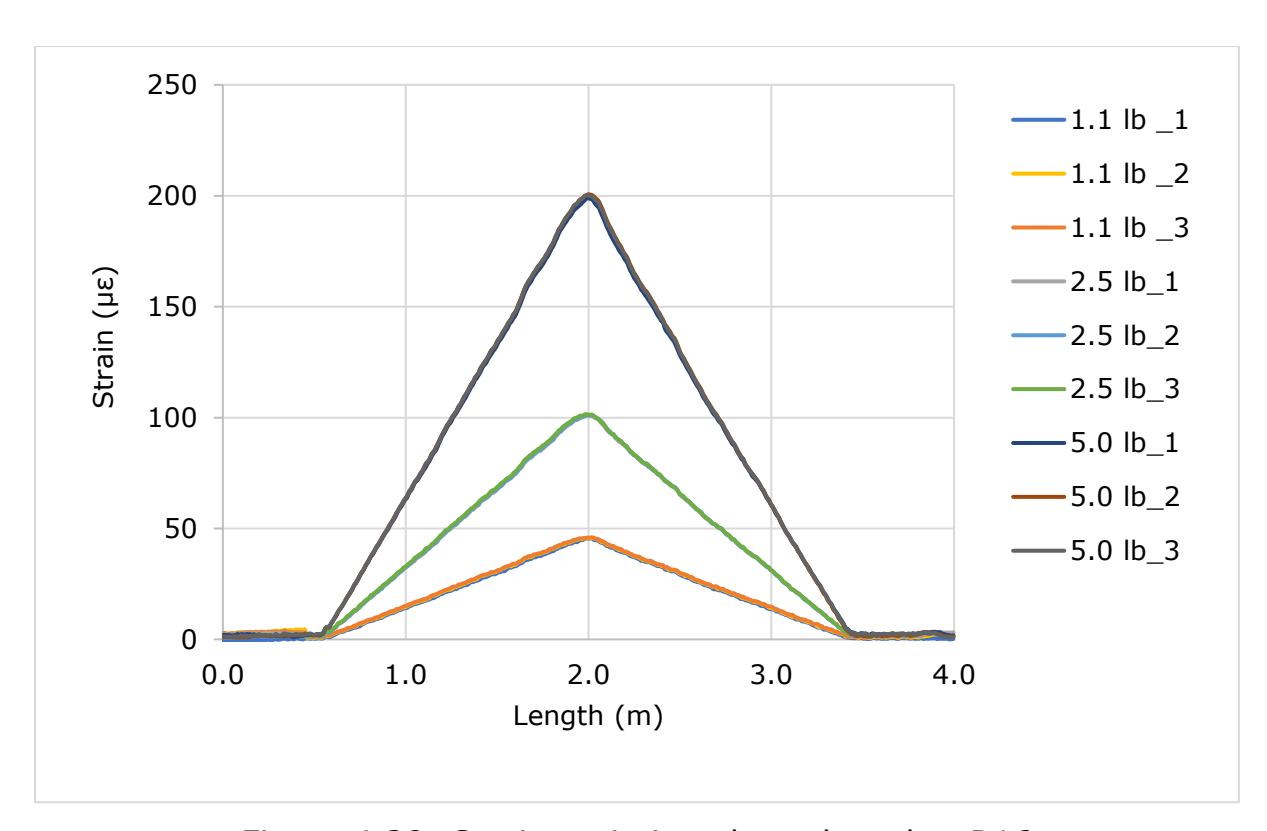


Figure 4.20: Strain variation along the rebar R16

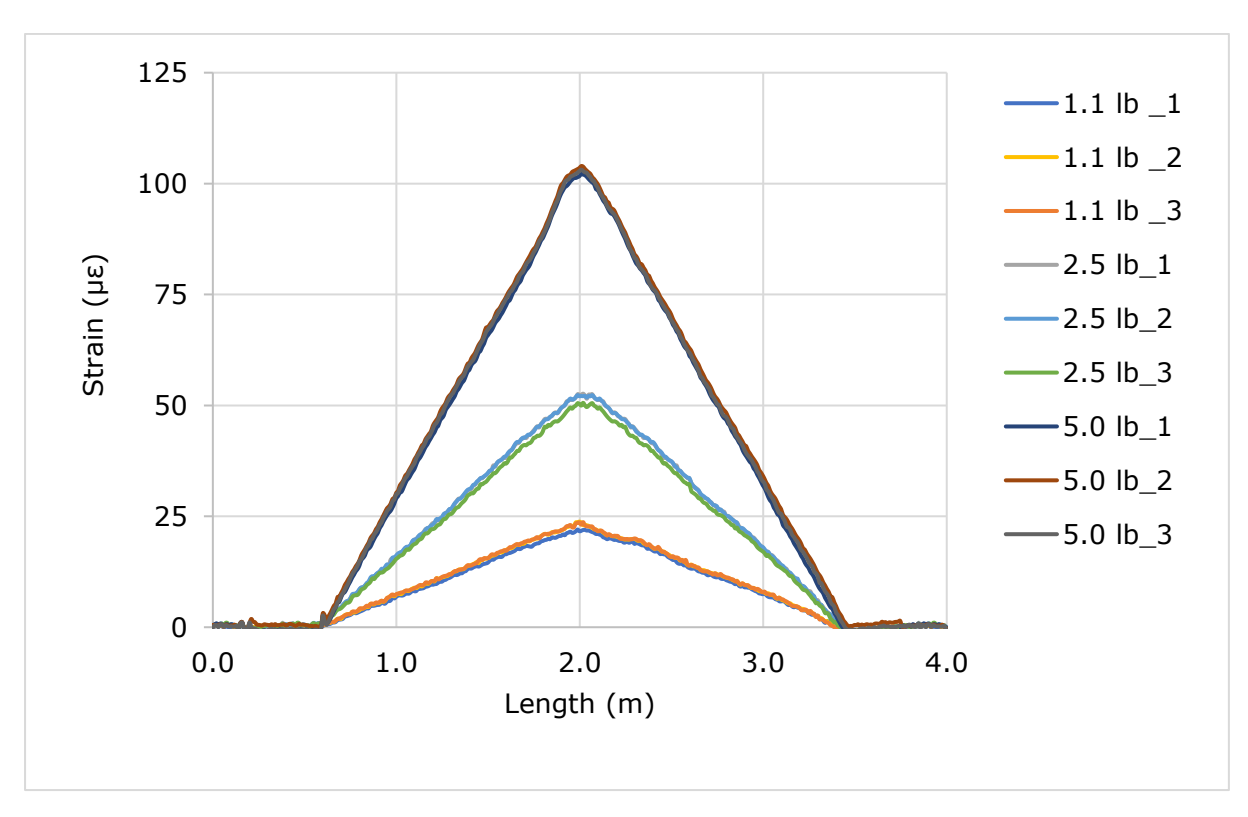


Figure 4.21: Strain variation along the rebar R20

The DOFS were attached to the concrete surface after 28 days of curing period after the casting. Figure 4.22 shows the mounted surface sensors on the side and the bottom.

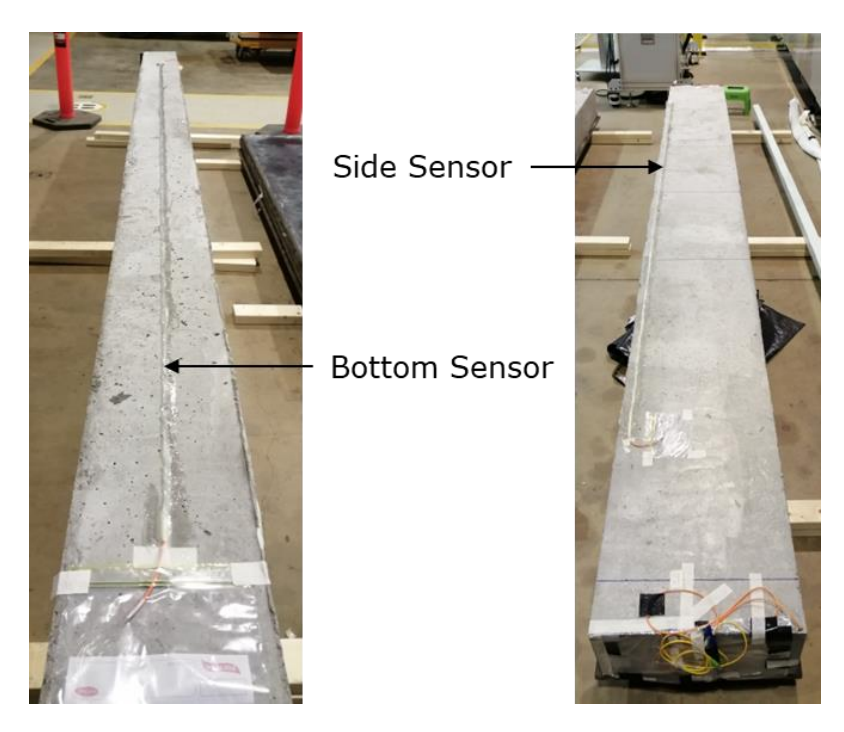


Figure 4.22: Mounted surface sensors

A hydraulically operated load frame with a 50 ton capacity was used for testing the beams. All beams were simply supported, and a four-point bending system was utilised for the loading. The beam's span was 3800 mm. Figure 4.23 displays the schematic diagram of the loading arrangement, and Figure 4.24 illustrates the experimental beam loading arrangement.

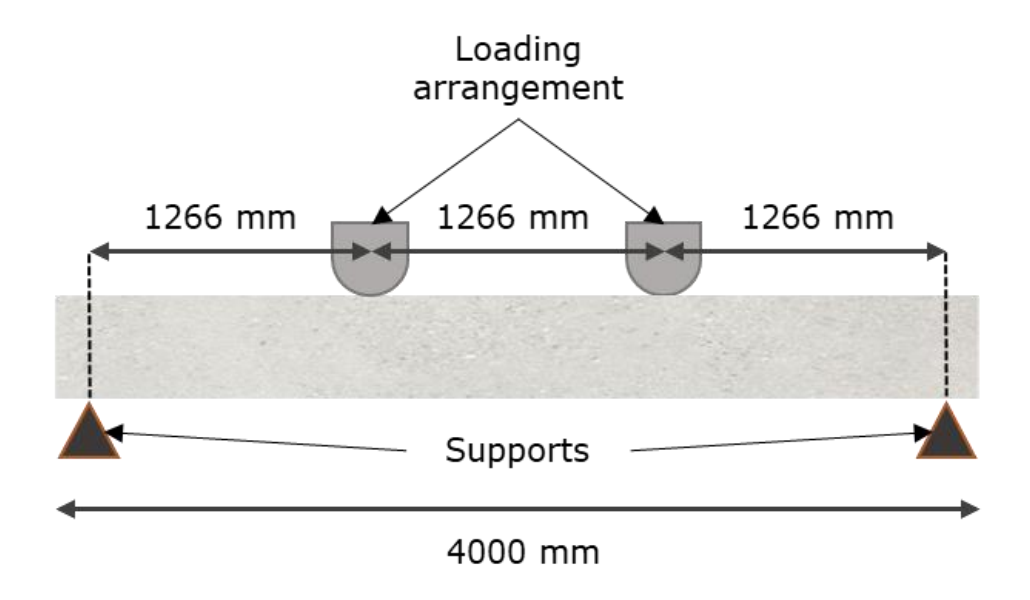


Figure 4.23: Schematic diagram of loading arrangement

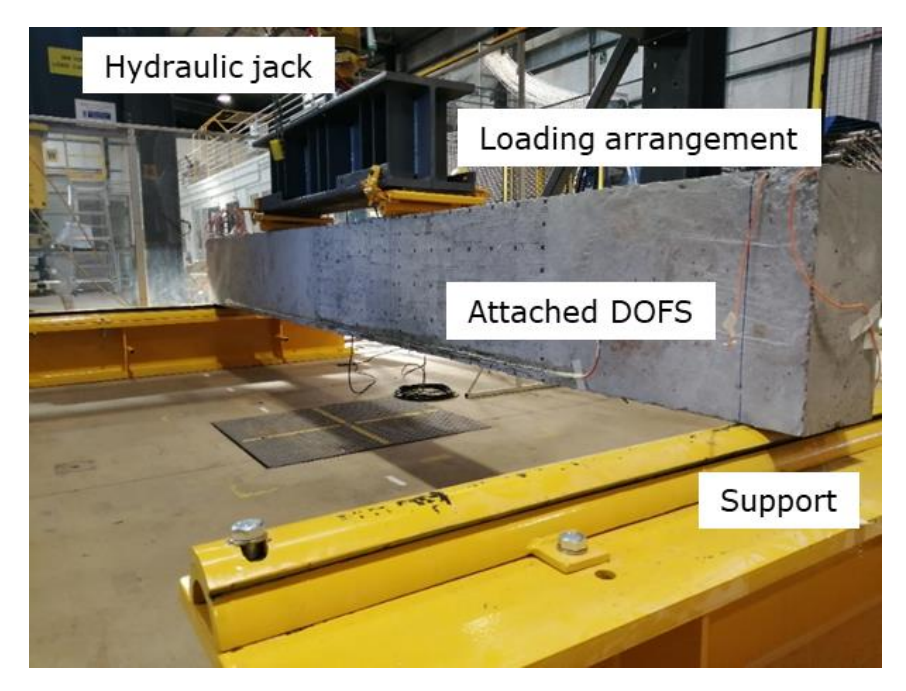


Figure 4.24: The experimental beam loading arrangement

R20C30 was the first beam to be tested since this beam attracts the highest bending moment. Hence, the same beam will have the highest shear demand in the current set of beams. The beam was loaded at 10 kN intervals until failure occurred, and the OBR 4600 recorded strain readings. The beam failed at 160 kN. Figure 4.25 shows the connected OBR 4600 with the beam.

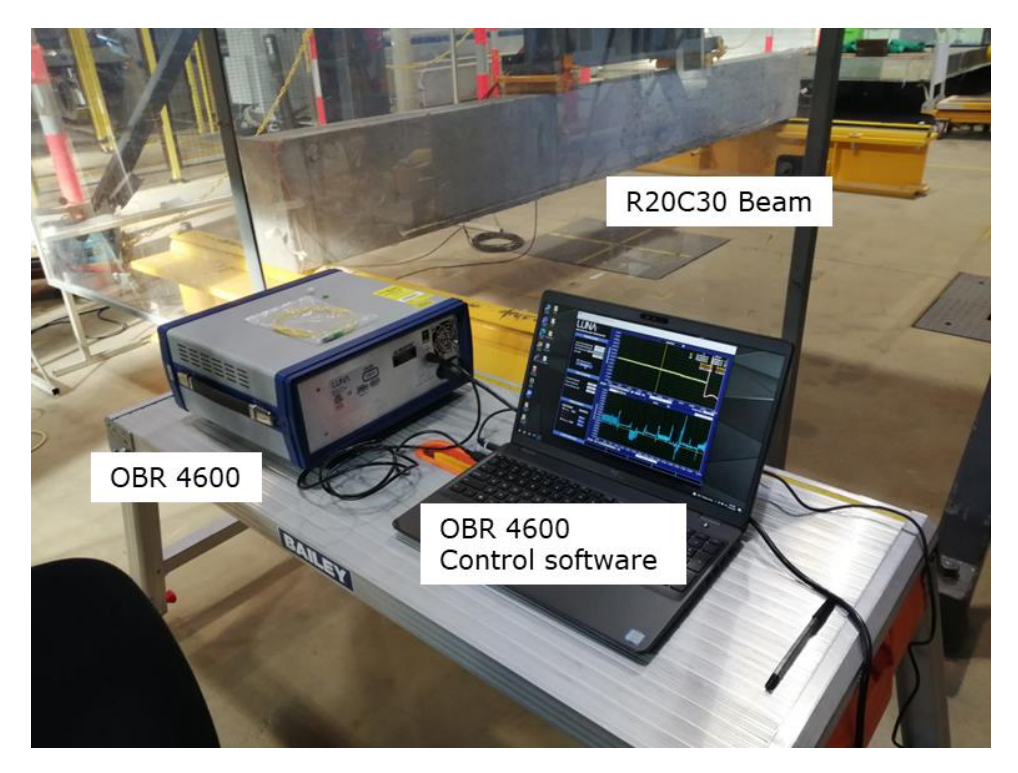


Figure 4.25: The connected OBR 4600 with the beam

R16C30 was the next beam to test. However, here the beam was not loaded until failure by incremental loading at once since understanding the DOFS behaviour under repetitive loading was necessary. The beam was loaded in four stages to gather strain data. The objective of this type of loading was to extract the strain data to analyse how well the DL model performed when these data were given as input.

The beam was loaded up to 25 kN in 5 kN intervals in the first stage. After obtaining data, the beam was unloaded and relaxed for 10 minutes. The purpose of relaxation time was to reduce the impact of any residual strains. The first stage was repeated in the second stage. In the third stage, the beam was loaded up to 50 kN in 5 kN intervals. After reaching the 50 kN limit, the beam was unloaded and relaxed for 10 minutes. As per the final stage, the beam was loaded until failure occurred, and the load at failure was 120 kN.

The R12C30 beam followed the same testing procedure as the R16C30 beam. However, the initial loading limit was reduced to 15 kN in 5 kN intervals since this beam attracts the lowest bending moment. Next, the

beam was unloaded and relaxed for 10 minutes. As per the second stage, the beam was loaded up to 15 kN again, and data were recorded. In the third stage, the beam was loaded up to 30 kN in 5 kN intervals by multiplying the initial load limit twice. After reaching the 30 kN limit, the beam was unloaded and relaxed for 10 minutes. As per the final stage, the beam was loaded until failure occurred; the load at failure was 80 kN. After successfully completing the second experimental session, the results indicated that DOFS measurements provide acceptable results in monitoring concrete beams under symmetric flexural loading (Chapter 5 provides further details).

To enhance the robustness of the DL model, the DL model must produce accurate results when strain data are entered from asymmetric loading conditions. Therefore, it is necessary to study asymmetric flexural loading conditions. The third series of experimental sessions thus commenced.

Three RC beams were cast using varying concrete grades and bottom cover thicknesses to enhance diversity. The same reinforcement arrangement was used, and the beams were instrumented with distributed FOSs, like the experimental session two, to extract strain data.

Figure 4.26 shows the beam definition. The concrete cover thickness and concrete grade were set to 60 mm and grade 50, respectively. The experimental value of the concrete's mean cylinder compressive strength was 58.5 MPa. The RC beams were designated according to the tension rebar sizes used as R12C60, R16C60, and R20C60.

Table 4.5 lists the description for R12C60, R16C60, and R20C60 beams. The beam design followed the European Community standard EN 1992-1-1: Eurocode 2: Design of concrete structures.

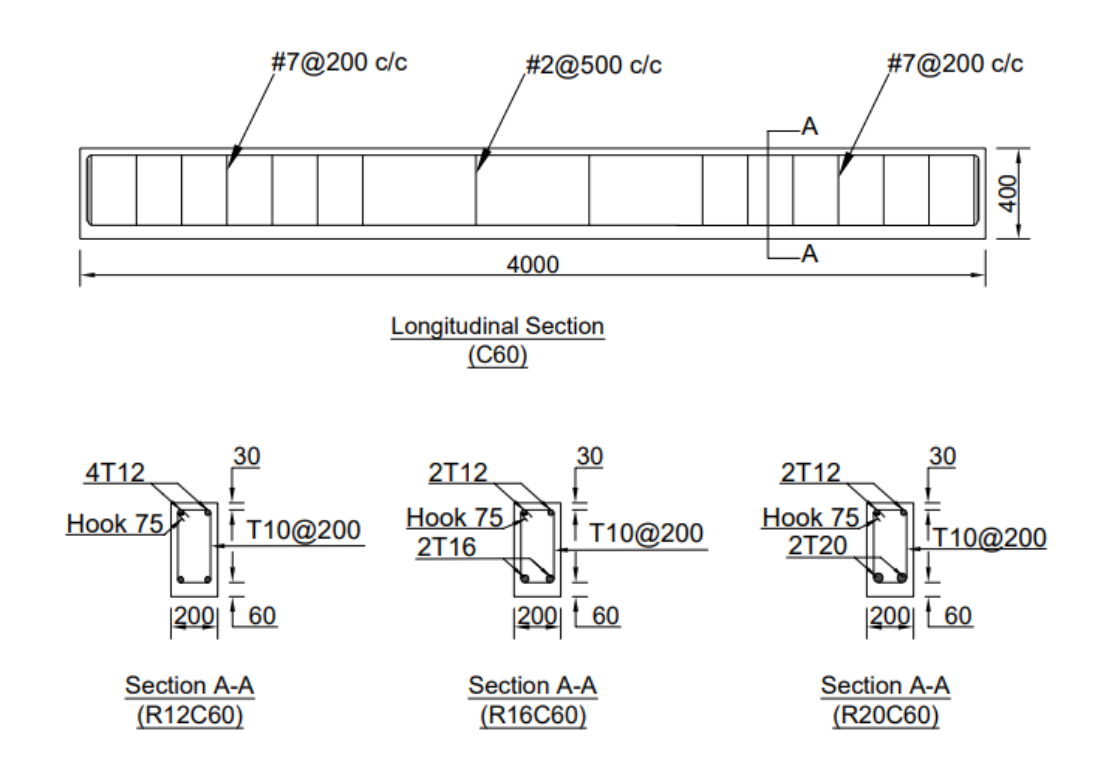


Figure 4.26: Beam definition of R12C60, R16C60, and R20C60

Table 4.5: Beam description for R12C60, R16C60, and R20C60

Beam	Concrete	Tension rebar	Compression	<b>Bottom cover</b>	
	grade	size (mm)	rebar size	thickness	
			(mm)	(mm)	
R12C30		12			
R16C30	50	16	12	60	
R20C30		20			

Figure 4.27 presents the proposed schematic diagrams for loading configurations. The first beam examined was R20C60, tested with loading configuration (a). The loading configuration (b) was used for R12C60 and R16C60 beams. All beams were loaded at 5 kN intervals until the spectral shift quality (SSQ) slightly exceeded the 0.15 limit (Chapter 5 will discuss further details).

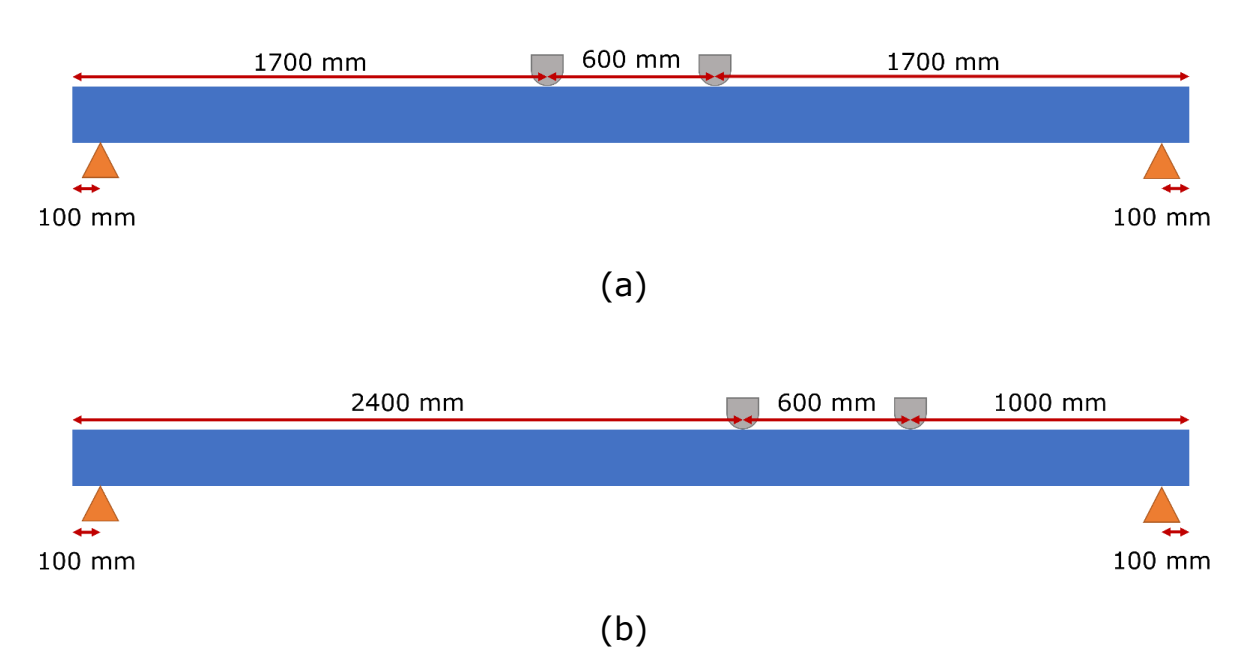


Figure 4.27: The proposed schematic diagrams for loading configurations

#### 4.5. Summary

This chapter examines the meticulous process of establishing distributed sensor networks using DOFS and the methodical approach to derive strain data from RC beams subjected to flexural loading in various configurations. These configurations consist of three-point and four-point bending for symmetric and asymmetric loading regimes. The process contributes directly to the overarching framework designed to create a robust SHM system.

The optical fibre SMF-28 serves as the DOFS and is used to measure strain. DOFS are attached to the rebars using a 1:1 mixture of TECHNIGLUE R15 and H15S. DOFS are affixed to the concrete surface using a 2:1 mixture of TECHNIGLUE R60 and H60S. The strain is monitored using a LUNA OBR 4600. The testing sessions maintain a spatial resolution of 1 cm, with a sensor length of 2.5 cm and a sensor spacing of 1 cm. This was maintained using OBR4600.

During the first experimental session, a single short-span RC beam is cast and instrumented with DOFS to collect strain data. After successful initial tests, it was determined that DOFS measurements yield acceptable results, making them suitable for monitoring concrete beams subjected to

flexural loading. Next, the collected data were evaluated using the DL model.

In a second series of experimental tests, larger beams were subjected to symmetric and asymmetric flexural loads. Variations in concrete grade and bottom cover thickness are incorporated to ensure the DL model's robustness and the SHM framework's efficacy in various structural scenarios.

All experimental results are presented in the subsequent chapter, with a detailed discussion of collected strain data and its analysis. This information helps evaluate the predictive capabilities of the DL model in the context of structural health. Consequently, this chapter contributes to the larger objective of developing a comprehensive and efficient SHM system.

# CHAPTER 5: PERFORMANCE EVALUATION OF SHM FRAMEWORK

#### 5.1. Introduction

This chapter investigates the efficacy of the DL model for predicting the structural health of RC beams which can assist with the inspection and maintenance of civil infrastructures. The chapter will present the study's experimental and simulation results, the training procedure for the DL model, and the structural health predictions for concrete beams subjected to symmetric and asymmetric flexural loading. Figure 5.1 illustrates the overview of the technical contents of Chapter 5.

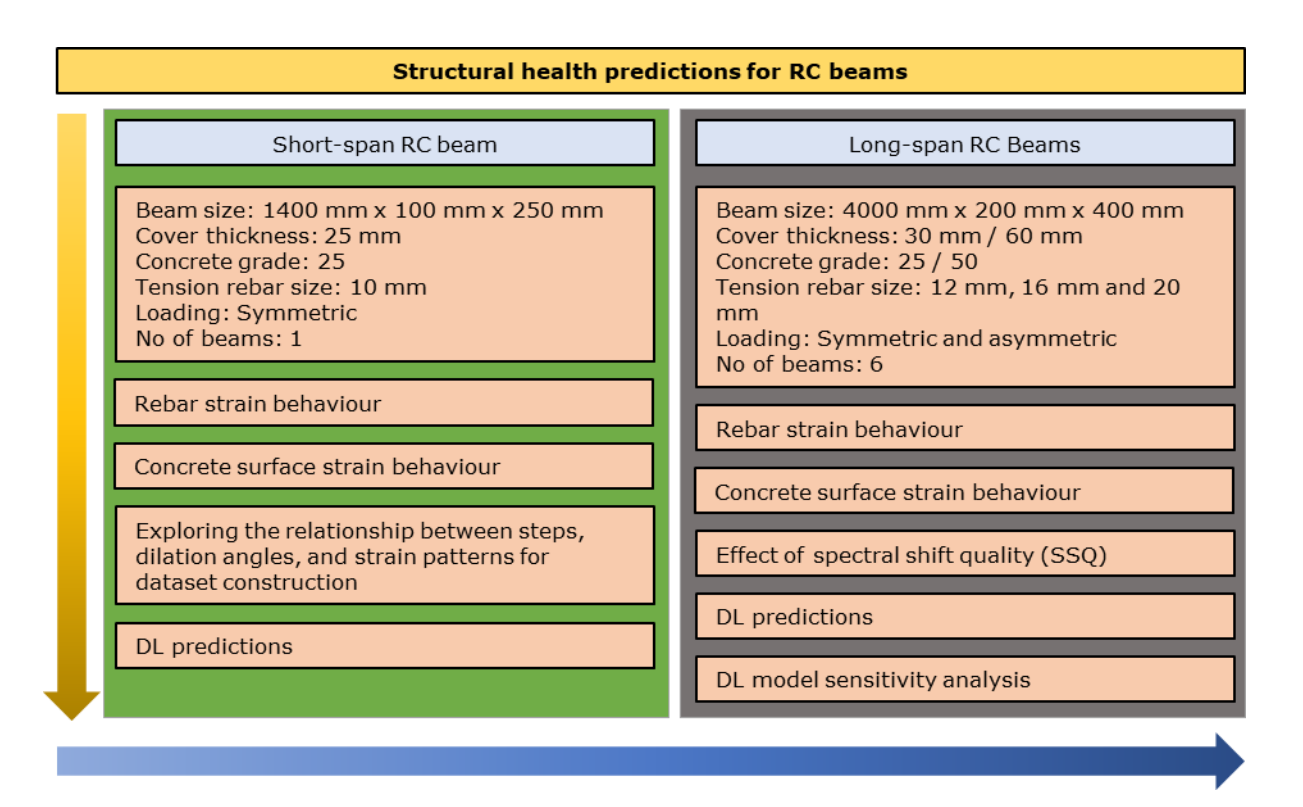


Figure 5.1: Overview of the technical contents of Chapter 5

The experimental data used in this analysis include strain data collected from concrete beams subjected to flexural loading using distributed fibre optic sensing as described in Chapter 4. Simulation data described in Chapter 3 were validated for the training DL model. The collected strain data behaviour was studied, and features representing the

structural health of the concrete beams were extracted. The trained DL model helped predict the structural health of seven concrete beams, which were compared with the actual structural health of the beams. The model accuracy was evaluated.

### 5.2. Comparison of experimental and simulation results for shortspan RC beam

This section presents a study on the strain patterns for a short-span RC concrete beam of size 1400 mm x 100 mm x 250 mm subjected to three-point bending under flexural loading. The experimental and simulation strain data were analysed to identify the strain behaviour of the concrete surface and the rebar of beam B1. The study focused on evaluating the capacity of DOFS to provide precise and valuable quantitative information on the strain experienced by RC elements under flexural loading. Additionally, the study aimed to pinpoint the areas where the highest strain values occurred and analyse the corresponding patterns of strain distribution, as elaborated in this section.

#### 5.2.1. Rebar and surface strain

The strain data obtained from the DOFSs attached to the rebar were examined with the strain values predicted by the simulations for beam B1. Figure 5.2 compares the experimental and simulated strain measurements for the bottom rebar of beam B1.

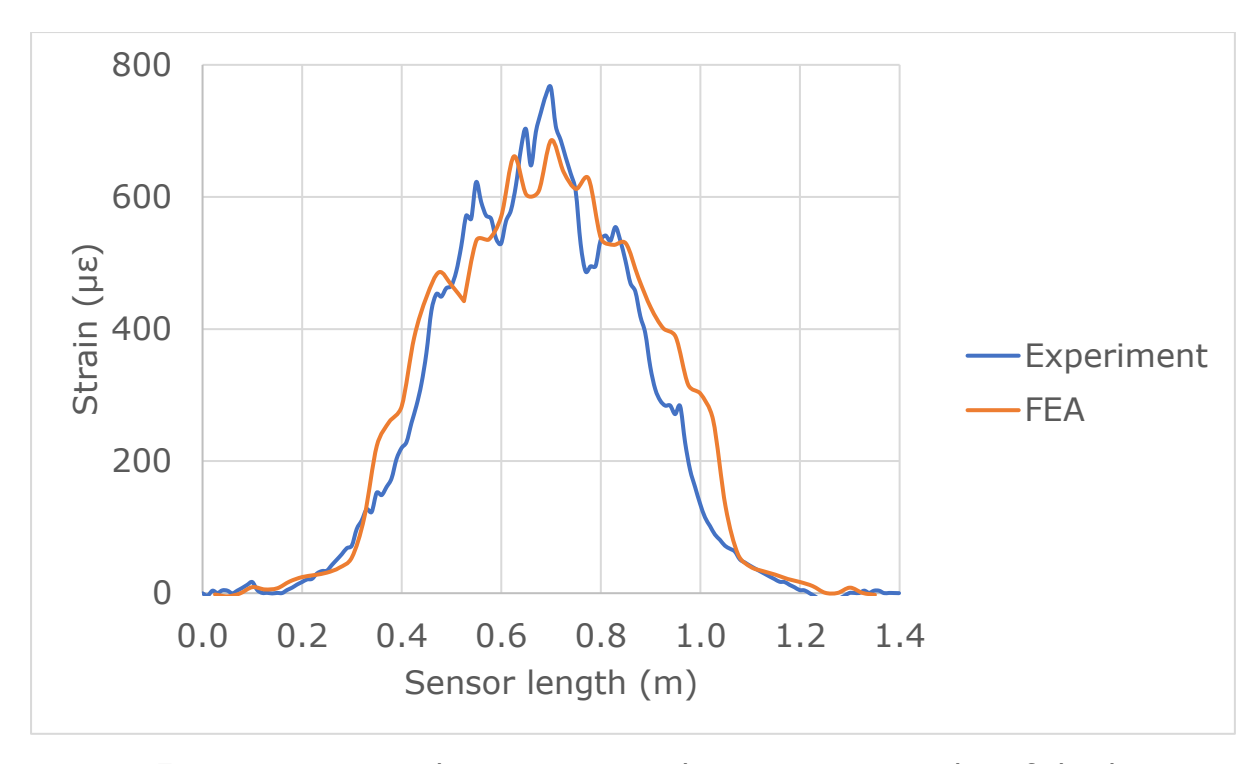


Figure 5.2: Experimental strain vs simulation strain results of the bottom rebar of the beam B1 at 16 kN load

Figure 5.2 depicts the highest experimental peak strain at mid-span as 766  $\mu\epsilon$ , while the simulated peak strain is 686  $\mu\epsilon$ . The experimental and simulation strain patterns show good alignment with each other. The higher experimental peak strains were due to the concrete surface cracking, which passes through the rebars. The strain pattern satisfactorily correlated with optical fibre strain measurements and FEA results.

Since the maximum rebar strain values recorded for both experiments were significantly lower than the 2500 micro strain limit, which represents the yielding of steel, the rebars have not undergone plastic deformation and have not reached the yield strain of the steel, even under the maximum applied load of 16 kN. Therefore, the beam is deemed to be in good structural health.

The strain measurements obtained by the concrete surface-mounted OFSs were used to verify the extracted surface strain values from the simulation for beam B1. The experimental strain curve in Figure 5.3 displays eight peak values along the beam length, with the highest peak

strain observed at the mid-span, measuring 1566  $\mu\epsilon$ . In contrast, the simulation strain curve indicates the highest peak value of 1196  $\mu\epsilon$  with eight peak values. Hence the number of peaks for experimental and simulation peaks were equal. All peaks of both curves are located between 0.2 m and 1.2 m along the beam length.

The primary failure modes of concrete are tension cracking and compression crushing (rather unlikely at this stage). Tensile stresses above the tensile strength of concrete lead to cracking, a significant vulnerability of concrete. The presence of rebars helps to limit the extent of these cracks in RC. Cracks provide valuable insights into the extent of damage within concrete structures.

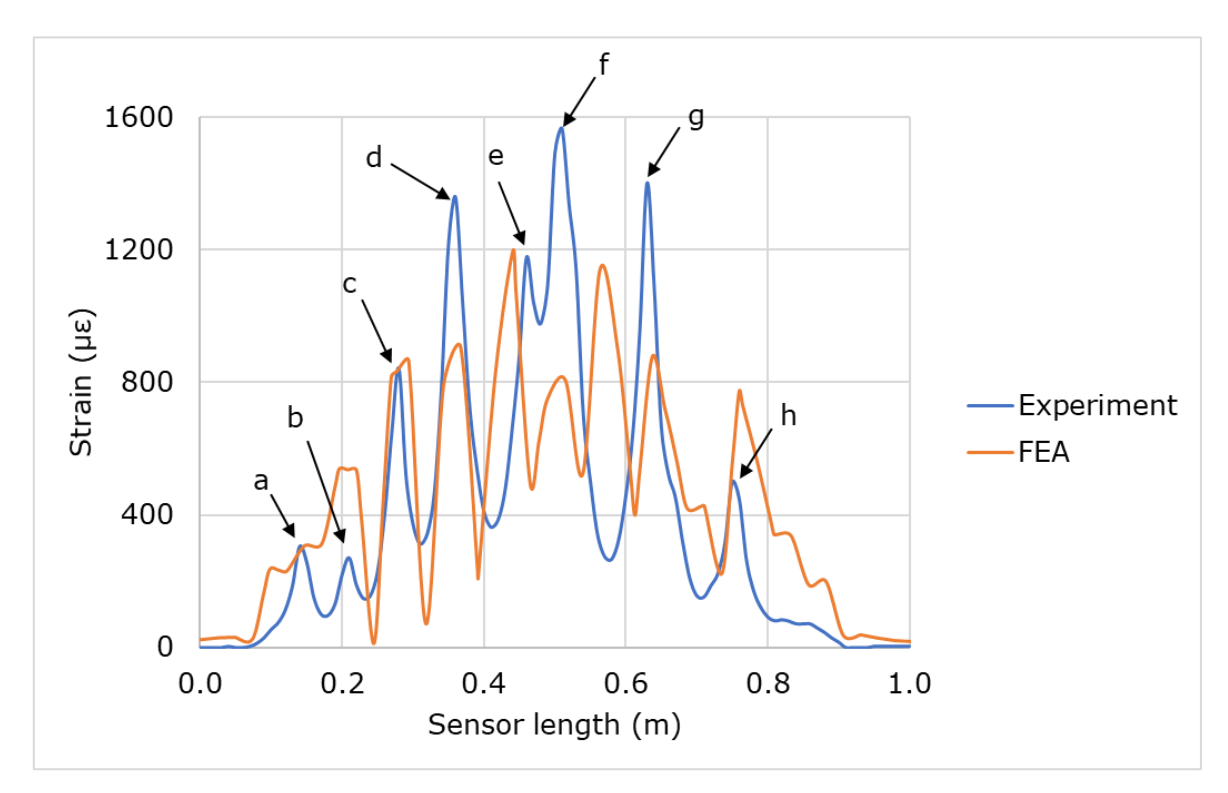


Figure 5.3: Experimental surface strain vs simulation surface strain results of the beam B2 at 16 kN load

Figures 5.3 display the wave behaviour of both experimental and simulated strain data. The appearance of strain spikes usually indicates the development of cracks due to tension, while valleys suggest lower concrete strain. Typically, concrete cracks when the tensile strain surpasses 100  $\mu\epsilon$ 

to 120  $\mu\epsilon$  [254]. There is a significant difference between the experimental and simulated strain values along the beam length. It could be due to possible debonding of the fibre with the concrete surface initiated by hairline cracks. This can cause the fibre to elongate independently, leading to unusually higher strain readings. It is a standard practice to draw the crack patterns manually. Hairline cracks were visible after the experiment, as shown in Figure 5.4, which displays visible hairline cracks on the fibre at the bottom surface of beam B1 under 16 kN load.

Figure 5.5 shows a FOS on a cracked concrete surface. An acceptable agreement was observed between the optical fibre strain readings and the FEA results. Additionally, the experimental results presented in Figure 5.3 agreed well with the locations where hairline cracks were visible, as depicted in Figure 5.4.

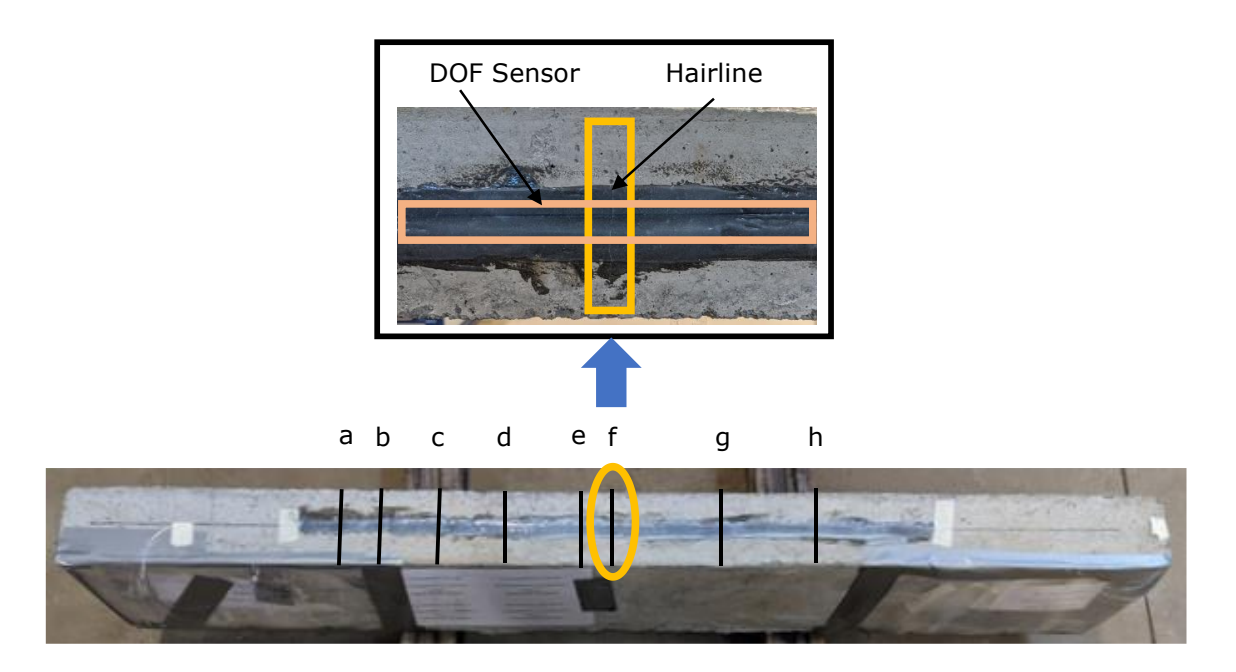


Figure 5.4: Hairline crack locations appeared on the bottom surface of the beams

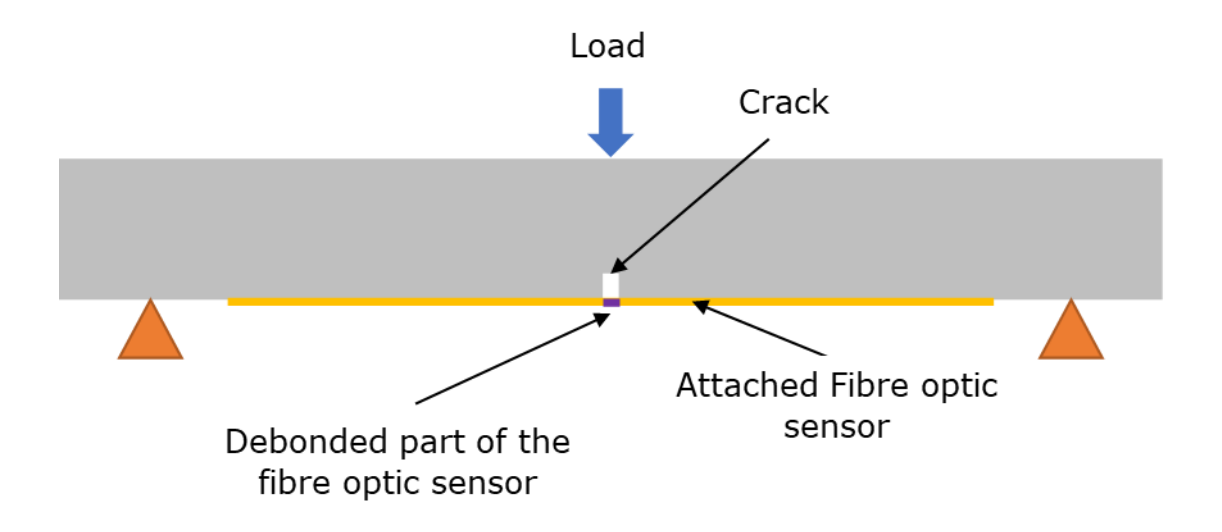


Figure 5.5: FOS in a cracked concrete surface

## 5.2.2. Exploring the relationship between steps, dilation angles, and strain patterns for dataset construction

Distributed strain data obtained from DFOS can be essential for SHM algorithms to make informed judgments about structural integrity. Recently, sophisticated AI techniques such as DL have been used for the same purpose. However, training these DL models requires thousands or even hundreds of thousands of data points, as more data means higher accuracy. Unfortunately, conducting a significant number of data extraction experiments is not feasible in terms of time and cost. However, FEA models can surmount this obstacle because they can extract tens of thousands of distributed data points by simply modifying model parameters such as loading rates, boundary conditions, loading conditions, and loads. In this investigation, a finite element model was created and analysed to extract distributed strain data concerning load variations.

The strain changes resulting from an increase in load were simulated using FEA for the surface and rebar of B1. These simulations were conducted in 20 steps, but for clarity, the strain changes are presented in ten steps in Table 5.1. The dilation angles for B1 were maintained at a constant 42° throughout the simulations. Figures 5.6 and 5.7 depict the strain variations observed in the surface and rebar, respectively.

Table 5.1: Load with respect to step

Step	1	2	3	4	5	6	7	8	9	10
Load (kN)	0.5	2	5.5	8.5	10	10.5	12.5	13.5	14.5	16
Maximum surface strain (με)	3	14	38	61	70	681	735	914	1019	1196
Maximum rebar strain (με)	3	13	34	54	62	499	515	554	630	686

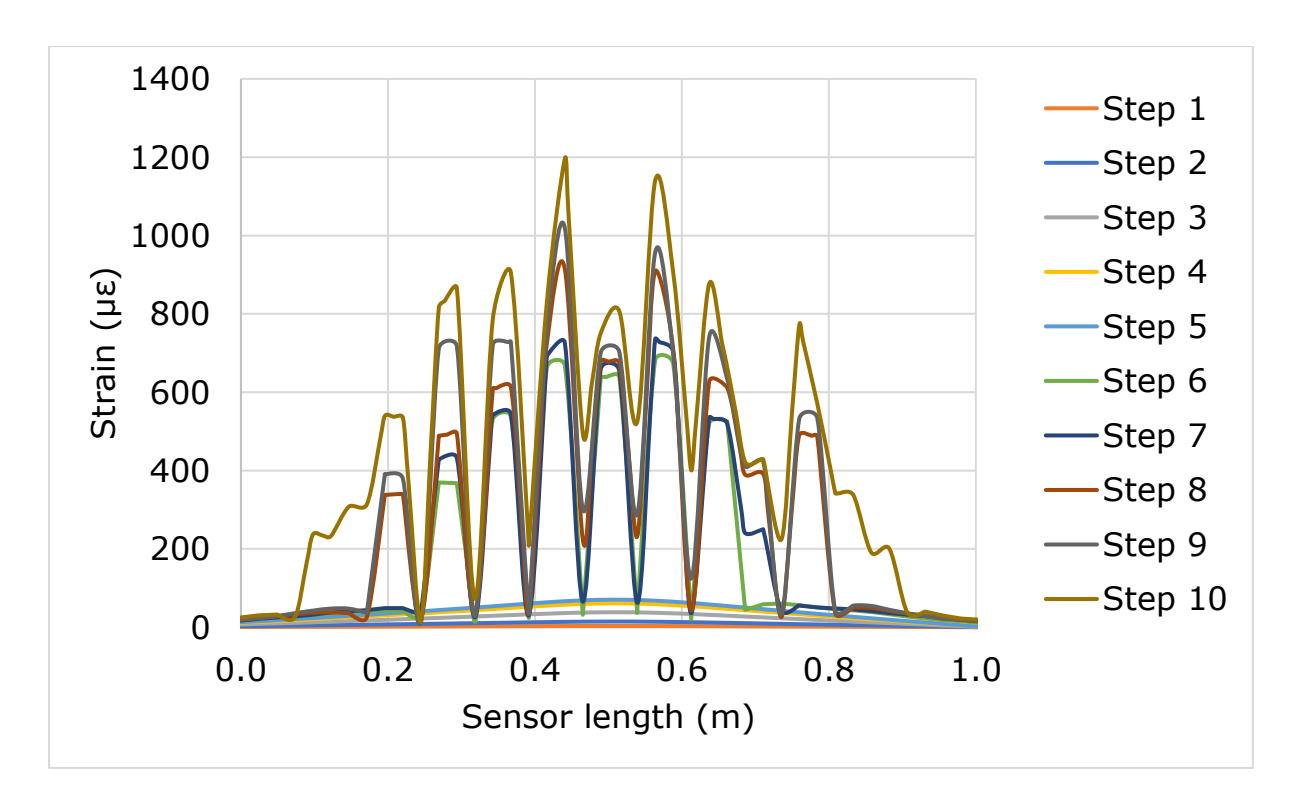


Figure 5.6: Surface strain against sensor length obtained from simulation under increasing load – Beam B1

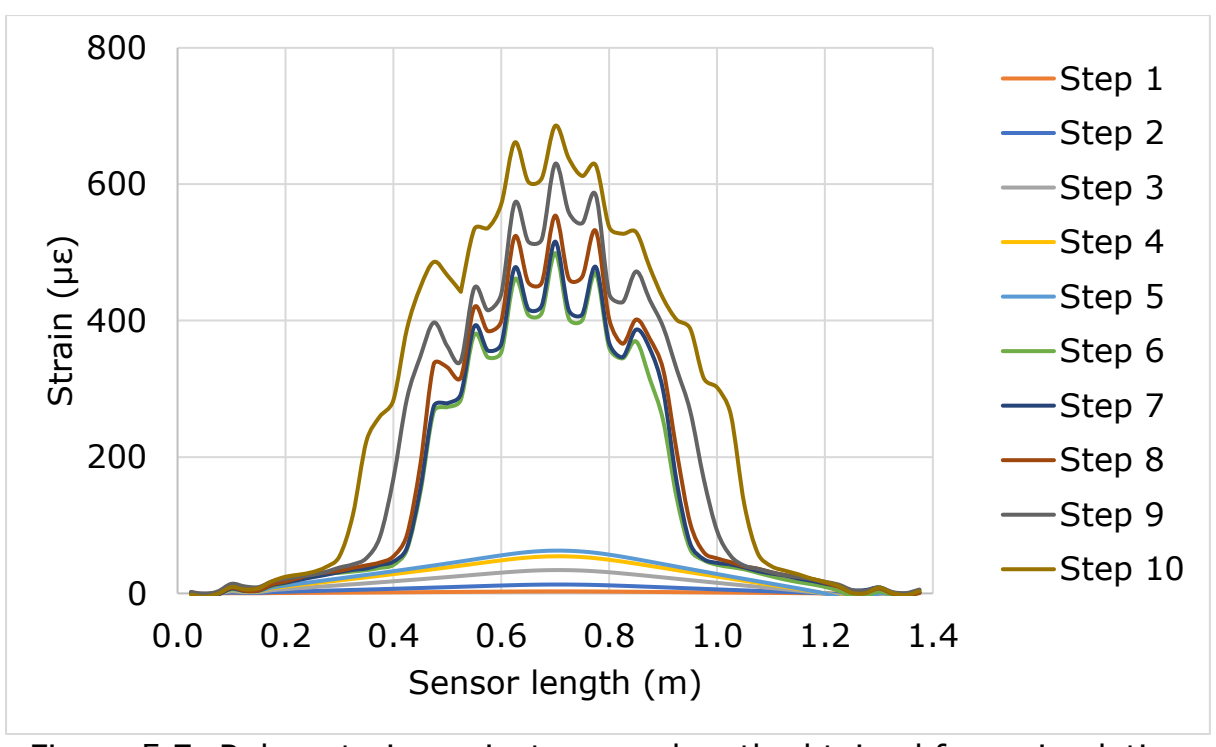


Figure 5.7: Rebar strain against sensor length obtained from simulation under increasing load – Beam B1

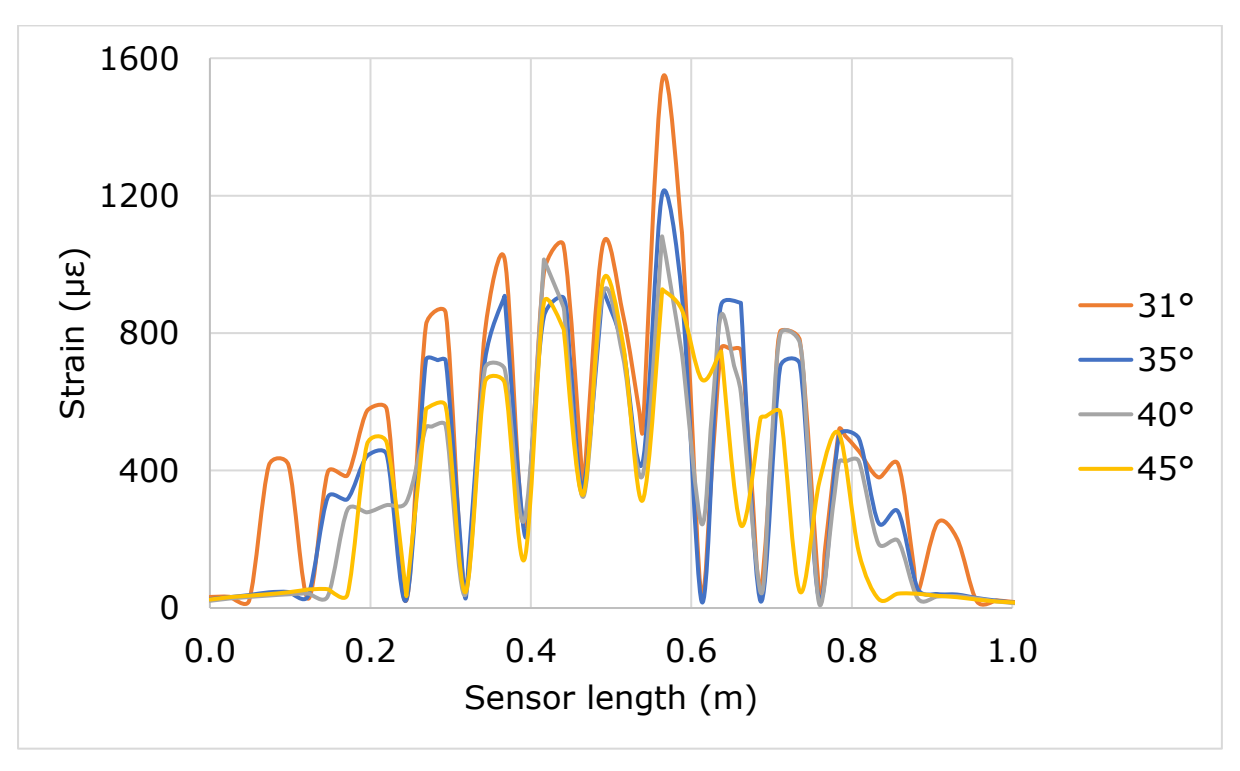


Figure 5.8: Surface strain against sensor length obtained from simulation for varying dilation angles – Beam B1

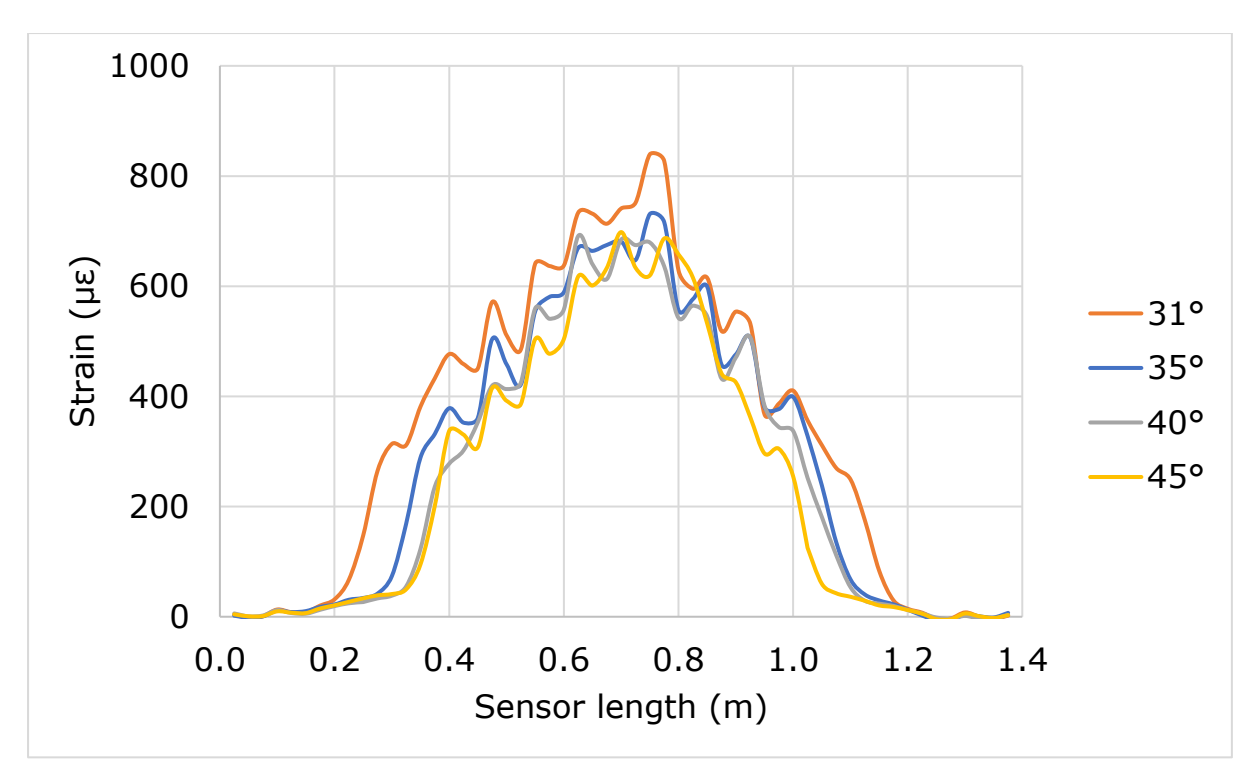


Figure 5.9: Rebar strain against sensor length obtained from simulation for varying dilation angles – Beam B1

According to Figures 5.6 and 5.7, the strain of the surface and the rebar increased with the step increment of the simulation. Nevertheless, there was a considerable difference between Step 5 and Step 6 since crack initiation occurred after Step 5. The relative loads for the fifth and sixth steps are 10 kN and 10.5 kN, respectively. Figures 5.8 and 5.9 shows how the dilation angle affects the strain variation along the concrete surface and rebar. Although 15 dilation angles were studied from 31° to 45°, the results presented here only for four angles to maintain the clarity. Considering both figures, the strain values over the length of the sensor vary significantly as the dilation angle increases. The cracked length is longer for lesser dilation angles and shorter for higher ones. Larger values of the dilation angle result in a stiffer material, whilst smaller values result in a more brittle material. Hence, it is reasonable for both figures to exhibit significant strain peaks along the sensor length for lower dilation angles.

Each step and angle of dilation had its unique strain pattern according to the load. Therefore, changing the number of steps and dilation angles could be a potential technique to construct a strain dataset. A strain dataset was generated using this method to train a DL model. Therefore, the proposed experimental and modelling methodologies based on CDP can create a strain dataset by considering variations in beam geometry, concrete grades, reinforcements, and loading conditions.

#### 5.3. Experimental and simulation results for long-span RC beams

This section details the strain pattern investigation of six concrete beams measuring 4000 mm x 200 mm x 400 mm, specifically R12C30, R16C30, R20C30, R12C60, R16C60, and R20C60, that underwent fourpoint bending under flexural loading. Experimental and simulation strain data were studied to determine the strain behaviour of the concrete surface and rebar for the R20C30 beam. The other beams were experimentally studied and kept for the prediction stage.

The primary objective of this study was to extract and analyse the strain measurements along the sensor lengths under flexural loading for all beams. Furthermore, the study aimed to utilise this strain data as a test set to evaluate the performance of a DL model in predicting the beams' structural health.

#### 5.3.1. Effect of SSQ on DOFS readings

According to the manufacturer of the data acquisition system (OBR 4600), the SSQ is a measure of the correlation between the reflected spectra obtained from the measured data and the reference data [255]. The SSQ values can be determined using the following formula (5.1):

$$Spectral Shift Quality (SSQ) = \frac{MAXIMUM(U_j(v) * U_j(v - v_j))}{\sum U_j(v)^2}$$
 (5.1)

Where,

 $U_i(v)$  = Baseline spectrum for a given data segment

 $U_j(v-v_j)$  = The spectrum measured during a strain or temperature change

\* = The symbol stands for the cross-correlation operator.

In theory, the SSQ should fall within the 0 to 1 range. Here, a value of 1 represents 'perfect correlation', and 0 represents 'no correlation'. The manufacturer recommends disregarding any data with an SSQ of 0.15 or lower since it is highly likely that the strain or temperature variation exceeds the measurable range after reaching this threshold. Consequently, any measurements with an SSQ value of 0.15 or lower were excluded from the analysis.

The following study analysed the effect of SSQ on DOFS readings of the R20C30 beam by considering the rebar attached sensor and bottom surface attached sensor.

The sensor readings were taken at 10 kN intervals, but to clarify the results, they were presented at 20 kN intervals. Figure 5.10 shows the raw strain data, strain data with values below the 0.15 SSQ threshold removed, SSQ variation, and the 0.15 SSQ threshold for the rebar DOFS at 120 kN, 140 kN, and 160 kN. The strain data for 120 kN indicates that data were not impacted, and the SSQ variation along the rebar was above the 0.15 SSQ threshold. However, the 140 and 160 kN graphs reveal that the SSQ variation was below the threshold at several locations. This provides clear evidence of the significant impact on the measured data.

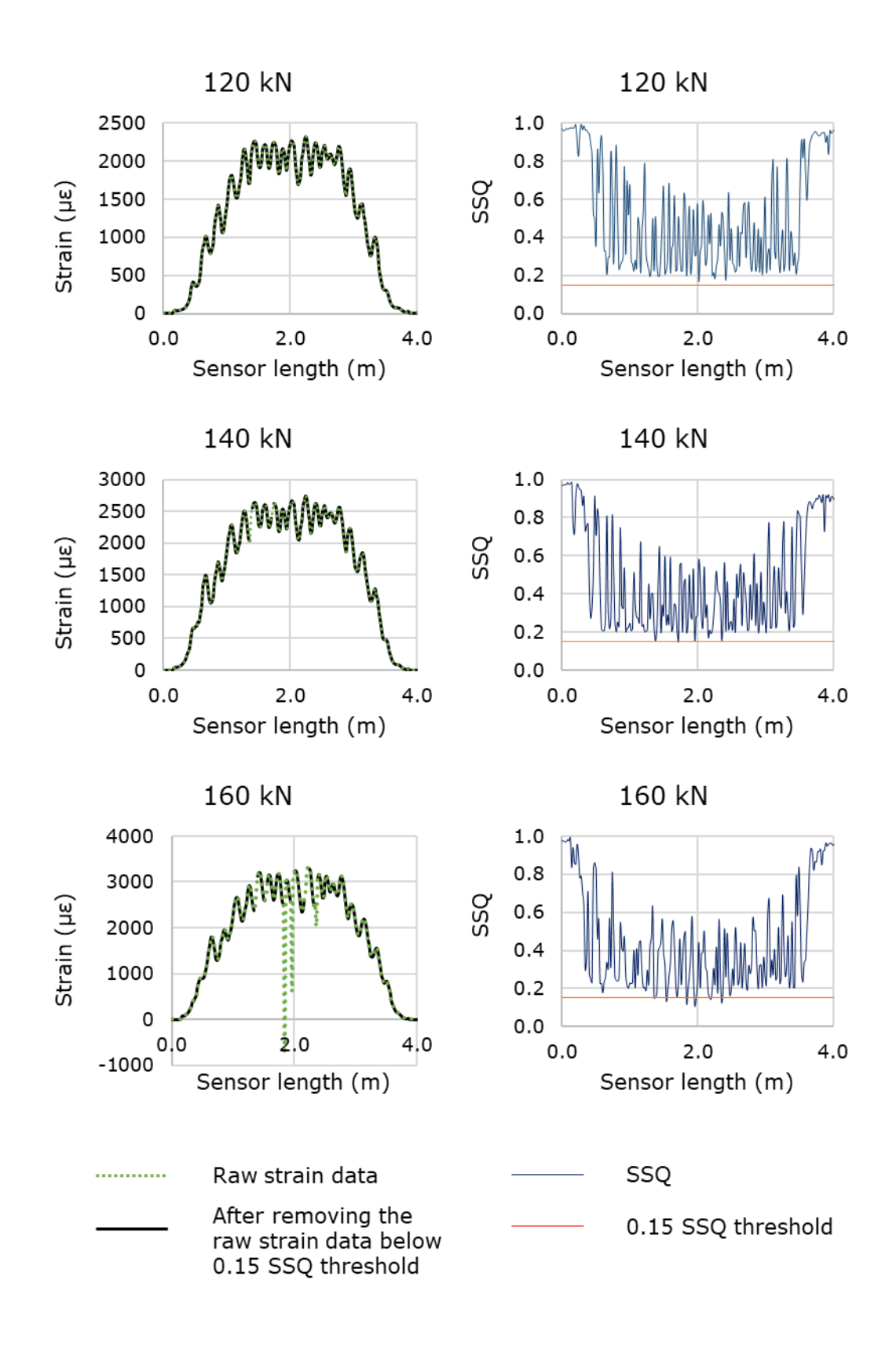


Figure 5.10: Raw strain data, after removing raw strain data below 0.15 SSQ threshold, SSQ and 0.15 SSQ threshold for rebar DOFS at different loadings

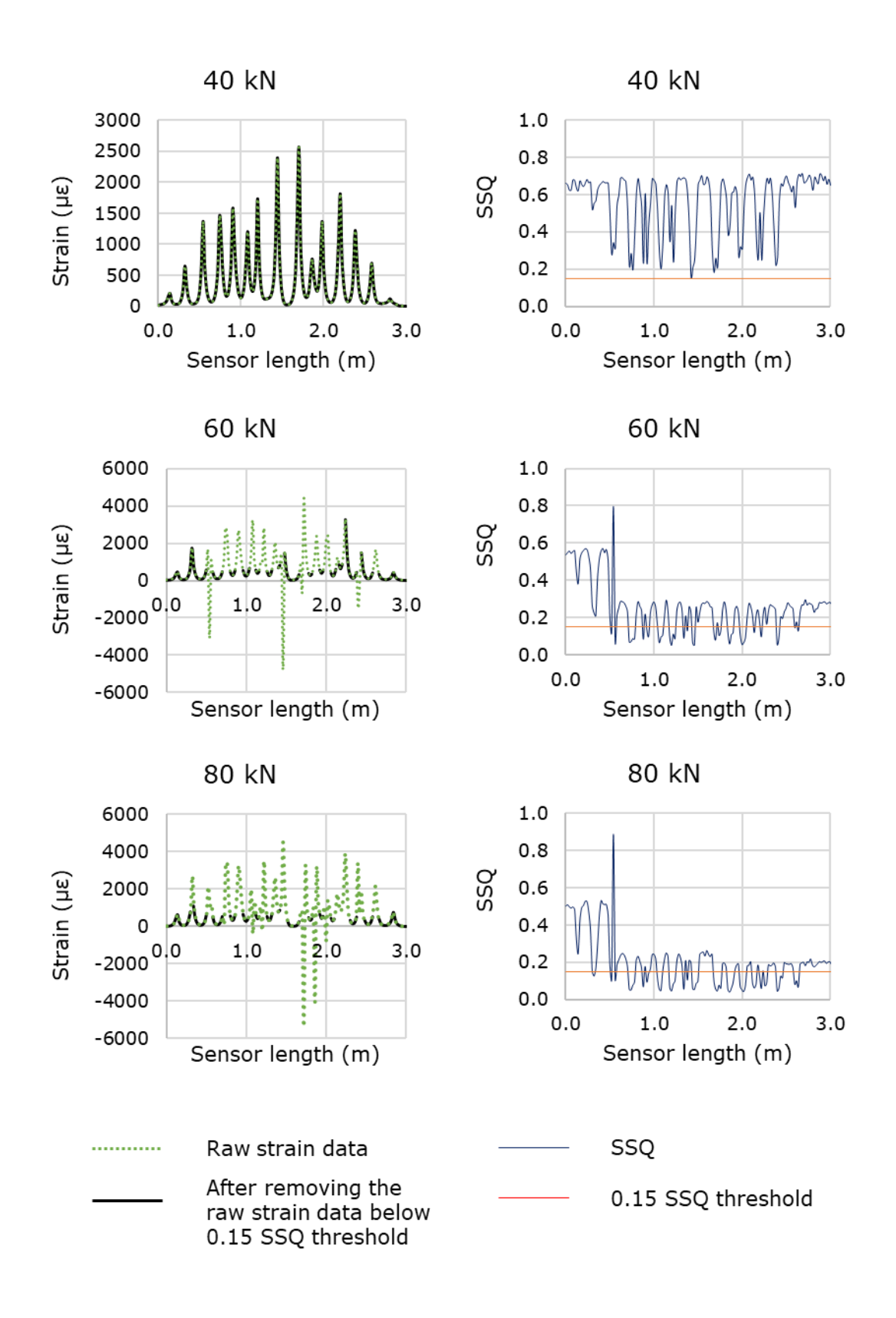


Figure 5.11: Raw strain data, after removing raw strain data below 0.15 SSQ threshold, SSQ and 0.15 SSQ threshold for bottom surface DOFS at different loadings

Figure 5.10 shows a clear trend where an increased applied load leads to decreased SSQ values, indicating many data points that fall outside the measurable range of DOFS. This was due to propagating cracks in the concrete cross-section, which resulted in higher strain transfer to the rebars that exceeded the measurable range of the DOFS sensors. Consequently, the raw data that fell below the threshold were deemed inaccurate and unreliable. They were removed based on the manufacturer's recommendations.

The DOFS sensor used in this application only withstands loads up to 120 kN and is limited to 75% of the failure load. However, the experimental results revealed a maximum strain measurement exceeding 80% of the rebar's yield strain. As such, it is recommended to utilise rebar-attached DOFS sensors in RC structures.

Figure 5.11 displays the analysis results of the strain data obtained from the bottom surface DOFS at different loadings, starting from 40 kN. The figure presents raw strain data, raw strain data after removing the data less than or equal to 0.15 SSQ threshold, SSQ variation, and 0.15 SSQ threshold. The strain data at 40 kN load is unaffected, and the SSQ variation along the DOFS was not below the 0.15 SSQ threshold. However, for the 60 kN and 80 kN loadings, the SSQ variation graph is below the threshold level at multiple locations.

Consequently, affected data were removed per the manufacturer's suggestions. The strain variation of the 60 kN and 80 kN graphs clearly illustrates how the data were affected. The SSQ levels decreased with increasing loads, and the number of affected data increased accordingly. It is worth noting that the surface-attached DOFS sensor can only withstand up to 40 kN load and 25% of the failure load. The concrete surface-attached DOFS was significantly affected by low SSQ values when compared with the rebar-attached DOFS. This is because the initiation of cracks and increasing crack widths on the concrete surface due to the increasing loads led to exceeding the measurable range of the DOFS-attached surface sensor.

Therefore, caution is advised when employing surface-attached DOFS sensors in RC structures, especially under high loads.

The experimental findings revealed that the bottom surface sensor was the first to reach the 0.15 SSQ threshold, followed by the side sensor for all six beams under investigation. Table 5.2 presents the Effect of SSQ on long-span RC beams.

Table 5.2: Effect of SSQ on beams

Load	R12C30		R16C30		R20C30	
(kN)	Bottom	Side	Bottom	Side	Bottom	Side
	sensor	sensor	sensor	sensor	sensor	sensor
10	SSQ > 0.15		SSQ > 0.15			
20				SSQ >	SSQ >	
30	SSQ ≤ 0.15			0.15	0.15	SSQ >
40						0.15
50			SSQ ≤ 0.15			
60				SSQ ≤	SSQ ≤	
70				0.15	0.15	SSQ ≤
						0.15
Load	R12C60		R16C60		R20C60	
(kN)	Bottom	Side	Bottom	Side	Bottom	Side
	sensor	sensor	sensor	sensor	sensor	sensor
5		1				
10	SSQ > 0.15		SSQ > 0.15			
15				SSQ > 0.15	SSQ > 0.15	SSQ >
20			0.15			0.15
25						0.15
30						
35	SSQ ≤ 0.15		SSQ ≤ 0.15	SSQ ≤ 0.15	SSQ ≤ 0.15	
40						SSQ ≤
				0.15	0.13	0.15

According to the manufacturer's instructions, measurements equal to or less than 0.15 SSQ were disregarded. Despite this, inconsistencies in the strain readings, also reported by other researchers [253, 256], were still

present in the data. Anomalous data points were identified and eliminated from the dataset to address this issue. Data presented in this section are exclusively based on the maximum load the side surface sensors could reach for the beams before falling below the 0.15 SSQ limit.

#### 5.3.2. Rebar and surface strain - R20C30

Figure 5.12 depicts strain measurements obtained from the experiment and simulation for the rebar in beam R20C30 for two different load scenarios, namely 40 kN and 60 kN. Both the experimental and simulated strain patterns exhibited a high degree of correlation. When the load was at 60 kN, the maximum strain observed in the experiment for the rebar was 992  $\mu\epsilon$ .

The strain peaks observed in the rebar exhibit a wave-like behaviour in all measurements, which becomes more pronounced with increasing load. The cause is the propagation of cracks along the concrete. Figure 5.13 provides a detailed explanation of this trend. It shows fluctuation in strain results for the bottom surface sensor and the rebar sensor under a 10 kN load for the beam R20C30. The graph shows that the spikes in the rebar strain correspond to the surface strain peaks. Typically, the appearance of strain peaks indicates the occurrence of tension-induced cracks in that area, while strain valleys imply less strain on the concrete. Since surface strain spikes result from crack formation, so do the spikes in rebar strain. Therefore, it can be concluded that the rebar strain peaks result from concrete cracks extending beyond the rebars.

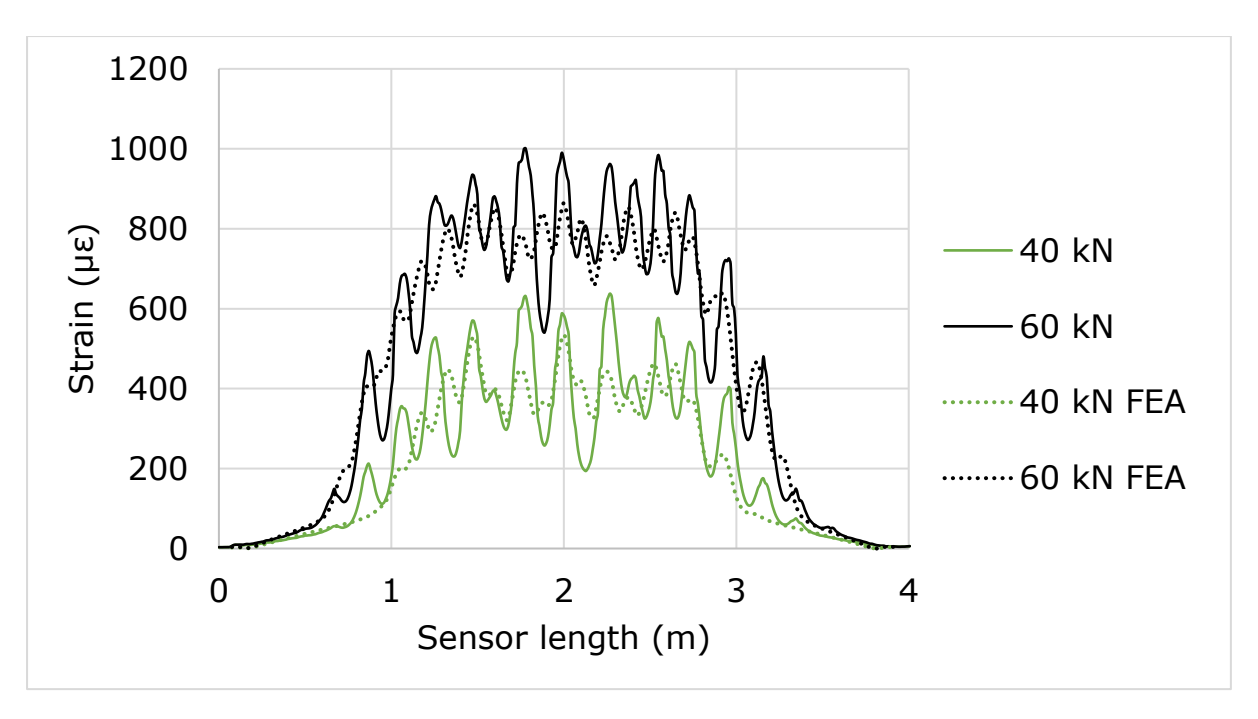


Figure 5.12: Experimental vs simulation rebar strain for beam R20C30

At 60 kN load, a difference of 128  $\mu\epsilon$  existed between the maximum experimental and simulation strains. The highest simulated rebar strain was 864  $\mu\epsilon$ . This was because the wave-like behaviour was much more pronounced in the experimental strain data than in the simulation results for all measurements.

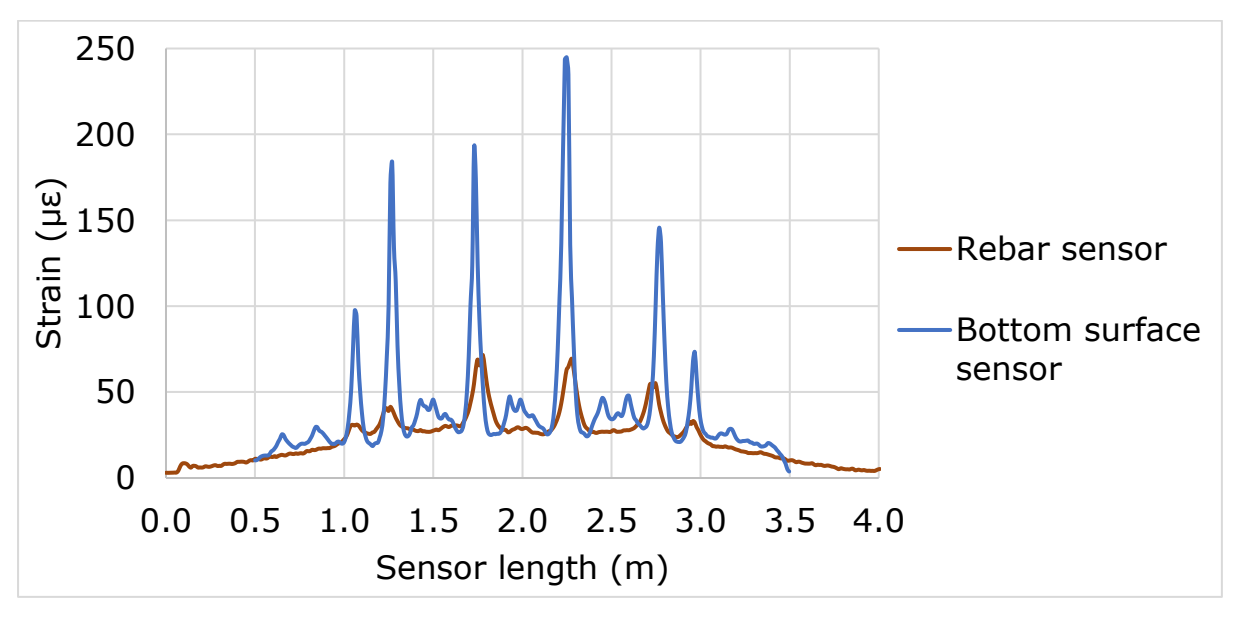


Figure 5.13: Strain variation of rebar and bottom surface sensor at 10 kN load for beam R20C30

Figure 5.14 presents the strain measurements collected from both the experiment and simulation for the R20C30 beam's bottom surface sensor at 40 kN. The maximum experimental strain was measured as 3557  $\mu\epsilon$ , while the peak strain recorded from the simulation was 2811  $\mu\epsilon$ .

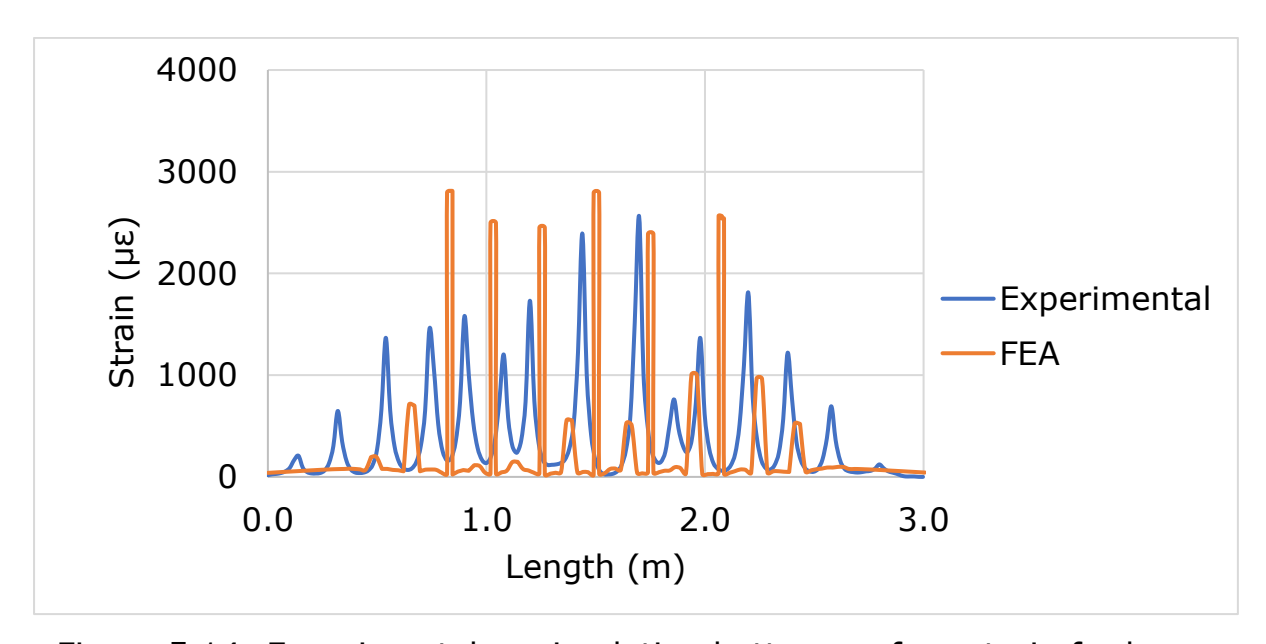


Figure 5.14: Experimental vs simulation bottom surface strain for beam R20C30 at 40kN

Figure 5.15 depicts the strain variation along the side surface of beam R20C30, as measured through experimentation and simulation, under two load conditions: 40 kN and 60 kN. At 60 kN load, the maximum experimental strain recorded was 5614  $\mu\epsilon$ , while the maximum strain registered in simulations was 4753  $\mu\epsilon$ . It should be noted that the surface sensor used for this measurement was positioned 25 mm above the bottom surface of the concrete beam wall.

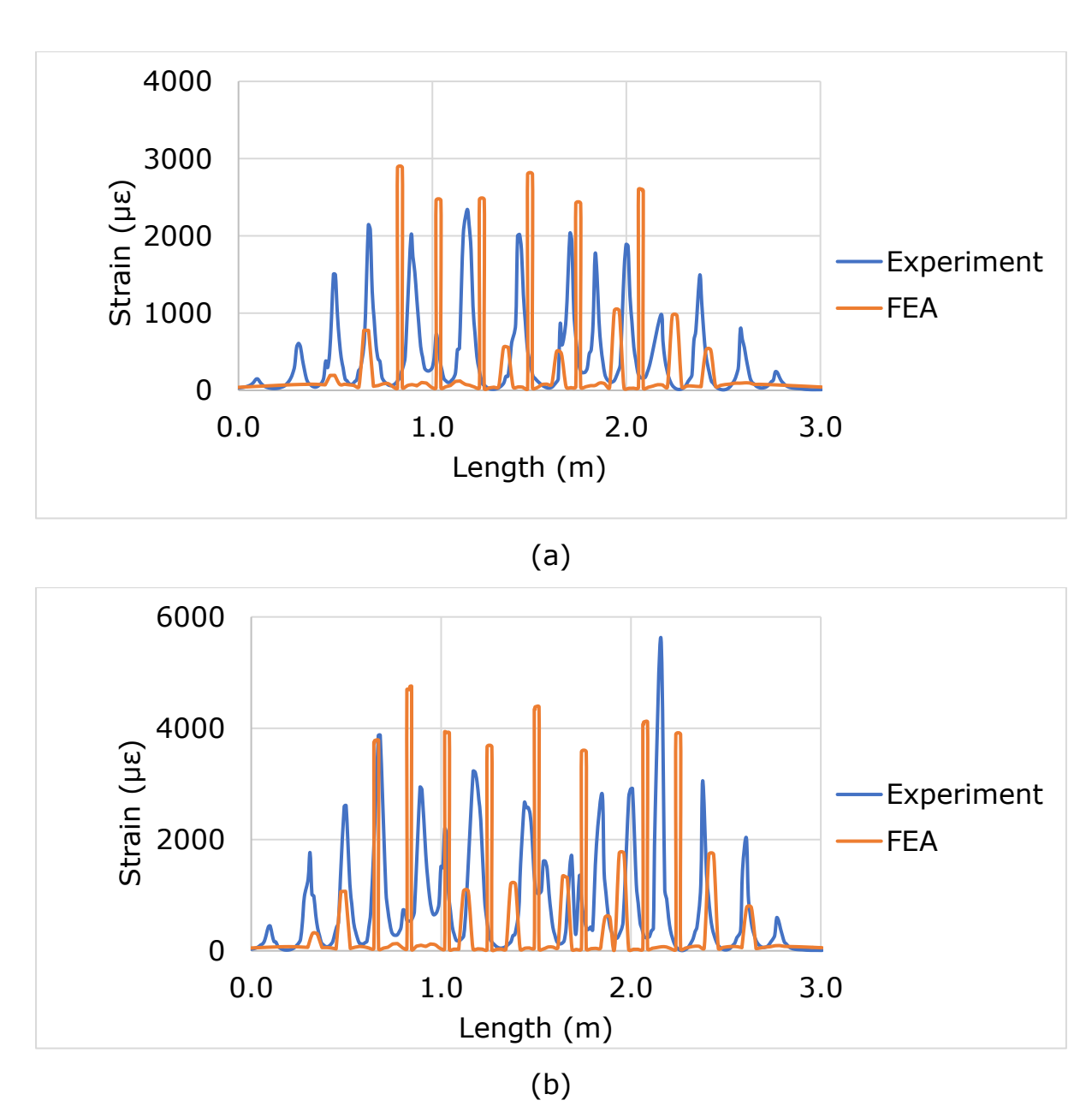


Figure 5.15: Experimental vs simulation side surface strain for beam R20C30 (a) at 40kN; (b) at 60kN

Figure 5.15 demonstrates an increase in the amplitude and frequency of strain peaks as the load increased, attributed to the initiation, and widening of cracks in the concrete material. Both the bottom and side surfaces of the beam exhibited significant cracking under the presented loads, and strain peaks were observable throughout the sensor length. Notably, there were differences between the experimental and simulated crack positions and the strain magnitude along the beam's length, and the

default CDP model's isotropic nature may limit its capacity to predict complex anisotropic cracking patterns accurately.

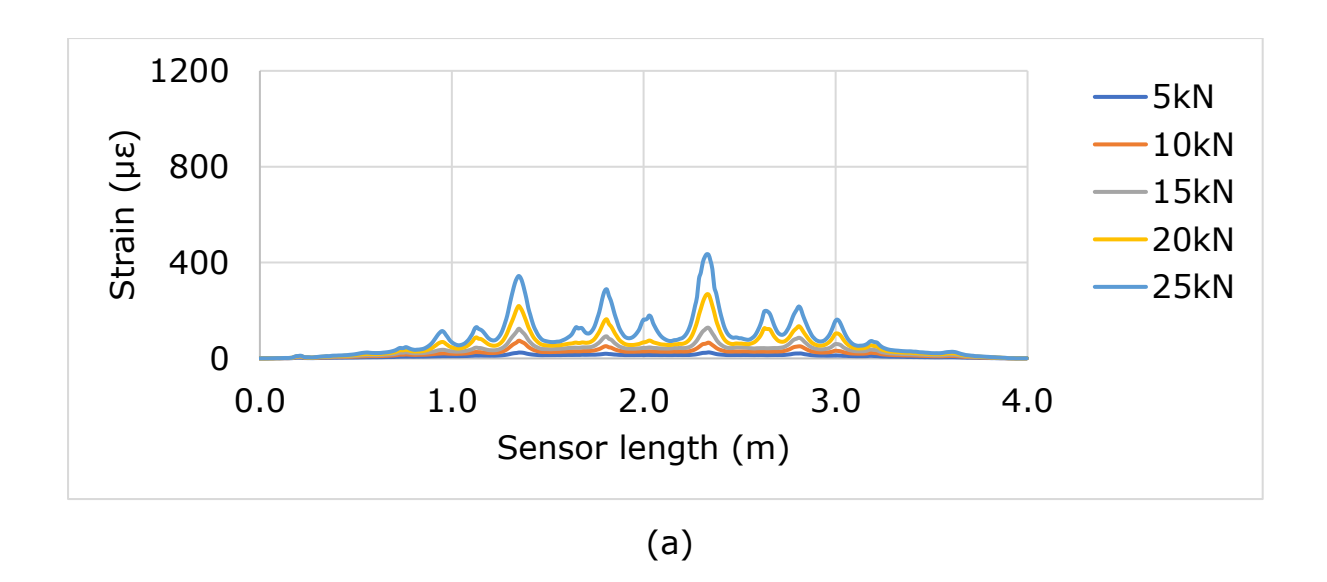
Despite these factors, the experimental and simulated data agreed on the number of peak strains and the overall strain pattern. Figure 5.14 indicated 14 instances of peak strain values in the experimental data and 13 instances in the FEA data. Figure 5.15 (a) showed 15 peak strains in the experimental data and 13 in the FEA data, while Figure 5.15 (b) demonstrated 17 instances of peak strains in the experimental and FEA analyses.

Therefore, the strain distribution (overall strain pattern) allows validation of the FEA model. The strain data were generated to train a DL model using CDP-based FEA data.

#### 5.3.3. Rebar and surface strain - R16C30

The beam R16C30 was loaded in three different loading stages: the first and the second stages involve loading up to 25 kN, and the third stage involves loading up to 40 kN. Notably, the data presented in these figures are based on a threshold of 0.15 SSQ. Figure 5.16 provides data for variation in the rebar strain during different loading stages.

Figures 5.17 and 5.18 present data for variation in the bottom and side surface strain during different stages of loading, respectively. Insights can be gained into the behaviour of the bottom and side surface of the beam under different loading conditions by analysing the data presented in Figures 5.17 and 5.18.



1200 5kN -10kN Strain (με) 800 -15kN -20kN 400 -25kN 0 0.0 1.0 4.0 2.0 3.0 Sensor length (m) (b)

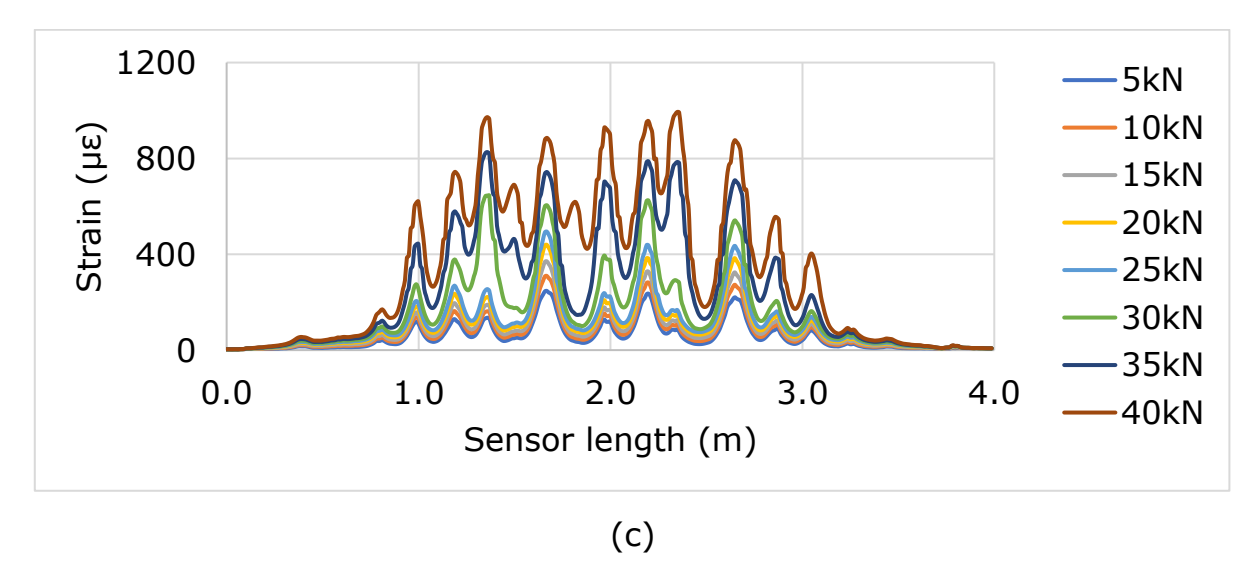
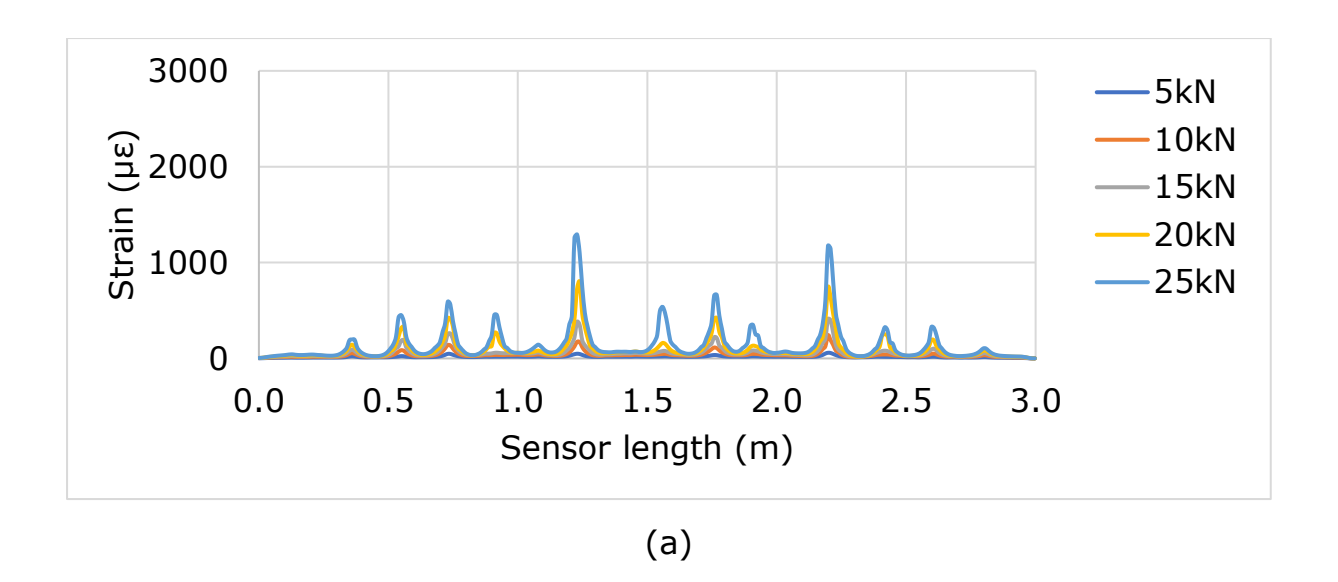
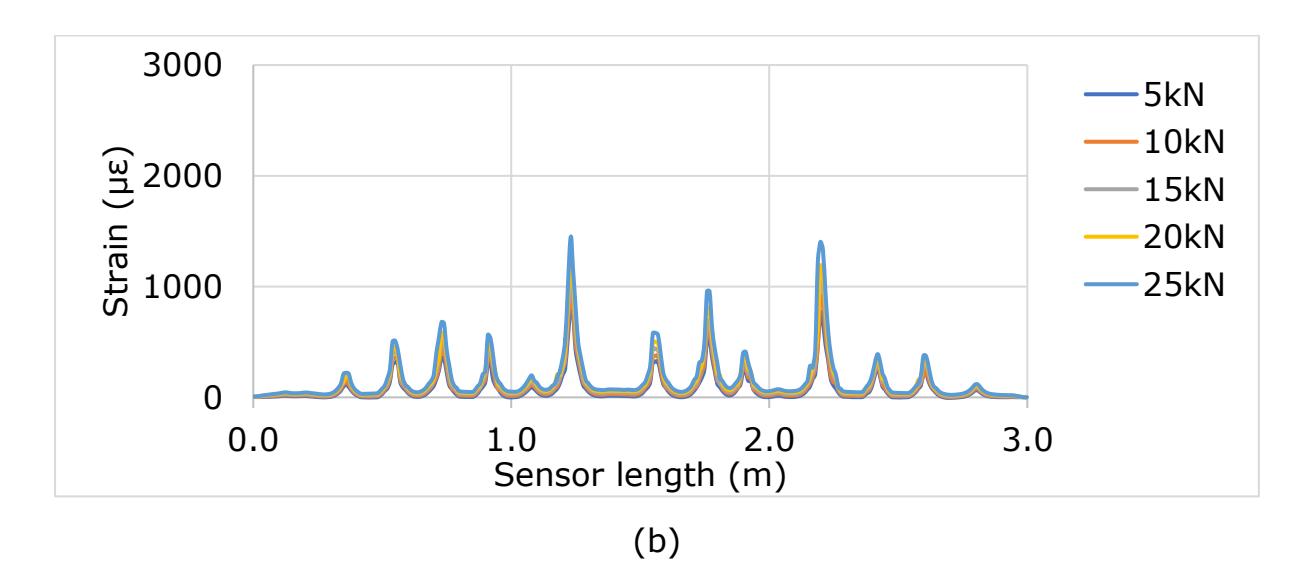


Figure 5.16: The experimental rebar strain variation for R16C30 (a) 0-25kN; (b) 0-25kN; (c) 0-40kN





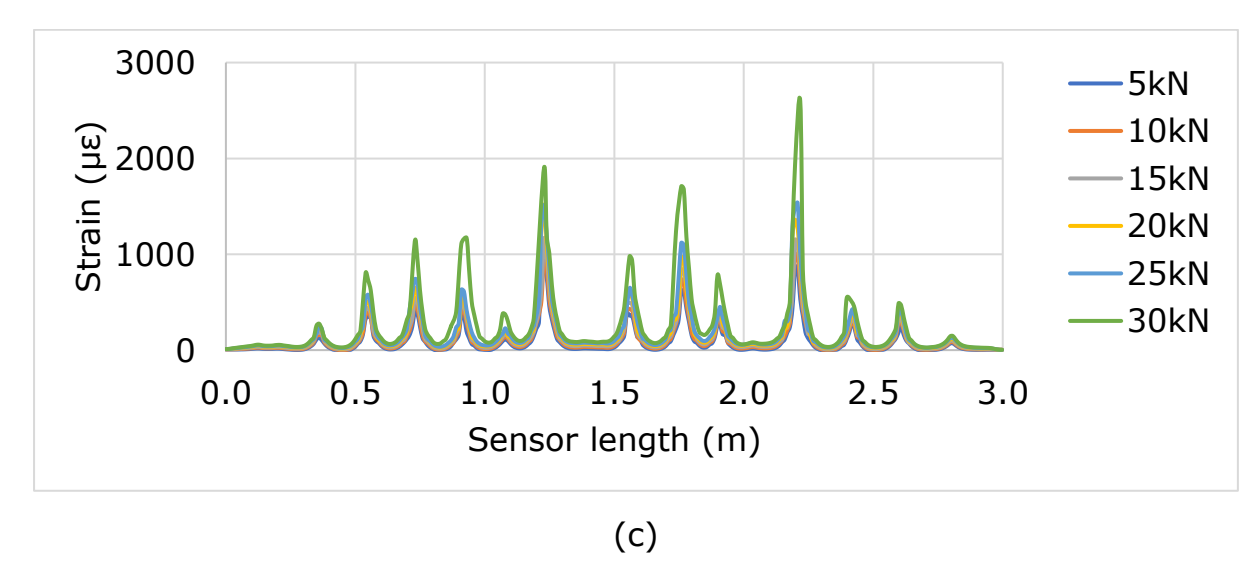
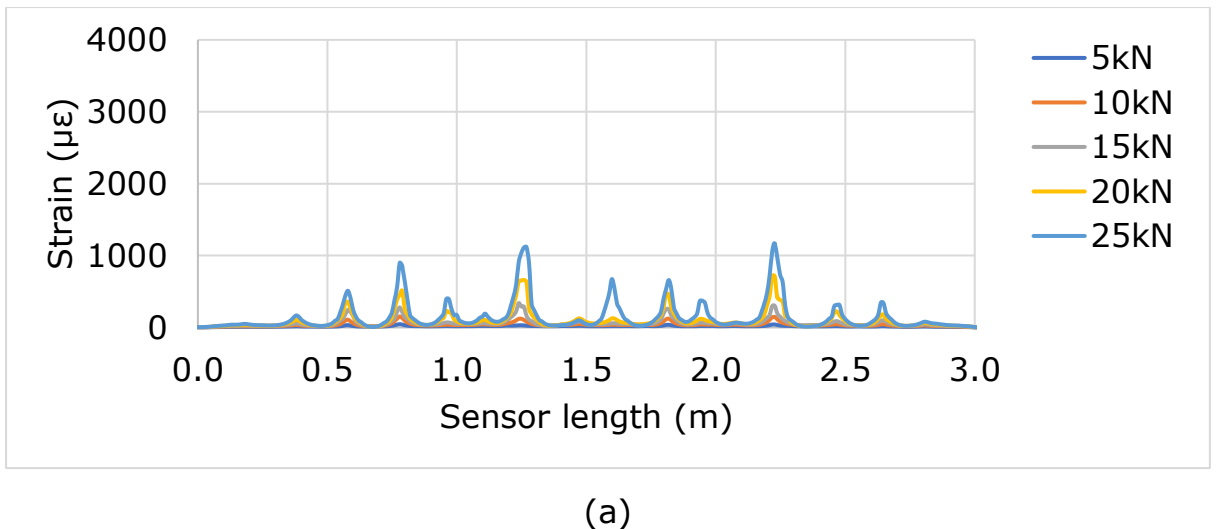
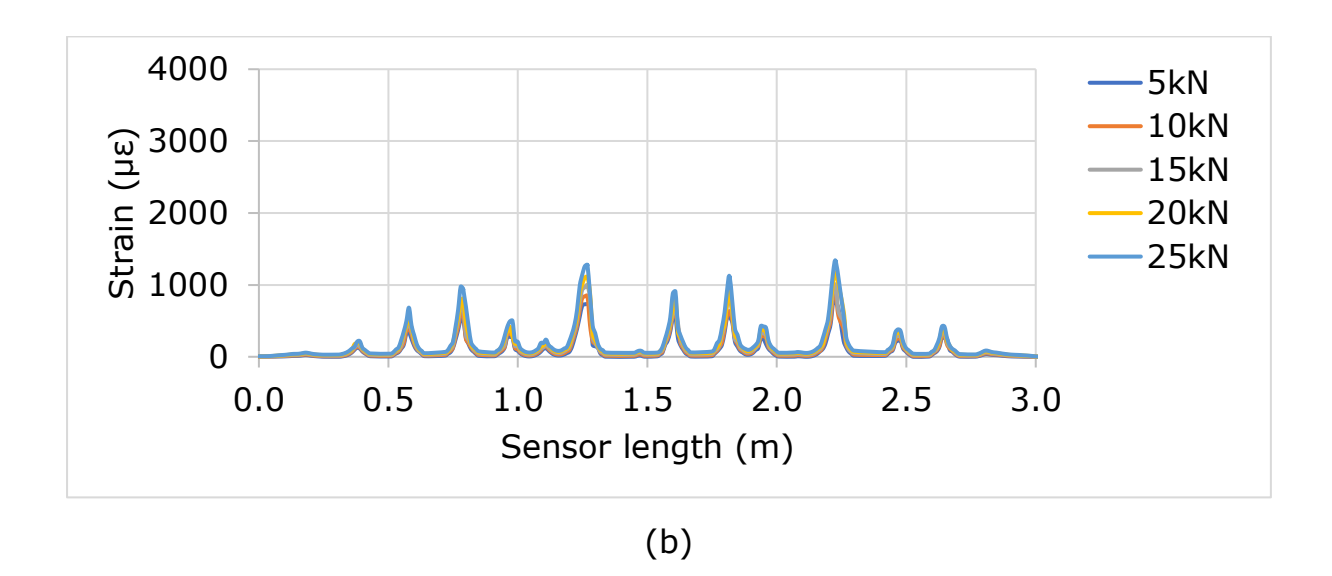


Figure 5.17: The experimental bottom surface strain variation for R16C30 (a) 0-25kN; (b) 0-25kN; (c) 0-30kN





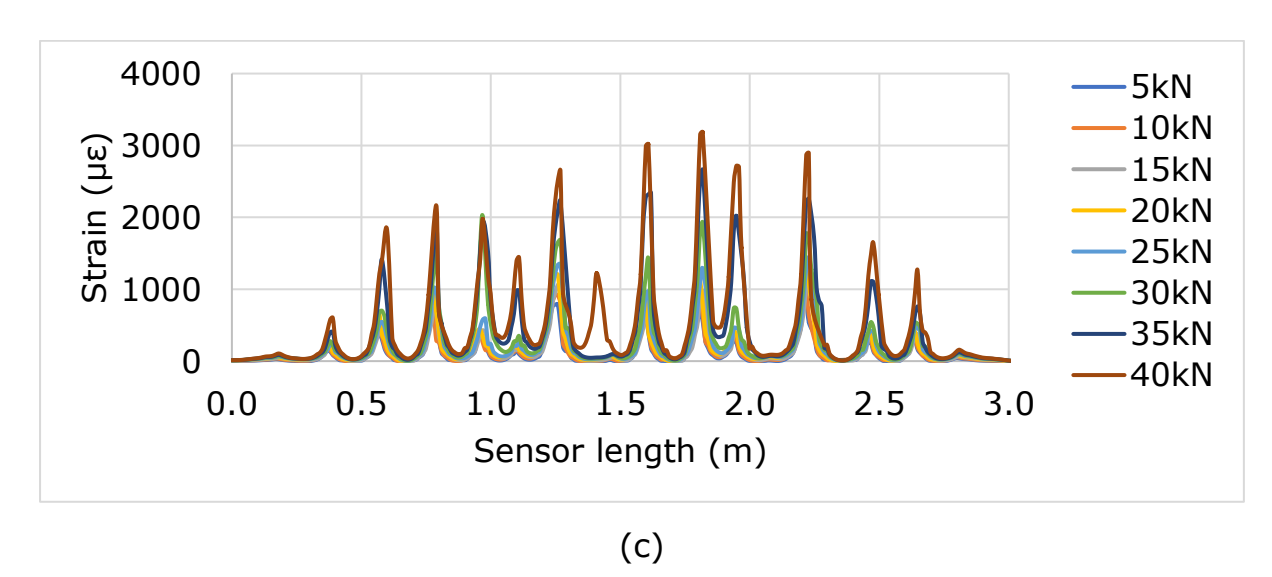


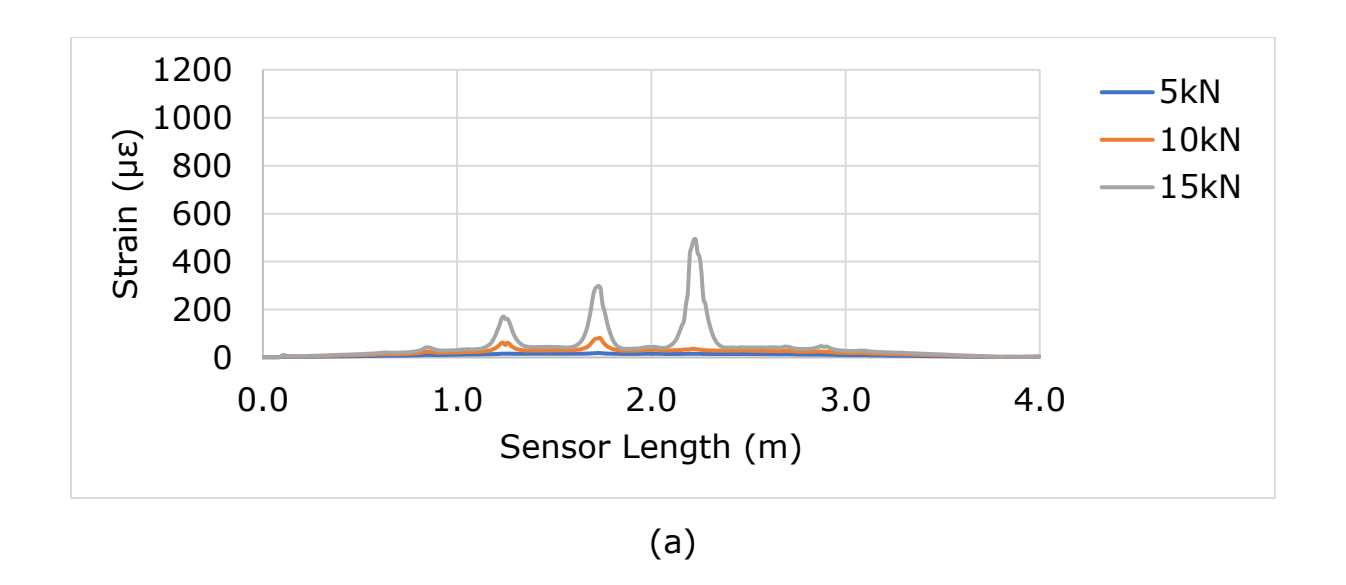
Figure 5.18: The experimental side surface strain variation for R16C30 (a) 0-25kN; (b) 0-25kN; (c) 0-40kN

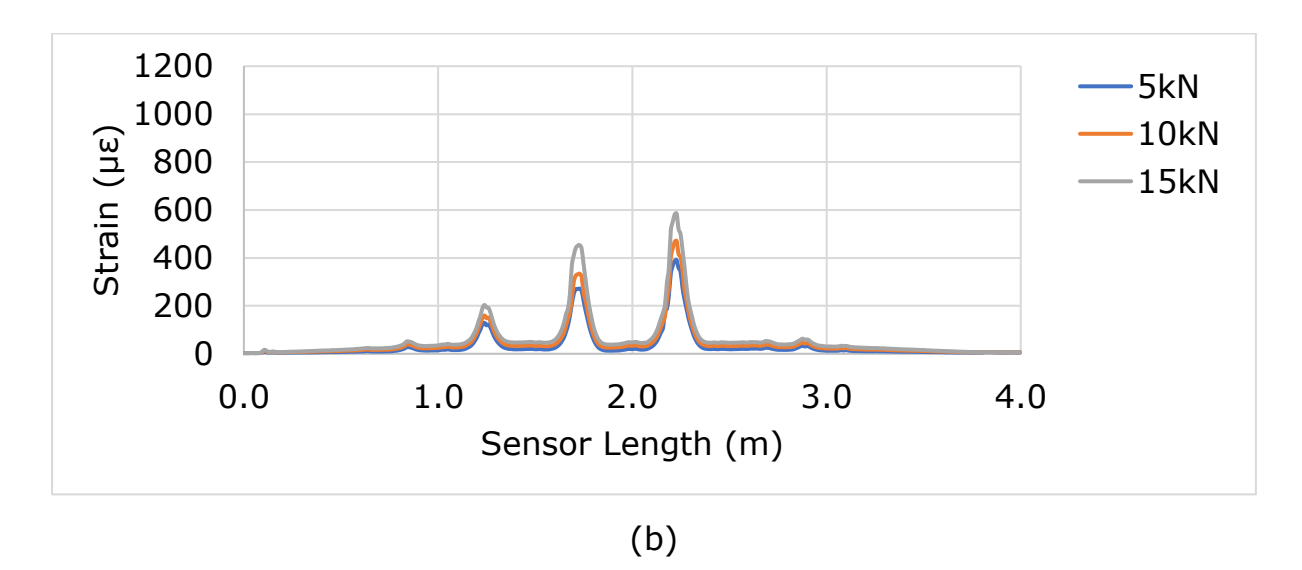
Upon analysing Figure 5.16, the main observation is the presence of a residual rebar strain in Figures 5.16 (b) and (c), despite the beam being relaxed for 10 minutes. A slight increase in rebar strain was noted during the second loading phase [see Figures 5.16 (a) and (b)]. One potential explanation for the slight increase in rebar strain could be attributed to cracks within the concrete. In contrast, Figure 5.16 (a) shows no residual rebar strain. Additionally, the figures showed strain peaks and valleys like those observed in beam R20C30.

Analysing Figures 5.17 and 5.18 reveals that the strain increases as the load is applied (which is expected). However, it should also be noted that a residual surface strain is present in Figures 5.17 (b), (c), and Figures 5.18 (b) and (c), like the residual rebar strain observed in Figures 5.16 (b) and (c). Even though the 25 kN limit was intended to ensure the beam remained within its elastic range according to the hand calculation, strain peaks were already evident and concrete surface cracking had occurred before reaching this limit.

#### 5.3.4. Rebar and surface strain - R12C30

The rebar strain changes at different stages of loading for beam R12C30 are illustrated in Figure 5.19. This beam was loaded in three stages. The first and second stages involved loading up to 15 kN each, and the third stage involved loading up to 30 kN. It is important to note that the data depicted in these figures were obtained using a 0.15 SSQ threshold.





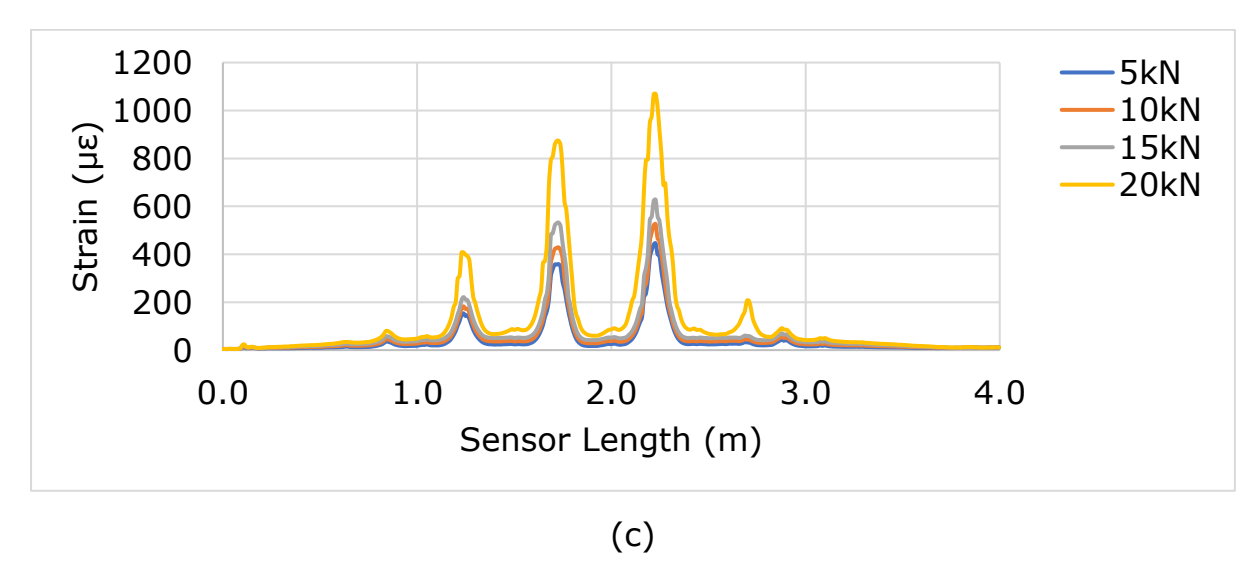
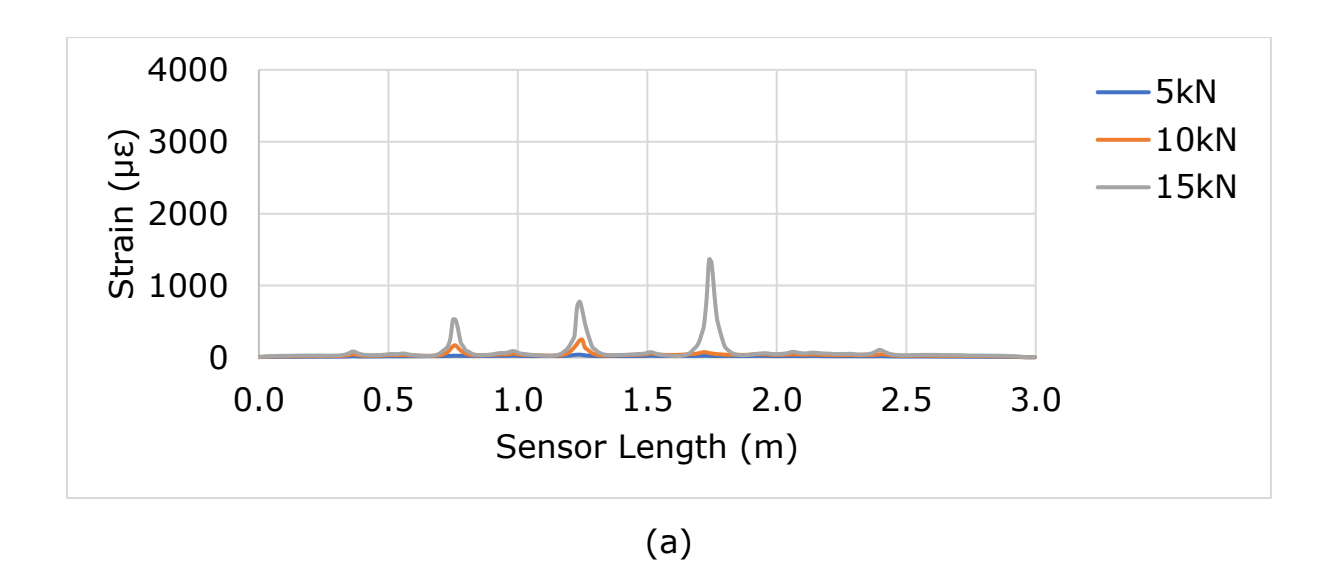
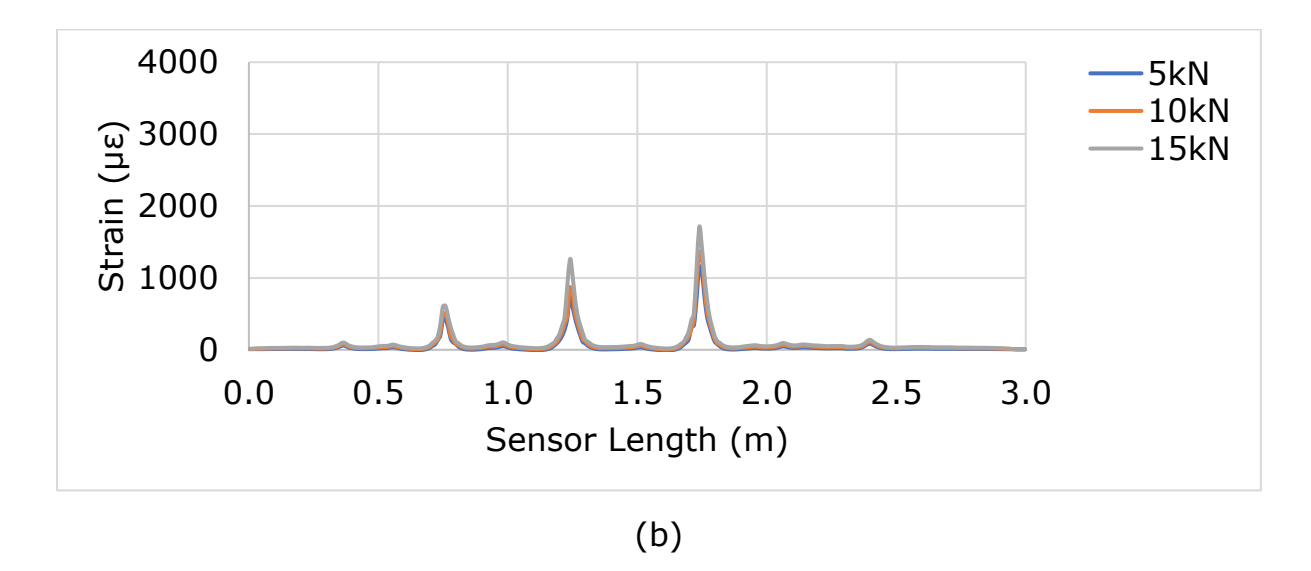


Figure 5.19: The experimental rebar strain variation for R12C30 (a) 0-15kN; (b) 0-15kN; (c) 0-20kN





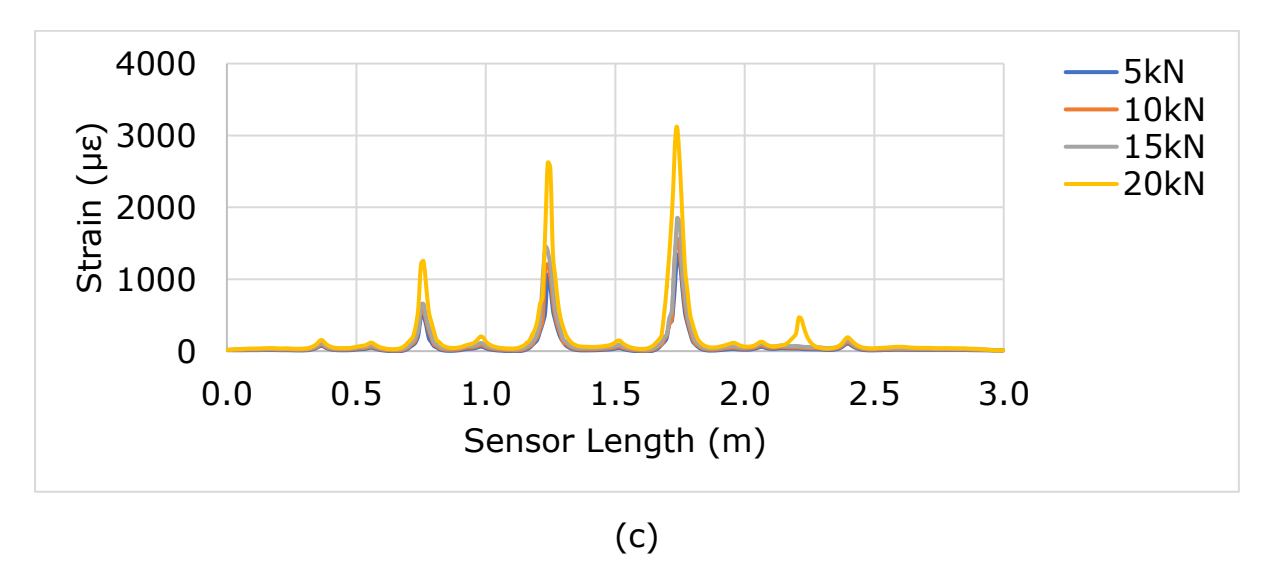
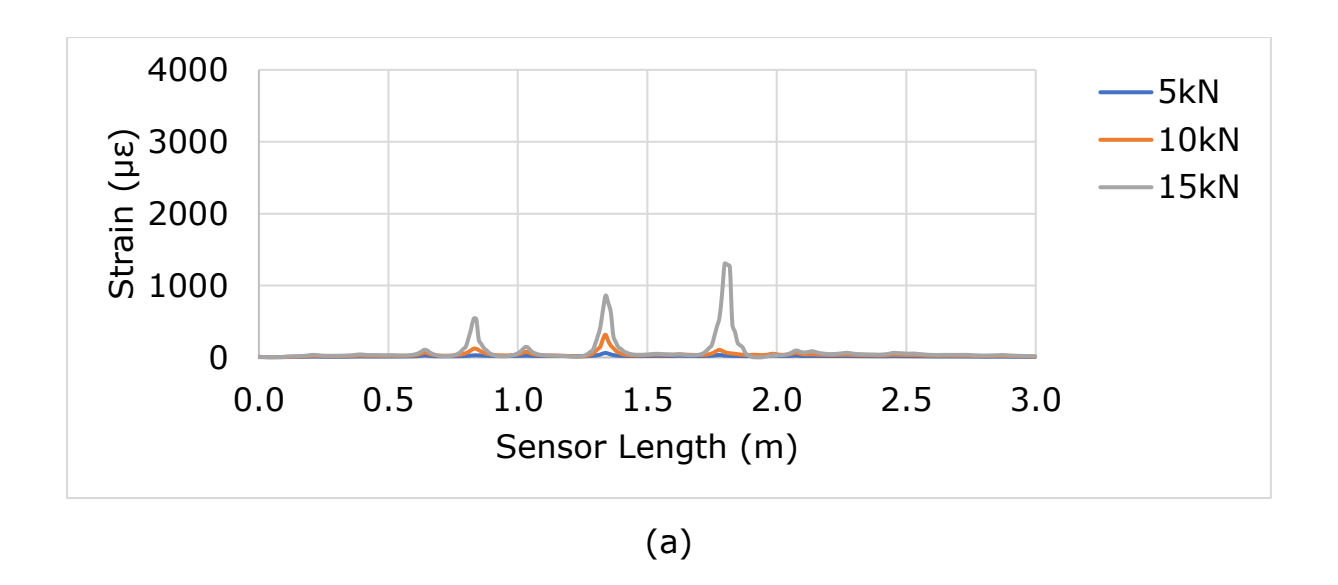
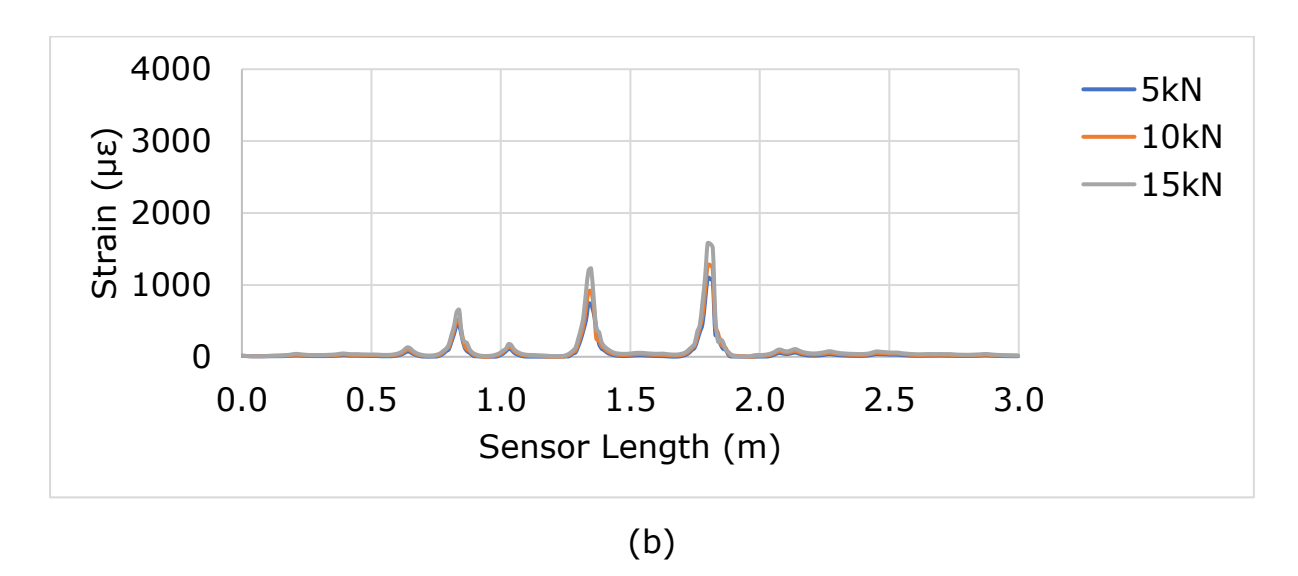


Figure 5.20: The experimental bottom surface strain variation for R12C30 (a) 0-15kN; (b) 0-15kN; (c) 0-20kN





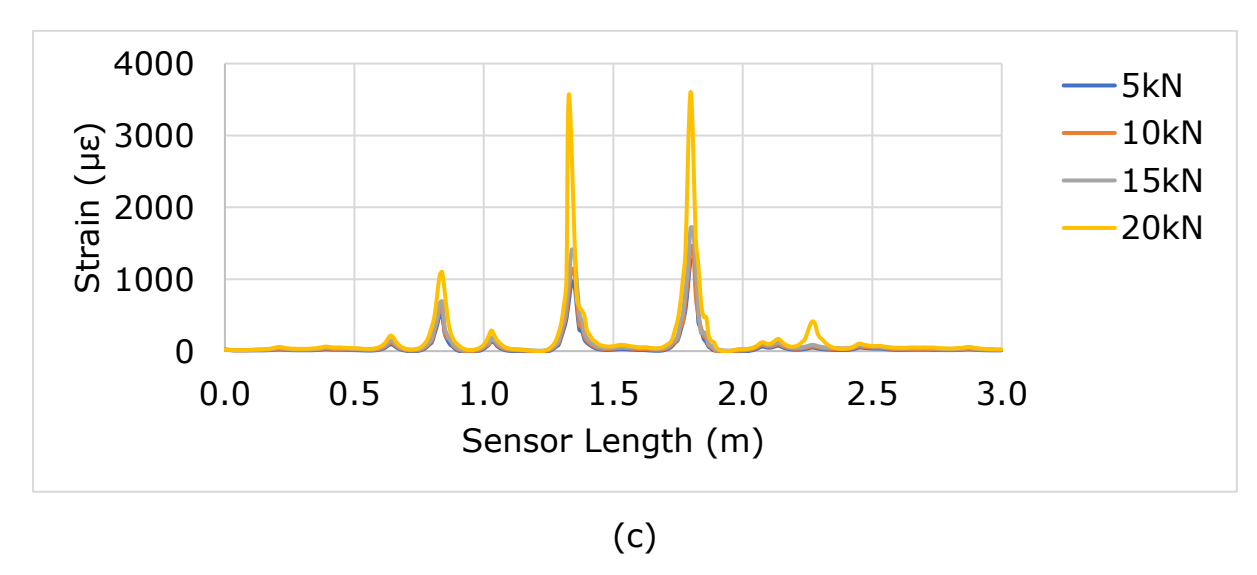


Figure 5.21: The experimental side surface strain variation for R12C30 (a) 0-15kN; (b) 0-15kN; (c) 0-20kN

The key finding of examining Figure 5.19 is that residual rebar strain noted in Figure 5.19 (b) and (c), even after the beam was allowed to relax for 10 minutes (the same observation as in R16C30). Furthermore, a slight rise in rebar strain was observed during the second loading phase. In contrast, Figure 5.19 (a) exhibits no residual rebar strain. Based on an analysis of Figures 5.20 and 5.21, there is a presence of residual surface strain in certain stages, specifically in Figures 5.20 (b) and (c) and Figure 5.21 (b) and (c). This is similar to the residual rebar strain in Figure 5.19 (b) and (c). Surface cracking of the concrete continued though the loading limit was 15 kN. Due to loading and reloading, the crack may not close due to aggregate interlocking and remain open to some extent, making it report some strain (residual) after unloading.

#### 5.3.5. The behaviour of residual strain

This section describes the assessment of the residual rebar strain in R12C30 and R16C30 beams after the initial and subsequent loading stages. Figures 5.22 and 5.23 compare the residual strain after each loading stage. The figures demonstrate a slight increase in the residual strain during the second loading stage compared to the first stage for both beams.

When an RC beam is subjected to a load, both the concrete and rebar undergo deformation, increasing their strain. However, after unloading, the concrete and rebar may not return to their original positions, which results in residual strain. One of the main reasons for residual strain is the presence of cracks in the concrete, which can cause the rebar to experience additional strain. This additional strain can contribute to the residual strain after unloading.

In this case, the residual strain was slightly increased during the second pass of loading when compared to the first pass. This increase in residual strain can be attributed to cracks in the concrete during the first stage, which may have weakened the structure (stiffness reduction after cracking) and made it more vulnerable to further damage during the second stage of loading.

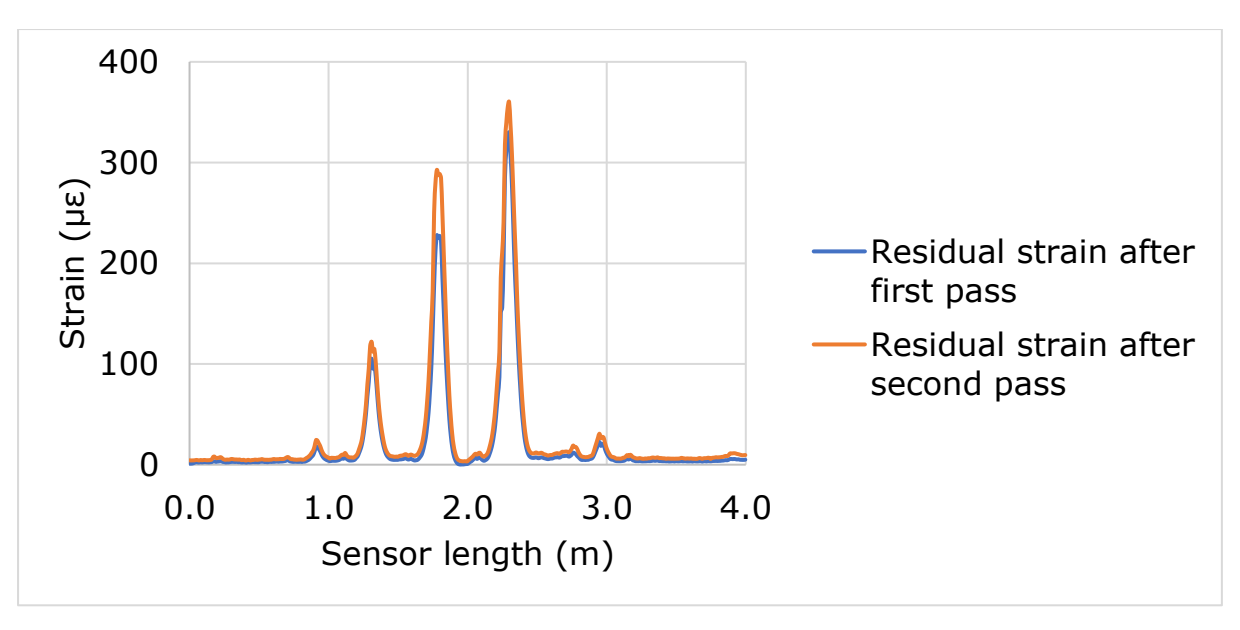


Figure 5.22: Comparison of residual rebar strain after the first stage of loading and second stage of loading for beam R12C30

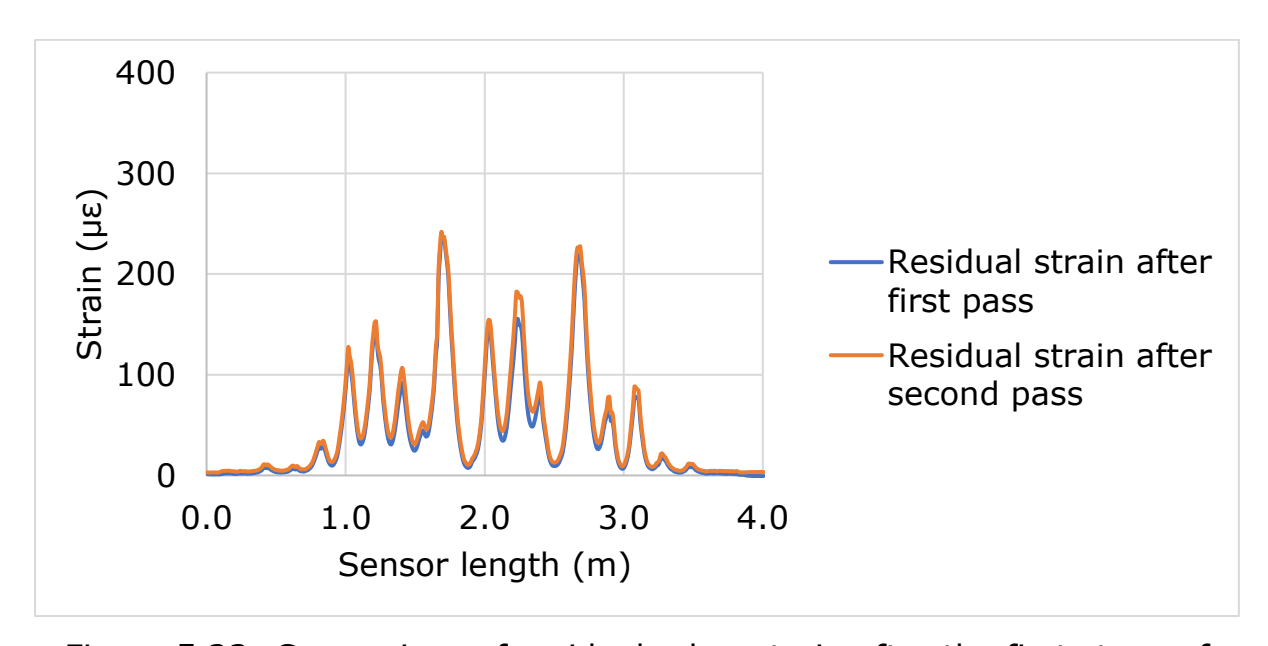


Figure 5.23: Comparison of residual rebar strain after the first stage of loading and second stage of loading for beam R16C30

A study investigated the effect of the adhesive used on the residual strain on the rebar. The experiment aimed to assess the residual strain of 12 mm and 16 mm diameter rebars with a procedure involving loading and unloading using a universal tensile machine. Figure 5.24 illustrates the

schematic diagram of the rebar with the attached DOFS, and Figure 5.25 presents the experimental setup.

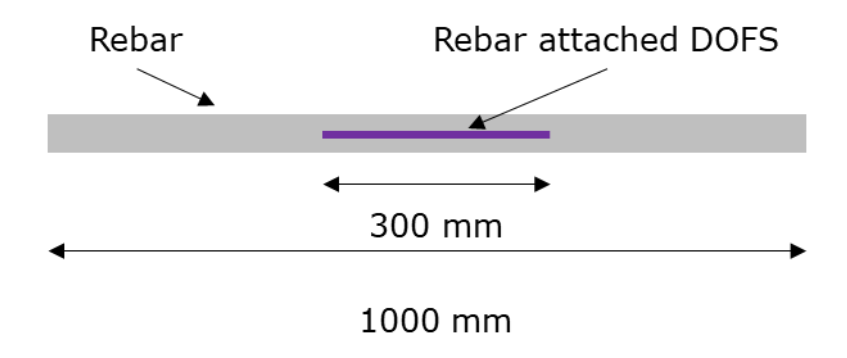
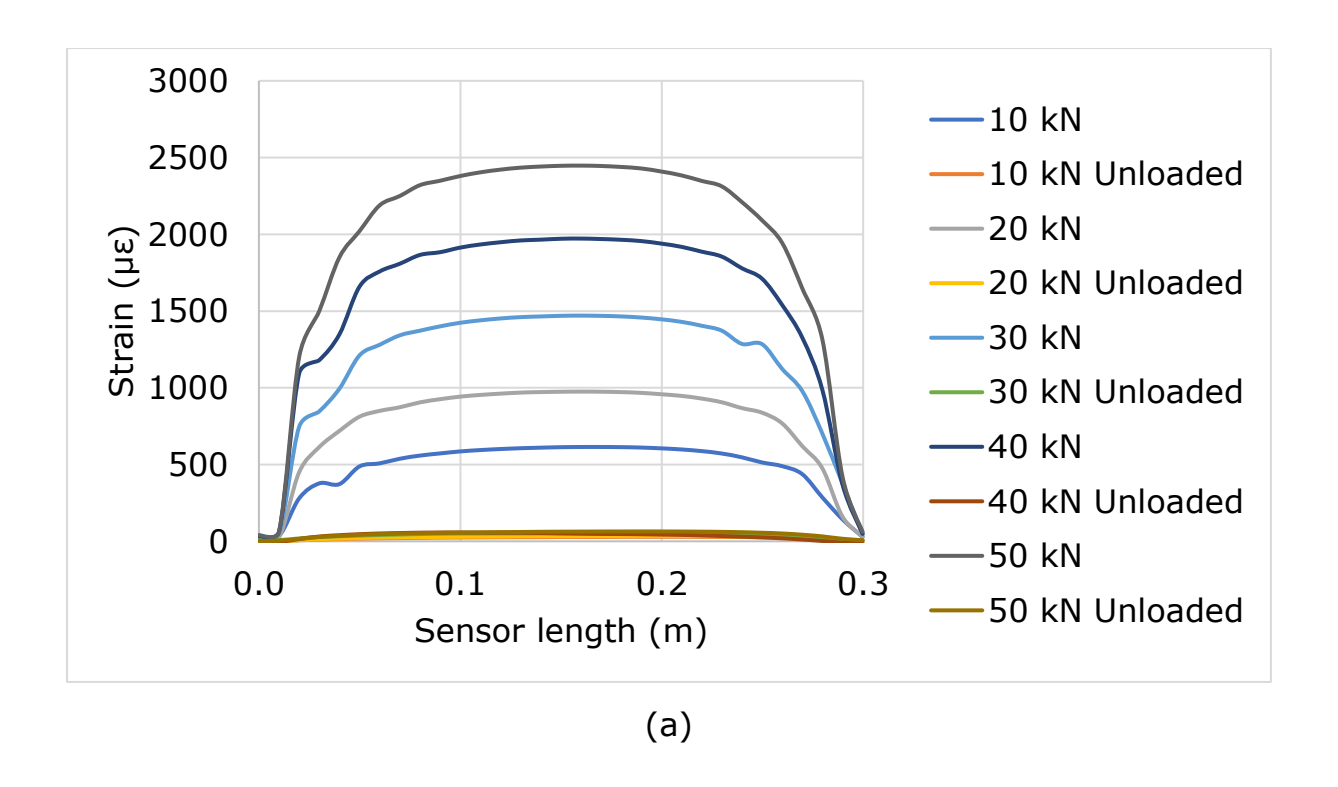


Figure 5.24: Schematic diagram of rebar with attached DOFS



Figure 5.25: Experimental setup of rebar testing



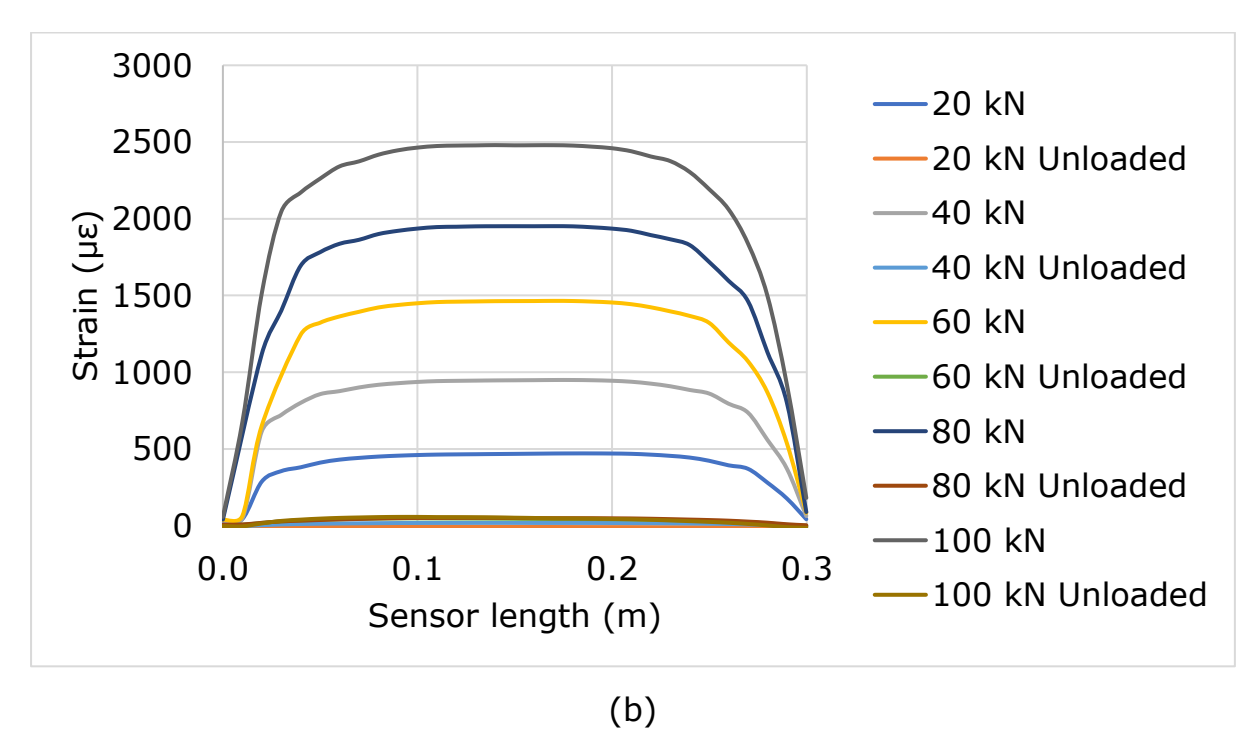


Figure 5.26: Rebar strain variation at loading and unloading (a) 12 mm diameter; (b) 16 mm diameter

Figure 5.26 (a) and (b) show the strain variations of rebar size 12 mm and 16 mm during loading and unloading. The rebars were strained up to a maximum of 2500  $\mu\epsilon$ , but the results indicate that the residual strain

on the rebars is insignificant. This concludes that the impact of adhesive on residual strain is negligible.

### 5.3.6. Rebar and surface strain - R20C60

Figure 5.27 illustrates the experimental rebar strain detected across the sensor length, with a maximum strain of 790  $\mu\epsilon$  recorded. The strain peaks were confined to the 1.0 to 3.0 m range. This is because the loading arrangement in the experiment had a relatively short-span of 600 mm, meaning that the applied load was concentrated within that small area. As a result, the strain readings were also concentrated within that sensor area.

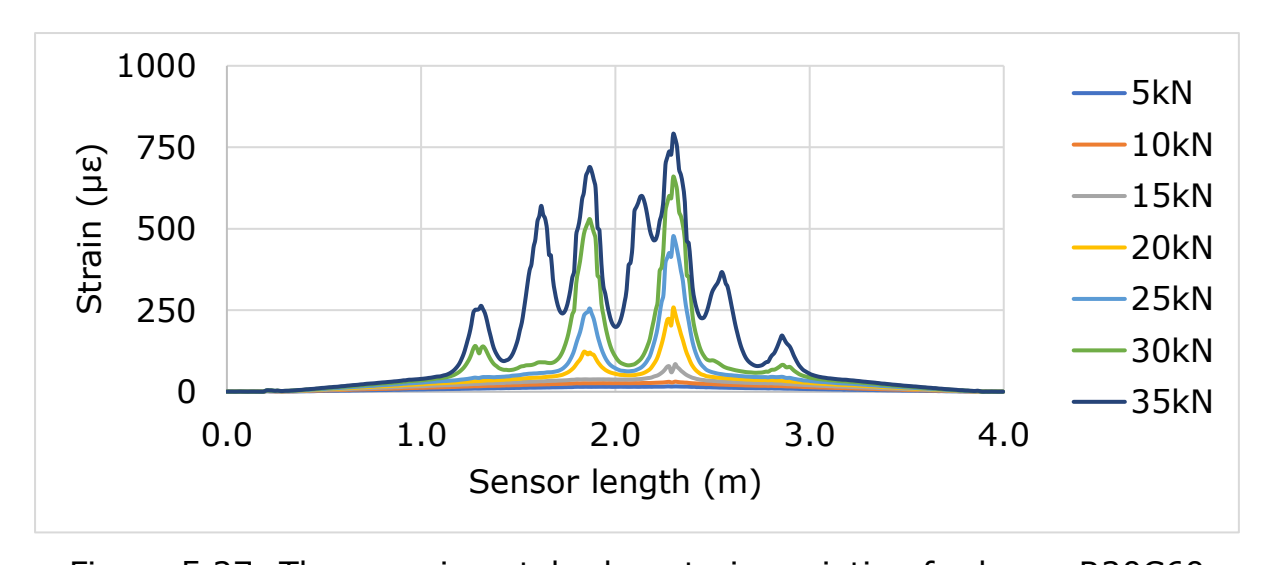


Figure 5.27: The experimental rebar strain variation for beam R20C60

Figures 5.28 and 5.29 illustrate experimental data on strain measured on the concrete specimen's bottom and side surfaces, respectively. Only a limited number of strain peaks were noted in both figures, up to a load of 30 kN. The maximum strain recorded for the bottom sensor at this load level was 3354  $\mu\epsilon$  and 4010  $\mu\epsilon$  at 35 kN for the side sensor.

Figure 5.29 displays the experimental data on strain measured on the side surface of the concrete beam. As the load increased, new strain peaks appeared, indicating the development of concrete cracks. Specifically, new peaks have unexpectedly appeared in the side sensor graph between 30

and 35 kN. Interestingly, the peak strain positions of the side sensor at 35 kN are well aligned with the peak strain positions of the rebar at 35 kN, which can be identified in Figure 5.27. This alignment of peak strains indicates damage in the concrete near the reinforcing bar.

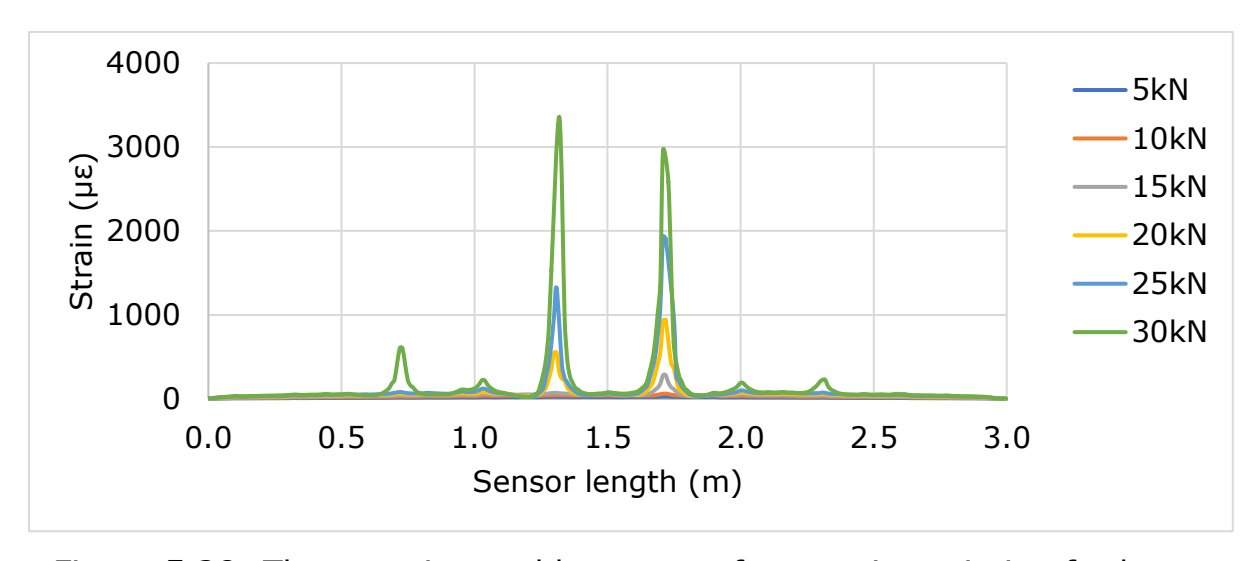


Figure 5.28: The experimental bottom surface strain variation for beam R20C60

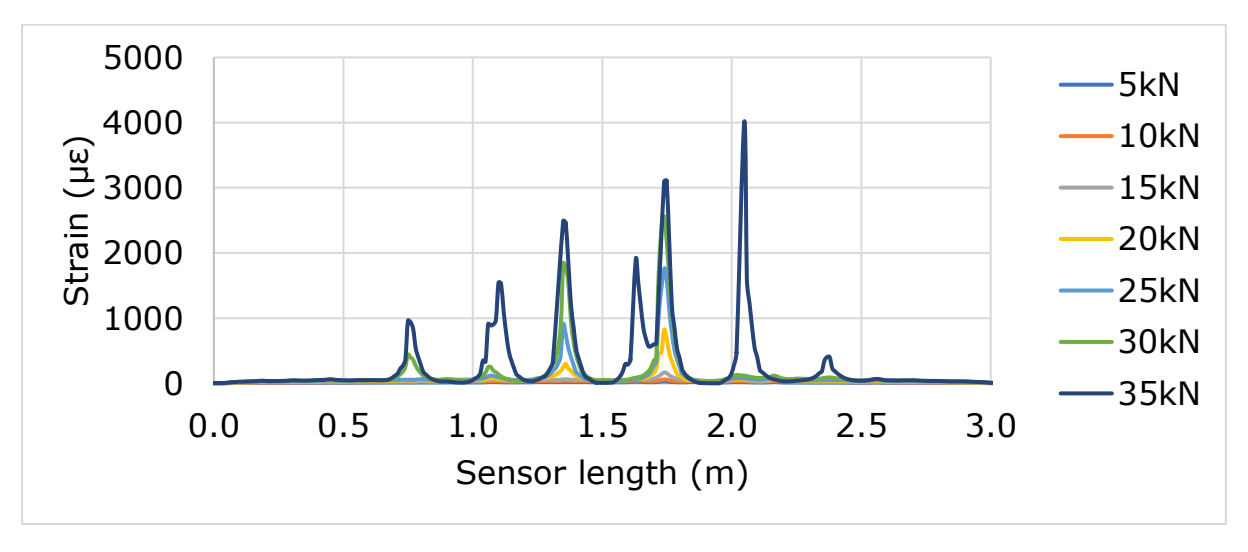


Figure 5.29: The experimental side surface strain variation for beam R20C60

## 5.3.7. Rebar and surface strain - R16C60

Asymmetric loading is an essential consideration in structural engineering, as it can significantly affect the behaviour and performance of

a structure. When a structure is subjected to asymmetric loading, the resulting stresses and strains can be distributed unevenly. Therefore, testing the effects of asymmetric loading on the proposed DL model is crucial for robust SHM predictions.

The beam was asymmetrically loaded, and the variation in rebar strain along the beam under experimental conditions is displayed in Figure 5.30, resulting in two distinct strain peaks of 725  $\mu\epsilon$  and 730  $\mu\epsilon$  under a load of 30 kN. The graph shows that the load-affected area is less than 1 meter along the beam length.

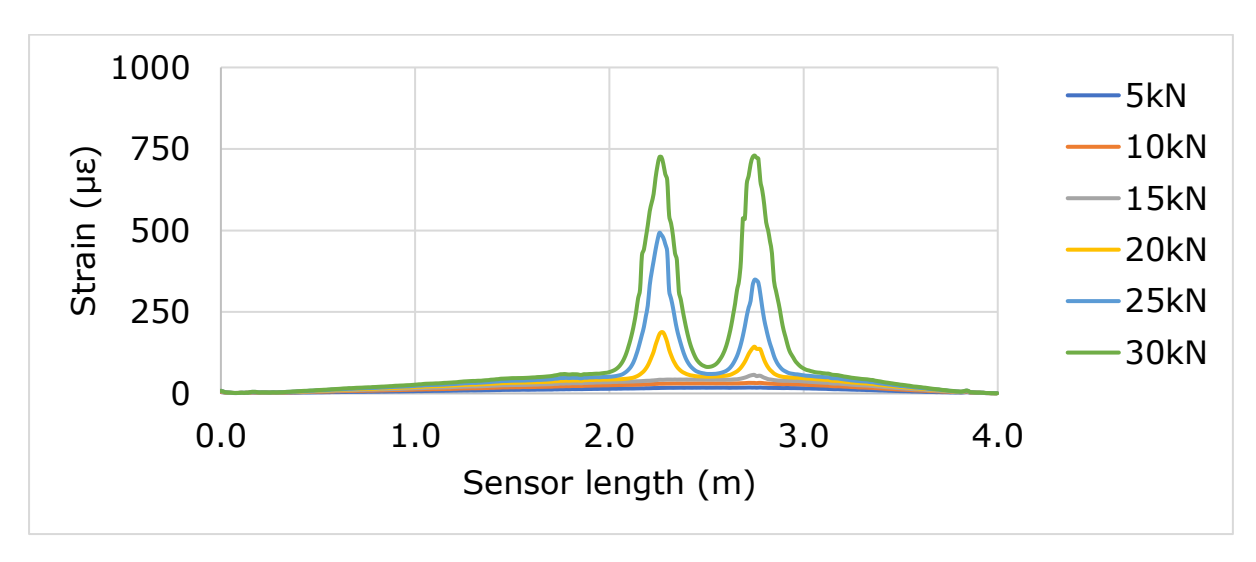


Figure 5.30: The experimental rebar strain variation for beam R16C60

Figures 5.31 and 5.32 present the surface strain variation along the bottom and side sensors. Both graphs display two separate strain peaks closely aligned, particularly when considering their position along the sensor. This concludes that only two cracks occurred during the loading process. The maximum strain recorded for the bottom sensors was 1929  $\mu\epsilon$  at a 25 kN load, while the side sensor recorded a maximum strain of 3759  $\mu\epsilon$ .

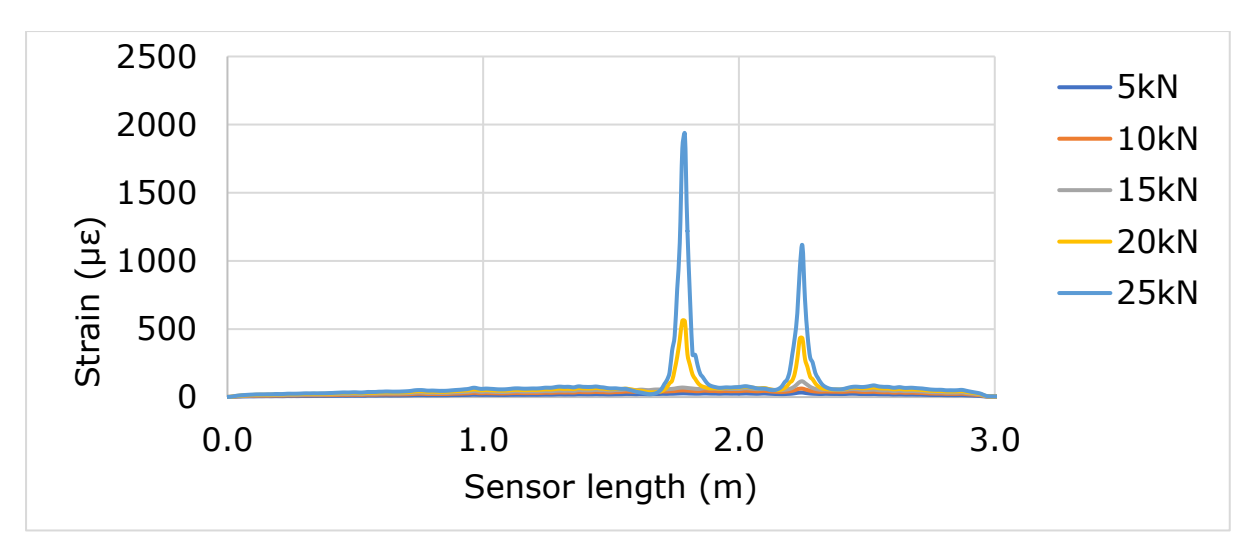


Figure 5.31: The experimental bottom surface strain variation for beam R16C60

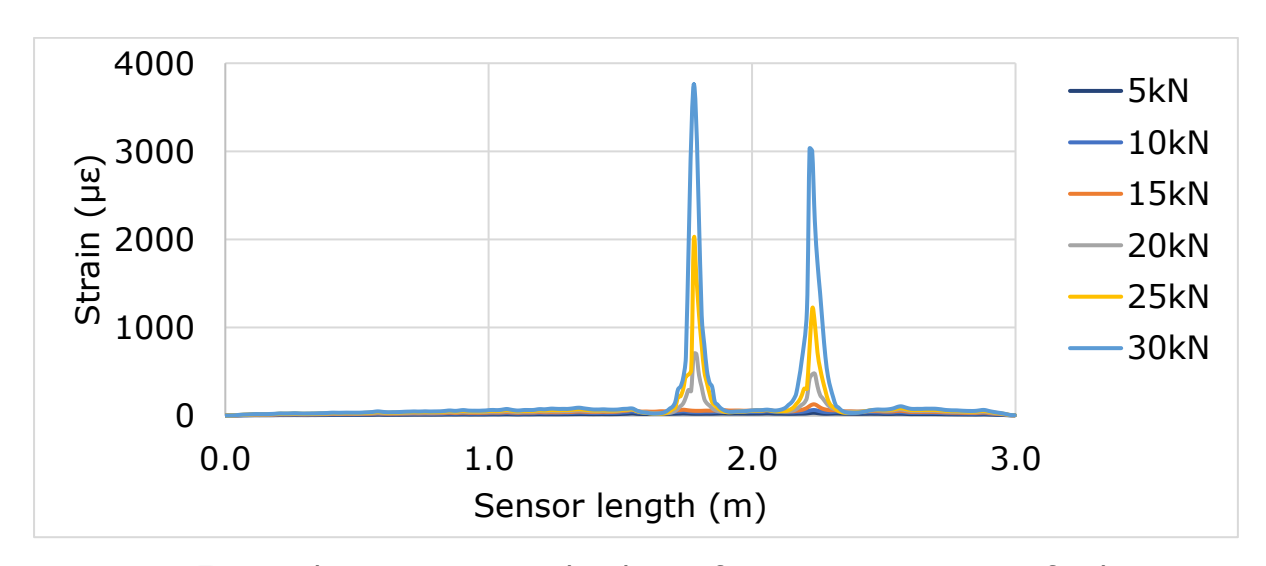


Figure 5.32: The experimental side surface strain variation for beam R16C60

### 5.3.8. Rebar and surface strain - R12C60

Figure 5.33 illustrates the experimental rebar strain for beam R12C60. While two peaks of strain are visible, one peak is more prominent than the other, indicating a maximum strain of 649  $\mu\epsilon$ . This suggests that the corresponding crack is larger in size compared to the other one. The difference between the values of the two strain peaks is 462  $\mu\epsilon$ .

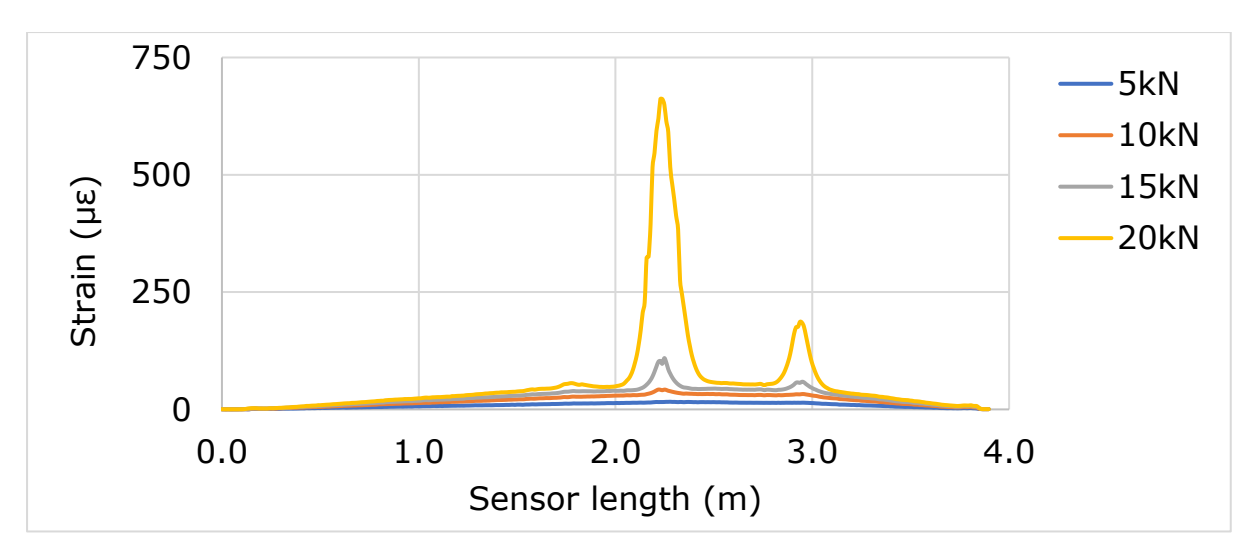


Figure 5.33: The experimental rebar strain variation for beam R12C60

Figures 5.34 and 5.35 depict the surface strain variation along the bottom and side sensors, respectively. The cracked length observed in both graphs is less than 1m. Two peaks of strain are visible, and one peak is more pronounced than the other, consistent with the findings described in Figure 5.33.

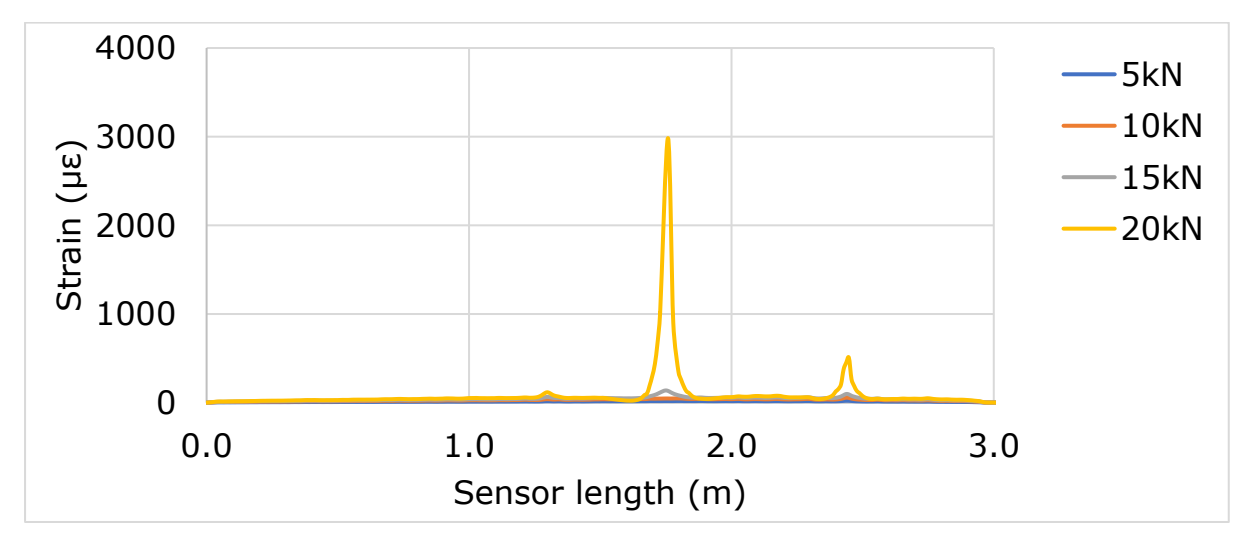


Figure 5.34: The experimental bottom surface strain variation for beam R12C60

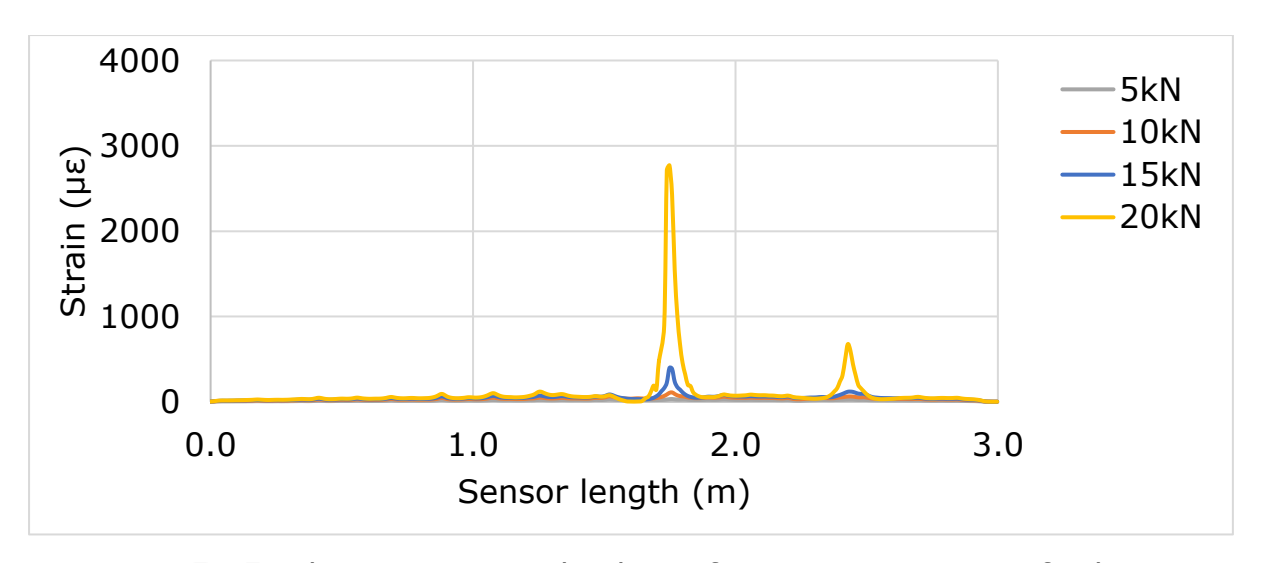


Figure 5.35: The experimental side surface strain variation for beam R12C60

## 5.4. DL model training and testing with experimental data

Within this section, the DL model developed in Chapter 3 underwent training using strain data extracted through FEA, followed by testing the DL model by experimental strain data acquired by DOFS. The optimal number of neurons was determined to achieve the highest training accuracy through a trial-and-error approach during the training process. This approach was preferred due to its flexibility and ability to provide faster initial results.

The task involved using strain data obtained from a surface sensor path in an FEA model as input to determine the rebar status (i.e., whether the present rebar strain had exceeded/or not) as output. An ANN was proposed to achieve this, with the output layer consisting of an output node. The output node was assigned a value of "1" (if the limit was exceeded) or "0" (if the limit was not exceeded) based on the rebar yield limit of 2500  $\mu\epsilon$ . The initial training of the ANN was conducted using a dataset of shortspan RC beams.

## 5.4.1. Short-span RC beams

The ANN suggested in this investigation consisted of 25 input neurons, with 15 neurons in the first hidden layer, 10 neurons in the second

hidden layer, and a single output neuron. The DL model was trained to predict the rebar tension status by 20% for this study.

The model's training accuracy was 99.91%, while its validation accuracy was 99.85%. Recall and precision were 0.9975 and 0.9972, respectively. Figures 5.36 and 5.37 display the proposed ANN for short-span RC beams and model accuracy plots, respectively. Five experimental data sets under multiple load regimes were inserted to evaluate the DL model, and Table 5.3 presents the outcomes.

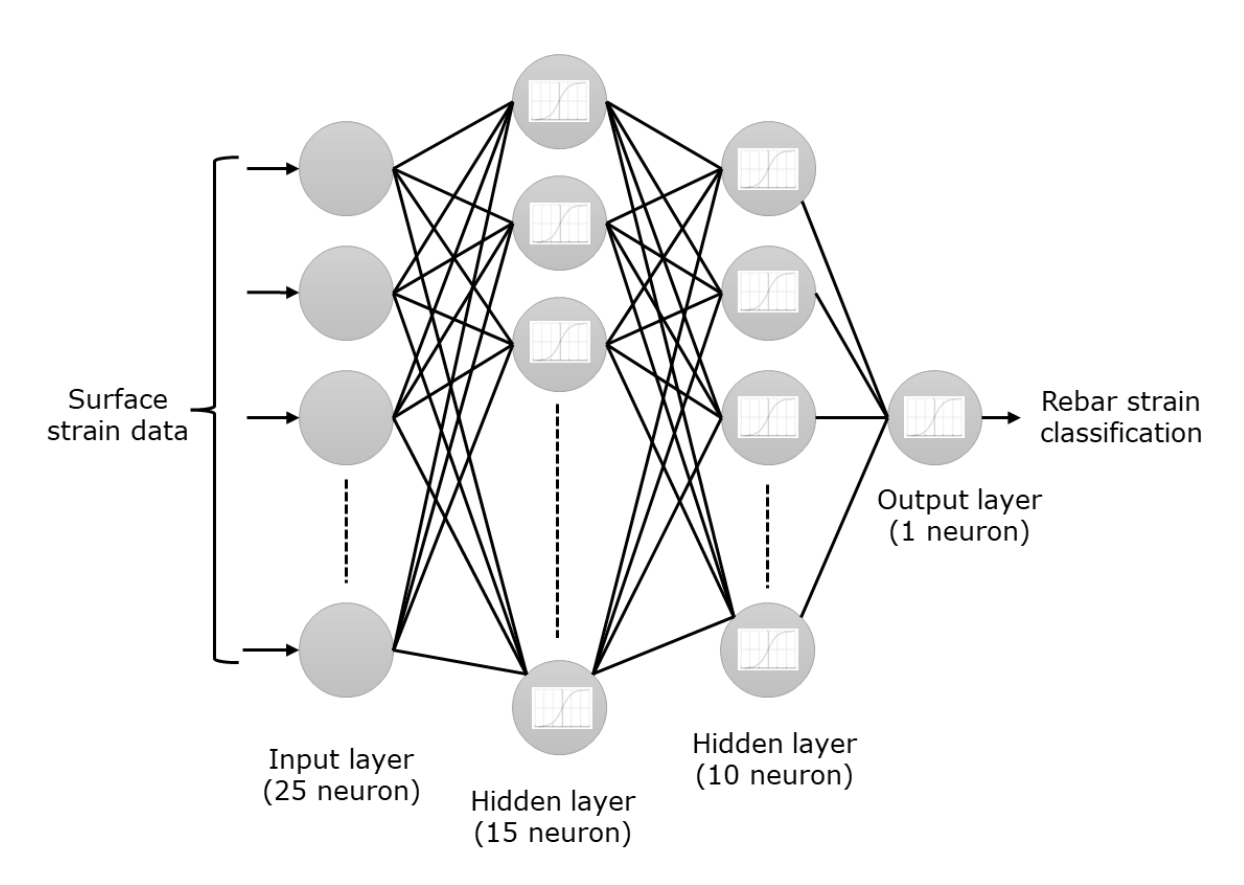


Figure 5.36: Proposed ANN for short-span RC beams

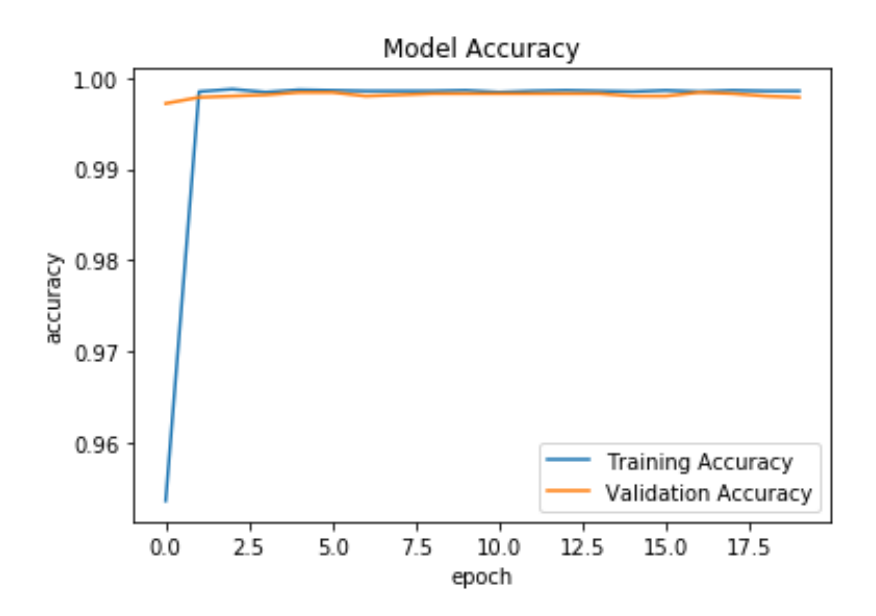


Figure 5.37: DL model accuracy vs number of epochs

Table 5.3: Comparison of experimental outcome vs predicted outcome of the DL model

Experimental	DOFS	Prediction of the DL model	
surface strain	measured	0 - 500 με limit not exceeded in the	
dataset (s)	maximum	rebar	
	rebar	1 - 500 με limit exceeded in the	
	strain (με)	rebar (20% limit)	
15	59	0	
30	411	0	
45	513	1	
60	660	1	
75	766	1	

The study findings reveal that the DL model developed could accurately categorise rebar strain by using experimental strain data for short-span RC beams. However, the created DL model should be capable

of predicting the structural health of long-span RC beams in concrete structures. More information is provided under the following heading.

## 5.4.2. Long-span RC beams

The DL model was trained using the R20C30 dataset containing 75,000 data points. The ANN employed in this study comprised 101 input neurons, 10 neurons in the first hidden layer, 8 neurons in the second hidden layer, and 1 output neuron. The model was trained to predict the rebar tension statuses at 10% increments from 10% to 90%, with the yield strain of steel as 2500  $\mu\epsilon$ . To evaluate the model performance, accuracy, precision, and recall were used for each case. Figure 5.38 shows the proposed ANN for long-span RC beams.

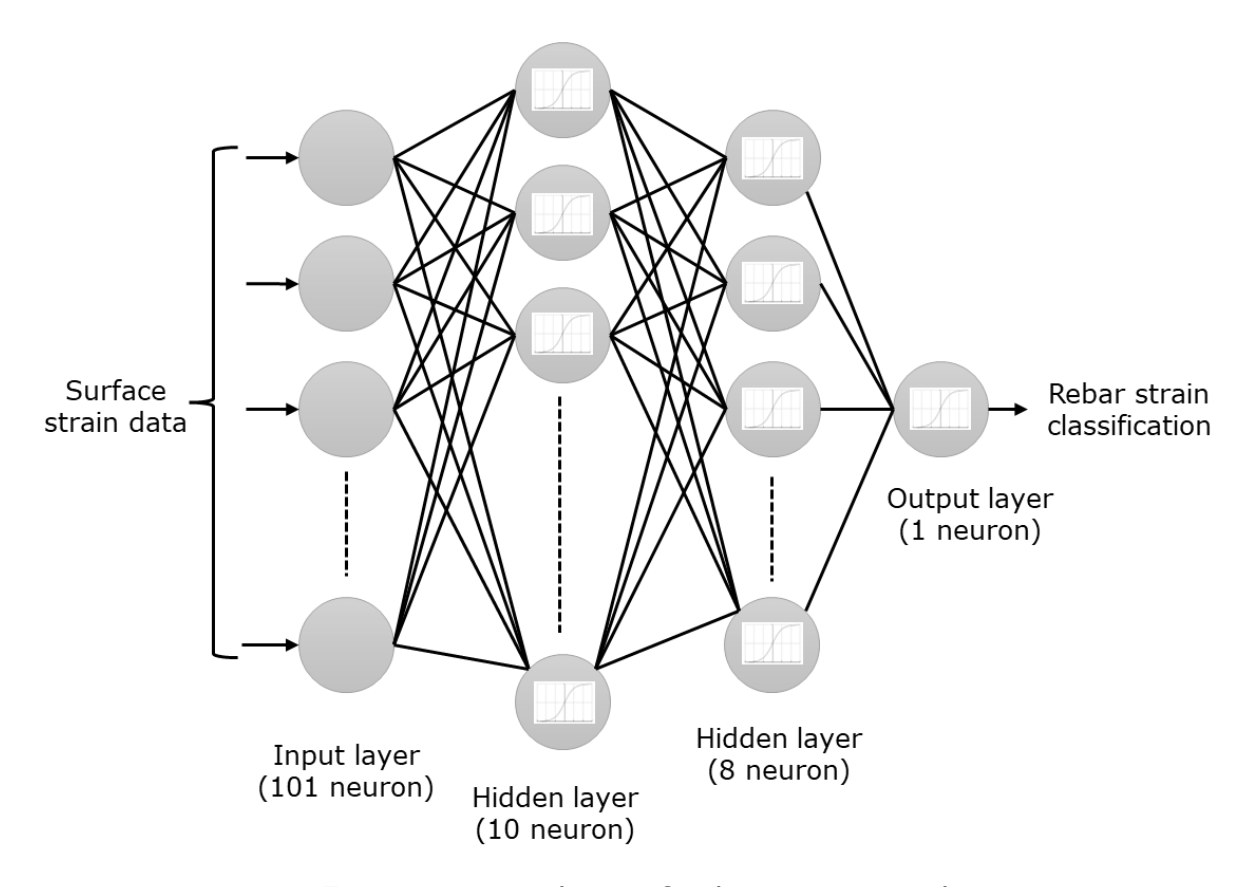


Figure 5.38: Proposed ANN for long-span RC beams

After training, the DL model was used to predict the rebar tension state for experimental data obtained using DOFS. Table 5.4 presents the

assigned classes for each rebar tension state, while Table 5.5 provides guidance for prediction. Table 5.6 shows the results of the DL model's predictions for the experimental data obtained from the bottom sensor and side sensor for beams R12C30, R16C30, and R20C30, respectively.

Table 5.4: Assigned classes

Class	Rebar tension state
Class 0	Rebar is strained within 0 με - 250 με
Class 1	Rebar is strained within 251 με - 500 με
Class 2	Rebar is strained within 501 με - 750 με
Class 3	Rebar is strained within 751 με - 1000 με
Class 4	Rebar is strained within 1001 με - 1250 με
Class 5	Rebar is strained within 1251 με – 1500 με
Class 6	Rebar is strained within 1501 με - 1750 με
Class 7	Rebar is strained within 1751 με - 2000 με
Class 8	Rebar is strained within 2001 με - 2250 με

Table 5.5: Guide for predictions

Colour	Description
	Correct prediction
	Incorrect prediction

Table 5.6: DL model predictions for R20C30, R16C30, and R12C30

Beam, loading	Load	Maximum	Rebar tension
and sensor	(kN)	experimental rebar	state
description		strain (με) in the	prediction
		input data set	
R20C30 bottom	10	71	Class 0
sensor	20	185	Class 0
	30	438	Class 1
	40	638	Class 2

R20C30 side	10	71	Class 0
sensor	20	185	Class 0
	30	438	Class 1
	40	638	Class 1
	50	823	Class 2
	60	992	Class 3
R16C30 bottom	5	25	Class 0
sensor - first	10	74	Class 0
stage up to 25 kN	15	127	Class 0
	20	266	Class 0
	25	434	Class 0
R16C30 side	5	25	Class 0
sensor - first	10	74	Class 0
stage up to 25 kN	15	127	Class 0
	20	266	Class 0
	25	434	Class 0
R16C30 bottom	5	232	Class 0
sensor – second	10	287	Class 0
stage up to 25 kN	15	346	Class 0
	20	408	Class 0
	25	469	Class 0
R16C30 side	5	232	Class 1
sensor – second	10	287	Class 1
stage up to 25 kN	15	346	Class 1
	20	408	Class 0
	25	469	Class 0
R16C30 bottom	5	247	Class 0
sensor – third	10	309	Class 0
stage up to 30 kN	15	370	Class 0
	20	439	Class 0
	25	494	Class 0

	30	645	Class 1
R16C30 side	5	247	Class 1
sensor - third	10	309	Class 1
stage up to 40 kN	15	370	Class 0
	20	439	Class 0
	25	494	Class 0
	30	645	Class 1
	35	826	Class 2
	40	993	Class 2
R12C30 bottom	5	18	Class 0
sensor – first	10	80	Class 0
stage up to 15 kN	15	492	Class 1
R12C30 side	5	18	Class 0
sensor - first	10	80	Class 0
stage up to 15 kN	15	492	Class 1
R12C30 bottom	5	391	Class 1
sensor – second	10	471	Class 1
stage up to 15 kN	15	586	Class 1
R12C30 side	5	391	Class 1
sensor – second	10	471	Class 1
stage up to 15 kN	15	586	Class 1
R12C30 bottom	5	344	Class 1
sensor – third	10	414	Class 1
stage up to 20 kN	15	498	Class 1
	20	776	Class 3
R12C30 side	5	344	Class 1
sensor – third	10	414	Class 1
stage up to 20 kN	15	498	Class 1
	20	776	Class 1

Despite achieving high scores for training accuracy, validation accuracy, precision, and recall (all above 99%), the model's class prediction accuracy was only 56% for experimental data, correctly predicting 36 out of 64 cases. The accuracy of predicting beam R20C30 was 80% because the DL model was trained using the R20C30 dataset, resulting in higher prediction accuracy for that particular beam. However, other beams had lower prediction accuracy. This indicates that the model is unreliable for making accurate predictions and requires further improvements.

Instead of using raw distributed R20C30 FEA strain data as inputs to the DL model, a study was conducted to train the DL model by basic statistical parameters such as maximum, minimum, average, and standard deviation, which were calculated for each row data in the R20C30 strain dataset. After optimising the model using these parameters, the DL model performed well using only maximum, minimum, and average strains as input training parameters. As a result, the proposed ANN will use these parameters as inputs for future studies. Figure 5.39 presents the proposed ANN with new input parameters.

On the basis of this foundational knowledge, a deeper delve into the parametric analysis reveals more nuanced details. To improve the performance of the DL model and streamline its input parameters, a comprehensive sensitivity analysis was conducted. This investigation investigated the accuracy of predictions derived from various statistical parameters and their combinations as summarises in Table 5.7. Individual reliance on the Minimum parameter resulted in an accuracy of 4.16%. However, the Maximum and Average parameters, when used separately, exhibited significantly superior accuracy, with values of 60.45% and 53.12%, respectively. Notable is the observation regarding combined parameters: while a pairing of Minimum and Maximum obtained a 64.58% accuracy rate, the combination of Minimum and Average significantly outperformed other sets, achieving an impressive 77.08% accuracy rate. Surprisingly, combining Maximum and Average produced an accuracy of 53.12%, identical to that of the Average parameter alone. This nuanced

investigation not only validates the crucial roles of the Maximum and Average parameters, but also highlights the combined effectiveness of the Minimum and Average parameters in the predictive model. Such discoveries have significant ramifications for future DL model configurations, highlighting the importance of judicious parameter selection for optimal performance.

Table 5.7: Sensitivity analysis of input parameters

	Input Parameter	Prediction Accuracy (%)
1	Minimum	4.16
2	Maximum	60.41
3	Average	53.12
4	Minimum and Maximum	64.58
5	Minimum and Average	77.08
6	Maximum and Average	53.12

Table 5.8 summarises the performance indicators of the DL model after training with stat parameters, which include the maximum training accuracy, validation accuracy, precision, and recall for each rebar strain limit. Table 5.8 presents the DL model predictions for R20C30, R16C30, R12C30, R20C30, R16C30, and R12C30.

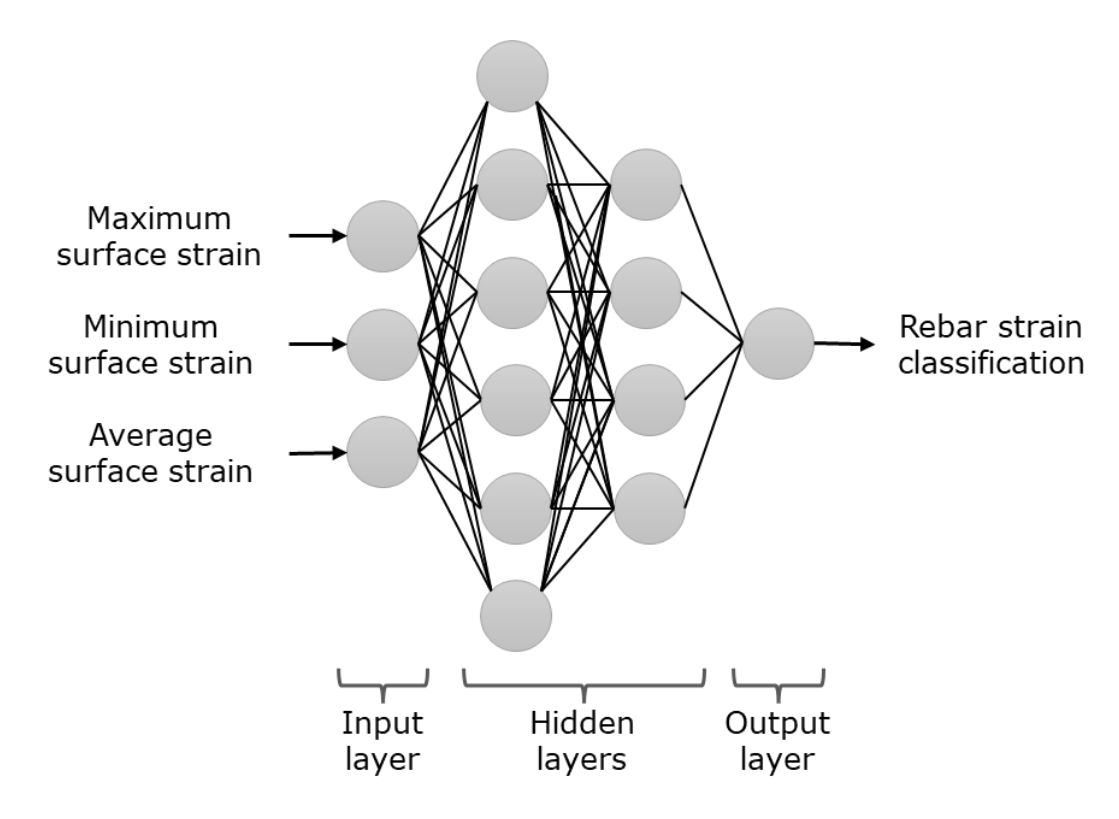


Figure 5.39: Proposed ANN with new input parameters

Table 5.8: DL Model performance indicators – Training with stat parameters

Model training	Model performance			
(Rebar strain	Training	Validation	Precision	Recall
limits)	accuracy	accuracy		
	(%)	(%)		
10%	99.80	99.75	0.9995	0.9961
20%	99.41	99.45	0.9944	0.9933
30%	99.45	99.37	0.9944	0.9950
40%	98.92	98.99	0.9919	0.9888
50%	99.24	99.20	0.9918	0.9929
60%	99.21	99.28	0.9909	0.9932
70%	98.96	98.98	0.9874	0.9892
80%	98.96	98.88	0.9873	0.9930
90%	98.64	98.51	0.9831	0.9899

Table 5.9: The DL model predictions for R20C30, R16C30, R12C30, R20C30, R16C30, and R12C30

Beam, loading and	Load	Maximum	Rebar tension
sensor description	(kN)	experimental	state
		rebar strain	prediction
		(με) in the	
		input data set	
R20C30 bottom	10	71	Class 0
sensor	20	185	Class 1
	30	438	Class 1
	40	638	Class 2
R20C30 side sensor	10	71	Class 0
	20	185	Class 1
	30	438	Class 1
	40	638	Class 2
	50	823	Class 3
	60	992	Class 3
R16C30 bottom	5	25	Class 0
sensor - first stage up	10	74	Class 0
to 25 kN	15	127	Class 0
	20	266	Class 1
	25	434	Class 1
R16C30 side sensor -	5	25	Class 0
first stage up to 25 kN	10	74	Class 0
	15	127	Class 0
	20	266	Class 1
	25	434	Class 1
R16C30 bottom	5	232	Class 0
sensor – second stage	10	287	Class 1
up to 25 kN	15	346	Class 1
	20	408	Class 1

	25	469	Class 1
R16C30 side sensor –	5	232	Class 1
second stage up to 25	10	287	Class 1
kN	15	346	Class 1
	20	408	Class 1
	25	469	Class 1
R16C30 bottom	5	247	Class 1
sensor – third stage	10	309	Class 1
up to 30 kN	15	370	Class 1
	20	439	Class 1
	25	494	Class 1
	30	645	Class 1
R16C30 side sensor –	5	247	Class 1
third stage up to 40	10	309	Class 1
kN	15	370	Class 1
	20	439	Class 1
	25	494	Class 1
	30	645	Class 1
	35	826	Class 2
	40	993	Class 2
R12C30 bottom	5	18	Class 0
sensor – first stage up	10	80	Class 0
to 15 kN	15	492	Class 1
R12C30 side sensor –	5	18	Class 0
first stage up to 15 kN	10	80	Class 0
	15	492	Class 1
R12C30 bottom	5	391	Class 1
sensor – second stage	10	471	Class 1
up to 15 kN	15	586	Class 1
	5	391	Class 1
	10	471	Class 1

R12C30 side sensor –	15	586	Class 1
second stage up to 15			
kN			
R12C30 bottom	5	344	Class 1
sensor – third stage	10	414	Class 1
up to 20 kN	15	498	Class 1
	20	776	Class 1
R12C30 side sensor –	5	344	Class 1
third stage up to 20	10	414	Class 1
kN	15	498	Class 1
	20	776	Class 2
R20C60 bottom	5	17	Class 0
sensor	10	31	Class 0
	15	85	Class 0
	20	258	Class 1
	25	476	Class 1
	30	659	Class 1
R20C60 side sensor	5	17	Class 0
	10	31	Class 0
	15	85	Class 0
	20	258	Class 0
	25	476	Class 1
	30	659	Class 1
	35	790	Class 2
R16C60 bottom	5	18	Class 0
sensor	10	32	Class 0
	15	57	Class 0
	20	188	Class 0
	25	493	Class 1
R16C60 side sensor	5	18	Class 0
	10	32	Class 0

	15	57	Class 0
	20	188	Class 0
	25	493	Class 1
	30	730	Class 2
R12C60 bottom	5	9	Class 0
sensor	10	20	Class 0
	15	35	Class 0
	20	614	Class 1
R12C60 side sensor	5	9	Class 0
	10	20	Class 0
	15	35	Class 0
	20	614	Class 1

According to Table 5.9, the DL model's class prediction accuracy was deemed acceptable, achieving a success rate of 81.25% (76 out of 96). The incorrect predictions can be separated into two categories. Firstly, incorrect predictions are possible if the actual rebar strain is extremely close to the limit that defines the classes. Secondly, as previously discussed in Section 5.3.3, the experimental rebar strain exhibited a "wavy behaviour" as loading increased, compared to the simulated rebar strain, which resulted in inaccurate predictions. Despite these limitations, the model's accuracy remains satisfactory as the DL model provided reliable predictions for both symmetric and asymmetric loading conditions. Hence, it can be utilised as the most suitable model to assess the structural health of RC beams.

It is recommended to analyse the results based on individual sensors. The attached bottom sensor was analysed initially, achieving an 84.45% accuracy rate by correctly predicting 38 out of 45 observations. The side sensor had a 78.43% accuracy rate, with 40 out of 51 observations predicted correctly. Since the accuracy of both sensors exceeded 78%, the suggested SHM system's usefulness can be improved by using either sensor as a substitute if one fails, thereby eliminating dependence on a single

sensor. However, the bottom sensor was significantly affected by low SSQ values (< 0.15) under increasing loads, despite its 84.45% accuracy. As a result, the author recommends using side sensors instead of bottom sensors for increasing loads.

# 5.4.3. DL model sensitivity analysis

Sensitivity analysis is a vital tool for assessing how the output of a DL model changes when the input parameters are varied. In the context of SHM prediction, sensitivity analysis is crucial for evaluating how changes in input parameters can affect the accuracy and reliability of SHM algorithms in detecting and predicting structural damage. The DL model's performance with limited information can be evaluated by limiting the input data. Therefore, to assess model robustness, the performance of the statistical parameter-based DL model with limited strain input data was evaluated. The DL model inputs, maximum, minimum, and average strain, were calculated considering this limited data input. This was conducted in two phases.

During the initial stage of the model assessment, strain data were obtained, as illustrated in Figure 5.40. Specifically, 25% of the sensor data was chosen for each segment, and the entire experimental dataset, consisting of 96 data points from the Experimental stage of long-span beam size, was evaluated. Table 5.10 presents the sensitivity analysis results using the proposed method during the first phase.

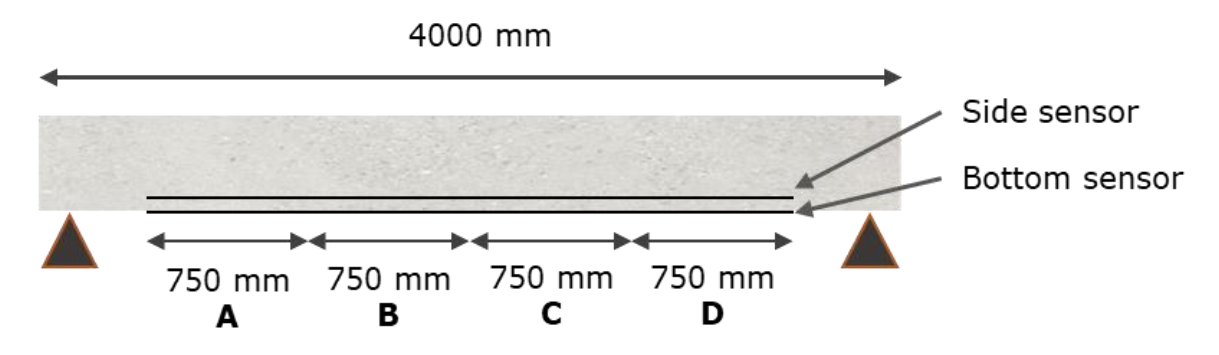


Figure 5.40: Strain data extracting segments for phase 1

Table 5.10: Sensitivity analysis for Phase 1

Segment	Prediction accuracy (%)
А	54
В	69
С	79
D	54

The information in Table 5.9 indicates that the accuracy obtained using strain data from Segment A and Segment D is the lowest at 54%. On the other hand, Segment B yields an accuracy of 69%, while Segment C provides the highest accuracy of 79%.

Segment C achieved the highest accuracy level because the asymmetric loading was applied above this segment, which positively impacted the increase in accuracy. The underlying reasons for higher accuracies obtained in segments C and D could be that these sections exhibit more strain variation than other sections. Consequently, data will be selected from the central region of the sensor to conduct phase 2 of the sensitivity analysis.

Figure 5.41 indicates that the sensitivity analysis for Phase 2 involved introducing strain data from the centre of the beam, beginning at 10% and increasing in 10% (0.3 m) increments up to 100%. Meanwhile, Figure 5.42 illustrates how the prediction accuracy varies concerning the percentage of input data.

As per Figure 5.42, the accuracy of prediction increases with the percentage of input data, but the rate of increase gradually diminishes. The data indicate that prediction accuracy begins at 52% when there is 10% input data and rises steadily to 81% when there is 100% input data. However, the rate of increase in accuracy decreases as the percentage of input data increases. For instance, there is a 22%-point increase in accuracy when the input data increases from 10 to 20%, but only a one per cent point increase in accuracy when the input data increases from 80 to 90%.

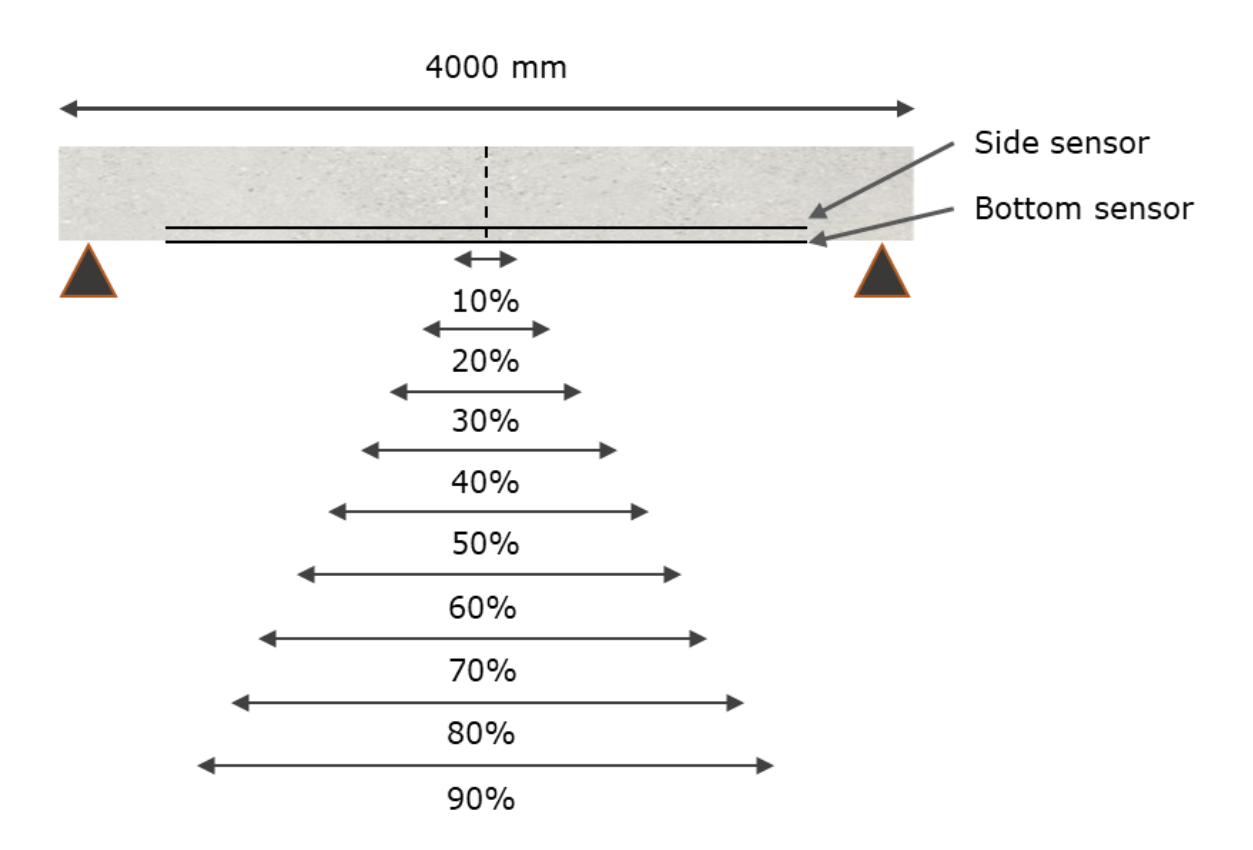


Figure 5.41: Strain data extracting segments for phase 2

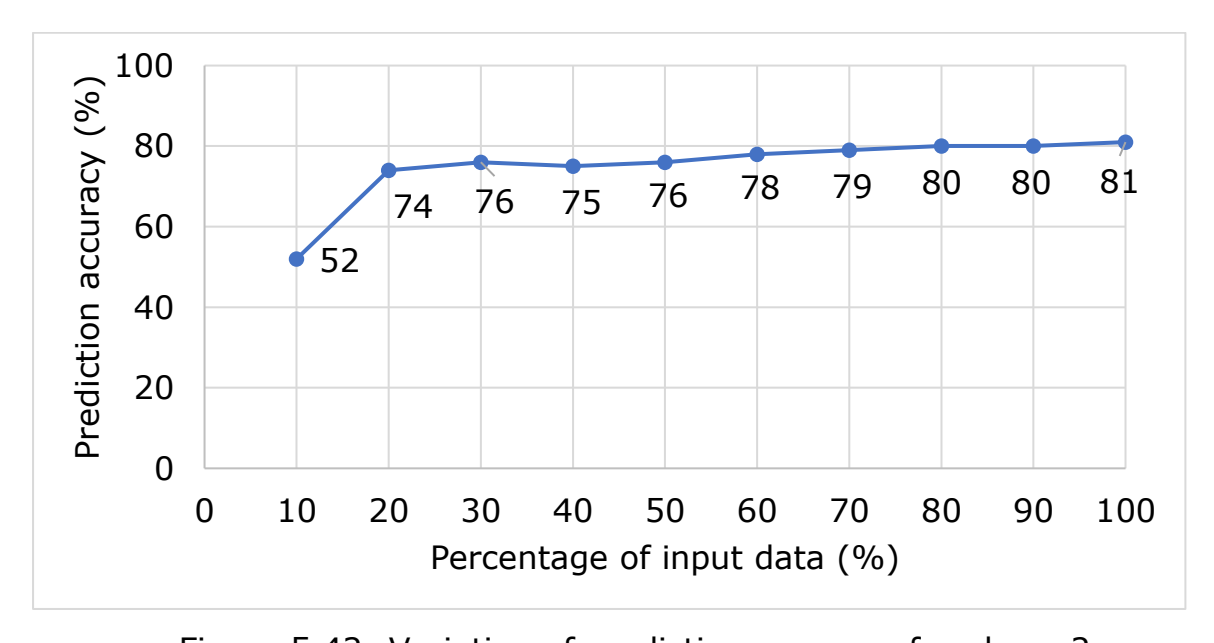


Figure 5.42: Variation of prediction accuracy for phase 2

During the DL model's testing phase, the substantial increase (22%) in predictive accuracy from 10% to 20% of the input data may be attributable to two critical factors.

First, the variation and range of the three parameters maximum strain, minimum strain, and average strain within the first 10% of the test data may make it difficult for the model to make accurate predictions, resulting in a reduced accuracy level. As the model is exposed to the remaining 10% of the test data, the distribution of the parameters may become more closely aligned with the training data, significantly improving predictive performance.

Second, the impact of each parameter on the model's prediction can vary. If, for example, maximum strain is a highly influential parameter and the initial 10% of test data exhibited atypical values for this parameter, the accuracy could be compromised. As the model is evaluated on the remaining 10% of the data, its accuracy will likely increase if these values lie within a more typical range. Even with 20% of the input data, it is evident that an acceptable accuracy level of 74% can be achieved. Therefore, the author recommends using at least 20% of input data with this DL model.

In the field of SHM for RC beams, established techniques such as AE monitoring, vibration-based monitoring, and ultrasonic testing have traditionally set the benchmark. The research introduces a novel framework that employs concrete surface strain as the primary input to a DL model, with the objective of predicting rebar strain classifications. To the best of author's knowledge, this framework for SHM in concrete beams has not been adopted, resulting in a lack of direct benchmarks for this technique.

While broader SHM techniques offer well-established benchmarks in terms of precision and adaptability, this framework's methodology stands out due to its uniqueness. The developed DL model displays a remarkable accuracy of 81.25 percent. Moreover, a sensitivity analysis reveals an accuracy of 74% when only 20% of the input data are utilized, highlighting its robustness. Recognized are the challenges posed by the absence of direct benchmarks for this specific method within the framework. However, it is anticipated that the research will set the groundwork for future studies in this pioneering field. The emergence of benchmarks is anticipated to

facilitate comparisons between studies with comparable objectives as the method gains widespread acceptance.

The primary contribution of this study is the development of a novel and versatile SHM framework that incorporates the capabilities of FOS, FEA, and DL. The primary goal was to develop a method that is adaptable and generalizable across a variety of structural applications. To validate and demonstrate the capability of this framework, RC beams were chosen as the first test subject since these beams could be parts of bigger infrastructure, like bridges, or smaller, simpler constructions in the real world. While the study did concentrate extensively on these beams, it is important to note that the SHM framework's principles are not limited to this specific application. In essence, other researchers and practitioners can adapt the framework to other structural forms, materials, and conditions with relative ease. The primary objective is to provide the community with a structured method that, while tested on RC beams, has the foundational scope to be extrapolated to diverse real-world situations.

Therefore, it provides a foundational model for those who wish to extend this research or employ the framework in various contexts, potentially leading to additional advancements and applications in the broader field of structural health monitoring.

### 5.5. Summary

The chapter presented the study's results on predicting the structural health of concrete beams using DL techniques to aid in maintaining and inspecting civil infrastructure. The chapter covered experimental and simulation results, the model training process, and predictions for symmetric and asymmetric flexural loading.

The strain behaviours of RC beams under flexural loading were investigated using a combination of empirical data and simulations to generate a robust dataset required for model development in an intensive and detailed two-tiered experimental process. The strain pattern and peak strain locations on the beam's concrete and rebar surface correlated with

FEA results, validating the effectiveness of CDP-based FEA for in-depth strain data mining. As a consequence of this preliminary phase, six long-span RC beams (R12C30, R16C30, R20C30, R12C60, R16C60, and R20C60) measuring 4000 mm × 200 mm × 400 mm were subjected to four-point bending tests. A benchmark was established for the predictive simulations of the remaining beams by experimentally validating the strain behaviour of the concrete surface and reinforcing rods of the R20C30 beam. These beams were subjected to both symmetric and asymmetric loading conditions, and strain measurements along sensor lengths were meticulously recorded under varying loading conditions to generate a comprehensive dataset. This data-driven, holistic comprehension of structural integrity is exemplified by using this robust and comprehensive strain data as a test set to evaluate the performance of a DL model in predicting the structural health of RC beams.

The DL model underwent training using the R20C30 dataset, which included 75,000 data points. Of this, 64% was allocated for training, 16% for validation, and 20% for testing. The model was designed to predict rebar tension statuses at 10% increments ranging from 10% to 90%. A study was conducted to incorporate basic statistical parameters such as maximum, minimum, average, and standard deviation instead of using solely distributed strain data as inputs. Optimising the model with these parameters revealed that the model performs well when utilising only maximum, minimum, and average as inputs. The model's class prediction accuracy was acceptable, achieving a success rate of 81.25% (76 out of 96).

Sensitivity analysis assessed the accuracy of DL model predictions. Two phases of sensitivity analysis were conducted using strain data from different sensor segments. The central region of the sensor was selected for Phase 2 after considering Phase 1 results. Notably, the prediction accuracy increases as the percentage of input data increases. Still, the rate of increase slows down, and with only 20% of input data, a reasonable accuracy of 74% can be achieved.

This extensive study anticipates that the experimental results validate the efficacy of CDP-based FEA for strain data mining, thereby reinforcing the foundational integrity of the proposed framework. The presence of a rigorous validation and testing phase within the framework not only ensures its accuracy but also emphasises its dependability. The model's ability to predict structural health is supported by an impressive class prediction accuracy of 81.25% (76 out of 96). The sensitivity analysis demonstrates a remarkable 74% accuracy with only 20% of the input data, indicating its efficacy and practical applicability despite limited data input. The inherent flexibility of the framework, designed to estimate rebar tension statuses in 10% increments, accommodates varying levels of analysis granularity and permits customisation to meet specific needs. In addition, incorporating fundamental statistical parameters such as maximum, minimum, and average as inputs makes the framework more user-friendly and accessible. The robustness of the proposed framework and its potential to pave the way for an innovative, data-driven approach to predicting and comprehending structural integrity is thus reaffirmed.

# CHAPTER 6: CONCLUSIONS AND FUTURE RESEARCH

### 6.1. Overview of the research work

Chapter Six provides a comprehensive overview of the research conducted for this thesis. This chapter reviews the main research findings and their implications for the field, summarises the research contributions presented in this doctoral thesis, and discusses their prospective impact on the field. Finally, it suggests potential areas for future research.

This study's primary outcome was a framework for monitoring the structural health of RC beams using distributed sensor networks, FEA, and DL. The research objectives were identifying critical components for sensor network installation, generating a strain dataset from a validated FEA model for DL model training, designing, and developing sensor attachment methods, and developing a DL model for structural health prediction in RC beams.

This study incorporated a literature review, experimental work, FEA modelling, and developing a DL model to form a framework. The research contributed to a better understanding of SHM in RC beams. It demonstrated the potential of distributed sensor networks, FEA modelling, and DL techniques to improve the safety of these structures.

## 6.2. Summary of the key findings

This research has introduced a new SHM method for RC beams that utilises DOFS, FEA, and DL to anticipate the rebar tension state of a structure while it is subjected to service loads. Key findings from each stage of the research are as follows:

1. The literature review highlighted the significance of identifying critical components in RC beams, choosing appropriate sensors, and the most suitable techniques of FE modelling and DL for SHM. Due to its significant role in flexural failure and its influence on structural health prediction, the rebar was chosen as the most critical component in RC beams in this

- study. DOFS were selected because of their sensitivity and precision in measuring strain along the beam's surface, outperforming conventional strain sensors in this application. A CDP-based FEA model was chosen to accurately simulate the behaviour of concrete beams and bridge the distance between experimental data and predictive modelling. In addition, a DL model based on ANN was selected for structural health prediction.
- 2. This study has successfully created a CDP-based FEA model for SHM applications to comprehend how a detailed FEA model for RC beams can be developed and correlated with experimental data from the DOFS sensor network. It revealed that the CDP-based FEA model correlates well with experimental stain data gathered by the DOFS network, which includes rebar sensors, side surface sensors, and bottom sensors. This admissible correlation demonstrates the model's precision and dependability. The model was validated in two distinct phases to ensure its robustness: the first phase focused on short-span RC beams, and the phase investigated long-span RC beams. second This demonstrates the credibility of the CDP-based FEA model in accurately anticipating the behaviour and integrity of RC structures by analysing the performance of the FEA model under flexural loading.
- 3. The most efficient method for creating a strain dataset from the FEA model for training the DL model was to generate a comprehensive and diverse dataset by strategically varying the dilation angle and the number of steps in the FEA model. This methodology ensures that the dataset encompasses a wide variety of strain scenarios. A comprehensive and diverse dataset is necessary for training a DL model because it enables the model to generalise well to new, unexplored data, thereby enhancing the model's overall performance. A reinforced concrete element has a unique dilation angle. However, the goal is to train how the DL model adapts to variations in the dilation angle, even though these variations may not occur in isolation in practice. A variety of strain patterns ranging from brittle to stiffer conditions were

introduced into the dataset by modifying the dilation angle in the FEA model. Concrete is a complex and heterogeneous material with inherent uncertainties and variations in its characteristics. It was expected that considering various dilation angles would help the SHM prediction model to enhance robustness and uncertainty quantification. Changing the number of FEA model steps is an additional essential aspect of the method. This parameter controls the granularity and resolution of the generated strain data, allowing the dataset to contain a range of levels of detail.

- 4. In the SHM context, it can be difficult to secure optimally and position sensors on the concrete surface and rebars of RC beams. The sensor attachment method and installation procedures devised in this study effectively addressed these obstacles. As the attachment method, two varieties of adhesive bonding using a two-component epoxy glue were chosen due to their numerous benefits, including ease of installation, durability, and minimal interference with the RC beam's structural integrity. The installation procedures were meticulously designed, considering variables such as surface preparation, curing time, and environmental conditions to ensure accurate sensor positioning - a crucial aspect for accurate strain measurements. The secure and optimal positioning of sensors enabled precise strain monitoring on the RC beams, resulting in accurate measurements for the DL model's input. By implementing these methods and procedures, the study accomplished a high level of reliability and precision in measuring the surface and rebar strain of RC beams, with potential applications in real-world structures.
- 5. The DL model was created to predict the structural health of RC beams using data obtained by the DOFS sensor network. This network is comprised of two types of concrete surface sensors: attached to the bottom surface and side surface, which monitor the structural health under several loading conditions, such as symmetric and asymmetric loads. The DL model's performance and its applicability for evaluating the structural health of concrete beams were assessed based on the

accuracy of its predictions. The outcomes demonstrate that the DL model performs well, attaining an overall accuracy of 81.25% (predicting 76 out of 96 instances correctly) for symmetric and asymmetric loading conditions. Each sensor's accuracy was analysed under section 5.4.2 to better understand the model's efficacy. The bottom sensor's accuracy rate was 84.45%, while the side sensor's accuracy rate was 78.43%. The comparably high levels of accuracy of both sensors enable their potential interchangeability or replacement. Due to its comparable accuracy in measurement, the alternative sensor could preserve the integrity of data collection in the event of sensor failure or unavailability. This interchangeability ensures data integrity and provides operational continuity during critical situations, thereby enhancing the system's overall robustness and resilience. In addition, this strategy offers practical and cost-effective benefits, as it eliminates the need for specific alternatives for each sensor type. This adaptability increases the robustness of the proposed SHM system by reducing its reliance on a single sensor type and assuring continued operation. The sensitivity analysis indicates that 74% accuracy can be achieved with just 20% of input data. This suggests that the model can make accurate predictions with a limited amount of data.

### **6.3. Summary of the contributions**

This doctoral thesis has significantly contributed to the field of SHM of the RC beams through the research presented. Following is a summary of key contributions:

1. A Comprehensive SHM Framework for RC Beams: This study presents an innovative framework for SHM in RC beams, including identifying critical components, the design of sensor attachment methods, generation of a strain dataset from a validated FEA model, and the development of a DL model for structural health prediction. This exhaustive framework will serve as a guide for future research in the sector and enhance the potential for SHM applications in RC structures.

- 2. CDP-Based FEA Model: The development and validation of a CDP-based FEA model for SHM applications in RC beams is a notable contribution of this study. This model precisely simulates the behaviour of RC beams under various loading conditions and provides a dependable method for generating strain datasets for DL model training. In addition, the validation of the model on both short and long-span RC beams by using strain data demonstrates its versatility and applicability across a wide range of structural dimensions.
- 3. Strain Dataset Generation Methodology: The research has developed a method for generating an exhaustive and diverse strain dataset from the FEA model. The proposed method, which entails varying the dilation angle and number of steps in the FEA model, ensures that the dataset contains a wide variety of strain scenarios, thereby augmenting the overall performance of the DL model.
- 4. Sensor Attachment Method and Installation Procedures: The research has produced reliable methods and procedures for installing sensors on RC beams. These protocols guarantee the optimal placement of sensors, resulting in accurate strain measurements that improve the dependability of SHM. This contribution is significant because it addresses a critical problem in SHM and thus offers a potential solution for accurate strain measurement in real world RC structures.
- 5. DL Model for Structural Health Prediction: The development of a DL model capable of accurately predicting the structural health of RC beams is a substantial contribution to SHM. The model's high accuracy and sensitivity analysis demonstrated its dependability and suitability for SHM in RC beams, which indicates the potential for accurate predictions with limited data. In addition, analysing the precision of various sensors under varying loading conditions provides potential strategies for ensuring data integrity and operational continuity in emergencies.

This thesis contributes substantially to the existing knowledge in SHM of RC beams. The exhaustive SHM framework, the methods for sensor installation, the validated FEA model, the novel strain dataset generation

methodology, and the reliable DL model all offer potential solutions to the challenges associated with SHM of RC beams. In addition, these contributions pave the way for future research and development in this vital field.

#### 6.4. Generalisation of the SHM framework

The SHM framework proposed in this study is for RC beams. Figure 6.1 presents the flowchart for the generalisation of the framework. The following stages explained in the text can generalise the framework for a variety of structures and conditions:

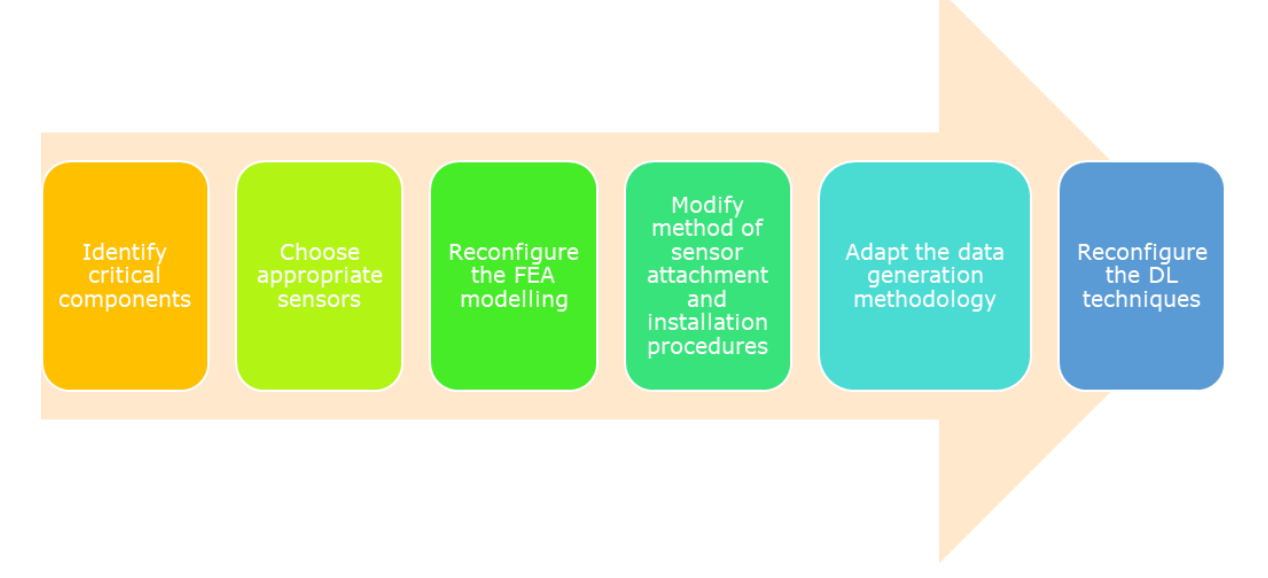


Figure 6.1: Flowchart for generalisation of the framework

- 1. *Identify critical components*: As per this study, a new analysis is necessary to identify the most crucial structural components for the type of structure under investigation. These components may differ depending on the structure type. This initial stage is essential for establishing the SHM framework's focus.
- Choose appropriate sensors: The selection of sensors must be reconsidered in light of the structure's type, and the identified critical components. For instance, if the structure is made of a distinct material, more sensitive sensors to that material may be necessary.

- 3. Reconfigure the FEA modelling: Depending on the complexity and characteristics of the new structure, it may be necessary to reconfigure the existing FEA model. This may involve selecting a different FEA model or modifying the current model's parameters.
- 4. Modify the method of sensor attachment and installation procedures:

  Depending on the material and geometry of the new structure, a new method for securing and positioning sensors may be required.
- 5. Adapt the data generation methodology: Depending on FEA and DL models, the data generation methodology may need to be modified. The dilation angle and number of steps may vary in the FEA model, if the structure is concrete.
- 6. Reconfigure the DL techniques: Depending on the complexity and characteristics of the new structure, reconfiguring the existing DL model may be necessary. The model may have to modify to accommodate various input data types or generate several predictions.

The framework introduced in this study can be generalised to other structures and conditions by following these procedures. Remembering that each new framework application may need modifications and adaptations to fit the particular context is necessary. Nonetheless, the study's overall methodology and lessons learned can serve as a valuable guide.

### 6.5. Suggestions for future research

Considering the advancements in SHM and the growing reliance on such systems for the safety of infrastructure, the following directions can provide valuable insights for future research:

1. Sensor Exploration: To optimise SHM systems, a comprehensive analysis of various DOFS sensors is required. To determine the optimal sensor for specific applications, its precision, sensitivity, durability, and price must be evaluated. In addition, exploring multi-sensor fusion techniques may provide a means to improve accuracy and guarantee redundant data acquisition in SHM scenarios.

- 2. Sensor Longevity: As sensors serve as the eyes and hearing of SHM systems, their durability and environmental stability are essential. Their operational life and dependability can be determined through rigorous testing in varying temperatures, humidity levels, and physical stressors. Such evaluations provide a greater comprehension of the sensor's performance over extended time periods and under varying conditions.
- 3. Framework Extension: Expanding the scope of the current SHM framework can cast light on its applicability to diverse RC structures including slabs, columns, and even expansive structures such as bridges and multi-story buildings. Incorporating additional non-destructive evaluation methods can enhance the framework and ensure an all-encompassing monitoring strategy.
- 4. FEA Models: A greater demand exists for sophisticated CDP based FEA models that can accurately depict the various types of damage, deterioration processes, and detailed non-linear behaviours that concrete exhibits under various loads.
- 5. Comparative Studies: A comparative study of various methodologies applied to similar RC structures can be useful for maximising the efficacy of SHM systems. This would highlight their respective benefits, limitations, and ideal applications. In addition, a combination of traditional monitoring systems and emerging DL models could provide an advanced SHM strategy that combines the best of both realms.

# REFERENCES

- 1. Figueiredo, E. and J. Brownjohn, *Three decades of statistical pattern recognition paradigm for SHM of bridges.* Structural Health Monitoring, 2022. **21**(6): p. 3018-3054.
- 2. He, Z., W. Li, H. Salehi, H. Zhang, H. Zhou, and P. Jiao, *Integrated structural health monitoring in bridge engineering*. Automation in Construction, 2022. **136**: p. 104168.
- 3. Xin, J., Y. Jiang, J. Zhou, L. Peng, S. Liu, and Q. Tang, *Bridge deformation prediction based on SHM data using improved VMD and conditional KDE.* Engineering Structures, 2022. **261**: p. 114285.
- 4. Sivasuriyan, A., D.S. Vijayan, W. Górski, Ł. Wodzyński, M.D. Vaverková, and E. Koda, *Practical implementation of structural health monitoring in multi-story buildings.* Buildings, 2021. **11**(6): p. 263.
- 5. Aytulun, E. and S. Soyöz, *Implementation and application of a SHM system for tall buildings in Turkey*. Bulletin of Earthquake Engineering, 2021: p. 1-24.
- 6. Zini, G., G. Bartoli, M. Betti, and F. Marafini. *A quality-based framework for data-driven SHM of heritage buildings*. in *2022 IEEE Workshop on Complexity in Engineering (COMPENG)*. 2022. IEEE.
- 7. Bouzenad, A.E., M. El Mountassir, S. Yaacoubi, F. Dahmene, M. Koabaz, L. Buchheit, and W. Ke, *A semi-supervised based k-means algorithm for optimal guided waves structural health monitoring: A case study.* Inventions, 2019. **4**(1): p. 17.
- 8. Wright, R.F., P. Lu, J. Devkota, F. Lu, M. Ziomek-Moroz, and P.R. Ohodnicki Jr, *Corrosion sensors for structural health monitoring of oil and natural gas infrastructure: A review.* Sensors, 2019. **19**(18): p. 3964.
- 9. Sen, D., A. Aghazadeh, A. Mousavi, S. Nagarajaiah, R. Baraniuk, and A. Dabak, *Data-driven semi-supervised and supervised learning algorithms for health monitoring of pipes.* Mechanical Systems and Signal Processing, 2019. **131**: p. 524-537.

- 10. Mitoulis, S.A., Challenges and opportunities for the application of integral abutment bridges in earthquake-prone areas: A review. Soil Dynamics and Earthquake Engineering, 2020. **135**: p. 106183.
- 11. Akiyama, M., D.M. Frangopol, and H. Ishibashi, *Toward life-cycle reliability-, risk-and resilience-based design and assessment of bridges and bridge networks under independent and interacting hazards: emphasis on earthquake, tsunami and corrosion.* Structure and Infrastructure Engineering, 2020. **16**(1): p. 26-50.
- 12. Chen, X., N. Xiang, Z. Guan, and J. Li, Seismic vulnerability assessment of tall pier bridges under mainshock-aftershock-like earthquake sequences using vector-valued intensity measure. Engineering Structures, 2022. **253**: p. 113732.
- 13. Argyroudis, S.A. and S.A. Mitoulis, *Vulnerability of bridges to individual and multiple hazards-floods and earthquakes.* Reliability engineering & system safety, 2021. **210**: p. 107564.
- 14. Mitoulis, S.A., S.A. Argyroudis, M. Loli, and B. Imam, *Restoration models for quantifying flood resilience of bridges.* Engineering structures, 2021. **238**: p. 112180.
- 15. Lamb, R., P. Garside, R. Pant, and J.W. Hall, *A probabilistic model of the economic risk to Britain's railway network from bridge scour during floods.* Risk Analysis, 2019. **39**(11): p. 2457-2478.
- 16. Capacci, L., F. Biondini, and A. Titi, *Lifetime seismic resilience of aging bridges and road networks.* Structure and Infrastructure Engineering, 2020. **16**(2): p. 266-286.
- 17. Vishwanath, B.S. and S. Banerjee, *Life-cycle resilience of aging bridges under earthquakes.* Journal of Bridge Engineering, 2019. **24**(11): p. 04019106.
- 18. Xu, J.-G., Z.-K. Cai, and D.-C. Feng, *Life-cycle seismic performance* assessment of aging RC bridges considering multi-failure modes of bridge columns. Engineering Structures, 2021. **244**: p. 112818.
- 19. Guo, S., R. Si, Q. Dai, Z. You, Y. Ma, and J. Wang, A critical review of corrosion development and rust removal techniques on the

- structural/environmental performance of corroded steel bridges. Journal of cleaner production, 2019. **233**: p. 126-146.
- 20. Menga, A., T. Kanstad, D. Cantero, L. Bathen, K. Hornbostel, and A. Klausen, Corrosion-induced damages and failures of posttensioned bridges: A literature review. Structural Concrete, 2023. 24(1): p. 84-99.
- 21. Fan, W., Y. Sun, C. Yang, W. Sun, and Y. He, *Assessing the response and fragility of concrete bridges under multi-hazard effect of vessel impact and corrosion.* Engineering structures, 2020. **225**: p. 111279.
- 22. Liu, X., W. Han, Y. Yuan, X. Chen, and Q. Xie, *Corrosion fatigue assessment and reliability analysis of short suspender of suspension bridge depending on refined traffic and wind load condition.*Engineering Structures, 2021. **234**: p. 111950.
- 23. Jiang, C., C. Wu, C. Cai, X. Jiang, and W. Xiong, *Corrosion fatigue analysis of stay cables under combined loads of random traffic and wind.* Engineering Structures, 2020. **206**: p. 110153.
- 24. Frangopol, D.M. and M. Liu, *Maintenance and management of civil infrastructure based on condition, safety, optimization, and life-cycle cost\*.* Structure and infrastructure engineering, 2007. **3**(1): p. 29-41.
- 25. Habel, W.R., *SHM systems supporting extension of the structures'* service life. 2013, Springer. p. 225-226.
- 26. Han, Q., Q. Ma, J. Xu, and M. Liu, *Structural health monitoring research under varying temperature condition: A review.* Journal of Civil Structural Health Monitoring, 2021. **11**: p. 149-173.
- 27. Chalioris, C.E., M.E. Voutetaki, and A.A. Liolios, *Structural health monitoring of seismically vulnerable RC frames under lateral cyclic loading.* Earthquakes and Structures, 2020. **19**(1): p. 29-44.
- 28. Singh, S., Cost model for reinforced concrete beam and slab structures in buildings. Journal of Construction Engineering and Management, 1990. **116**(1): p. 54-67.

- 29. Jumaat, M.Z., M. Kabir, and M. Obaydullah, *A review of the repair of reinforced concrete beams.* Journal of Applied Science Research, 2006. **2**(6): p. 317-326.
- 30. Jayawickrema, U., H. Herath, N. Hettiarachchi, H. Sooriyaarachchi, and J. Epaarachchi, *Fibre-optic sensor and deep learning-based structural health monitoring systems for civil structures: A review.*Measurement, 2022: p. 111543.
- 31. Stewart, M.G., Reliability safety assessment of corroding reinforced concrete structures based on visual inspection information. ACI Structural Journal, 2010. **107**(6): p. 671.
- 32. Omar, T. and M.L. Nehdi, *Condition assessment of reinforced concrete bridges: Current practice and research challenges.*Infrastructures, 2018. **3**(3): p. 36.
- 33. Alsharqawi, M., T. Dawood, S. Abdelkhalek, M. Abouhamad, and T. Zayed, *Condition assessment of concrete-made structures using ground penetrating radar.* Automation in Construction, 2022. **144**: p. 104627.
- 34. Verstrynge, E., C. Van Steen, E. Vandecruys, and M. Wevers, *Steel corrosion damage monitoring in reinforced concrete structures with the acoustic emission technique: A review.* Construction and Building Materials, 2022. **349**: p. 128732.
- 35. Yang, Y., Y. Zhang, and X. Tan, *Review on vibration-based structural health monitoring techniques and technical codes.* Symmetry, 2021. **13**(11): p. 1998.
- 36. Jain, K.K. and B. Bhattacharjee, *Application of fuzzy concepts to the visual assessment of deteriorating reinforced concrete structures.*Journal of Construction Engineering and Management, 2012. **138**(3): p. 399-408.
- 37. Oikonomopoulou, E.C., V.A. Palieraki, I.P. Sfikas, and C.G. Trezos, Reliability and limitations of GPR for identifying objects embedded in concrete–Experience from the lab. Case Studies in Construction Materials, 2022. **16**: p. e00898.

- 38. Godin, N., P. Reynaud, and G. Fantozzi, *Challenges and limitations in the identification of acoustic emission signature of damage mechanisms in composites materials.* Applied sciences, 2018. **8**(8): p. 1267.
- 39. Berrocal, C.G., I. Fernandez, M.F. Bado, J.R. Casas, and R. Rempling, Assessment and visualization of performance indicators of reinforced concrete beams by distributed optical fibre sensing. Structural Health Monitoring, 2021. **20**(6): p. 3309-3326.
- 40. Li, H.-J., H.-H. Zhu, D.-Y. Tan, B. Shi, and J.-H. Yin, *Detecting pipeline leakage using active distributed temperature Sensing: Theoretical modeling and experimental verification.* Tunnelling and Underground Space Technology, 2023. **135**: p. 105065.
- 41. Narisetty, C., T. Hino, M.-F. Huang, R. Ueda, H. Sakurai, A. Tanaka, T. Otani, and T. Ando, *Overcoming challenges of distributed fiber-optic sensing for highway traffic monitoring.* Transportation Research Record, 2021. **2675**(2): p. 233-242.
- 42. Bao, X. and L. Chen, *Recent progress in distributed fiber optic sensors*, sensors, 2012. **12**(7): p. 8601-8639.
- 43. Gupta, B.D., *Fiber optic sensors: principles and applications*. 2006: New India Publishing.
- 44. Udd, E. and W.B. Spillman Jr, *Fiber optic sensors: an introduction for engineers and scientists*. 2011: John Wiley & Sons.
- 45. Marcus, M.A. and B. Culshaw. Fiber optic sensor technology and applications IV (24-26 October 2005, Boston, Massachusetts, USA). in Proceedings of SPIE, the International Society for Optical Engineering. 2005. SPIE.
- 46. Majumder, M., T.K. Gangopadhyay, A.K. Chakraborty, K. Dasgupta, and D.K. Bhattacharya, *Fibre Bragg gratings in structural health monitoring—Present status and applications.* Sensors and Actuators A: Physical, 2008. **147**(1): p. 150-164.

- 47. Yin, J., H. Zhu, K. Fung, W. Jin, L. Mak, and K. Kuo. *Innovative optical fiber sensors for monitoring displacement of geotechnical structures*. in *HKIE Geotechnical Division. Seminar*. 2008.
- 48. Ren, L., T. Jiang, Z.-g. Jia, D.-s. Li, C.-l. Yuan, and H.-n. Li, *Pipeline corrosion and leakage monitoring based on the distributed optical fiber sensing technology.* Measurement, 2018. **122**: p. 57-65.
- 49. Liu, T., Y. Wei, G. Song, B. Hu, L. Li, G. Jin, J. Wang, Y. Li, C. Song, and Z. Shi, *Fibre optic sensors for coal mine hazard detection.*Measurement, 2018. **124**: p. 211-223.
- 50. He, X., Y. Pan, H. You, Z. Lu, L. Gu, F. Liu, D. Yi, and M. Zhang, *Fibre optic seismic sensor for down-well monitoring in the oil industry.*Measurement, 2018. **123**: p. 145-149.
- 51. Ghimire, M., C. Wang, K. Dixon, and M. Serrato, *In situ monitoring of prestressed concrete using embedded fiber loop ringdown strain sensor.* Measurement, 2018. **124**: p. 224-232.
- 52. Gong, J., G.M. Png, J.W. Arkwright, A.W. Papageorgiou, P.R. Cook, M.F. Lambert, A.R. Simpson, and A.C. Zecchin, *In-pipe fibre optic pressure sensor array for hydraulic transient measurement with application to leak detection.* Measurement, 2018. **126**: p. 309-317.
- 53. Amanzadeh, M., S.M. Aminossadati, M.S. Kizil, and A.D. Rakić, Recent developments in fibre optic shape sensing. Measurement, 2018. **128**: p. 119-137.
- 54. Campanella, C.E., A. Cuccovillo, C. Campanella, A. Yurt, and V.M. Passaro, *Fibre Bragg grating based strain sensors: Review of technology and applications.* Sensors, 2018. **18**(9): p. 3115.
- 55. López-Higuera, J.M., L.R. Cobo, A.Q. Incera, and A. Cobo, *Fiber optic sensors in structural health monitoring*. Journal of lightwave technology, 2011. **29**(4): p. 587-608.
- 56. Sigurdardottir, D. and B. Glisic, *On-site validation of fiber-optic methods for structural health monitoring: Streicker Bridge.* Journal of Civil Structural Health Monitoring, 2015. **5**: p. 529-549.

- 57. Lai, J., J. Qiu, H. Fan, Q. Zhang, Z. Hu, J. Wang, and J. Chen, *Fiber bragg grating sensors-based in situ monitoring and safety assessment of loess tunnel.* Journal of Sensors, 2016. **2016**.
- 58. Barrias, A., J.R. Casas, and S. Villalba, *SHM of reinforced concrete elements by Rayleigh backscattering DOFS.* Frontiers in Built Environment, 2019. **5**: p. 30.
- 59. Wong, L., W.K. Chiu, and J. Kodikara, *Using distributed optical fibre sensor to enhance structural health monitoring of a pipeline subjected to hydraulic transient excitation.* Structural Health Monitoring, 2018. **17**(2): p. 298-312.
- 60. Zhang, F., Z. Zhou, Q. Liu, and W. Xu, *An intelligent service matching method for mechanical equipment condition monitoring using the fibre Bragg grating sensor network.* Enterprise Information Systems, 2017. **11**(2): p. 284-309.
- 61. Xue, R., B. Ren, J. Huang, Z. Yan, and Z. Du, *Design and evaluation of FBG-based tension sensor in laparoscope surgical robots.* Sensors, 2018. **18**(7): p. 2067.
- 62. Lvov, N., S. Khabarov, A. Todorov, and A. Barabanov, *Versions of fiber-optic sensors for monitoring the technical condition of aircraft structures.* Civil Engineering Journal, 2018. **4**(12): p. 2895-2902.
- 63. Goossens, S., B. De Pauw, T. Geernaert, M.S. Salmanpour, Z.S. Khodaei, E. Karachalios, D. Saenz-Castillo, H. Thienpont, and F. Berghmans, Aerospace-grade surface mounted optical fibre strain sensor for structural health monitoring on composite structures evaluated against in-flight conditions. Smart Materials and Structures, 2019. **28**(6): p. 065008.
- 64. Berri, P., M. Dalla Vedova, P. Maggiore, and T. Scolpito. *Feasibility study of FBG-based sensors for prognostics in aerospace applications*. in *Journal of Physics: Conference Series*. 2019. IOP Publishing.
- 65. Pei, Y., T. Liao, J. Xu, H. Lin, and T. Ning. *FBG strain sensor applied in harsh environment of aerospace*. in *2018 IEEE 3rd Optoelectronics Global Conference (OGC)*. 2018. IEEE.

- 66. Hong, C.-Y., Y.-F. Zhang, M.-X. Zhang, L.M.G. Leung, and L.-Q. Liu, Application of FBG sensors for geotechnical health monitoring, a review of sensor design, implementation methods and packaging techniques. Sensors and Actuators A: Physical, 2016. **244**: p. 184-197.
- 67. Zhou, J., L. Sun, and H. Li, *Study on dynamic response measurement of the submarine pipeline by full-term FBG sensors.* The Scientific World Journal, 2014. **2014**.
- Leung, C.K., K.T. Wan, D. Inaudi, X. Bao, W. Habel, Z. Zhou, J. Ou, M. Ghandehari, H.C. Wu, and M. Imai, *Optical fiber sensors for civil engineering applications*. Materials and Structures, 2015. 48: p. 871-906.
- 69. Zeng, X., X. Bao, C.Y. Chhoa, T.W. Bremner, A.W. Brown, M.D. DeMerchant, G. Ferrier, A.L. Kalamkarov, and A.V. Georgiades, *Strain measurement in a concrete beam by use of the Brillouin-scattering-based distributed fiber sensor with single-mode fibers embedded in glass fiber reinforced polymer rods and bonded to steel reinforcing bars.* Applied optics, 2002. **41**(24): p. 5105-5114.
- 70. Sahota, J.K., N. Gupta, and D. Dhawan, *Fiber Bragg grating sensors* for monitoring of physical parameters: A comprehensive review. Optical Engineering, 2020. **59**(6): p. 060901-060901.
- 71. Tan, C., Y. Shee, B. Yap, and F.M. Adikan, *Fiber Bragg grating based sensing system: Early corrosion detection for structural health monitoring.* Sensors and Actuators A: Physical, 2016. **246**: p. 123-128.
- 72. Guo, H., G. Xiao, N. Mrad, and J. Yao, *Fiber optic sensors for structural health monitoring of air platforms.* Sensors, 2011. **11**(4): p. 3687-3705.
- 73. Rocha, R., J. Gomes, J. Carmo, A. Silva, and J. Correia, *Low-cost/high-reproducibility flexible sensor based on photonics for strain measuring.* Optics & Laser Technology, 2014. **56**: p. 278-284.

- 74. Di Sante, R., Fibre optic sensors for structural health monitoring of aircraft composite structures: Recent advances and applications. Sensors, 2015. **15**(8): p. 18666-18713.
- 75. Bal, H.K., F. Sidiroglou, Z. Brodzeli, S.A. Wade, G.W. Baxter, and S.F. Collins. *Temperature independent bend measurement using a pi-phase shifted FBG at twice the Bragg wavelength*. in *Fourth European Workshop on Optical Fibre Sensors*. 2010. SPIE.
- 76. Shao, L.-Y., L. Xiong, C. Chen, A. Laronche, and J. Albert, *Directional bend sensor based on re-grown tilted fiber Bragg grating.* Journal of Lightwave Technology, 2010. **28**(18): p. 2681-2687.
- 77. Zhou, D.-P., L. Wei, W.-K. Liu, and J.W. Lit, *Simultaneous strain and temperature measurement with fiber Bragg grating and multimode fibers using an intensity-based interrogation method.* IEEE Photonics Technology Letters, 2009. **21**(7): p. 468-470.
- 78. Leal-Junior, A.G., C.A. Díaz, A. Frizera, C. Marques, M.R. Ribeiro, and M.J. Pontes, *Simultaneous measurement of pressure and temperature with a single FBG embedded in a polymer diaphragm.*Optics & Laser Technology, 2019. **112**: p. 77-84.
- 79. Guo, J.-Y., B. Shi, M.-Y. Sun, C.-C. Zhang, G.-Q. Wei, and J. Liu, Characterization of an ORMOCER®-coated FBG sensor for relative humidity sensing. Measurement, 2021. **171**: p. 108851.
- 80. Woyessa, G., A. Fasano, C. Markos, H.K. Rasmussen, and O. Bang, Low loss polycarbonate polymer optical fiber for high temperature FBG humidity sensing. IEEE Photonics Technology Letters, 2017. **29**(7): p. 575-578.
- 81. Kakei, A.A., M. Islam, J. Leng, and J.A. Epaarachchi, *Use of an elasto-*plastic model and strain measurements of embedded fibre Bragg

  grating sensors to detect Mode I delamination crack propagation in

  woven cloth (0/90) composite materials. Structural health

  monitoring, 2018. **17**(2): p. 363-378.

- 82. Li, T., Y. Tan, Z. Zhou, and K. Zheng, *A non-contact FBG vibration sensor with double differential temperature compensation.* Optical Review, 2016. **23**: p. 26-32.
- 83. Lv, J., Z. Hu, G. Ren, C. Zhang, and Y. Liu, *Research on new FBG displacement sensor and its application in Beijing Daxing airport project.* Optik, 2019. **178**: p. 146-155.
- 84. Hong, C., Y. Zhang, Y. Yang, and Y. Yuan, *A FBG based displacement transducer for small soil deformation measurement.* Sensors and Actuators A: Physical, 2019. **286**: p. 35-42.
- 85. Yazdizadeh, Z., H. Marzouk, and M.A. Hadianfard, *Monitoring of concrete shrinkage and creep using Fiber Bragg Grating sensors.*Construction and Building Materials, 2017. **137**: p. 505-512.
- 86. Zheng, R., L. Liu, X. Zhao, Z. Chen, C. Zhang, and X. Hua, Investigation of measurability and reliability of adhesive-bonded built-in fiber Bragg grating sensors on steel wire for bridge cable force monitoring. Measurement, 2018. **129**: p. 349-357.
- 87. Zhu, W., Q. Shen, and H. Qin, *Monitoring of prestress and bond stress of self-sensing FBG steel strand.* Measurement, 2021. **177**: p. 109246.
- 88. Kaklauskas, G., A. Sokolov, R. Ramanauskas, and R. Jakubovskis, Reinforcement strains in reinforced concrete tensile members recorded by strain gauges and FBG sensors: experimental and numerical analysis. Sensors, 2019. **19**(1): p. 200.
- 89. Li, W., C. Xu, S.C.M. Ho, B. Wang, and G. Song, *Monitoring concrete deterioration due to reinforcement corrosion by integrating acoustic emission and FBG strain measurements.* Sensors, 2017. **17**(3): p. 657.
- 90. Zhao, Y., D. Hu, M. Zhang, W. Dai, and W. Zhang, *The location monitoring of fatigue crack damage by using the spectral area extracted from FBG spectra.* Sensors, 2020. **20**(8): p. 2375.

- 91. Wu, Q., Y. Semenova, A. Sun, P. Wang, and G. Farrell, *High resolution temperature insensitive interrogation technique for FBG sensors.*Optics & Laser Technology, 2010. **42**(4): p. 653-656.
- 92. Bednarz, B., P. Popielski, R. Sieńko, T. Howiacki, and Ł. Bednarski, Distributed fibre optic sensing (DFOS) for deformation assessment of composite collectors and pipelines. Sensors, 2021. **21**(17): p. 5904.
- 93. Verstrynge, E., K. De Wilder, A. Drougkas, E. Voet, K. Van Balen, and M. Wevers, *Crack monitoring in historical masonry with distributed strain and acoustic emission sensing techniques.* Construction and Building Materials, 2018. **162**: p. 898-907.
- 94. Kim, S.-T., Y.-S. Park, C.-H. Yoo, S. Shin, and Y.-H. Park, *Analysis of Long-Term Prestress Loss in Prestressed Concrete (PC) Structures Using Fiber Bragg Grating (FBG) Sensor-Embedded PC Strands.*Applied Sciences, 2021. **11**(24): p. 12153.
- 95. Ma, F., X. Cheng, X. Zhu, G. Wu, D.-C. Feng, S. Hou, and X. Kang, Safety Monitoring of Bearing Replacement for a Concrete High-Speed Railway Bridge Based on Acoustic Emission. Journal of Performance of Constructed Facilities, 2022. **36**(3): p. 04022014.
- 96. Ho, S.C.M., L. Ren, H.-N. Li, and G. Song, *A fiber Bragg grating sensor* for detection of liquid water in concrete structures. Smart Materials and Structures, 2013. **22**(5): p. 055012.
- 97. Guo, Y., J. Kong, H. Liu, D. Hu, and L. Qin, *Design and investigation of a reusable surface-mounted optical fiber Bragg grating strain sensor.* IEEE Sensors Journal, 2016. **16**(23): p. 8456-8462.
- 98. Ye, X.-W., Y.-H. Su, and P.-S. Xi, Statistical analysis of stress signals from bridge monitoring by FBG system. Sensors, 2018. **18**(2): p. 491.
- 99. Liang, M. and X. Fang, Application of fiber Bragg grating sensing technology for bolt force status monitoring in roadways. Applied Sciences, 2018. **8**(1): p. 107.
- 100. Bonopera, M., K.-C. Chang, C.-C. Chen, Z.-K. Lee, Y.-C. Sung, and N. Tullini, *Fiber Bragg grating-differential settlement measurement*

- system for bridge displacement monitoring: Case study. Journal of Bridge Engineering, 2019. **24**(10): p. 05019011.
- 101. Zhang, C., Y. Ge, Z. Hu, K. Zhou, G. Ren, and X. Wang, *Research on deflection monitoring for long span cantilever bridge based on optical fiber sensing.* Optical Fiber Technology, 2019. **53**: p. 102035.
- 102. Li, D.S., L. Ren, H.-N. Li, and G. Song, Structural Health Monitoring of a Tall Building during Construction with Fiber Bragg Grating Sensors. International Journal of Distributed Sensor Networks, 2012.
- 103. Chao, C.-R., W.-L. Liang, and T.-C. Liang, *Design and testing of a 2D optical fiber sensor for building tilt monitoring based on fiber Bragg gratings.* Applied System Innovation, 2017. **1**(1): p. 2.
- 104. Bao, X. and L. Chen, *Recent progress in Brillouin scattering based fiber sensors*. Sensors, 2011. **11**(4): p. 4152-4187.
- 105. Miah, K. and D.K. Potter, A review of hybrid fiber-optic distributed simultaneous vibration and temperature sensing technology and its geophysical applications. Sensors, 2017. **17**(11): p. 2511.
- 106. Barrias, A., J.R. Casas, and S. Villalba, A review of distributed optical fiber sensors for civil engineering applications. Sensors, 2016. 16(5): p. 748.
- 107. Glisic, B. and D. Inaudi, *Development of method for in-service crack detection based on distributed fiber optic sensors.* Structural Health Monitoring, 2012. **11**(2): p. 161-171.
- 108. Güemes, A., A. Fernández-López, and B. Soller, *Optical fiber distributed sensing-physical principles and applications*. Structural Health Monitoring, 2010. **9**(3): p. 233-245.
- 109. Du, C., S. Dutta, P. Kurup, T. Yu, and X. Wang, *A review of railway infrastructure monitoring using fiber optic sensors.* Sensors and Actuators A: Physical, 2020. **303**: p. 111728.
- 110. Wang, H., Q. Sun, X. Li, J. Wo, P.P. Shum, and D. Liu, *Improved location algorithm for multiple intrusions in distributed Sagnac fiber sensing system.* Optics express, 2014. **22**(7): p. 7587-7597.

- 111. Liang, S., X. Sheng, S. Lou, P. Wang, and Y. Zhang, *Novel Lissajous figure based location method for fiber-optic distributed disturbance sensor.* Optik, 2015. **126**(23): p. 4362-4366.
- 112. Berrocal, C.G., I. Fernandez, and R. Rempling, *Crack monitoring in reinforced concrete beams by distributed optical fiber sensors.*Structure and Infrastructure Engineering, 2021. **17**(1): p. 124-139.
- 113. Barrias, A., J.R. Casas, and S. Villalba, *Fatigue performance of distributed optical fiber sensors in reinforced concrete elements.*Construction and Building Materials, 2019. **218**: p. 214-223.
- 114. Sieńko, R., M. Zych, Ł. Bednarski, and T. Howiacki, *Strain and crack analysis within concrete members using distributed fibre optic sensors.* Structural Health Monitoring, 2019. **18**(5-6): p. 1510-1526.
- 115. Fan, L., X. Tan, Q. Zhang, W. Meng, G. Chen, and Y. Bao, *Monitoring corrosion of steel bars in reinforced concrete based on helix strains measured from a distributed fiber optic sensor.* Engineering Structures, 2020. **204**: p. 110039.
- 116. Zhang, S., B. Liu, and J. He, *Pipeline deformation monitoring using distributed fiber optical sensor.* Measurement, 2019. **133**: p. 208-213.
- 117. Yoon, H.-J., K.-Y. Song, C. Choi, H.-S. Na, and J.-S. Kim, *Real-time distributed strain monitoring of a railway bridge during train passage by using a distributed optical fiber sensor based on brillouin optical correlation domain analysis.* Journal of Sensors, 2016. **2016**.
- 118. Barrias, A., G. Rodriguez, J.R. Casas, and S. Villalba, *Application of distributed optical fiber sensors for the health monitoring of two real structures in Barcelona.* Structure and Infrastructure Engineering, 2018. **14**(7): p. 967-985.
- 119. Siwowski, T., M. Rajchel, R. Sienko, and L. Bednarski. *Smart monitoring of the FRP composite bridge with distributed fibre optic sensors*. in *Proceedings of the 9th International Conference on Fibre-Reinforced Polymer (FRP) Composites in Civil Engineering (CICE 2018), Paris.* 2018.

- 120. Rodriguez, G., J.R. Casas, and S. Villalba, Shear crack pattern identification in concrete elements via distributed optical fibre grid. Structure and Infrastructure Engineering, 2019. 15(12): p. 1630-1648.
- 121. Teguedy, M.C., C. Joly-Lapalice, L. Sorelli, and D. Conciatori, *Optical fiber sensors implementation for monitoring the early-age behavior of full-scale Timber-Concrete Composite slabs.* Construction and Building Materials, 2019. **226**: p. 564-578.
- 122. Bassil, A., X. Chapeleau, D. Leduc, and O. Abraham, *Concrete crack monitoring using a novel strain transfer model for distributed fiber optics sensors.* Sensors, 2020. **20**(8): p. 2220.
- 123. Bado, M.F., J.R. Casas, and G. Kaklauskas, *Distributed Sensing* (DOFS) in Reinforced Concrete members for reinforcement strain monitoring, crack detection and bond-slip calculation. Engineering Structures, 2021. **226**: p. 111385.
- 124. Tarfaoui, M., M. Nachtane, and H. Boudounit, *Finite element analysis of composite offshore wind turbine blades under operating conditions.*Journal of Thermal Science and Engineering Applications, 2020.

  12(1).
- 125. Saini, M.K., A.K. Bagha, S. Kumar, and S. Bahl, *Finite element analysis for predicting the vibration characteristics of natural fiber reinforced epoxy composites.* Materials Today: Proceedings, 2021. **41**: p. 223-227.
- 126. Sur, A., P. Pal, S. Mondal, and M. Kanoria, *Finite element analysis in a fiber-reinforced cylinder due to memory-dependent heat transfer.*Acta Mechanica, 2019. **230**: p. 1607-1624.
- 127. Ali, L., X. Liu, B. Ali, S. Mujeed, and S. Abdal, *Finite element analysis of thermo-diffusion and multi-slip effects on MHD unsteady flow of casson nano-fluid over a shrinking/stretching sheet with radiation and heat source.* Applied Sciences, 2019. **9**(23): p. 5217.

- 128. Cervera, M. and M. Chiumenti, *Smeared crack approach: back to the original track.* International journal for numerical and analytical methods in geomechanics, 2006. **30**(12): p. 1173-1199.
- 129. Dahlblom, O. and N.S. Ottosen, *Smeared crack analysis using generalized fictitious crack model.* Journal of engineering mechanics, 1990. **116**(1): p. 55-76.
- 130. Edalat-Behbahani, A., J.A. Barros, and A. Ventura-Gouveia, *Three dimensional plastic-damage multidirectional fixed smeared crack approach for modelling concrete structures.* International Journal of Solids and Structures, 2017. **115**: p. 104-125.
- 131. Bejarano-Urrego, L., E. Verstrynge, G. Giardina, and K. Van Balen, Crack growth in masonry: numerical analysis and sensitivity study for discrete and smeared crack modelling. Engineering Structures, 2018. 165: p. 471-485.
- 132. Thybo, A.E.A., A. Michel, and H. Stang, *Smeared crack modelling approach for corrosion-induced concrete damage.* Materials and Structures, 2017. **50**: p. 1-14.
- 133. Ngo, T. and P. Mendis, Modelling the dynamic response and failure modes of reinforced concrete structures subjected to blast and impact loading. Structural Engineering and Mechanics, 2009. **32**(2): p. 269-282.
- 134. Theiner, Y. and G. Hofstetter, *Numerical prediction of crack propagation and crack widths in concrete structures.* Engineering structures, 2009. **31**(8): p. 1832-1840.
- 135. Sato, Y. and K. Naganuma, *Discrete-like crack simulation by smeared crack-based FEM for reinforced concrete.* Earthquake engineering & structural dynamics, 2007. **36**(14): p. 2137-2152.
- 136. Rimkus, A., V. Cervenka, V. Gribniak, and J. Cervenka, *Uncertainty* of the smeared crack model applied to RC beams. Engineering Fracture Mechanics, 2020. **233**: p. 107088.
- 137. Dias-da-Costa, D., V. Cervenka, and R. Graça-e-Costa, *Model uncertainty in discrete and smeared crack prediction in RC beams*

- *under flexural loads.* Engineering Fracture Mechanics, 2018. **199**: p. 532-543.
- 138. Barros, J.A., H. Baghi, and A. Ventura-Gouveia, *Assessing the applicability of a smeared crack approach for simulating the behaviour of concrete beams flexurally reinforced with GFRP bars and failing in shear.* Engineering Structures, 2021. **227**: p. 111391.
- 139. Genikomsou, A.S. and M.A. Polak. *Damaged plasticity modelling of concrete in finite element analysis of reinforced concrete slabs*. in 9th International Conference on Fracture Mechanics of Concrete and Concrete Structures University of California. 2016.
- 140. Tao, Y. and J.-F. Chen, *Concrete damage plasticity model for modeling FRP-to-concrete bond behavior*. Journal of composites for construction, 2015. **19**(1): p. 04014026.
- 141. Minh, H.-L., S. Khatir, M.A. Wahab, and T. Cuong-Le, *A concrete damage plasticity model for predicting the effects of compressive high-strength concrete under static and dynamic loads.* Journal of Building Engineering, 2021. **44**: p. 103239.
- 142. Hafezolghorani, M., F. Hejazi, R. Vaghei, M.S.B. Jaafar, and K. Karimzade, *Simplified damage plasticity model for concrete*. Structural Engineering International, 2017. **27**(1): p. 68-78.
- 143. Chi, Y., M. Yu, L. Huang, and L. Xu, *Finite element modeling of steel-polypropylene hybrid fiber reinforced concrete using modified concrete damaged plasticity.* Engineering Structures, 2017. **148**: p. 23-35.
- 144. Sümer, Y. and M. Aktaş, *Defining parameters for concrete damage plasticity model*. Challenge Journal of Structural Mechanics, 2015. **1**(3): p. 149-155.
- 145. Gao, D., Z. Gu, C. Wei, C. Wu, and Y. Pang, Effects of fiber clustering on fatigue behavior of steel fiber reinforced concrete beams.

  Construction and Building Materials, 2021. **301**: p. 124070.

- 146. Shokoohfar, A. and A. Rahai, *Nonlinear analysis of pre-stressed concrete containment vessel (PCCV) using the damage plasticity model.* Nuclear engineering and design, 2016. **298**: p. 41-50.
- 147. Li, S., Y. Yang, Q. Pu, D. Yang, B. Sun, and X. Li, *Three-dimensional nonlinear creep and shrinkage effects of a long-span prestressed concrete box girder bridge.* Structural Concrete, 2019. **20**(2): p. 638-649.
- 148. Singh, M., A. Sheikh, M.M. Ali, P. Visintin, and M. Griffith, Experimental and numerical study of the flexural behaviour of ultrahigh performance fibre reinforced concrete beams. Construction and Building Materials, 2017. **138**: p. 12-25.
- 149. Lee, S.-H., A. Abolmaali, K.-J. Shin, and H.-D. Lee, *ABAQUS modeling* for post-tensioned reinforced concrete beams. Journal of Building Engineering, 2020. **30**: p. 101273.
- 150. Kadhim, M.M., A.R. Jawdhari, M.J. Altaee, and A.H. Adheem, *Finite element modelling and parametric analysis of FRP strengthened RC beams under impact load.* Journal of Building Engineering, 2020. **32**: p. 101526.
- 151. Zhu, Y., Y. Zhang, X. Li, and G. Chen, *Finite element model to predict* structural response of predamaged RC beams reinforced by toughness-improved UHPC under unloading status. Engineering Structures, 2021. **235**: p. 112019.
- 152. Raza, A. and A. Ahmad, *Numerical investigation of load-carrying capacity of GFRP-reinforced rectangular concrete members using CDP model in ABAQUS.* Advances in Civil Engineering, 2019. **2019**.
- 153. Hanif, M.U., Z. Ibrahim, M. Jameel, K. Ghaedi, and M. Aslam, *A new approach to estimate damage in concrete beams using non-linearity.*Construction and Building Materials, 2016. **124**: p. 1081-1089.
- 154. Rad, M.M., S.K. Ibrahim, and J. Lógó. *Limit design of reinforced concrete haunched beams by the control of the residual plastic deformation*. in *Structures*. 2022. Elsevier.

- 155. Lakavath, C., S.S. Prakash, and S. Dirar, *Experimental and numerical studies on shear behaviour of macro-synthetic fibre reinforced prestressed concrete beams.* Construction and Building Materials, 2021. **291**: p. 123313.
- 156. Nabi, J. and A.A. Rahim. *On the possibility of using damaged plasticity models in the assessment of structural response of gravity beams*. in *Structures*. 2021. Elsevier.
- 157. Solhmirzaei, R. and V. Kodur, *Modeling the response of ultra high performance fiber reinforced concrete beams.* Procedia engineering, 2017. **210**: p. 211-219.
- 158. Rahman, A.F., W. Goh, N. Mohamad, M.S. Kamarudin, and A.A. Jhatial, *Numerical analysis and experimental validation of reinforced foamed concrete beam containing partial cement replacement.* Case Studies in Construction Materials, 2019. **11**: p. e00297.
- 159. Pham, D.Q., T.N. Nguyen, S.T. Le, T.T. Pham, and T.D. Ngo. *The structural behaviours of steel reinforced geopolymer concrete beams:*An experimental and numerical investigation. in Structures. 2021. Elsevier.
- 160. Jasim, W.A., Y.B.A. Tahnat, and A.M. Halahla. *Behavior of reinforced concrete deep beam with web openings strengthened with (CFRP) sheet.* in *Structures*. 2020. Elsevier.
- 161. Mansour, W. and B.A. Tayeh, *Shear behaviour of RC beams strengthened by various ultrahigh performance fibre-reinforced concrete systems.* Advances in Civil Engineering, 2020. **2020**: p. 1-18.
- 162. Yan, J.-B. and J. Xie, *Behaviours of reinforced concrete beams under low temperatures.* Construction and Building Materials, 2017. **141**: p. 410-425.
- 163. Abouali, S., M. Shahverdi, M. Ghassemieh, and M. Motavalli, Nonlinear simulation of reinforced concrete beams retrofitted by near-surface mounted iron-based shape memory alloys. Engineering Structures, 2019. **187**: p. 133-148.

- 164. Jumaa, G.B. and A.R. Yousif. *Numerical modeling of size effect in shear strength of FRP-reinforced concrete beams*. in *Structures*. 2019. Elsevier.
- 165. LeCun, Y., Y. Bengio, and G. Hinton, *Deep learning*. nature, 2015. **521**(7553): p. 436-444.
- 166. Abdughani, M., J. Ren, L. Wu, J.-M. Yang, and J. Zhao, *Supervised deep learning in high energy phenomenology: a mini review.*Communications in Theoretical Physics, 2019. **71**(8): p. 955.
- 167. Pumsirirat, A. and Y. Liu, *Credit card fraud detection using deep learning based on auto-encoder and restricted boltzmann machine.*International Journal of advanced computer science and applications, 2018. **9**(1).
- 168. Gangwar, A.K. and V. Ravi. Wip: Generative adversarial network for oversampling data in credit card fraud detection. in Information Systems Security: 15th International Conference, ICISS 2019, Hyderabad, India, December 16–20, 2019, Proceedings 15. 2019. Springer.
- 169. Pandey, T.N., A.K. Jagadev, S. Dehuri, and S.-B. Cho, *A novel committee machine and reviews of neural network and statistical models for currency exchange rate prediction: An experimental analysis.* Journal of King Saud University-Computer and Information Sciences, 2020. **32**(9): p. 987-999.
- 170. Gudelek, M.U., S.A. Boluk, and A.M. Ozbayoglu. *A deep learning based stock trading model with 2-D CNN trend detection*. in *2017 IEEE symposium series on computational intelligence (SSCI)*. 2017. IEEE.
- 171. Gugulothu, N., V. Tv, P. Malhotra, L. Vig, P. Agarwal, and G. Shroff, Predicting remaining useful life using time series embeddings based on recurrent neural networks. arXiv preprint arXiv:1709.01073, 2017.

- 172. Zhang, S., Y. Yao, J. Hu, Y. Zhao, S. Li, and J. Hu, *Deep autoencoder neural networks for short-term traffic congestion prediction of transportation networks.* Sensors, 2019. **19**(10): p. 2229.
- 173. Talo, M., O. Yildirim, U.B. Baloglu, G. Aydin, and U.R. Acharya, Convolutional neural networks for multi-class brain disease detection using MRI images. Computerized Medical Imaging and Graphics, 2019. **78**: p. 101673.
- 174. Yildirim, O., M. Talo, B. Ay, U.B. Baloglu, G. Aydin, and U.R. Acharya, Automated detection of diabetic subject using pre-trained 2D-CNN models with frequency spectrum images extracted from heart rate signals. Computers in biology and medicine, 2019. **113**: p. 103387.
- 175. Bouktif, S., A. Fiaz, A. Ouni, and M.A. Serhani, *Optimal deep learning lstm model for electric load forecasting using feature selection and genetic algorithm: Comparison with machine learning approaches.*Energies, 2018. **11**(7): p. 1636.
- 176. Chen, K., K. Chen, Q. Wang, Z. He, J. Hu, and J. He, *Short-term load forecasting with deep residual networks.* IEEE Transactions on Smart Grid, 2018. **10**(4): p. 3943-3952.
- 177. Zheng, L., V. Noroozi, and P.S. Yu. *Joint deep modeling of users and items using reviews for recommendation*. in *Proceedings of the tenth ACM international conference on web search and data mining*. 2017.
- 178. He, X., L. Liao, H. Zhang, L. Nie, X. Hu, and T.-S. Chua. *Neural collaborative filtering*. in *Proceedings of the 26th international conference on world wide web*. 2017.
- 179. Wang, N., Y. Jiang, Y. Zhong, and L. Shao, *An adaptive damage detection method based on differential evolutionary algorithm for beam structures.* Measurement, 2021. **178**: p. 109227.
- 180. Das, S. and P. Saha, *Performance of swarm intelligence based chaotic meta-heuristic algorithms in civil structural health monitoring.*Measurement, 2021. **169**: p. 108533.

- 181. Zhou, Y., S. Zhou, G. Hao, and J. Zhang, *Bridge influence line identification based on big data and interval analysis with affine arithmetic.* Measurement, 2021. **183**: p. 109807.
- 182. Chen, Y., J. Liang, X. Gu, Q. Zhang, H. Deng, and S. Li, *An improved minimal path selection approach with new strategies for pavement crack segmentation.* Measurement, 2021. **184**: p. 109877.
- 183. Fukushima, K. and S. Miyake, *Neocognitron: A new algorithm for pattern recognition tolerant of deformations and shifts in position.*Pattern recognition, 1982. **15**(6): p. 455-469.
- 184. Hossain, M.S., Z.C. Ong, Z. Ismail, S. Noroozi, and S.Y. Khoo, Artificial neural networks for vibration based inverse parametric identifications: A review. Applied Soft Computing, 2017. **52**: p. 203-219.
- 185. Grekousis, G., Artificial neural networks and deep learning in urban geography: A systematic review and meta-analysis. Computers, Environment and Urban Systems, 2019. **74**: p. 244-256.
- 186. Bengio, Y., *Learning deep architectures for AI.* Foundations and trends® in Machine Learning, 2009. **2**(1): p. 1-127.
- 187. Schmidhuber, J., *Deep learning in neural networks: An overview.*Neural networks, 2015. **61**: p. 85-117.
- 188. Kim, B. and S. Cho, *Automated vision-based detection of cracks on concrete surfaces using a deep learning technique.* Sensors, 2018.

  18(10): p. 3452.
- 189. Atha, D.J. and M.R. Jahanshahi, *Evaluation of deep learning approaches based on convolutional neural networks for corrosion detection.* Structural Health Monitoring, 2018. **17**(5): p. 1110-1128.
- 190. Frniak, M., M. Markovic, P. Kamencay, J. Dubovan, M. Benco, and M. Dado, *Vehicle classification based on fbg sensor arrays using neural networks.* Sensors, 2020. **20**(16): p. 4472.
- 191. Derakhshani, A. and A.H. Foruzan, *Predicting the principal strong ground motion parameters: A deep learning approach.* Applied Soft Computing, 2019. **80**: p. 192-201.

- 192. Pathirage, C.S.N., J. Li, L. Li, H. Hao, W. Liu, and P. Ni, *Structural damage identification based on autoencoder neural networks and deep learning*. Engineering structures, 2018. **172**: p. 13-28.
- 193. Rafiei, M.H. and H. Adeli, *A novel unsupervised deep learning model* for global and local health condition assessment of structures. Engineering Structures, 2018. **156**: p. 598-607.
- 194. Moon, H.S., S. Ok, P.-j. Chun, and Y.M. Lim, *Artificial neural network* for vertical displacement prediction of a bridge from strains (Part 1): Girder bridge under moving vehicles. Applied Sciences, 2019. **9**(14): p. 2881.
- 195. Tan, Z.X., D.P. Thambiratnam, T.H. Chan, M. Gordan, and H. Abdul Razak, *Damage detection in steel-concrete composite bridge using vibration characteristics and artificial neural network.* Structure and Infrastructure Engineering, 2020. **16**(9): p. 1247-1261.
- 196. Xu, W.-Z., C.B. Li, J. Choung, and J.-M. Lee, *Corroded pipeline failure* analysis using artificial neural network scheme. Advances in engineering software, 2017. **112**: p. 255-266.
- 197. Mangalathu, S., G. Heo, and J.-S. Jeon, *Artificial neural network based multi-dimensional fragility development of skewed concrete bridge classes.* Engineering Structures, 2018. **162**: p. 166-176.
- 198. Khandel, O. and M. Soliman, *Integrated framework for assessment of time-variant flood fragility of bridges using deep learning neural networks.* Journal of Infrastructure Systems, 2021. **27**(1): p. 04020045.
- 199. Xu, H., X. Su, H. Xu, and H. Li. Autonomous bridge crack detection using deep convolutional neural networks. in 3rd International Conference on Computer Engineering, Information Science & Application Technology (ICCIA 2019). 2019. Atlantis Press.
- 200. Liang, X., Image-based post-disaster inspection of reinforced concrete bridge systems using deep learning with Bayesian optimization. Computer-Aided Civil and Infrastructure Engineering, 2019. **34**(5): p. 415-430.

- 201. Xu, Y., Y. Bao, J. Chen, W. Zuo, and H. Li, Surface fatigue crack identification in steel box girder of bridges by a deep fusion convolutional neural network based on consumer-grade camera images. Structural Health Monitoring, 2019. **18**(3): p. 653-674.
- 202. Li, S. and L. Sun, Detectability of bridge-structural damage based on fiber-optic sensing through deep-convolutional neural networks.

  Journal of Bridge Engineering, 2020. **25**(4): p. 04020012.
- 203. Ayele, Y.Z., M. Aliyari, D. Griffiths, and E.L. Droguett, *Automatic crack segmentation for UAV-assisted bridge inspection*. Energies, 2020. **13**(23): p. 6250.
- 204. Nguyen, D.H., Q.B. Nguyen, T. Bui-Tien, G. De Roeck, and M.A. Wahab, *Damage detection in girder bridges using modal curvatures gapped smoothing method and Convolutional Neural Network: Application to Bo Nghi bridge.* Theoretical and Applied Fracture Mechanics, 2020. **109**: p. 102728.
- 205. Ma, R., Z. Zhang, Y. Dong, and Y. Pan, *Deep learning based vehicle detection and classification methodology using strain sensors under bridge deck.* Sensors, 2020. **20**(18): p. 5051.
- 206. Rizzo, F. and L. Caracoglia, *Artificial Neural Network model to predict the flutter velocity of suspension bridges.* Computers & Structures, 2020. **233**: p. 106236.
- 207. Wang, D., Y. Zhang, Y. Pan, B. Peng, H. Liu, and R. Ma, *An automated inspection method for the steel box girder bottom of long-span bridges based on deep learning.* Ieee Access, 2020. **8**: p. 94010-94023.
- 208. Shang, Z., L. Sun, Y. Xia, and W. Zhang, *Vibration-based damage detection for bridges by deep convolutional denoising autoencoder.*Structural Health Monitoring, 2021. **20**(4): p. 1880-1903.
- 209. Bae, H., K. Jang, and Y.-K. An, Deep super resolution crack network (SrcNet) for improving computer vision-based automated crack detectability in in situ bridges. Structural Health Monitoring, 2021. **20**(4): p. 1428-1442.

- 210. Yu, Y., C. Wang, X. Gu, and J. Li, *A novel deep learning-based method for damage identification of smart building structures.* Structural Health Monitoring, 2019. **18**(1): p. 143-163.
- 211. Perez, H., J.H. Tah, and A. Mosavi, *Deep learning for detecting building defects using convolutional neural networks.* Sensors, 2019. **19**(16): p. 3556.
- 212. Nex, F., D. Duarte, F.G. Tonolo, and N. Kerle, *Structural building damage detection with deep learning: Assessment of a state-of-the-art CNN in operational conditions.* Remote sensing, 2019. **11**(23): p. 2765.
- 213. Moosazadeh, S., E. Namazi, H. Aghababaei, A. Marto, H. Mohamad, and M. Hajihassani, *Prediction of building damage induced by tunnelling through an optimized artificial neural network.* Engineering with Computers, 2019. **35**: p. 579-591.
- 214. Cao, B.-T., M. Obel, S. Freitag, P. Mark, and G. Meschke, *Artificial neural network surrogate modelling for real-time predictions and control of building damage during mechanised tunnelling.* Advances in Engineering Software, 2020. **149**: p. 102869.
- 215. Gonzalez, D., D. Rueda-Plata, A.B. Acevedo, J.C. Duque, R. Ramos-Pollan, A. Betancourt, and S. Garcia, *Automatic detection of building typology using deep learning methods on street level images.*Building and Environment, 2020. 177: p. 106805.
- 216. Wight, J.K. and J.G. MacGregor, *Reinforced Concrete: Mechanics and Design*. 2011: Pearson Education.
- 217. Nilson, A.H., D. Darwin, and C.W. Dolan, *Design of Concrete Structures*. 2010: McGraw-Hill Higher Education.
- 218. Institution, B.S. and E.C.f. Standardization, Eurocode 2: Design of Concrete Structures: Part 1-1: General Rules and Rules for Buildings. 2004: British Standards Institution.
- 219. Tam, H.-y., K.-k. Lee, S.-y. Liu, L.-h. Cho, and K.-c. Cheng. Intelligent optical fibre sensing networks facilitate shift to predictive

- maintenance in railway systems. in 2018 International Conference on Intelligent Rail Transportation (ICIRT). 2018. IEEE.
- 220. Wang, Y., H. Yao, J. Wang, and X. Xin, *Distributed Optical Fiber Sensing System for Large Infrastructure Temperature Monitoring*. IEEE Internet of Things Journal, 2021. **9**(5): p. 3333-3345.
- 221. Najafabadi, M.M., F. Villanustre, T.M. Khoshgoftaar, N. Seliya, R. Wald, and E. Muharemagic, *Deep learning applications and challenges in big data analytics.* Journal of big data, 2015. **2**(1): p. 1-21.
- 222. Cai, X., W. Chang, L. Gao, and C. Zhou, *Design and application of real-time monitoring system for service status of continuously welded turnout on the high-speed railway bridge.* Journal of Transportation Safety & Security, 2021. **13**(7): p. 735-758.
- 223. Robles Urquijo, I., A. Quintela Incera, S. Van Vaerenbergh, D. Inaud, and J.M. Lopez Higuera. *Risks and opportunities of using fibre optic sensors for long term infrastructure health monitoring systems in an 18 year old installation*. in *International Conference on Smart Infrastructure and Construction 2019 (ICSIC) Driving data-informed decision-making*. 2019. ICE Publishing.
- 224. Ni, F., J. Zhang, and M.N. Noori, *Deep learning for data anomaly detection and data compression of a long-span suspension bridge.*Computer-Aided Civil and Infrastructure Engineering, 2020. **35**(7): p. 685-700.
- 225. Khandel, O., M. Soliman, R.W. Floyd, and C.D. Murray, *Performance assessment of prestressed concrete bridge girders using fiber optic sensors and artificial neural networks.* Structure and Infrastructure Engineering, 2021. **17**(5): p. 605-619.
- 226. Mustapha, S., A. Kassir, K. Hassoun, Z. Dawy, and H. Abi-Rached, Estimation of crowd flow and load on pedestrian bridges using machine learning with sensor fusion. Automation in Construction, 2020. **112**: p. 103092.

- 227. Oh, B.K., K.J. Kim, Y. Kim, H.S. Park, and H. Adeli, *Evolutionary learning based sustainable strain sensing model for structural health monitoring of high-rise buildings.* Applied Soft Computing, 2017. **58**: p. 576-585.
- 228. Kong, X., C. Cai, J. Hu, W. Xiong, and H. Peng, Field application of an innovative bridge scour monitoring system with fiber Bragg grating sensors. Journal of Aerospace Engineering, 2017. 30(2): p. B4016008.
- 229. Xiao, F., D. Meng, Y. Yu, Y. Ding, L. Zhang, G.S. Chen, W. Zatar, and J.L. Hulsey, *Estimation of vehicle-induced bridge dynamic responses using fiber Bragg grating strain gages.* Science Progress, 2020. **103**(1): p. 0036850419874201.
- 230. Bao, Y., Z. Tang, H. Li, and Y. Zhang, *Computer vision and deep learning-based data anomaly detection method for structural health monitoring*. Structural Health Monitoring, 2019. **18**(2): p. 401-421.
- 231. Li, N.-L., S.-F. Jiang, M.-H. Wu, S. Shen, and Y. Zhang, *Deformation monitoring for Chinese traditional timber buildings using fiber Bragg grating sensors.* Sensors, 2018. **18**(6): p. 1968.
- 232. McCulloch, W.S. and W. Pitts, *A logical calculus of the ideas immanent in nervous activity.* The bulletin of mathematical biophysics, 1943. **5**(4): p. 115-133.
- 233. Bishop, C.M., *Neural Networks and Their Applications*. Review of Scientific Instruments, 1994. **65**(6): p. 1803-1832.
- 234. Gasteiger, J. and J. Zupan, *Neural networks in chemistry*. Angewandte Chemie International Edition in English, 1993. **32**(4): p. 503-527.
- 235. Oliveira, R., R.C. Araújo, F.J. Barros, A.P. Segundo, R.F. Zampolo, W. Fonseca, V. Dmitriev, and F.S. Brasil, A system based on artificial neural networks for automatic classification of hydro-generator stator windings partial discharges. Journal of Microwaves, Optoelectronics and Electromagnetic Applications, 2017. 16: p. 628-645.

- 236. Hecht-Nielsen, R., *On the algebraic structure of feedforward network weight spaces*, in *Advanced Neural Computers*. 1990, Elsevier. p. 129-135.
- 237. Saikia, P., R.D. Baruah, S.K. Singh, and P.K. Chaudhuri, *Artificial Neural Networks in the domain of reservoir characterization: A review from shallow to deep models.* Computers & Geosciences, 2020. **135**: p. 104357.
- 238. Ramberg, W. and W.R. Osgood, *Description of stress-strain curves* by three parameters. 1943.
- 239. Concrete, F.I.B.I.F.S., *CEB-FIP Model Code 1990: Design Code*. 1993: T. Telford.
- 240. Qingfu, L., G. Wei, and K. Yihang. *Parameter calculation and verification of concrete plastic damage model of ABAQUS*. in *IOP conference series: Materials science and engineering*. 2020. IOP Publishing.
- 241. Simulia, D., *ABAQUS 6.11 analysis user's manual.* Abaqus, 2011. **6**: p. 22.2.
- 242. Hillerborg, A., M. Modéer, and P.-E. Petersson, *Analysis of crack formation and crack growth in concrete by means of fracture mechanics and finite elements.* Cement and concrete research, 1976. **6**(6): p. 773-781.
- 243. Hillerborg, A., *The theoretical basis of a method to determine the fracture energyG F of concrete.* Materials and structures, 1985. **18**(4): p. 291-296.
- 244. Chen, H., B. Xu, J. Wang, X. Nie, and Y.-L. Mo, *XFEM-based multiscale simulation on monotonic and hysteretic behavior of reinforced-concrete columns.* Applied Sciences, 2020. **10**(21): p. 7899.
- 245. Mahmud, G.H., Z. Yang, and A.M. Hassan, *Experimental and numerical studies of size effects of Ultra High Performance Steel Fibre Reinforced Concrete (UHPFRC) beams.* Construction and Building materials, 2013. **48**: p. 1027-1034.

- 246. Genikomsou, A.S. and M.A. Polak, *Finite element analysis of punching shear of concrete slabs using damaged plasticity model in ABAQUS.*Engineering structures, 2015. **98**: p. 38-48.
- 247. Othman, H. and H. Marzouk, *Finite-element analysis of reinforced concrete plates subjected to repeated impact loads.* Journal of Structural Engineering, 2017. **143**(9): p. 04017120.
- 248. Behnam, H., J. Kuang, and B. Samali, *Parametric finite element analysis of RC wide beam-column connections.* Computers & Structures, 2018. **205**: p. 28-44.
- 249. Milligan, G.J., M.A. Polak, and C. Zurell, *Finite element analysis of punching shear behaviour of concrete slabs supported on rectangular columns.* Engineering Structures, 2020. **224**: p. 111189.
- 250. Bhartiya, R., D.R. Sahoo, and A. Verma, *Modified damaged plasticity* and variable confinement modelling of rectangular CFT columns.

  Journal of Constructional Steel Research, 2021. **176**: p. 106426.
- 251. Le Thanh, C., H.-L. Minh, and T. Sang-To, *A nonlinear concrete damaged plasticity model for simulation reinforced concrete structures using ABAQUS.* Frattura ed Integrità Strutturale, 2022. **16**(59): p. 232-242.
- 252. Kaushik, A., G. Patnaik, A. Rajput, and G. Prakash, *Nonlinear behaviour of concrete under low-velocity impact by using a damaged plasticity model.* Iranian Journal of Science and Technology, Transactions of Civil Engineering, 2022. **46**(5): p. 3655-3677.
- 253. Barrias, A., J.R. Casas, and S. Villalba, *Distributed optical fibre sensors in concrete structures: Performance of bonding adhesives and influence of spatial resolution.* Structural Control and Health Monitoring, 2019. **26**(3): p. e2310.
- 254. Leonhardt, F., *Cracks and crack control in concrete structures.* Pci Journal, 1988. **33**(4): p. 124-145.
- 255. Technologies, L., *Optical Backscatter Reflectometer Model 4600.* 2013.

256. Barrias, A., J. R. Casas, and S. Villalba, *Embedded distributed optical fiber sensors in reinforced concrete structures—A case study.*Sensors, 2018. **18**(4): p. 980.